



CHARACTERISATION OF THE MECHANO-CHEMICAL  
RELATIONSHIP BETWEEN ACTIN AND MICROTUBULE  
CYTOSKELETONS AND THE ACTIVE MOTION OF  
CYTOPLASMIC COMPONENTS

Layla Ammar al-Khatib

*Supervisor: Isabel Palacios*

*School of Biological and Behavioural Sciences*

*Department of Biochemistry*

*Submitted in partial fulfilment of the requirements of the Degree of Doctor of Philosophy*

# STATEMENT OF ORIGINALITY

I, Layla Ammar al-Khatib, confirm that the research included within this thesis is my own work or that where it has been carried out in collaboration with, or supported by others, that this is duly acknowledged below and my contribution indicated. Previously published material is also acknowledged below.

I attest that I have exercised reasonable care to ensure that the work is original, and does not to the best of my knowledge break any UK law, infringe any third party's copyright or other Intellectual Property Right, or contain any confidential material.

I accept that the College has the right to use plagiarism detection software to check the electronic version of the thesis. I confirm that this thesis has not been previously submitted for the award of a degree by this or any other university.

The copyright of this thesis rests with the author and no quotation from it or information derived from it may be published without the prior written consent of the author.

Signature:

Date: 21 Jun 2024

In collaboration with Fabio Giavazzi and Roberto Cerbino (Department BIOMETRA, University of Milan).

Publications: Drechsler M, Lang LF, Al-Khatib L, Dirks H, Burger M, Schönlieb CB, Palacios IM. Optical flow analysis reveals that Kinesin-mediated advection impacts the orientation of microtubules in the *Drosophila* oocyte. Mol Biol Cell. 2020 Jun 1;31(12):1246-1258. <https://doi.org/10.1091/mbc.E19-08-0440>

# ACKNOWLEDGEMENTS

This endeavour would not have been possible without the support of QMUL and SBBS, for which I am very grateful.

Mama, Baba and Samir – my beam of light through the darkness, thank you for helping me back on the path when I needed it. This one is for you.

Bea – you and I both know I would not have made it this far without you. You are my inspiration and the best co-worker I will ever have. I am going to make sure we continue to work and gossip together throughout our undoubtedly very successful lives. Thank you for always being there to remind me who I am. I cannot wait to do the same for you.

Stephen – your unrelenting support and faith in me from afar helped me get through this arduous journey more than you know. Thank you for emulating the type of academic I strive to be and showing me time and time again that I am more capable than I think.

Nat – my bro, if you weren't around, I would have given up a long time ago. Thank you for being my home and my safe space. Thank you for always reminding me of the world outside. You are my saving grace.

Samhita – my lifeboat. Thank you a million times over for always providing me with the respite I needed and always knowing when not to ask how my writing was going.

Adam – thank you for reminding me of the true meaning of 'work smart, not hard'.

## ABSTRACT

The advancements in imaging techniques have markedly enhanced the ability to observe and reconstruct dynamic cellular processes, thereby deepening our understanding of cell behaviour. This study's primary objective is to probe the intricate dynamics influencing organelle motion within the *Drosophila melanogaster* oocyte, aiming to unravel the nuanced mechanochemical relationship between cytoskeletal networks and organelle dynamics, and the forces governing organelle motion in the cell. Utilizing a combination of confocal microscopy, differential dynamic microscopy and single particle tracking, this research explores the reciprocal relationship between actin and microtubules and their impact on the morphology, motion, and distribution of endosomes and mitochondria in the oocyte. The findings underscore a tightly interconnected system involving organelle dynamics and cytoskeletal function for proper distribution, morphology, and transport of organelles. Notably, this intricate orchestration suggests that susceptibility to certain types of motion and modes of transport extends beyond the physical characteristics of the cytoplasm and the mechanisms generating force in that environment. Instead, it is significantly shaped by the dynamic interplay with other cellular components, subtly influencing their mutual functions. The results reveal variations in advective and diffusive rates among organelle populations, with Rab5-positive early endosomes and mitochondria exhibiting the highest and most consistent advective motion, while Rab7-positive late endosomes display higher diffusive rates. The study also sheds light on the influence of mitochondrial dynamics and morphology on the motility of other organelles, namely endosomes. This investigation carries broader implications for disease research, drawing parallels with abnormal mitochondrial morphologies found in neuropathies and neurodegeneration. In essence, this research contributes to unravelling the intricate mechanisms governing organelle motion, adding to the foundational understanding of biophysical principles influencing cellular processes. *Word count: 272*



# LIST OF FIGURES AND TABLES

## Figures

### Chapter 1

**Figure 1.1. *Drosophila melanogaster* as a model organism.** (pg.18)

**(A-B)** the male and female fruit fly (photos taken from Thomas Cline/UC Berkeley). Male flies have shorter abdomens that round at the bottom while female flies have longer abdomens that point at the bottom with comparatively more stripes than males.

**Figure 1.2. *Drosophila oogenesis.*** (pg.20)

**(A)** Schematic and scanning electron microscopy (SEM) image of *st14* mature egg (latter image taken from Dr. Bob Argiropoulos of UBC Department of Zoology). **(B)** Schematic of *Drosophila* ovaries each containing 18 ovarioles. **(B')** Schematic and fluorescent images of ovariole showing stages of oogenesis starting with the germarium and ending with a mature egg competent for fertilisation (Image taken from Quinlan 2016). The germarium at the anterior of the ovariole contains somatic and germline stem cells. Egg chambers develop inside the germarium from germline cyst cells and exit the structure once they are surrounded by follicle cells (FCs) and one of the 16 cells within the cyst differentiates as the oocyte. **(C)** Schematic of *st10* egg chamber. Each egg chamber is surrounded by a monolayer of follicular epithelia. FCs synthesise and transport yolk peptides into the oocyte, secrete eggshell components and participate in cell signalling events for establishment of oocyte polarity and axis formation (anterior - A, posterior - P).

**Figure 1.3. Cytoskeletal networks in eukaryotic cells.** (pg.22)

**(A)** The MT and actin cytoskeletal network in the eukaryotic cell. The  $\alpha$ - and  $\beta$ -tubulin monomers that comprise microtubule filaments form a heterodimer and associate with other dimers in a head-to-tail formation forming laterally arranged linear protofilaments. The  $\beta$ -tubulin monomer is oriented towards the faster growing end (plus-end) while  $\alpha$ -tubulin is oriented towards the slower growing end (minus-end) conferring polarity to the MT filament. Approximately 13 protofilaments assemble around a hollow core creating a tube-like structure. **(B)** Filaments alternate stochastically between two states growing (rescue) and shrinking (catastrophe) for rapid reorganisation and the ability to 'search' its environment. **(C)** The actin can be found in its monomeric (G-actin) or filamentous (F-actin) form. Polymerisation occurs at the plus-ends, or barbed ends, of filaments while depolymerisation occurs at the minus-ends or pointed ends and is regulated by nucleotide hydrolysis.

**Figure 1.4. Superfamilies of motor proteins: myosin, kinesin, and dynein.** (pg.25)

**(A)** Myosin is composed of four domains: the motor head, the lever arm, the targeting domain, and the coiled coil. Myosin II contains two heavy chains, two essential light chains and two regulatory light chains. The structural changes undergone for ATP hydrolysis cause the myosin lever arm to move, creating the 'myosin powerstroke' creating force for movement along the actin filament. Kinesin-1 is a tetramer with a homodimer of two kinesin-1 heavy chains and two light chains. Heavy chains are responsible for kinesin motor activity while light chains are involved in cargo-binding. ATP hydrolysis triggers conformational changes that allow kinesin to interact with MTs and generate force. Cytoplasmic dynein is a two-headed motor. Conformational changes of the dynein globular head from nucleotide binding creates a swing-like motion for translocation along the filaments.

(B) Dynein activity requires dynactin. Dynactin is a multisubunit protein which creates a complex by binding to the dynein intermediate chain through its p150 glued subunit.

**Figure 1.5 Microtubule organisation in different cells.** (pg.27)

(A) Schematic of microtubule organisation in the neuron where kinesin drives anterograde motion in the axon towards the periphery while dynein drives retrograde transport towards the cell centre. (B) Schematic of radially polarised microtubule organisation in mouse fibroblast cells (C) Schematic of microtubule organisation in *st9* and *st11* oocytes. During mid-oogenesis (*st9*) microtubules are nucleated from the cortex of the oocyte with plus ends biased toward the posterior. During late oogenesis (*st11*) microtubules are organised in thick bundles along the cortex in coordination with the initiation of fast streaming. (C') Left image: projection of 8 images of autofluorescent yolk granules in *st9* oocytes where the actin mesh is still present halting movement of the granules. Right image: projection of 8 images of autofluorescent yolk granules in *st11* oocytes after the actin mesh has disappeared allowing for rapid movement of granules under the force of fast cytoplasmic streaming (Adapted from Quinlan 2016). (D-G) Asymmetric localisation of body determinants *oskar* (*osk*), *bicoid* (*bic*) and *gurken* (*grk*). *osk* localises in a crescent shape at the posterior pole specifying where the pole plasm forms for abdomen and germline development (E), *bcd* localises anteriorly for segmentation of the head and thorax in embryogenesis (F) and *gurken* (*grk*) localises near the nucleus where it triggers dorsal differentiation (G). (Images adapted from Becalska & Gavis 2009; anterior - A, posterior - P; oocyte - oo; follicle cell - fc; nurse cell - nc).

**Figure 1.6. The actin mesh in wildtype, *capu* and *spire* mutant *st9* oocytes.** (pg.31)

(A-C') Egg chambers stained with TRITC-Phalloidin to label F-actin. Gray scale bar represents 30  $\mu\text{m}$ , white scale bar represents 10  $\mu\text{m}$ . (Images taken from Dahlggaard et al. 2007). (A-A') *St9* wildtype oocytes (B-B') *St9 capu<sup>2F</sup>* mutant oocytes. *capu<sup>2F</sup>* contains a point mutation in the FH2 domain and is one of the weakest alleles of *capu* explaining the residual actin mesh in these mutants (C-C') *St9 capu<sup>G7</sup>/Df(2L)ed<sup>5Z1</sup>* mutant oocytes. *capu* levels are lower in this mutant than (B-B') coinciding with an imperceptible actin mesh (D-G) F-actin binding UTRN-GFP (green, left panel) and DIC (right panel) in *st9* oocytes (Images taken from Drechsler et al. 2017). (D) *St9* control oocytes with intact actin mesh (E) *St9* oocytes overexpressing actin nucleator SpireB. Overexpression of SpireB leads to an increase in the levels of F-actin in the oocyte (F) *spire* mutant oocytes incubated in control DMSO-containing medium (G) *spire* mutant oocyte incubated in colchicine-containing medium. The actin mesh fails to form in *spire* mutant oocytes. Scale bar represents 30 $\mu\text{m}$

**Figure 1.7. Distribution of kinesin, dynein and *grk* mRNA in the oocyte.** (pg.33)

(A) Dynein and kinesin heavy chain accumulation is observed in the posterior of wildtype *st9* oocytes (top row). Staining for Khc is absent in the null mutants and posterior localisation of Dhc is abolished (bottom row) (Image taken from Palacios & St Johnston 2002; anterior - A, posterior - P). (B) Disruption of *Khc* also affects *grk* localisation in *st8* (left column) and *st10* (right column) oocytes. White asterisk denotes nucleus positioning, scale bars represent 50 $\mu\text{m}$  (Image taken from Brendza et al. 2002).

**Figure 1.8. MT orientation according to speed of flows.** (pg.34-35)

(A) EB-1 attaches to plus ends of MTs and serves as a readout for spatial orientation, represented here as an angle deviating from an imaginary anterior (180°) to posterior axis (0°). (B) Underlying principle of OF-based motion estimation. Two consecutive frames of a 5 × 5 pixel-wide image sequence containing a rectangular object of different pixel intensities—from light green (little

signal) to dark green (maximum signal). OF assumes signal intensity does not to change along the objects' trajectory. A displacement vector for each pixel can then be calculated using variational OF as indicated by the yellow arrow, showing the displacement vector of the centre pixel. **(C)** Definition of growth directions: angles of velocities between  $90^\circ$  and  $270^\circ$  are anterior (A, blue hemicircle) and the complementary set of angles as posterior (P, orange hemicircle). The subpopulation of all posterior signals (orange) that fall between  $330^\circ$  and  $30^\circ$  (light orange sector) are considered to grow toward the posterior tip. **(D)** Raw image demonstrating EB1 expression, magnified area indicated by dashed box (anterior - A, posterior - P) MTs grow one order magnitude faster than cytoplasmic flow and images were taken every 650ms with low spatial resolution and the presence of a lot of noise. Images thus required denoising **(E)**. Scale bars are  $10\ \mu\text{m}$ . **(F)** Temporal projection of EB1 in control oocyte (65s image sequence). Oocytes were orientated with the posterior pole to the right during imaging and the angles given in the rose diagrams **(G,L,Q)** reflect the directional movement of EB1 comets in each cell. Distribution was also averaged across all cells of a given phenotype **(H,M,R)**. We determined the mean angular direction of the estimated motion of EB1 signals ( $\theta_{\text{avg}}$ ) of a single phenotype to quantitatively describe MT orientation **(I,N,S)**. **(G)** Angular histogram with 50 bins for EB1 directions in individual control cells, each colour representing the angular histogram of EB1 direction from one oocyte. **(H)** Data from **(G)** averaged over all cells ( $n = 8$ ), error bars (black) represent standard deviation for each bin (blue). **(I)** Mean angular direction  $\theta_{\text{avg}}$  of **(H)**, red line in **(H)**, and length  $r$  between 0 and 1 of mean resultant vector, depicted by length of black line originating from centre of **(H)** relating to the circular variance  $S = 1-r$  of distribution shown in **(H)**. **(J)** Similar rose diagram to **(G,L,Q)** but growth directions are put into four bins:  $30^\circ\text{--}90^\circ$ ,  $90^\circ\text{--}270^\circ$ ,  $270^\circ\text{--}330^\circ$ , and  $330^\circ\text{--}30^\circ$ . Same analysis in control cells **(F-J)** applied to *khc<sup>slow</sup>* oocytes **(K-O)** and *khc<sup>null</sup>* oocytes **(P-T)**. All images taken from Drechsler et al. 2020.

**Figure 1.9 Endolysosomal pathway (taken from Yang & Wang 2021).** (pg.39)

To transport endosomal proteins to lysosomes, early endosomes undergo a maturation process characterized by the switching of Rab5 and phosphatidylinositol 3-phosphate (PtdIns3P) to late endosome-specific Rab7 and phosphatidylinositol 3,5-bisphosphate (PtdIns(3,5)P2). Proteins that are destined for lysosomal degradation undergo recycling through retromer-dependent and retromer-independent pathways, returning to the plasma membrane or Golgi apparatus. The process of autophagy transports cytoplasmic material to the lysosome for degradation. This process supports cell survival by removing damaged organelles and protein aggregates, and maintaining bioenergetic homeostasis. Autophagosomes undergo a maturation process to fuse with late endosomes/lysosomes, employing essentially the same sets of proteins (Rab7/HOPS/SNAREs) as those involved in the fusion of endosomes and lysosomes (Yang & Wang 2021).

**Figure 1.10. Mitochondria dynamics.** (pg.43)

**(A)** Simplified schematic of mitochondrial fusion. Mfn1/Mfn2 are found on the outer mitochondrial membrane (OMM) while Opa1 mediates fusion on the IMM. Fusion thus begins with fusing of the OMM mediated by Mfn1/2 followed by fusing of the IMM through the activity of Opa1. **(B)** Simplified schematic of mitochondria fission. Dynamin-related protein 1 (Drp1) and dynamin-2 (Dnm2) found on the OMM drive fission through constriction and scission, respectively, recruited by mitochondrial fission factor (Mff) and mitochondrial dynamics proteins 49 and 51 (MiD49 and MiD51). Fission can also be ER-mediated for larger mitochondrial tubules where the diameters of Drp1 and Dnm2 are not wide enough to form contractile rings.

**Figure 1.11. Changes in mitochondrial morphology upon mutation of fusion-fission machinery.** (pg.44-45)

(A-F) (Images taken from Chen et al. 2003) Mitochondria-EYFP counterstained with rhodamine-phalloidin in mouse embryonic fibroblast (MEF) cells. (A-B) Mitochondrial morphology in wild-type MEF cells. (C-D) Mitochondria morphology in *Mfn1* mutant MEF cells (E-F) Mitochondrial morphology in *Mfn2* mutant. Arrow indicates a tubule >10 $\mu$ m in length. (G-H) HeLa cells transfected with GFP-siRNA for controls (cont.) or human Opa1 and cells were stained with MitoTracker (Images taken from Ishihara et al. 2006). (H) Mitochondrial network was fragmented in *Opa1* mutants. (I-N) Mitochondria visualised by GFP-tagging mitochondria in *mitochondrial genome maintenance-1 (mgm1)* mutant *Saccharomyces cerevisiae (S. cerevisiae)* cells. Mgm1 is a dynamin-like GTPase necessary for mitochondrial fusion in yeast (Images taken from Wong et al. 2000). (J-M) *mgm1* mutant cells displayed fragmented mitochondria when compared to controls (I-L). (K-N)  $\Delta$ *mgm1* mutants also displayed a fragmented mitochondrial network when compared to controls with a slightly more dramatic phenotype. Scale bars represent 2 $\mu$ m. (O-T) MEF cells expressing mitochondria-DsRed and YFP-tagged  $\alpha$ -tubulin (Images taken from Ishihara et al. 2009). (O-Q) *Drp1 lox/lox* MEFs. (P) In the early mitotic phase, mitochondria are fragmented and spread throughout the cytoplasm in control cells. (R-T) *Drp1<sup>-/-</sup>* MEFs. (S) Mitochondria displayed filamentous morphology and clustered leading to asymmetric division of the mitochondrial network between daughter cells (T).

**Figure 1.12. Motion and crowding in the cell.** (pg.52)

(A) Cargo can undergo direct transport as motor protein cargo on cytoskeletal filaments, advection because of the viscous drag created by the translocation of motor proteins, ATP-driven active diffusion, and thermal diffusion (red strands - actin filaments). (B) A cartoon of the crowded cytoplasm in a eukaryotic cell. The image illustrates a section of the cytoplasm with an edge length of 100nm. Sizes, shapes, and number of macromolecules are approximately correct (Image taken from Ellis (2001)).

**Figure 1.13. Simulated and in vivo actin filaments and ER taken from Novak (2009).** (pg.54)

(A) Electron micrograph of actin filaments in a keratocyte (B) Long thin cylinders representing cytoskeletal filaments (C) Optical section of ER of the unfertilized sea urchin eggs (D) Random three-dimensional disks modelling ER sheets.

## Chapter 2

**Figure 2.1 Schematic of the Drosophila UAS/Gal4 system.** (pg.57)

The driver line (left) contains Gal4, the expression of which is controlled by a tissue-specific enhancer, and the UAS reporter line (right) contains the gene of interest (gene x). Gal4 will then bind to UAS to activate transcription of gene x. Progeny will carry the UAS-gene expressed in a pattern according to Gal4 tissue-specificity.

**Figure 2.2 Fourier transform decomposition.** (pg.61)

Decomposition of an image into its constituent signals relating to their length scales. Each image describes the evolution of a system at these length scales (Image courtesy of Fabio Giavazzi).

**Figure 2.3 Dynamic analysis of vesicle motion: ISF and decorrelation rates as a function of spatial frequency.** (pg.62)

(A) Intermediate scattering functions (ISF)  $f(q, \Delta t)$  for different wave vectors  $q$  in the range  $1.8\mu\text{m}^{-1} < q < 8\mu\text{m}^{-1}$ . (B) Decorrelation rates  $\Gamma_1(q)$  (solid black boxes) and  $\Gamma_2(q)$  (open boxes) from the fit of the ISF plotted against the wave

vector  $q$ .  $\Gamma_1(q)$ , which accounts for the ballistic contribution to the motion of the vesicles, exhibits a linear scaling  $\Gamma_1(q) = v_{ves}q$  (dashed line), while  $\Gamma_2(q)$  which describes a diffusive-like relaxation process, is well fitted to a quadratic law  $\Gamma_2(q) = D_{ves}q^2$  (continuous line).

**Figure 2.4. Vesicle selection process.** (pg. 67)

Representative images showcasing the criteria used for vesicle selection. Vesicles with a clearly discernible membrane circumference were prioritized for measurement. Additionally, preference was given to vesicles displaying an absence of fluorescence in the central region, as indicated by a black appearance (yellow arrowheads – selected, red arrowheads – not selected).

### Chapter 3

**Figure 3.1 Motion and dynamics of Rab7 vesicle subgroups and mitochondria.** (pg. 75)

**(A)** The two predominant groups of Rab7 vesicles observed are characterised as group (1) 'small' vesicles (white arrows) showcasing strongly directed and persistent motion, and group (2) 'large' or 'donut-like' vesicles (yellow arrows) **(B-B')** Single particle tracking of group (1) Rab7 vesicles using ImageJ plugin TrackMate to reconstruct trajectory of vesicles and measure velocity. Scale bar represents 30 $\mu$ m (anterior - A, posterior - P). **(C)** Histogram presenting mean velocities of small Rab7 vesicles (nm/s) in the oocyte falling within the range of the velocity of kinesin. **(D-D')** Single particle tracking of mitochondria moving in directed and persistent manner. Scale bar represents 30 $\mu$ m. **(E)** Histogram presenting mean velocities of mitochondria (nm/s) in the oocyte. Scale bar represents 30 $\mu$ m.

**Figure 3.2. Changes in distribution of Rab7 vesicles in oocytes mutant for kinesin.** (pg. 77)

**(A)** YFP-tagged Rab7 vesicles in control oocyte. Rab7 vesicles in control oocytes vary in size from small vesicles (diffraction limited, 250-300nm) to larger 'donut-like' vesicles (average diameter 0.5-2.5  $\mu$ m). Vesicle distribution here is widespread in the oocyte with a higher density of larger endosomes towards the posterior at the location of MT plus ends (white arrowheads) (anterior – A, posterior - P). **(A')** DIC vesicles in the same control oocyte. Sizes vary similarly to Rab7 vesicles and are also widely distributed across the oocyte. **(B)** YFP-tagged Rab7 vesicles in *KhcRNAi* background developed at 25°C. There is a distinct lack of large vesicles in this condition and a 'cloud' of YFP concentrated at the posterior of the oocyte which may be an accumulation of stationary Rab7 vesicles (white arrowhead). **(B')** DIC vesicles in the same oocyte. Vesicles here do not display abnormal distribution but there is an observable reduction in size when compared to vesicles in A'. **(C)** YFP-tagged Rab7 vesicles in *KhcRNAi* background developed at 28°C. Here we see a drastic difference in vesicle distribution and size. Small endosomes are concentrated along the cortex (white arrowheads) and in a small area in the middle of the oocyte towards the anterior (yellow arrowhead). No group 2 Rab7 vesicles are visible. **(C')** DIC vesicles in the same oocyte. In addition to vesicles being concentrated along the cortex, vesicles accumulate at the posterior and are absent in the centre and towards the anterior of the oocyte (white arrowhead). Scale bar represents 20 $\mu$ m.

**Figure 3.3 YFP-tagged Rab5 and Rab7 vesicle distribution in st9 wildtype oocytes.** (pg.89)

**(A)** YFP-tagged Rab5 vesicles. Distribution of Rab5 vesicles is concentrated mainly along the cortex of the oocyte (white arrows). **(B)** YFP-tagged Rab7 vesicles. Rab7 vesicles are distributed extensively within the cytoplasm, exhibiting a significant concentration cortically and at the posterior of the oocyte (white arrows). Scale bar represents 10µm.

**Figure 3.4. Variable morphology of the mitochondrial network in wildtype st9 oocytes.** (pg.80)

**(A)** YFP-tagged mitochondria in st9 oocytes. A closer look at the different morphologies displayed by mitochondria in the same cell. Scale bar represents 20µm. **(B)** Magnified image of mitochondria with punctate morphology. Scale bar 10µm. **(C)** Magnified image of interconnected tubular mitochondria. Scale bar represents 10µm.

**Figure 3.5 Age-related morphological changes of YFP-tagged mitochondria in st9 oocytes.** (pg. 81)

**(A)** 1-day old control oocyte. (anterior – A, posterior – P) **(B)** 20-day old oocyte. Mitochondrial morphology is comparable to wildtype in variation and distribution, demonstrating a mix of clustered (yellow arrowheads) and punctate (white arrowheads) organelles traversing the entirety of the cytoplasm. **(C)** After 30 days, we observe aggregates of filamentous mitochondria in the centre and near the cortex (yellow arrowheads) and fewer punctate structures as well as a depletion in the posterior of the oocyte (white arrowheads). This phenotype is even more dramatic after 40 days **(D)** with strongly visible domains lacking mitochondria in the posterior (white arrowheads) and an increase in filamentous aggregates (yellow arrowheads). Scale bar represents 10µm.

**Figure 3.6. Fusion and fission mutants affect mitochondrial morphology and distribution.** (pg. 85)

**(A,B,C,D)** YFP-tagged mitochondria in control oocytes. Mitochondria in control oocytes vary in size from punctate to longer, filamentous organelles that may be undergoing either fission, fusion, or tethering (anterior – A, posterior - P). **(A',D')** YFP-tagged mitochondria in *UASMarfRNA<sup>GD40478</sup>; nos-Gal4* and *UASMarfRNA<sup>Guo</sup>; nos-Gal4* genetic background, respectively, where fusion is interrupted. Mitochondria in the Marf mutants appear more fragmented and punctate when compared to controls and have a cloudy appearance. **(B')** YFP-tagged mitochondria in *UASDrp1[WT]; nos-Gal4* genetic background where fission is upregulated. Similarly, mitochondria in these oocytes appear more punctate and fragmented. **(C')** YFP-tagged mitochondria in oocytes heterozygous for the *Drp1<sup>T26</sup>* loss-of-function fission allele displaying largely globular morphology, concentrated at the posterior while filamentous mitochondria in the anterior appear thicker than controls (white arrowheads). Scale bar represents 30µm.

**Figure 3.7. Absence of MT and actin cytoskeletons affect motion, morphology and distribution of Rab7 and DIC vesicles.** (pg.89)

**(A)** YFP-tagged Rab7 vesicles in control oocytes. Rab7 vesicles in control oocytes vary in size from punctate, small vesicles (diffraction limited, 250-300nm) to larger 'donut-like' vesicles (0.5-2.5 µm) (anterior – A, posterior - P). **(A')** DIC vesicles in the same control oocyte. Sizes vary similarly to Rab7 vesicles. **(B)** YFP-tagged Rab7 vesicles in the absence of the actin mesh. Vesicle morphology in this condition is not affected as much as distribution; vesicles are concentrated to the right and left posteriorly (yellow arrowheads) and close to the cortex anteriorly (white arrow head) **(B')** DIC vesicles in the same oocyte as B. Distribution of these vesicles reflects that of Rab7 vesicles with even fewer vesicles concentrated in the middle (yellow square). **(C')** YFP-tagged Rab7 vesicles in the absence of the MT cytoskeleton, indicated by the displaced nucleus (n). In this condition, individual Rab7 vesicles are very difficult to discern, instead they form cloudy aggregates spanning the oocyte with a few scattered bright fluorescent dots that resemble the small vesicles we observe in control and no actin oocytes. The cortical membrane of these

oocytes is also affected by the absence of MTs particularly anteriorly where the membrane seems to cave in (white arrowheads). **(C)** DIC vesicles in the same oocyte as C. Distribution of DIC vesicles reflects that of Rab7 vesicles in this condition. Individual vesicles are visible but appear smaller when compared to control DIC vesicles. Vesicles also fail to accumulate in regions near the nucleus (yellow circles) **(D)** YFP-tagged Rab7 vesicles in the absence of both actin and MT cytoskeletons. In this condition, the borders of individual vesicles are hard to discern, similarly to the no MT condition, and form merged clusters near the posterior of the oocyte (white arrowheads). **(D')** DIC vesicles in the same oocyte as D. Larger DIC vesicles (white arrowheads) are scarce particularly when compared to control and no actin conditions and the smaller vesicles are concentrated in clusters predominantly in one area near the posterior (yellow arrowhead) unlike the other conditions where DIC vesicles are found both posteriorly and anteriorly despite changes in distribution. Scale bar represents 30 $\mu$ m.

**Figure 3.8. Absence of MT and actin cytoskeletons affect morphology and distribution of mitochondria and DIC vesicles.** (pg.90)

**(A)** YFP-tagged mitochondria in control oocyte. In this condition, mitochondria morphology is varied displaying both filamentous and punctate organelles (anterior – A, posterior - P). **(A')** DIC vesicles in the same control oocyte. **(B)** YFP-tagged mitochondria in the absence of the actin mesh. The lack of the mesh results in distribution of organelles in distinct clusters across the cytoplasm (yellow circles). **(B')** DIC vesicles in the same oocyte as B. DIC vesicle size and distribution differs when compared to controls, particularly absent near the posterior cortex (white arrowheads). **(C)** YFP-tagged mitochondria in the absence of the MT cytoskeleton, indicated by the displaced nucleus (n). In this condition, mitochondria display perinuclear clustering and longer filaments near the cortex and towards the posterior tip of the oocyte (yellow arrowheads). **(C')** DIC vesicles in the same oocyte as C. The distribution of DIC vesicles is more dramatically affected than in no actin conditions failing to accumulate in several regions of the oocyte particularly near the nucleus (yellow arrows) and clustering in a thin line around the cortex (white arrowheads). Individual vesicles are visible but are decreased in size when compared to control DIC vesicles. **(D)** YFP-tagged mitochondria in the absence of both actin and MT cytoskeletons. In this condition, mitochondria display branched morphology (yellow arrowheads) and cluster in aggregates near the nucleus and cortex (white arrowheads). **(D')** DIC vesicles in the same oocyte as D. Vesicles are even more sparse in the absence of both cytoskeletons compared to B' and C' (yellow arrowheads) but display highest concentration near the cortex (white arrowheads). Scale bar represents 30 $\mu$ m.

## Chapter 4

**Figure 4.1 DIC vesicles in Rab7-YFP oocytes differ in morphology when compared to w-, Mito-YFP and GFP::UTRN backgrounds.**

(pg.96)

**(A-C)** DIC image of vesicles in GFP::UTRN, w<sup>-</sup> and YFP::Mito oocytes. Vesicles here display more homogenous morphology and size averaging at 0.23 $\mu$ m, 0.19 $\mu$ m, 0.30 $\mu$ m respectively ( $n=12$ ). **(D)** DIC image of vesicles in YFP::Rab7 oocytes average at 0.51 $\mu$ m in diameter ( $n=16$ ). Scale bar represents 30 $\mu$ m.

**Figure 4.2 Contact sites of F-actin and Rab7 vesicles** (pg.104)

**(A)** Actin mesh in white stained with phalloidin **(B)** Actin mesh in red stained with phalloidin, Rab7-positive vesicles in green. White arrowheads indicate contact sites named F-actin foci. These foci are associated with filaments from the mesh suggesting potential actin nucleation from the vesicular membrane. Scale bar represents 10 $\mu$ m.

## Tables

**Table 2.1. Fly lines used and their origins.** (pg.59)

**Table 2.2. Statistical significance (p-value) comparisons of velocity, representing advective motion and diffusivity of experimental groups derived from Mann-Whitney U and Student's t-tests.** (pg,75)

**Table 3.1. DDM analysis of velocity, representing advective motion, and diffusivity of early (Rab5-positive), late (Rab7-positive) endosomes and mitochondria in st9 wildtype oocytes.** (pg.77)

**Table 3.2. DDM analysis of velocity, representing advective motion, and diffusivity of DIC vesicles in the same oocytes as late (Rab7-positive) endosomes and mitochondria in st9 wildtype oocytes.** (pg. 78)

**Table 3.3. Mean and standard deviation of central and peripheral fluorescent intensity of Rab5 and Rab7 vesicles in wildtype oocytes.** (pg. 85)

**Table 3.4. Mean and standard deviation of anterior and posterior fluorescent intensity of mitochondria in control, 30 day old, and 40 day old oocytes.** (pg. 88)

**Table 3.5. DDM analysis of velocity, representing advective motion, and diffusivity of mitochondria at different ages (1, 20, 30 and 40 days old).** (pg. 89)

**Table 3.6. Mean and standard deviation of central, peripheral, anterior and posterior fluorescent intensities of mitochondria in oocytes mutant for Marf and Drp1.**(pg. 93)

**Table 3.7. DDM analysis of velocity, representing advective motion, and diffusivity of mitochondria in interrupted fusion and fission conditions.** (pg. 94)

**Table 3.8. Mean and standard deviation of cortical fluorescent intensities of mitochondria in control oocytes and oocytes in conditions with compromised cytoskeletal networks.** (pg. 100)

**Table 3.9. DDM analysis of velocity, representing advective motion, and diffusivity of late (Rab7-positive) endosomes and mitochondria in conditions with compromised cytoskeletal networks.** (pg. 101)

**Table 4.1. DDM analysis of velocity, representing advective motion, and diffusivity of DIC vesicles in control oocyte groups.** (pg.106)



# TABLE OF CONTENTS

<b>STATEMENT OF ORIGINALITY</b>	<b>2</b>
<b>ACKNOWLEDGEMENTS</b>	<b>3</b>
<b>ABSTRACT</b>	<b>4</b>
<b>LIST OF FIGURES AND TABLES</b>	<b>5</b>
Figures	5
<b>TABLE OF CONTENTS</b>	<b>13</b>
<b>ABBREVIATIONS</b>	<b>16</b>
<b>Chapter 1: Introduction</b>	<b>19</b>
1.1 <i>Drosophila melanogaster</i> as a model organism for investigating cytoskeletal dynamics, force generation and interactions with cytoplasmic content.	19
1.2 The cytoskeletal system and associated proteins.	22
1.3 Cytoskeletal network dynamics and function during oogenesis.	31
1.4 Intercellular trafficking pathways and the involvement of the microtubule and actin networks.	37
1.5 Role of actin and microtubules in the motion, function, and dynamics of the mitochondrial network.	42
1.6 Characteristics of the cytoplasmic medium and the impact on molecular motion.	52
1.7 Research aims	57
<b>Chapter 2: Materials &amp; Methods</b>	<b>58</b>
2.1 Fly stocks and genetics.	58
2.2 Fixed samples.	60
2.3 Live imaging of Rab vesicles and mitochondria.	60
2.4 Differential dynamic microscopy.	61
2.5 Manual single-particle tracking.	64
2.6 Measuring vesicle diameter.	67
2.7 Analysing distribution of organelles under different experimental conditions.	69
2.8 Enhancing borders of mitochondria.	73
2.9 Statistical analysis.	73

<b>Chapter 3: Results</b>	<b>77</b>
3.1 Early endosomes, late endosomes and mitochondria exhibit a combination of advective and diffusive motion in <i>st9 Drosophila</i> oocytes with variability in rates.	77
3.2 Integrating DIC imaging analysis with organelle-specific fluorescent imaging reveals variable and shared motion characteristics between DIC vesicles and late endosomes and mitochondria.	78
3.3 Analysis of individual Rab7 vesicles and mitochondria moving in directed and ballistic manner suggests transport as cargo on motors.	80
3.4 Distribution and morphology of early endosomes, late endosomes, and mitochondria in <i>st9 Drosophila</i> oocytes and age-related morphological changes of the mitochondrial network.	84
3.5 Ageing adversely affects mitochondrial motility in <i>st9 Drosophila</i> oocytes.	89
3.6 Perturbing the balance of mitochondrial fusion and fission using <i>Marf</i> and <i>Drp1</i> mutants affects morphology and distribution of mitochondria in <i>st9 Drosophila</i> oocytes.	91
3.7 Perturbing the balance of mitochondrial fusion and fission using <i>Marf</i> and <i>Drp1</i> mutants reduces advective and diffusive motion of mitochondria and DIC vesicles in <i>st9 Drosophila</i> oocytes.	94
3.8 Depolymerising microtubules and the actin mesh affects the distribution and morphology of late endosomes and mitochondria in <i>st9 Drosophila</i> oocyte.	96
3.9 Absence of microtubules and actin mesh impedes advective and diffusive motion of late endosomes, DIC vesicles and mitochondria.	101
4.1 Dynamic variations in distribution, advection and diffusion rates among organelle populations in <i>Drosophila</i> oocytes and implications of fluorescent tagging on Rab7.	103
4.2 Impact of ageing and disrupting the fusion-fission equilibrium on mitochondrial motion and organelle distribution.	107
4.3 Exploring the role of kinesin in mitochondrial and endosomal dynamic and implications for cellular organization and function of the <i>Drosophila</i> oocyte.	110
4.4 The role of microtubule-driven motion and actin-mediated forces in <i>Drosophila</i> oocyte organelle dynamics.	111
<b>Chapter 5: Conclusion</b>	<b>115</b>
<b>References</b>	<b>117</b>
<b>Appendix</b>	<b>170</b>
Section 1. List of Timelapse movies.	170
Section 2. Raw data - centroid coordinates	172
Section 3. Raw data – fluorescent intensity measurements, p-values and Python script analysis.	174

Section 4. Raw data – DDM values of velocity ( $nm s^{-1}$ ) and diffusivity ( $\mu m^2 s^{-1} \times 10^{-3}$ ) for each oocyte, respective box plots and single-particle tracking velocities from which mean $\pm$ SD was calculated and compared.	188
Section 5. Example DDM decorrelation rates $\Gamma_{1q}$ and $\Gamma_{2q}$ plotted against the wave vector $q$ for YFP-tagged organelles and DIC vesicles for each experimental condition.	196
Section 6. Attempt to enhance edges of mitochondria in mutant backgrounds using the Fiji (ImageJ) “Find Edges” function.	198

# ABBREVIATIONS

AAA+ - ATPases associated with diverse cellular activities

ABPs - actin binding proteins

ADP - adenosine diphosphate

ATP - adenosine triphosphate

Bb - Balbiani body

*bic* - *bicoid*

*Bic-D* - *Bicaudal-D*

*C. elegans* - *Caenorhabditis elegans*

Ca<sup>2+</sup> - calcium

*capu* - *cappuccino*

CMT2A - Charcot-Marie-Tooth type 2A

CytoD - cytochalasin D

*D* - diffusivity; effective diffusion coefficient

DDM - differential dynamic microscopy

Dhc - dynein heavy chain

DIC - differential interference contrast

Dic - dynein intermediate chain

Dmn - dynamitin

DNA - deoxyribonucleic acid

Drosophila - *Drosophila melanogaster*

Drp1 - dynamin-related protein 1

Dynamin - Dnm

EE - early endosome

*egl* - *egalitarian*

ER - endoplasmic reticulum

F-actin - filamentous actin

FC- follicle cell

Fzo1 - fuzzy onion

G-actin - globular actin

GFP - green fluorescent protein

*Gl1* - *Glued*

*grk - gurken*

GTP - guanosine-5'-triphosphate

IFN2 - inverted formin 2

IFs - intermediate filaments

ILVs - intraluminal vesicles

IMM - inner mitochondrial membrane

Khc - kinesin heavy chain

Kinesin-1 - conventional kinesin

Klc - kinesin light chain

I-Opa1 - long form-Opa1

LE - late endosome

Marf - mitochondria assembly regulatory factor

MEF - mouse embryonic fibroblasts

Mff - mitochondrial fission factor

Mfn - mitofusin

Mgm1 - mitochondrial genome maintenance-1

MiD - mitochondrial dynamics proteins

Miro - mitochondria Rho GTPase

Mito - mitochondria

mRNA - messenger RNA

MSD - mean squared displacement

MT - microtubule

mtDNA - mitochondrial DNA

MTOC - microtubule organising center

MVB - multivesicular bodies

Myo19 - myosin XIX

Myosin II - conventional myosin

NCs - nurse cells

OF - optical flow

OMM - outer mitochondrial membrane

Opa1 - optic atrophy 1

*osk - oskar*

OXPPOS - oxidative phosphorylation

PFA - paraformaldehyde

Pe - Peclet number  
PH domain - pleckstrin homology domain  
PI - phosphoinositides  
PI3K - phosphatidylinositol 3-kinase  
PIV - particle image velocimetry  
RE - recycling endosome  
Re - Reynold's number  
RNA - ribonucleic acid  
RNAi - RNA interference  
s-Opa1 - short form-Opa1  
*S. cerevisiae* - *Saccharomyces cerevisiae*  
siRNA - small interfering RNA  
sqh - spaghetti squash  
st - stage (of oogenesis)  
UAS - upstream activating sequence  
UTRN - utrophin  
 $v$  - velocity of flow speed  
 $w$  - white eyes  
WH2 domain - WASP homology 2 domain  
YFP - yellow fluorescent protein

# Chapter 1: Introduction

1.1 *Drosophila melanogaster* as a model organism for investigating cytoskeletal dynamics, force generation and interactions with cytoplasmic content.

*Drosophila melanogaster*, known colloquially as the fruit fly, has been used as a model organism for over a hundred years (Figure 1.1). It boasts several advantages including low-cost maintenance, short lifespan, rapid generation, and an array of genetic tools at its disposal making it an indispensable model for a variety of diseases and biological phenomena and processes. Many of the mechanisms and pathways identified and investigated in *Drosophila* are conserved across species making these findings relevant to both fundamental and biomedical research. The *Drosophila* genome shares 60% homology with the human genome and 75% homology with genes responsible for human diseases (Chien et al. 2002, Yamamoto et al. 2014, Ugur et al. 2016, Bellosta et al. 2019). In recent years, we have witnessed an exponential increase in the use of *Drosophila* to model cancer as well as neurodegenerative diseases such as Alzheimer's and Parkinson's (Lu & Vogel 2009; Mirzoyan et al. 2019; Yamamura et al. 2020; Bolus et al. 2020; Gong et al. 2021; Nilta & Sugie 2022; Sharpe et al. 2023).

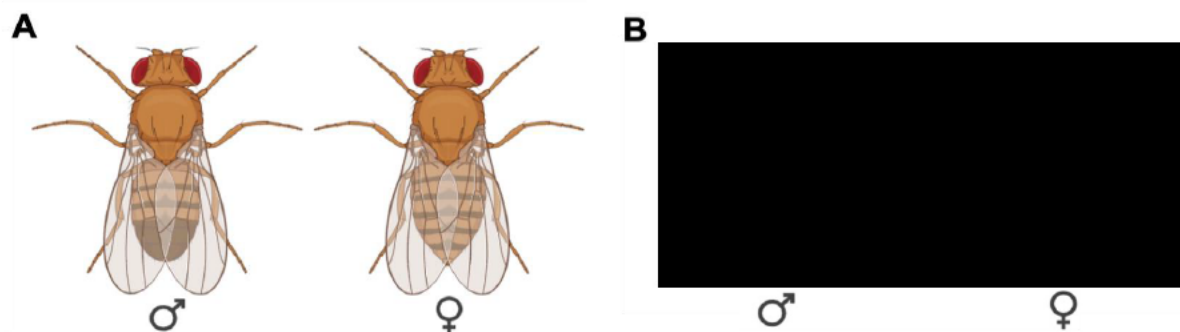


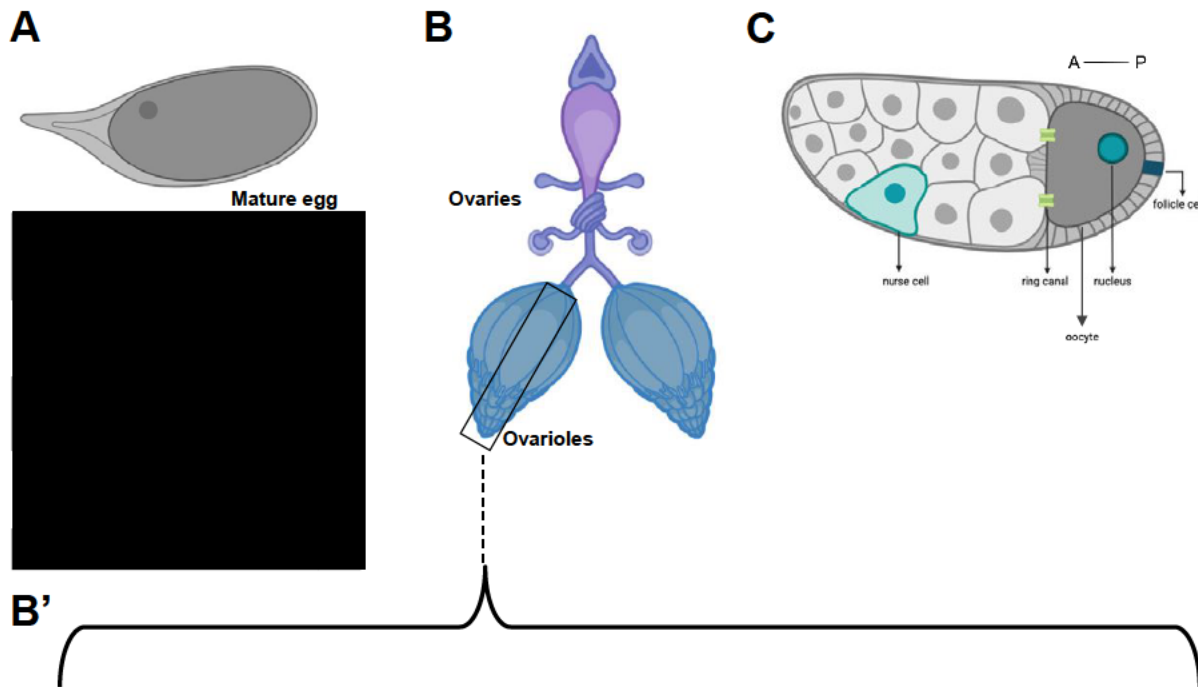
Figure 1.1. *Drosophila melanogaster* as a model organism (A-B) the male and female fruit fly (photos taken from Thomas Cline/UC Berkeley). Male flies have shorter abdomens that round at the bottom while female flies have longer abdomens that point at the bottom with comparatively more stripes than males.

In addition to the homology between *Drosophila* and human genes, highlighting the translational relevance of findings, the *Drosophila* oocyte emerges as a highly suitable

model for investigating organelle interactions and visualizing cytoplasmic structures and dynamics (Figure 1.2A). Studies focusing on the development of the egg chamber have yielded critical insights into cellular dynamics, such as axis specification, polarity, cytoskeleton dynamics, and mRNA localization (Bastock & St Johnston 2008; Becalska & Gavis 2009; Montell et al. 2011; Quinlan 2016). The oocyte's robust and permeable membrane, coupled with its large size, facilitates dynamic live imaging, enabling the observation of key cellular processes in real-time. The literature discussed in the following sections highlights a reciprocal relationship between cytoskeletal activity and structure and the function and morphology of organelles. This study aims to uncover the effects of disrupting cytoskeletal and organelle dynamics in the oocyte to identify the factors influencing cytoskeletal structural integrity, force generation, and the dynamics of endosomes and mitochondria.

The process of oogenesis takes roughly a week and is divided into 14 arbitrary stages based on morphology (Figure 1.2B'). *Drosophila* have two ovaries consisting of 18 ovarioles which can be viewed as an egg production line containing each stage of egg development, starting with the germarium and ending with a mature egg competent for fertilisation (King et al. 1956). The germarium is found at the anterior of the ovariole and contains somatic and germline stem cells. Egg chambers develop inside the germarium from germline cyst cells and exit the structure once they are surrounded by follicle cells. One of the 16 cells within the cyst differentiates as the oocyte while the rest develop into nurse cells (NCs) which synthesise and transport nutrients and cytoplasmic components to the oocyte (Figure 1.2C). Egg chambers thus bud off from the germarium entering the posterior region of the ovariole called the vitellarium, attached to the progressively more mature egg chamber by stalk cells (Figure 1.2B'; Deng & Lin 2001; Steinhauer & Kalderon 2006; Poulton & Deng 2007; Bastock & St Johnston 2008).





Images redacted due to copyright permissions

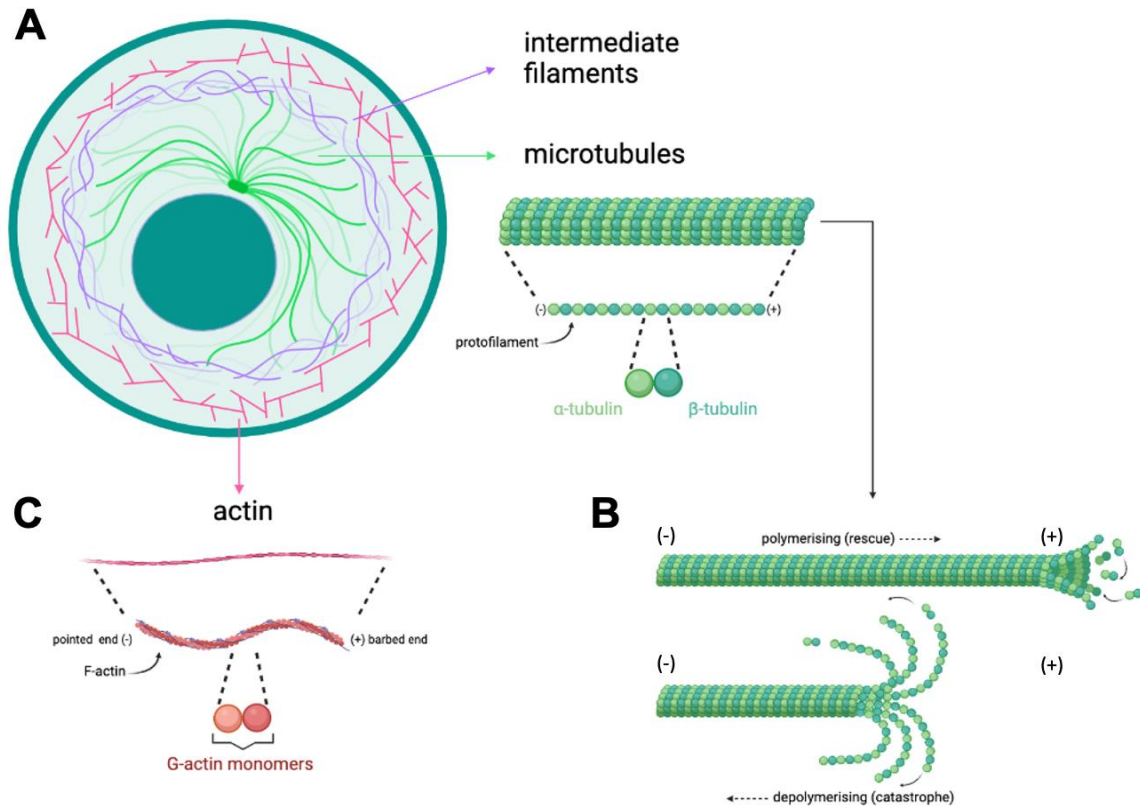
Images available at source in figure legend.

**Figure 1.2. *Drosophila oogenesis*** (A) Schematic and scanning electron microscopy (SEM) image of *st14* mature egg (latter image taken from Dr. Bob Argiropoulos of UBC Department of Zoology). (B) Schematic of *Drosophila* ovaries each containing 18 ovarioles. (B') Schematic and fluorescent images of ovariole showing stages of oogenesis starting with the germarium and ending with a mature egg competent for fertilisation (Image taken from Quinlan 2016). The germarium at the anterior of the ovariole contains somatic and germline stem cells. Egg chambers develop inside the germarium from germline cyst cells and exit the structure once they are surrounded by follicle cells (FCs) and one of the 16 cells within the cyst differentiates as the oocyte. (C) Schematic of *st10* egg chamber. Each egg chamber is surrounded by a monolayer of follicular epithelia. FCs synthesise and transport yolk peptides into the oocyte, secrete eggshell components and participate in cell signalling events for establishment of oocyte polarity and axis formation (anterior - A, posterior - P).

Stereotypical morphological characteristics of the egg chamber define its stages of development: (1) size, shape, and location of the egg chamber in the ovariole, (2) the size of the oocyte, (3) nucleus positioning in the oocyte and (4) follicle cell shape (King et al. 1956; Bastock & St Johnston 2008; Quinlan 2016). Each egg chamber is surrounded by a monolayer of follicular epithelia, follicle cells (FCs), which are involved in patterning of the oocyte and maintaining the structural integrity of the egg chamber. FCs synthesise and transport yolk peptides into the oocyte and participate in cell signalling events by coordinating with the cytoskeletal networks for establishment of oocyte polarity and axis formation (Badovinac & Bilder 2005; Wu et al. 2008; Bastock & St Johnston 2008; He et al. 2011).

## 1.2 The cytoskeletal system and associated proteins.

The cytoskeletal network is a dynamic, viscoelastic, intracellular structure necessary for movement, transformation, and regulation of the cell. It is responsible for spatial organisation of cellular content and coordinating forces for movement and shape changes during morphogenesis and providing a physical and biochemical link to the cell's external environment (Fletcher & Mullins 2010; Ando et al. 2015; Pegoraro et al. 2017; Cardanho-Ramos et al. 2020). The cytoskeletal network in the eukaryotic cell constitutes three main structures composed of filamentous polymers: MTs, actin and intermediate filaments (IFs) (Figure 1.3A). MTs and the actin cytoskeleton are highly dynamic, undergoing constant polymerisation and depolymerisation in response to stress and throughout the course of development. IFs are also very dynamic but play a slightly different role in the cell, better suited to resist tensile stress and unlike MTs and actin are not polarised and thus do not support directional movement of motor proteins (Flitney et al. 2009; Fletcher & Mullins 2010; Dey et al. 2014). *Drosophila* have both MTs and actin but no IFs. Due to the structural polarity of both MT and actin cytoskeletons, they are fit to function as tracks for molecular motors. There are three superfamilies of motor proteins that direct transport along cytoskeletal filaments: myosin, which is associated with actin, and kinesin and dynein which are MT-associated motors (Figure 1.4A; Hirokawa 1998; Mehta et al. 1999; Sweeny & Holzbaur 2018).



**Figure 1.3. Cytoskeletal networks in eukaryotic cells (A)** The MT and actin cytoskeletal network in the eukaryotic cell. The  $\alpha$ - and  $\beta$ -tubulin monomers that comprise microtubule filaments form a heterodimer and associate with other dimers in a head-to-tail formation forming laterally arranged linear protofilaments. The  $\beta$ -tubulin monomer is oriented towards the faster growing end (plus-end) while  $\alpha$ -tubulin is oriented towards the slower growing end (minus-end) conferring polarity to the MT filament. Approximately 13 protofilaments assemble around a hollow core creating a tube-like structure. **(B)** Filaments alternate stochastically between two states growing (rescue) and shrinking (catastrophe) for rapid reorganisation and the ability to ‘search’ its environment. **(C)** The actin can be found in its monomeric (G-actin) or filamentous (F-actin) form. Polymerisation occurs at the plus-ends, or barbed ends, of filaments while depolymerisation occurs at the minus-ends or pointed ends and is regulated by nucleotide hydrolysis.

The MT cytoskeleton is a robust structure that can resist compression and externally applied forces. In dividing cells, MTs form the mitotic spindle required for chromosome segregation while in non-dividing cells helps in organising the cytoplasm and its contents, positioning the nucleus, and providing structure to the cell with the help of molecular motor proteins (Hayden et al. 1990; Rieder & Alexander 1990; Wollman et al. 2005; Tamura & Draviam 2012; Rizzelli et al. 2020). MTs are the stiffest of all

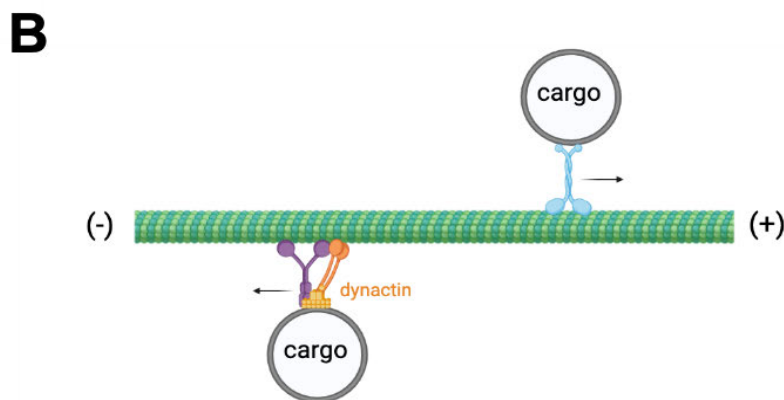
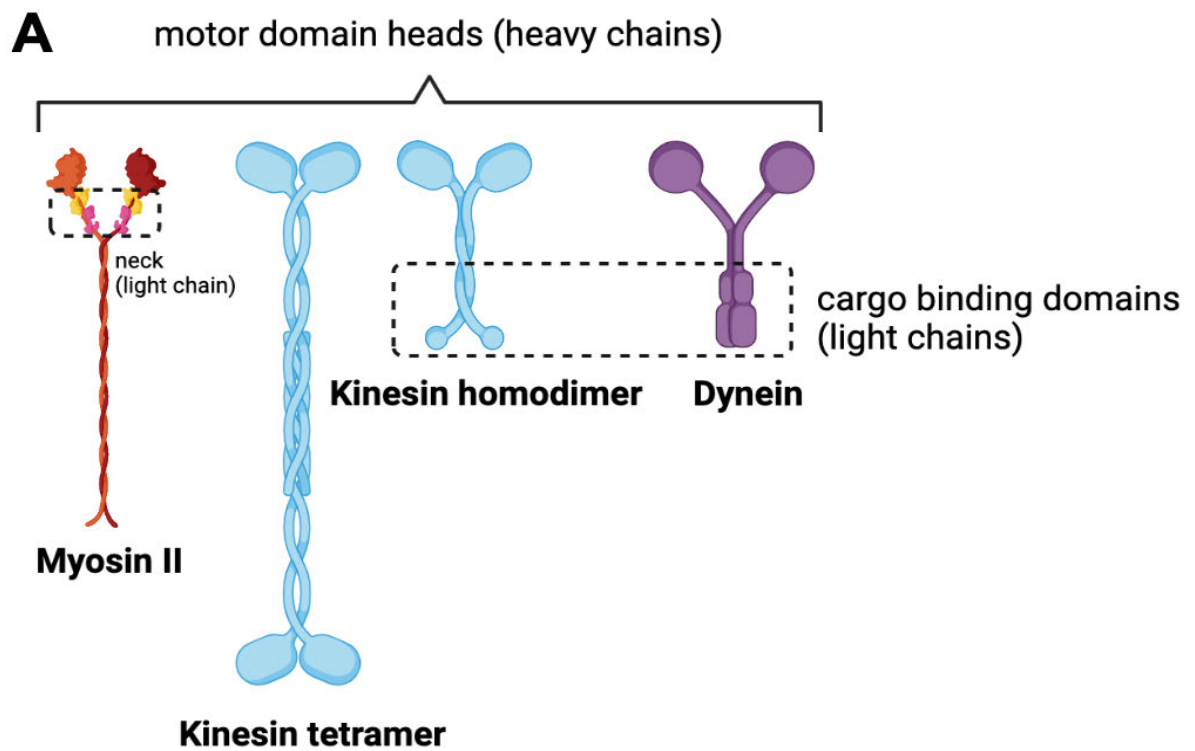
cytoskeletal elements, organised as a noncovalent polymer composed of  $\alpha$ - and  $\beta$ -tubulin subunits. The  $\alpha$ - and  $\beta$ -tubulin monomers form a heterodimer and associate with other dimers in a head-to-tail formation forming linear protofilaments arranged laterally creating 25nm wide hollow cylindrical polymers of approximately 13 protofilaments (Figure 1.3A). The polarity of the  $\alpha$ - and  $\beta$ -tubulin dimer confers polarity to the entire microtubule filament controlling the polymerisation rates on either end; the  $\beta$ -tubulin monomer is oriented towards the faster growing end, referred to as the plus-end, while  $\alpha$ -tubulin is oriented towards the slower growing end, referred to as the minus-end (Allen & Borisy 1974; Holy & Leibler 1994; Desai & Mitchison 1997; Budde et al. 2006; Bieling et al. 2007; Sept 2007; Fletcher & Mullins 2010).

During polymerisation,  $\beta$ -tubulin hydrolyses GTP altering the conformation of the MTs as well as providing the energy required to maintain dynamic instability. Dynamic instability is a phenomenon observed in MTs whereby filaments alternate stochastically between two states, growing (rescue) and shrinking (catastrophe), which allows for rapid reorganisation and the ability to 'search' its environment, *e.g.*, for chromosomes during segregation (Figure 1.3B; Mitchison & Kirschner 1984; Holy & Leibler 1994; Desai & Mitchison 1997; Fletcher & Mullins 2010; Horio & Murata 2014). This process differs from reversible or equilibrium polymerisation which is competitive and dependent on the concentration of monomers available and presence of regulatory proteins. This adaptability allows MTs to perform their function of maintaining cell shape and integrity under stress and creating tracks for motor proteins that can span the entire cell.

MTs function as highways for cellular cargo. Kinesin motors play critical roles in microtubule-based transportation in both neuronal and non-neuronal cells. Kinesin is essential for proper axis determination during development, sensory capabilities in ciliated neurons, and opsin movement and function in photoreceptor cells to name a few (Brendza et al. 2000; Marszalek et al. 2000; Palacios & St Johnston 2002; Cohen 2002; Evans et al. 2006; Lu et al. 2020). Kinesin motors belong to a superfamily of 14 classes and are characterised by a high-homology ATP-binding domain, called the motor domain in kinesins involved in active transport of cargo. Conventional kinesin, kinesin-1,

is a tetramer with a homodimer of two heavy chains responsible for kinesin motor activity and two light chains involved in cargo-binding (Figure 1.4A; Hirokawa et al. 1989; Brendza et al. 2000; Januschke et al. 2002; Marx et al. 2009). Research shows that the steps of ATP hydrolysis trigger conformational changes that allow kinesin to interact with MTs and generate force; ATP hydrolysis allows the head in the dimer to detach from the tubulin subunit and move to its next binding site creating directed movement along the filament towards the plus-end (Figure 1.4B; Yildiz & Selvin 2005; Gigant et al. 2013; Hwang et al. 2017; Qin et al. 2020).

Dynein activity is involved in intracellular transport, axis determination, Golgi apparatus maintenance and ciliary and flagellar movement (Takei et al. 1998; Vallee & Tai 2002; Sakato & King 2004; Roberts et al. 2013). Dynein belongs to the ATPases associated with diverse cellular activities (AAA+) superfamily characterised by conserved nucleotide-binding and catalytic modules. This conserved feature is exemplified in the dynein heavy chain which, much like kinesin, generates force from ATP hydrolysis for directed movement but towards the minus-end of the MT (Snider et al. 2008; Roberts et al. 2013; Khan et al. 2022). Both MT motor proteins contain two heads but differences in structure and mechanisms of activity suggest an alternate mechanism of processivity (Figure 1.4A). A coiled-coil stalk emerging from the AAA+ domain contains a microtubule-binding domain (MTBD). It has been proposed that conformational changes of the dynein globular head caused by ATP hydrolysis causes a bending and straightening of the linker creating power-strokes and allowing minus-end directed translocation along MT filaments (Burgess et al. 2004; Dewitt et al. 2011; Roberts et al. 2012; Allan 2014; McKenney et al. 2014, Schmidt et al. 2015). Dynein requires dynactin for most if not all its functions. Dynactin is a multisubunit protein which creates a complex by binding to the dynein intermediate chain through its p150<sup>Glued</sup> subunit with the help of bicaudal D homologue 2 (BICD2) (Figure 1.4B; Waterman-Storer et al. 1997; Schroer 2004; Walter et al. 2010; Yao et al. 2012; Splinter et al. 2012).

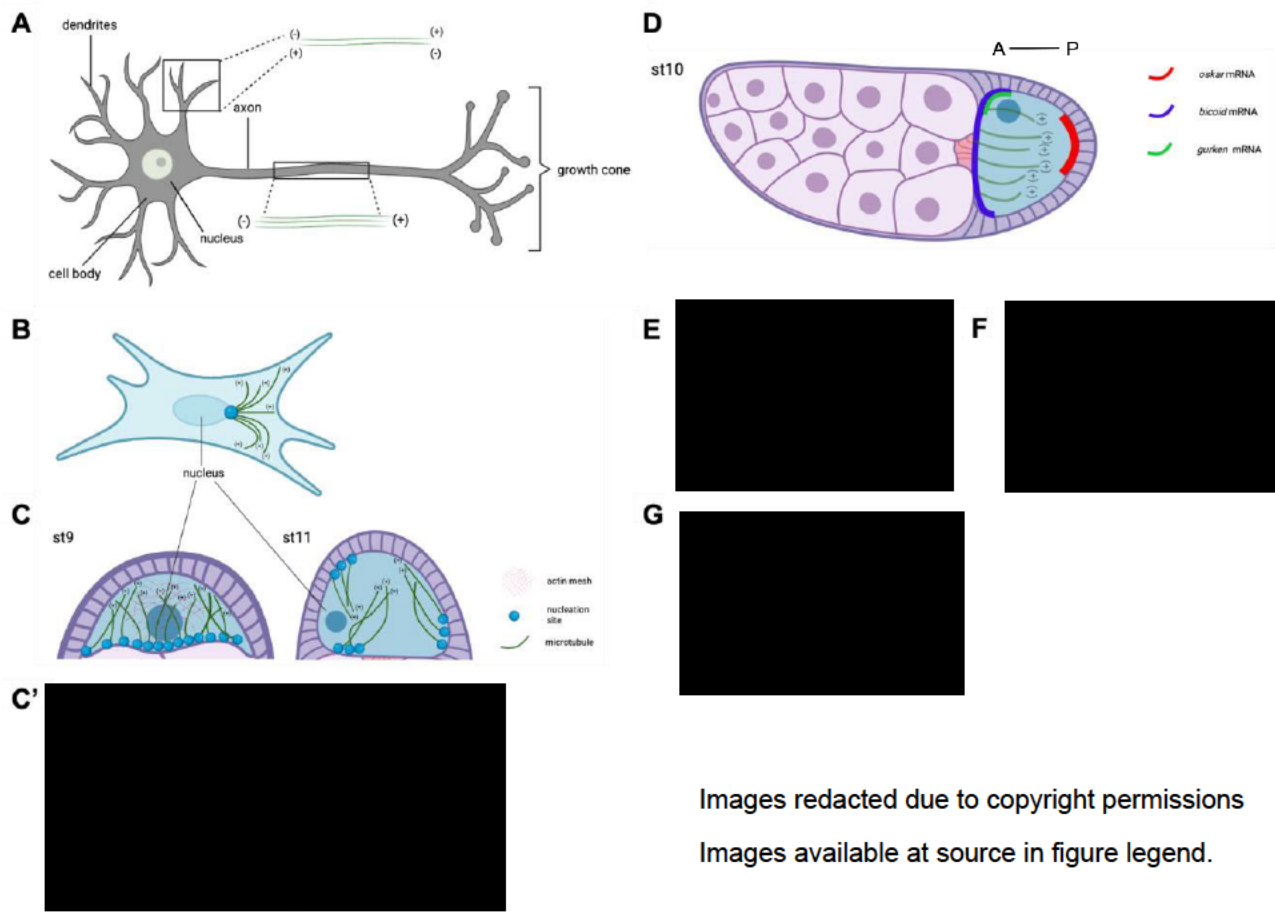


**Figure 1.4. Superfamilies of motor proteins: myosin, kinesin, and dynein.** (A) Myosin is composed of four domains: the motor head, the lever arm, the targeting domain, and the coiled coil. Myosin II contains two heavy chains, two essential light chains and two regulatory light chains. The structural changes undergone for ATP hydrolysis cause the myosin lever arm to move, creating the ‘myosin powerstroke’ creating force for movement along the actin filament. Kinesin-1 is a tetramer with a homodimer of two kinesin-1 heavy chains and two light chains. Heavy chains are responsible for kinesin motor activity while light chains are involved in cargo-binding. ATP hydrolysis triggers conformational changes that allow kinesin to interact with MTs and generate force. Cytoplasmic dynein is a two-

headed motor. Conformational changes of the dynein globular head from nucleotide binding creates a swing-like motion for translocation along the filaments. **(B)** Dynein activity requires dynactin. Dynactin is a multisubunit protein which creates a complex by binding to the dynein intermediate chain through its p150 glued subunit.

In most eukaryotic cells, opposite-polarity motors like kinesin and dynein transport cargo in a bidirectional manner up and down the MT filaments. In neurons, kinesin drives anterograde motion in the axon towards the periphery while dynein drives retrograde transport towards the cell centre (Figure 1.5A; Hurd & Saxton 1996; Martin et al. 1999; Hirokawa & Takemura 2005). Disrupting the function of one motor causes an abrogation in the function of the other, first identified in extruded squid axoplasm, where inhibition of kinesin, dynein and/or dynactin function leads to an interruption of bidirectional transport (Waterman-Storer et al. 1997; Hurd & Saxton 1996; Martin et al. 1999). The absence of kinesin in hypomorphic and null alleles interrupts retrograde transport of mitochondria in *Drosophila* neurons (Hollenbeck & Saxton 2005; Pilling et al. 2006). Additionally, in *Drosophila* neurons, a lack of kinesin leads to the formation of axonal swellings due to 'organelle jams', accumulations of organelles transported as both anterograde and retrograde cargo, a prominent feature of Alzheimer's and Parkinson's disease (Brady et al. 1990; Saxton et al. 1991; Hurd & Saxton 1996; Martin et al. 1999; Welte 2004; Pilling et al. 2006; Barkus et al. 2008; Kanaan et al. 2013). These findings imply a balance needs to be maintained between opposite-polarity motors for the proper transport and distribution of content in the cell.

Actin is one of the most abundant proteins in eukaryotic cells and, much like microtubules, plays a crucial role in intracellular transport and polarity maintenance, existing as both soluble monomers (globular actin or G-actin) or filaments (F-actin) in the cytoplasm and nucleus (Figure 1.3C; Jacinto & Baum 2003; Hoffman et al. 2004; Hu et al. 2004; Schoenenberger et al. 2005; McDonald et al. 2006; Dominguez & Holmes 2011; Svitkina 2018). The actin motor protein myosin was first discovered in muscle and powers contractility, cytokinesis, and cell polarity. Myosin's structure comprises a motor head, targeting domain, a coiled coil for dimeric myosins, and a lever arm which undergoes a 'powerstroke' upon ATP hydrolysis to generate force and motion on actin



Images redacted due to copyright permissions  
 Images available at source in figure legend.

**Figure 1.5 Microtubule organisation in different cells.** (A) Schematic of microtubule organisation in the neuron where kinesin drives anterograde motion in the axon towards the periphery while dynein drives retrograde transport towards the cell centre. (B) Schematic of radially polarised microtubule organisation in mouse fibroblast cells (C) Schematic of microtubule organisation in *st9* and *st11* oocytes. During mid-oogenesis (*st9*) microtubules are nucleated from the cortex of the oocyte with plus ends biased toward the posterior. During late oogenesis (*st11*) microtubules are organised in thick bundles along the cortex in coordination with the initiation of fast streaming. (C') Left image: projection of 8 images of autofluorescent yolk granules in *st9* oocytes where the actin mesh is still present halting movement of the granules. Right image: projection of 8 images of autofluorescent yolk granules in *st11* oocytes after the actin mesh has disappeared allowing for rapid movement of granules under the force of fast cytoplasmic streaming (Adapted from Quinlan 2016). (D-G) Asymmetric localisation of body determinants *oskar* (*osk*), *bicoid* (*bic*) and *gurken* (*grk*). *osk* localises in a crescent shape at the posterior pole specifying where the pole plasm forms for abdomen and germline development (E), *bcd* localises anteriorly for segmentation of the head and thorax in embryogenesis (F) and *gurken* (*grk*) localises near the nucleus where it triggers dorsal differentiation (G). (Images adapted from Becalska & Gavis 2009; anterior - A, posterior - P; oocyte - oo; follicle cell - fc; nurse cell - nc).



filaments (Figure 1.4A; Simons et al. 1991; Bresnick 1999; Cooper 2000; Craig & Woodhead 2006; Odrionitz & Kollmar 2007; Vicente-Manzanares et al. 2009; Hartman & Spudich 2012; Dasbiswas et al. 2018; Sweeney & Holzbaur 2018). The balance between monomeric and filamentous actin is regulated by nucleotide hydrolysis and the activity of actin-binding proteins (ABPs) in response to morphological changes and external cues. This turnover regulates the rate of filament polymerisation and depolymerisation (Carlier et al. 1997; Paavilainen et al. 2004; Dominguez & Holmes 2011; Rivero & Cvrcková 2013). Like MTs, actin polymerisation occurs at the plus-ends or 'barbed' ends of filaments while depolymerisation occurs at the minus-ends or 'pointed' ends. Plus-end growth is ATP-dependent; filaments grow as ATP-actin monomers preferentially attach to barbed ends. Over time, the ATP is hydrolysed, phosphate is released and the filaments depolymerise through the loss of ADP-actin monomers from the pointed ends through the activity of actin-severing proteins. Nucleotide exchange then occurs to produce ATP-actin monomers for a new round of polymerisation (Carlier et al. 1997; Pollard et al. 2000; Jacinto & Baum 2003; Paavilainen et al. 2004; Rivero & Cvrcková 2013). This directional growth of actin filaments is referred to as 'treadmilling'.

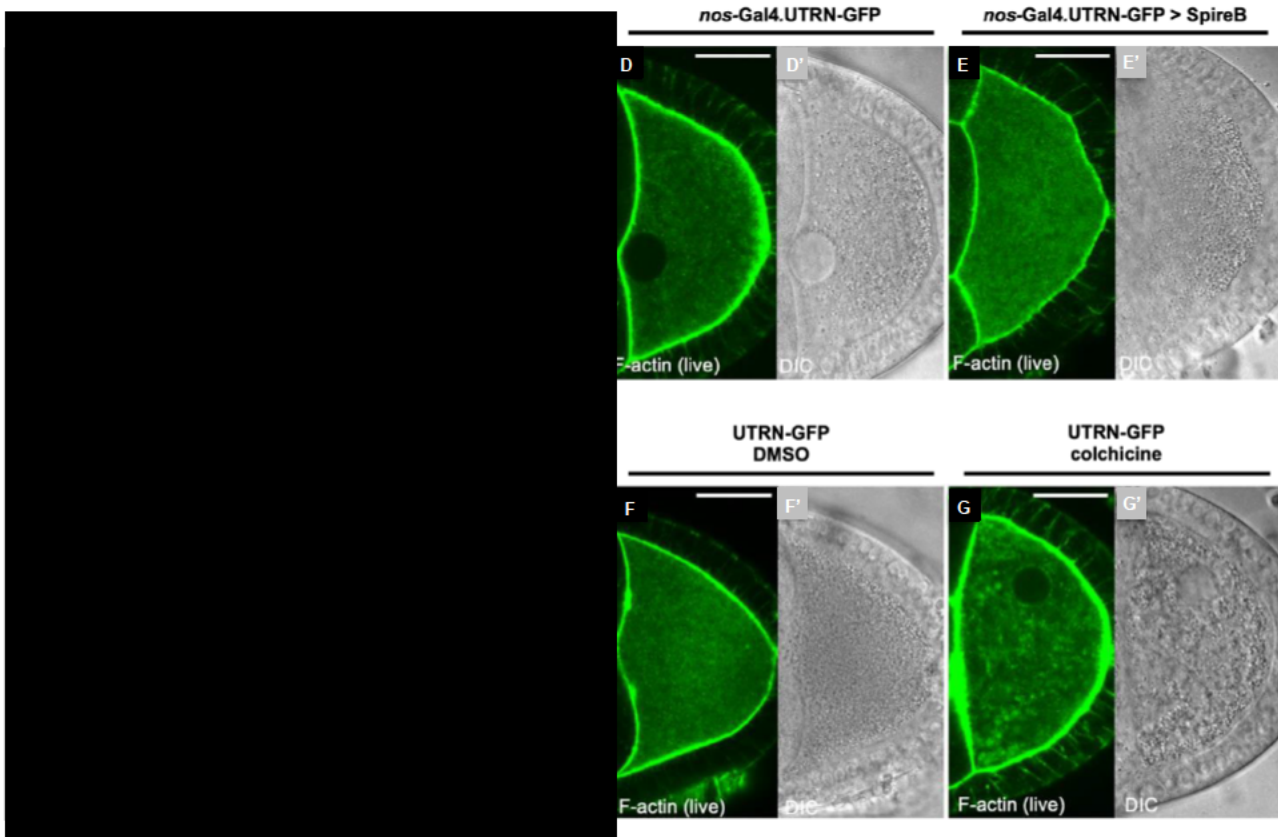
ABPs are not only involved in actin polymerisation and depolymerisation but also function to sever and crosslink filaments. Individual actin filaments are fragile and easily breakable and thus need to be interlinked to create highly organised rigid structures for the formation of isotropic, bundled and/or branched networks (Pollard & Cooper 1986; Winder & Ayscough 2005; Pollard 2016). Unlike MTs, actin polymerisation and bundling is not initiated from a single region or centre, it is instead triggered by initiation of local signalling pathways. For example, chemoattractants trigger the formation of branched actin networks for the propulsion of cells like neutrophils, and signals from the invaginating plasma membrane during endocytosis initiates the local assembly of actin filaments near the cortex for internalisation (Zigmond 1974; Weiner et al. 1999; Parent 2004; Fletcher & Mullins 2010; Šamaj et al. 2004; Galletta & Cooper 2009; Fletcher & Mullins 2010; Mooren et al. 2012).

Actin nucleators and ABPs are related but distinct categories of proteins that interact with actin filaments. Where ABPs bind to and associate with existing actin filaments, actin nucleators, such as the Arp2/3 complex, formins, and Spire proteins, promote the formation of new actin filaments by catalysing the initial polymerisation of actin monomers. Cappuccino is a formin found only in *Drosophila* and is one of two homologues of the mammalian formin, *Fmn-2*. While the roles of nucleators and ABPs differ, some proteins can have dual nucleation and binding capabilities and both work in coordination to regulate actin remodelling and function (Manseau & Schüpbach 1989; Quinlan et al. 2005; Pollard 2007; Dahlgard et al. 2007; Chesarone & Goode 2009; Pechlivanis et al. 2009; Campellone & Welch 2010; Vizcarra et al. 2011; Yoo et al. 2015; Bradley et al. 2020).

The Arp2/3 complex consists of seven subunits and nucleates new “daughter” actin filaments off existing “mother” filaments to generate branched actin networks. Arp2 and Arp3 resemble a dimer of actin subunits allowing the complex to initiate a new filament off an existing filament with the fast growing ‘barbed’ end facing outward (Rouiller et al. 2008; Campellone & Welch 2010; Xu et al. 2022). Spire exists in five isoforms and contains four actin-binding WH2 domains that can interact with actin monomers and localises to sites of actin assembly like vesicle trafficking pathways and the leading edge of cells (Kerkhoff et al. 2001; Quinlan et al. 2005; Ducka et al. 2010; Pfender et al. 2011). *spire* and *capu* are maternal effect genes that play a role in pole determination and fertility and interact to build the oocyte actin mesh. Spire proteins nucleate actin assembly independently of existing filaments, activating actin monomers, and promoting spontaneous linear filament formation by binding of the WH2 domains to actin monomers at the ‘pointed’ end (Manseau & Schüpbach 1989; Pruyne et al. 2002; Quinlan et al. 2005; Goode & Eck 2007; Campellone & Welch 2010; Drechsler et al. 2017). Formins, including *Drosophilla* Cappuccino, also nucleate linear actin filaments, creating unbranched actin networks and facilitating filament elongation through the high affinity binding of their FH2 domain to the ‘barbed’ ends of actin filaments (Quinlan et al. 2005; Kerkhoff 2006; Bosch et al. 2007; Chesarone & Goode 2008; Qualmann & Kessels 2009).

### 1.3 Cytoskeletal network dynamics and function during oogenesis.

*Drosophila* oogenesis involves a series of coordinated, spatiotemporal changes in cytoskeletal architecture, generating forces for the motion and transport of mRNA and organelles (Gutzeit & Koppa 1982; Theurkauf et al. 1992; Clark et al. 1994; Brendza et al. 2000; Quinlan 2016). Fluid flows, also referred to as streaming, are present in many large cells to facilitate long-distance transport and compartmentalisation of cellular material, essential for polarity establishment and fertility (Manseau & Schupbach 1989; Serbus et al. 2005; Quinlan 2013; Bor et al. 2015; Alberti 2015; Pieuchot et al. 2015; Quinlan 2016). In the oocyte, there are two types of cytoplasmic streaming that occur at mid- and late oogenesis: slow streaming and fast streaming, respectively. Both types of streaming are driven by the translocation of cargo-loaded kinesin-1 along microtubules, creating a viscous drag that entrains cytoplasmic content due to the viscous nature of the surrounding cytosol. Fast streaming is driven by the change in MT organisation towards the cortex at *st10B* and is crucial for the appropriate mixing of newly contributed NC content (Figure 1.5C-C'; Gutzeit 1986; Palacios & St Johnston 2002; Serbus et al. 2005; Drechsler et al. 2017). The transition from slow to fast streaming is influenced by the actin network which is present in the oocyte in two main structures, cortical actin, and as a uniform network of F-actin called the actin mesh nucleated by *spire* and *capu* traversing the entire cytoplasm in the earlier stages of oogenesis and disappearing on the initiation of fast streaming at around *st10B-11*. Mutations in *capu* and *spire* and depolymerisation of the MT network lead to aberrations in the actin mesh (Figure 1.6; Gutzeit & Koppa 1982; Theurkauf et al. 1992; Theurkauf 1994; Palacios & St Johnston 2002; Dahlgaard et al. 2007; Quinlan 2013; Quinlan 2016; Drechsler et al. 2017).



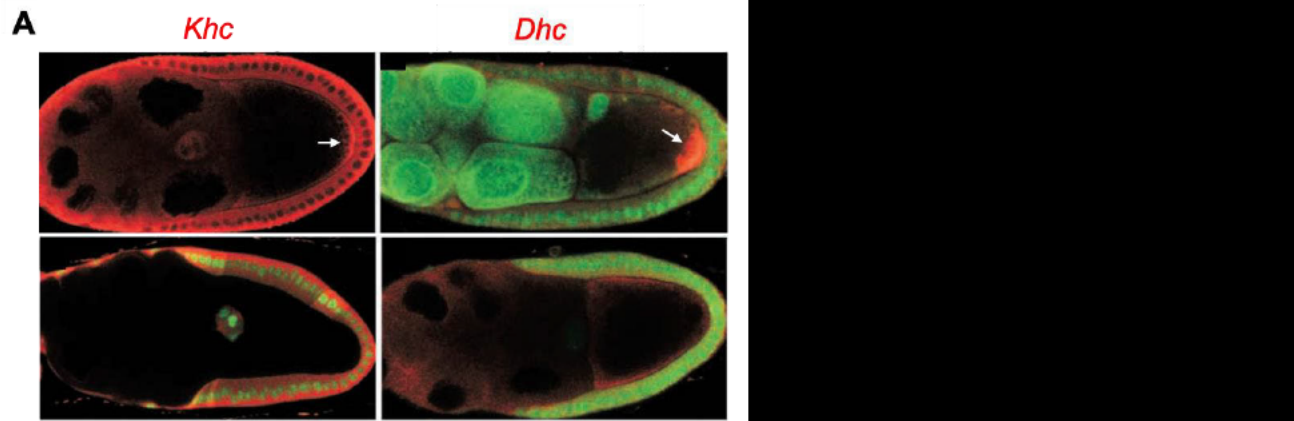
**Figure 1.6. The actin mesh in wildtype, *capu* and *spire* mutant *st9* oocytes.** (A-C') Egg chambers stained with TRITC-Phalloidin to label F-actin. Gray scale bar represents 30  $\mu\text{m}$ , white scale bar represents 10  $\mu\text{m}$ . (Images taken from Dahlggaard et al. 2007). (A-A') *St9* wildtype oocytes (B-B') *St9 capu<sup>2F</sup>* mutant oocytes. *capu<sup>2F</sup>* contains a point mutation in the FH2 domain and is one of the weakest alleles of *capu* explaining the residual actin mesh in these mutants (C-C') *St9 capu<sup>G7</sup>/Df(2L)ed<sup>SZ1</sup>* mutant oocytes. *capu* levels are lower in this mutant than (B-B') coinciding with an imperceptible actin mesh (D-G) F-actin binding UTRN-GFP (green, left panel) and DIC (right panel) in *st9* oocytes (Images taken from Drechsler et al. 2017). (D) *St9* control oocytes with intact actin mesh (E) *St9* oocytes overexpressing actin nucleator SpireB. Overexpression of SpireB leads to an increase in the levels of F-actin in the oocyte (F) *spire* mutant oocytes incubated in control DMSO-containing medium (G) *spire* mutant oocyte incubated in colchicine-containing medium. The actin mesh fails to form in *spire* mutant oocytes. Scale bar represents 30 $\mu\text{m}$ .

Research has shown that FCs trigger a MT repolarising event at the onset of mid-oogenesis believed to involve the upregulation of serine/threonine kinase Par-1N1 isoform and recruitment of the actin cytoskeleton. This signal disassembles a posteriorly localised microtubule organising centre (MTOC), initiating the formation of an anteroposterior gradient of MTs and is also thought to trigger the migration of the oocyte nucleus to the anterior, near the NC border (Shulman et al. 2000; Januschke et al.

2005; Doerflinger et al. 2006; Poulton & Deng 2007). This event is crucial in establishing the body axis as Par-1N1 facilitates the posterior localisation of *oskar* (*osk*) mRNA by kinesin-1 and anterior localisation of *bicoid* (*bic*) mRNA by dynein through the redirection of MT plus-ends towards the posterior (Figure 1.5D-G; Ephrussi & Lehmann 1992; Brendza et al. 2000; Palacios & St Johnston 2002). The presence of the Oskar protein at the posterior recruits even more Par-1N1 creating a positive feedback loop maintaining both mRNA localisation and MT organisation (Shulman et al. 2000; Tomancack et al. 2000; Zimyanin et al. 2007; Poulton & Deng 2007; Bastock & St Johnston 2008). During late oogenesis, before the degeneration of NCs and the formation of a mature egg, NCs contract and initiate a process called 'dumping' where all the cellular content is pushed into the oocyte including the dynein gene, situating it in the perinuclear region. In mutants for kinesin or dynein, and oocytes treated with MT-depolymerising drugs like colchicine, proper localisation of mRNAs is impeded, consistent with the idea that this localisation relies on the organisation of MTs and the activity of the associated motor proteins (Figure 1.7B; Gutzeit 1986; Pokrywka & Stephenson 1991; Clark et al. 1994; St Johnston 1995; Lipshitz & Smibert 2000; Reichmann & Ephrussi 2001; Januschke et al. 2002; Palacios & St Johnston 2002; MacDougall 2003; Steinhauer & Kalderon 2006; Brendza et al. 2007; Quinlan 2016).

Although dynein is a minus end motor and mainly localises at the anterior of the oocyte based on MT orientation, dynein antigen accumulation is also observed in the posterior of *st9* oocytes along with pole plasm components *Staufen* and *osk* mRNA. Localisation of dynein here could possibly occur via kinesin-mediated transport as suggested in *Khc* null germline clones where there is no posterior *cDhc* localisation, only anterior accumulation, a defect rescued by insertion of a wildtype kinesin transgene (Figure 1.7A; Palacios & St Johnston 2002). Additionally, in *Khc*<sup>27</sup> null mutations, *osk* mRNA is distributed throughout the anterior of the oocyte and is enriched at the lateral cortex and mutants demonstrate defects in dorsoventral axis formation due to the aberrant accumulation of *grk* mRNA across the anterior instead of being concentrated near the nucleus (Figure 1.7B; Clark et al. 1994; Li et al. 1994; Brendza et al. 2002; Palacios & St Johnston 2002). The proposed model thus states that the action of kinesin-1 either

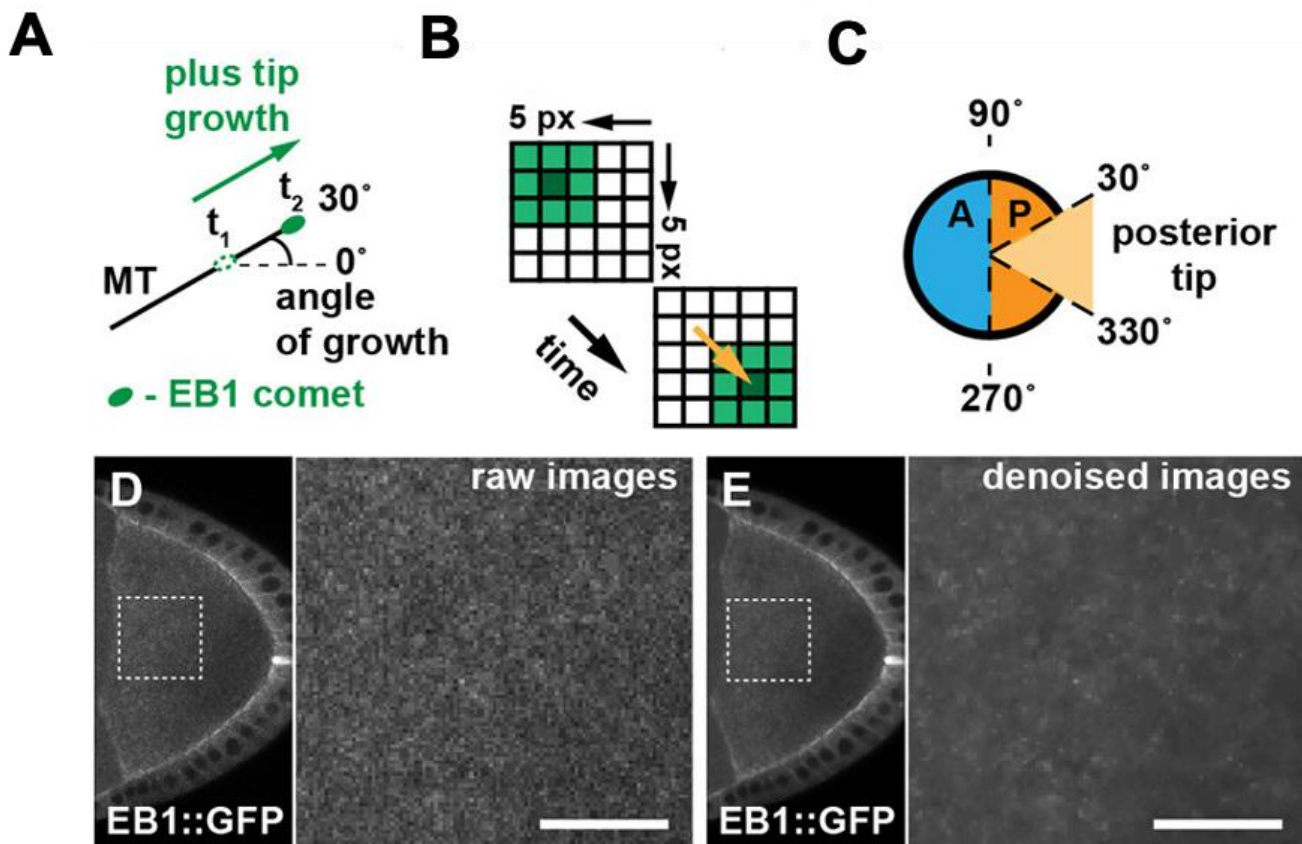
directly or indirectly is responsible for the transport of dynein to the posterior to allow 'recycling' of dynein to the plus-ends to continue anterior-directed transport of molecules.



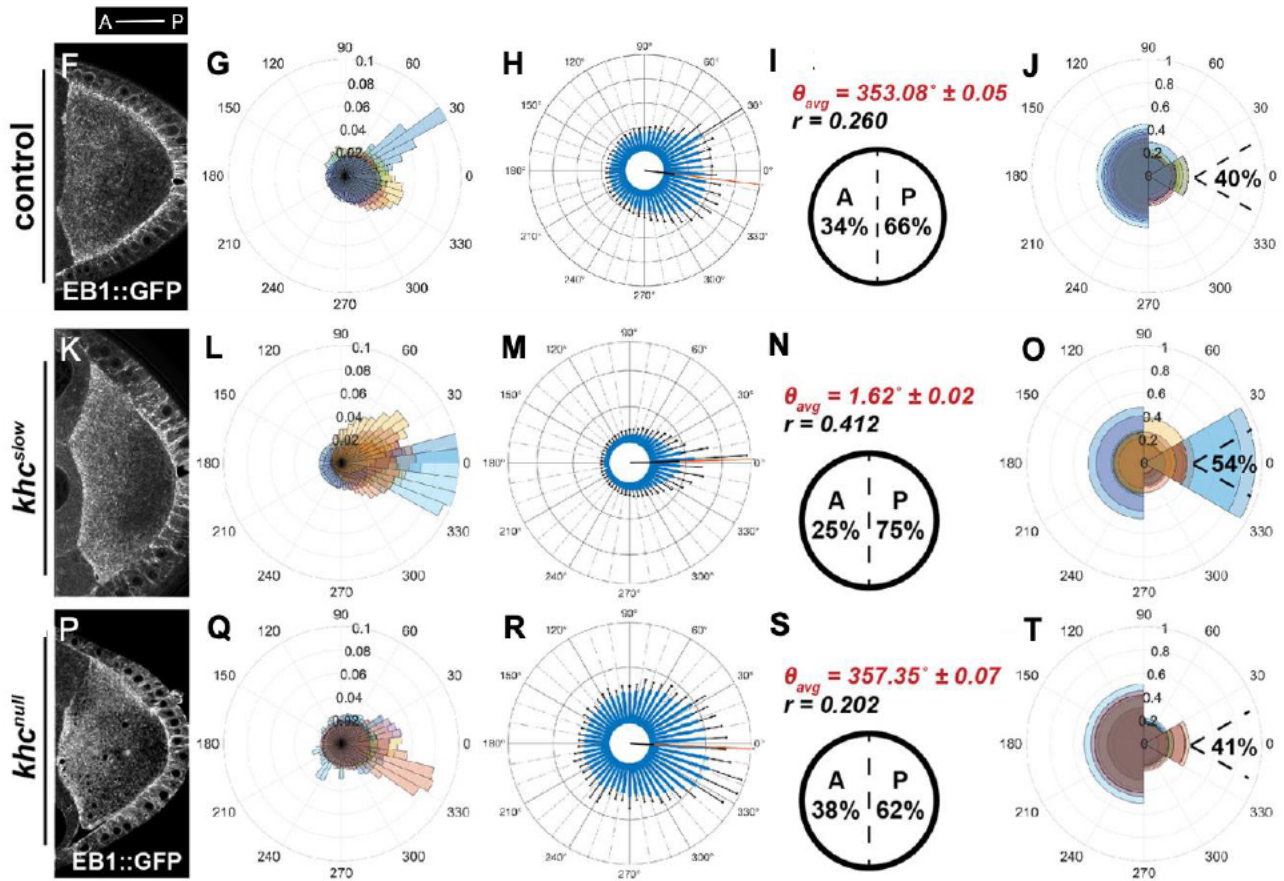
**Figure 1.7.** *Distribution of kinesin, dynein and grk mRNA in the oocyte.* (A) Dynein and kinesin heavy chain accumulation is observed in the posterior of wildtype *st9* oocytes (top row). Staining for Khc is absent in the null mutants and posterior localisation of Dhc is abolished (bottom row) (Image taken from Palacios & St Johnston 2002; anterior - A, posterior - P). (B) Disruption of *Khc* also affects *grk* localisation in *st8* (left column) and *st10* (right column) oocytes. White asterisk denotes nucleus positioning, scale bars represent 50µm (Image taken from Brendza et al. 2002).

Using optical flow (OF) analysis, observing MT orientation and direction of growth in oocytes with mutated kinesin motors demonstrates the role of kinesin in MT orientation (Drechsler et al. 2020). Mean angular direction of MT growth was determined by the direction of the vector fields of plus-end binding protein EB-1 and represented by polar coordinates (Figure 1.8A-C). To investigate how posterior-focused MT growth is at *st9*, the frequency of EB-1 signals falling within a sector of 60° of these coordinates was calculated. 66% of EB-1 comets fall within this area that encompasses the 'posterior tip', where determinants localise and the pole plasm forms implying that growing MT orientation exhibits a global posterior bias (Figure 1.8F-J). In the absence of streaming in *Khc*<sup>27</sup> null mutants, MTs appear motionless and stiff with a lack of posterior-directed transport while in oocytes expressing slower kinesin motors (*Khc*<sup>23</sup> and *Khc*<sup>17</sup>) and an intact actin mesh, MTs display the same stiff and motionless phenotype as null mutants. EB-1 comets in null mutants revealed a 10% decrease in posterior tip-directed MT

organisation while those in the 'slow' mutant displayed a 10% increase (Figure 1.8K-T). When kinesin-dependent streaming is upregulated in mutants of actin nucleators *capu* or *spier*, MTs form tight bundles of filaments and tagging of EB-1 shows a cluster of comets moving in close proximity and as a consequence of the faster flows (Figure 1.8U-Z). Altogether, this data demonstrates the precise regime of motion, particularly cytoplasmic streaming, required to ensure correct localisation of determinants and thus proper development of the oocyte. This regime involves both cytoskeletons and their associated proteins whose precise function contributes to a delicate reciprocal interplay between the cytoskeletal system and its environment.







**Figure 1.8. MT orientation according to speed of flows.** (A) EB-1 attaches to plus ends of MTs and serves as a readout for spatial orientation, represented here as an angle deviating from an imaginary anterior (180°) to posterior axis (0°). (B) Underlying principle of OF-based motion estimation. Two consecutive frames of a 5 × 5 pixel-wide image sequence containing a rectangular object of different pixel intensities—from light green (little signal) to dark green (maximum signal). OF assumes signal intensity does not to change along the objects' trajectory. A displacement vector for each pixel can then be calculated using variational OF as indicated by the yellow arrow, showing the displacement vector of the centre pixel. (C) Definition of growth directions: angles of velocities between 90° and 270° are anterior (A, blue hemicircle) and the complementary set of angles as posterior (P, orange hemicircle). The subpopulation of all posterior signals (orange) that fall between 330° and 30° (light orange sector) are considered to grow toward the posterior tip. (D) Raw image demonstrating EB1 expression, magnified area indicated by dashed box (anterior - A, posterior - P) MTs grow one order magnitude faster than cytoplasmic flow and images were taken every 650ms with low spatial resolution and the presence of a lot of noise. Images thus required denoising (E). Scale bars are 10  $\mu\text{m}$ . (F) Temporal projection of EB1 in control oocyte (65s image sequence). Oocytes were orientated with the posterior pole to the right during imaging and the angles given in the rose diagrams (G,L,Q) reflect the directional movement of EB1 comets in each cell. Distribution was also averaged across all cells of a given phenotype (H,M,R). We determined the mean angular direction of the estimated motion of EB1 signals ( $\theta_{\text{avg}}$ ) of a single phenotype to quantitatively describe MT orientation (I,N,S). (G) Angular histogram with 50 bins for EB1 directions in individual control cells, each colour representing the angular histogram of EB1



direction from one oocyte. (H) Data from (G) averaged over all cells ( $n = 8$ ), error bars (black) represent standard deviation for each bin (blue). (I) Mean angular direction  $\theta_{\text{avg}}$  of (H), red line in (H), and length  $r$  between 0 and 1 of mean resultant vector, depicted by length of black line originating from centre of (H) relating to the circular variance  $S = 1-r$  of distribution shown in (H). (J) Similar rose diagram to (G,L,Q) but growth directions are put into four bins:  $30^\circ\text{--}90^\circ$ ,  $90^\circ\text{--}270^\circ$ ,  $270^\circ\text{--}330^\circ$ , and  $330^\circ\text{--}30^\circ$ . Same analysis in control cells (F-J) applied to *khc<sup>slow</sup>* oocytes (K-O) and *khc<sup>null</sup>* oocytes (P-T). All images taken from Drechsler et al. 2020.

As mentioned previously, the actin mesh disappears at *st10B-11* to facilitate the transition into the fast-streaming stage. *Capu* and *spire* mutants present disrupted MT organization, premature streaming and mislocalised *osk* and *grk* mRNAs, the same phenotype as oocytes treated with the actin depolymerising drug cytochalasin D (CytoD), while the overexpression of either nucleator halts streaming (Theurkauf 1994; Clark et al. 1994, Emmons et al. 1995; Manseau et al. 1996; Dahlgaard et al. 2007; Quinlan 2013; Lu et al. 2016; Drechsler et al. 2017). Additionally, reducing the movement of kinesin with a missense mutation in the motor domain, *Khc<sup>17</sup>*, in *capu* mutants prevented premature streaming. This data suggests that actin nucleators and the presence of an intact actin mesh indirectly regulates microtubules by constraining kinesin-driven flows (Dahlgaard et al. 2007; Drechsler et al. 2017). Thus, the assembly of the actin mesh by *capu* and *spire* influences MT organisation at mid-oogenesis demonstrating the interplay between the two cytoskeletons necessary for the reorganization of the oocyte.

#### 1.4 Intercellular trafficking pathways and the involvement of the microtubule and actin networks.

Communication between cells and intracellular compartments relies on vesicle transport. Membrane-bound vesicles shuttle proteins, lipids, and organelles to different regions of the cell or between cells via exocytic and endocytic pathways with the help of motor proteins and cytoskeletal force generation (Bloom & Goldstein 1998; Hirokawa & Noda 2008; Ross et al. 2008; Schuh 2011). Exocytosis is the process by which constitutive and facultative secretory products, including neurotransmitters and hormones, whose release is often triggered by rises in cytoplasmic calcium ( $\text{Ca}^{2+}$ ) levels, are released from the cell into the extracellular matrix by fusing of the vesicular

membrane to the plasma membrane. Regulated exocytosis and secretion of vesicles in response to extracellular stimuli is a fundamental process in many eukaryotic cells, including neurons, hematopoietic, endocrine and exocrine cells (Morgan 1995; Burgoyne & Morgan 2003; Xu et al. 2018; Hessvik & Llorente 2018).

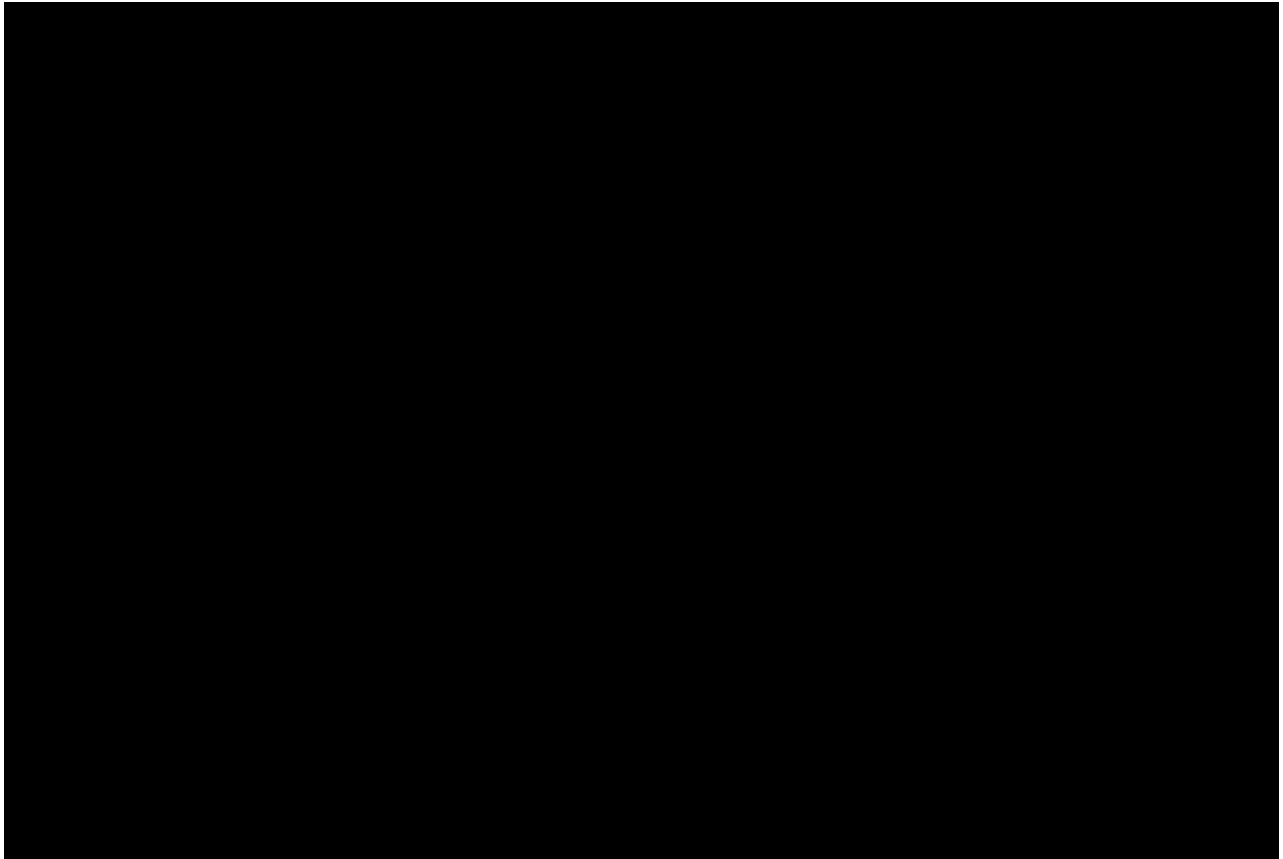
Endocytosis is the process by which extracellular material is internalised by the cell as cargo with typically three fates: recycling back to the membrane, lysosomal degradation or transcytosis. All vesicular trafficking processes occur through endosomes with the help of specialised protein complexes needed to harness and regulate membrane fusion, fission and tethering including the Ras superfamily of small GTPases and Rab GTPases (Sato et al. 1992; Zhang et al. 2007; Šamaj et al. 2004; Donaldson et al. 2009; Grant & Donaldson 2009; Huotari & Helenius 2011; Podinovskaia & Spang 2018). Clathrin-dependent endocytosis is the most well-defined process of endocytosis and begins when the clathrin triskelia is recruited to the plasma membrane by adaptor proteins that recognize signals on the cytoplasmic tails of cargo proteins. The self-assembling properties of clathrin, along with curvature-inducing proteins like epsins and BAR domain containing proteins, lead to the formation of clathrin-coated pits which pinch off with the aid of the dynamin pinchose to form clathrin-coated vesicles containing internalized cargo (Mellman 1996; ter Haar et al. 1998; Doherty & McMahon 2009; Antony et al. 2016). Clathrin-independent endocytosis (CIE) pathways can utilize the GTPase dynamin for vesicle scission or operate independently of dynamin and rely more on the actin cytoskeleton and BAR domain proteins like endophilin-A2 and endophilin-A1 (Mayor & Pagano 2007; Johannes et al. 2015; Boucrot et al. 2015; Renard et al. 2015).

Irrespective of their origin or destination, once sequestered in endosomes, cargo becomes a part of the endosomal network which acts as a highway system for transfer between vesicles. This network is highly dynamic and in a constant state of flux as endosomes go through the maturation process to reach their final destinations. Also referred to as the endosomal-lysosomal system, this network is composed of endosomes at all stages of maturation; early endosomes (EE), late endosomes (LE),

recycling endosomes (RE) and lysosomes (Šamaj et al. 2004; Behnia & Munro 2005; Huotari & Helenius 2011). The identification of endosomes through these stages is largely based on the presence of different Rab GTPases and phosphoinositides (PIs) on the surface which dictate endosomal function and coordinate membrane traffic. Rabs are critical membrane components as they function as a molecular switch between inactivated (GDP-bound) and activated (GTP-bound) forms and associate with specific organelles, also functioning as markers for specific subcellular compartments (Zhang et al. 2007; Huotari & Helenius 2011; Mesaki et al. 2011; Birgisdottir & Johansen 2020).

The various protein and lipid constituents sequestered by endosomes undergo discriminating selection processes within the EE network to dispatch them along their respective post-endocytic trafficking trajectories. EEs sort recycling material back to the membrane or transport to lysosomes for degradation via maturation (Figure 1.9; Donaldson et al. 2009; Huotari & Helenius 2011; Hu et al. 2015). Endosomes undergo four main morphological and biological changes as they mature starting with an increase in intraluminal vesicles (ILVs), followed by a decrease in luminal pH, retrograde movement towards the MTOC and, lastly, the switching of Rab proteins. Cytosolic proteins are recruited to the membrane of EEs that facilitate and define its function such as Rab5, its effector VPS34/p150 and phosphatidylinositol 3-kinase (PI3K) (Huotari & Helenius 2011; Hu et al. 2015; Langemeyer et al. 2018). The diameter of EEs ranges from 100-500nm, with a pH of 6.8-5.9 for dissociation of internalised receptors from their ligands. The EE to LE maturation process is initiated by a decrease in the intraluminal pH to within the range of 6.0-4.9 and an accumulation of intraluminal vesicles (ILVs) that eventually form into multivesicular bodies (MVBs), followed by the conversion of Rab5 to Rab7 (Helenius et al. 1983; Maxfield & Yamashiro 1987; Christoforidis et al. 1999; Zerial & McBride 2001; Behnia & Munro 2005; Huotari & Helenius 2011; Liu et al. 2015). MVBs are considered an intermediary stage between early and late endosomes, transitioning to LEs once they have acquired all fusion proteins required for lysosomal transfer. In addition to directing LE transport, Rab7 activity is crucial for lysosome biogenesis and positioning demonstrated in the failure of lysosomal perinuclear aggregation and reduction in intraluminal acidity in

dominant negative Rab7 mutants (Aniento et al. 1993; Behnia & Munro 2005; Luzio et al. 2007; Vanlandingham & Ceresa 2009; Huotari & Helenius 2011; Liu et al. 2015; Jacomin et al. 2016; Bucci et al. 2017; Birgisdottir & Johansen 2020).



**Figure 1.9 Endolysosomal pathway (taken from Yang & Wang 2021).** To transport endosomal proteins to lysosomes, early endosomes undergo a maturation process characterized by the switching of Rab5 and phosphatidylinositol 3-phosphate (PtdIns3P) to late endosome-specific Rab7 and phosphatidylinositol 3,5-bisphosphate (PtdIns(3,5)P<sub>2</sub>). Proteins that are destined for lysosomal degradation undergo recycling through retromer-dependent and retromer-independent pathways, returning to the plasma membrane or Golgi apparatus. The process of autophagy transports cytoplasmic material to the lysosome for degradation. This process supports cell survival by removing damaged organelles and protein aggregates, and maintaining bioenergetic homeostasis. Autophagosomes undergo a maturation process to fuse with late endosomes/lysosomes, employing essentially the same sets of proteins (Rab7/HOPS/SNAREs) as those involved in the fusion of endosomes and lysosomes (Yang & Wang 2021).

Once LEs are formed in the cell periphery, they move towards the perinuclear area to initiate the process of lysosomal degradation. Several theories have been proposed to explain the mechanism by which LEs transfer material to lysosomes including maturation, direct fusion, kiss-and-run, and fusion-fission (Aniento et al. 1993; Nielsen et al. 1999; Šamaj et al. 2004; Hoepfner et al. 2005; Mesaki et al. 2011). The kiss-and-run process involves transient contact between LEs and lysosomes for transfer of material followed by dissociation of the two organelles. Fusion-fission involves a similar process but creates a hybrid organelle that would require a fission event to reform the lysosome. A combination of direct fusion and kiss-and-run processes has been demonstrated to be the predominant mechanism by which this transfer occurs (Storrie & Desjardins 1996; Mullock et al. 1998; Bright et al. 2005; Luzio et al. 2007; Skjelda et al. 2021). In yeast, actin is essential for clathrin-dependent endocytosis while in mammalian cells, actin aids endocytosis when more force is needed to bud rigid membrane regions or ingest large cargos and helps stabilize the elongating vesicle neck by pushing against the membrane (Sun et al. 2006; Aghamohammadzadeh & Ayscough 2009; Cureton et al. 2009; Boulant et al. 2011; Collins et al. 2011). The clathrin- and dynamin-independent CLIC/GEEC (CG) pathway relies heavily on the actin cytoskeleton machinery and is the main route for ingesting a large portion of glycosylphosphatidylinositol-anchored proteins (GPI-APs) and fluid phase markers in mammalian and *Drosophila* cells, further evidenced by CG regulation by Cdc42, which modulates actin polymerization (Sabharanjak et al. 2002; Guha et al. 2003; Kalia et al. 2006; Sun et al. 2006; Chadda et al. 2007; Kumari & Mayor 2008; Rossatti et al. 2019). In human skin melanoma SK-MEL-28 cells, depolymerising the actin cytoskeleton with low levels of latrunculin A showed reduced endocytosis and in motile cells, the ABP cortactin has been found to localise on the surface of endosomes in lamellipodia. Moreover, disrupting the MT or actin cytoskeletal networks impedes cargo distribution from EEs into compartments with low pH (*i.e.*, LEs) delaying cargo degradation (Bayer et al. 1998; Kaksonen et al. 2000; Šamaj et al. 2002; Baravalle et al. 2005; Galletta & Cooper 2009; Mesaki et al. 2011; Tanabe et al. 2011; Mooren et al. 2012; Cheng et al. 2012).

The movement of endosomes is variable and dependent on their cargo and stage of maturation associating with different motor proteins and cytoskeletons at different timepoints. Fusion and fission of EEs to one another and the long-range transport of EEs towards the perinuclear region for fusion with lysosomes or back to the plasma membrane for recycling is largely mediated by kinesin and dynein activity. A few kinesin motor proteins have been identified as key players in endosomal trafficking including kinesin-1 (human homologue KIF5B), kinesin-2 (human homologue KIF3A) and kinesin-3 (human homologue KIF16B) the disruption of which leads to delays in EE maturation and anomalous distribution of endosomes and lysosomes (Gruenberg et al. 1989; Aniento et al. 1993; Nakata & Hirokawa 1995; Hoepfner et al. 2005; Brown et al. 2005; Chen & Yu 2015; Birgisdottir & Johansen 2020). KIF5B transports organelles towards the MT plus-ends and in its absence leads to perinuclear clustering of Rab6 endosomes similar to KIF3A mutations which result in abnormal clustering of endosomes in HeLa cells and neurons (Tanaka et al. 1990; Schuchardt et al. 2005; Nath et al. 2007; Barkus et al. 2008; Serra-Marques et al. 2020). When Rab5 is activated, KIF16B binds to the Rab5 effector VPS34 on EEs via its PI(3)P-binding PX domain regulating the balance of degradation and recycling, while in the absence of KIF16B, cargo recycling decreases and degradation increases (Christoforidis et al. 1999; Nielsen et al. 1999; Gillyooly et al. 2000; Murray et al. 2002; Hoepfner et al. 2005; Farkhondeh et al. 2015). Additionally, Rab7 and its effector RILP and Rab5 and its effector the FHF complex have been shown to mediate retrograde transport of endosomes through interactions with the dynein-dynactin complex (Vanlandingham & Ceresa 2009; Dodson et al. 2012; Xiang X et al. 2015; Guo et al. 2016; Bucci et al. 2017; Christensen et al. 2021).

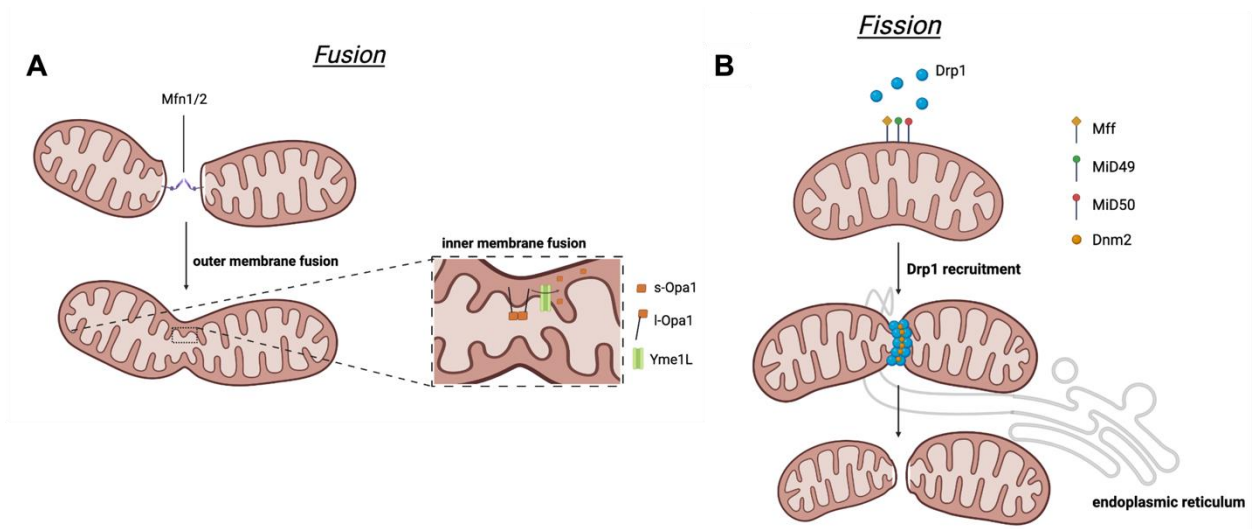
### 1.5 Role of actin and microtubules in the motion, function, and dynamics of the mitochondrial network.

It is now widely accepted that mitochondria form a very dynamic, interconnected membrane-bound tubular network, rather than static and isolated structures, undergoing constant change in response to biochemical stimuli and energetic demands. The size,

number and distribution of mitochondria is regulated by processes of fusion and fission collectively referred to as mitochondrial dynamics. The dynamics and arrangement of the mitochondrial network are influenced by cellular signals that adapt to changes in energy requirements,  $\text{Ca}^{2+}$  transients and posttranslational modifications and are dependent on MTs and actin (Saotome et al. 2008; MacAskill et al. 2009; Wang & Schwarz 2009). For example, mitochondria in the sperm cell are localised to the proximal region of the flagellum to provide ATP for force-generation while in the neuron, mitochondria are trafficked by MT motor proteins to the axonal terminals to drive synaptic vesicle release (Pilling et al. 2006; Ferramosca et al. 2012; Sheng & Cai 2016; Mandal & Drerup 2019; Cardanho-Ramos et al. 2020). In organelle movement assays and *in vivo*, mitochondria have been observed to localise with murine KIF1B and KIF5B (Nangaku et al. 1994; Tanaka et al. 1998; Henrichs et al. 2020). Association of mitochondria to actin was first identified through the discovery of the preferential binding of human unconventional Myosin XIX (Myo19) to the outer mitochondrial membrane mobilising for the formation of stress-induced filopodia and mitochondrial inheritance during cytokinesis and the overexpression of *Myo19* in mammalian cells was shown to result in a 2-fold increase in mitochondrial velocity (Quintero et al. 2009; Shneyer et al. 2016; Sato et al. 2022). In mouse oocytes treated with the MT depolymerising drug nocodazole, MTs failed to form and mitochondria were unable to localise correctly to the perinuclear region while in oocytes treated with taxol, a MT stabilising drug, MT bundles formed followed by the localisation of large aggregates of mitochondria near the MTOCs (Van Blerkom 1991; Dalton & Carroll 2013).

The precise regulation of fusion and fission events drives the adaptability of the network to nutrient availability and metabolic requirements of the cell. The balance of fusion and fission dictate the number, size, distribution, and health of mitochondria. Mitochondria need to be degraded or repaired to maintain a homogenous population of organelles. The process of fusion drives content transfer and mixing of mtDNA to bolster fitness while fission ensures a population of organelles available for segregation into daughter cells and contributes to homogenisation by fragmenting dysfunctional mitochondria for efficient engulfment by autophagosomal machinery (Twig et al. 2008; Chen & Chan

2009; Mishra & Chan 2014; Friedman & Nunnari 2014; Tilokani et al. 2018). These processes require the activity of multiple molecular complexes in the inner mitochondrial membrane (IMM) and outer mitochondrial membrane (OMM) and help coordinate the mitochondrial network through morphological changes. Dysregulation of either process and subsequent disruption of the balance of fusion and fission is associated with several pathologies and diseases marked by changes in mitochondrial morphology and function such as Charcot-Marie-Tooth type 2A, a peripheral neuropathy, and dominant optic atrophy, an inherited optic neuropathy (Chen et al. 2007; Chen & Chan 2009; Cardoso et al. 2012; Mishra & Chan 2014; Cardoso et al. 2012).

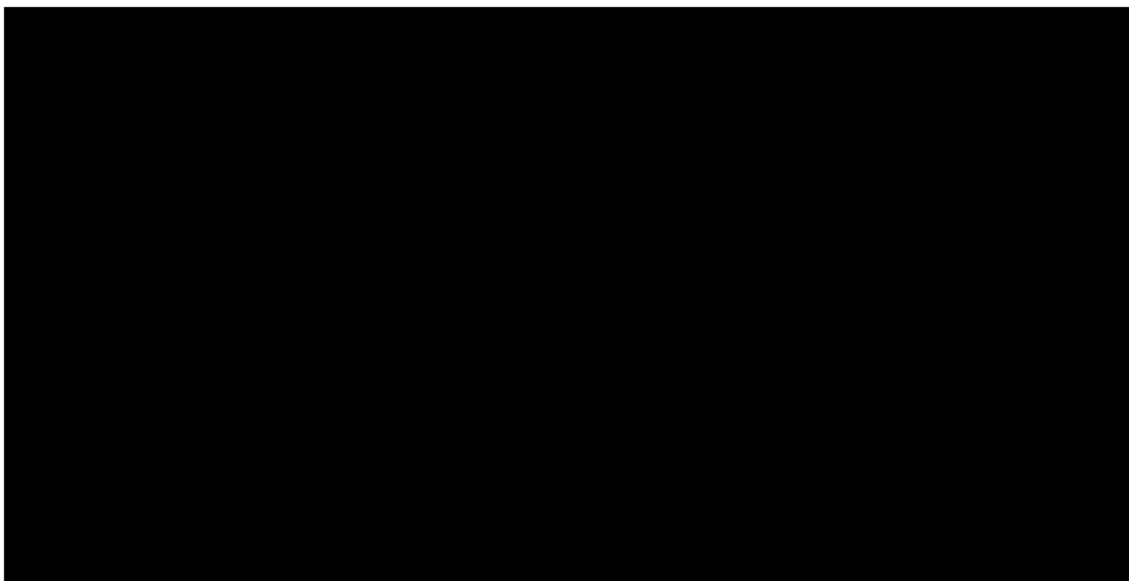


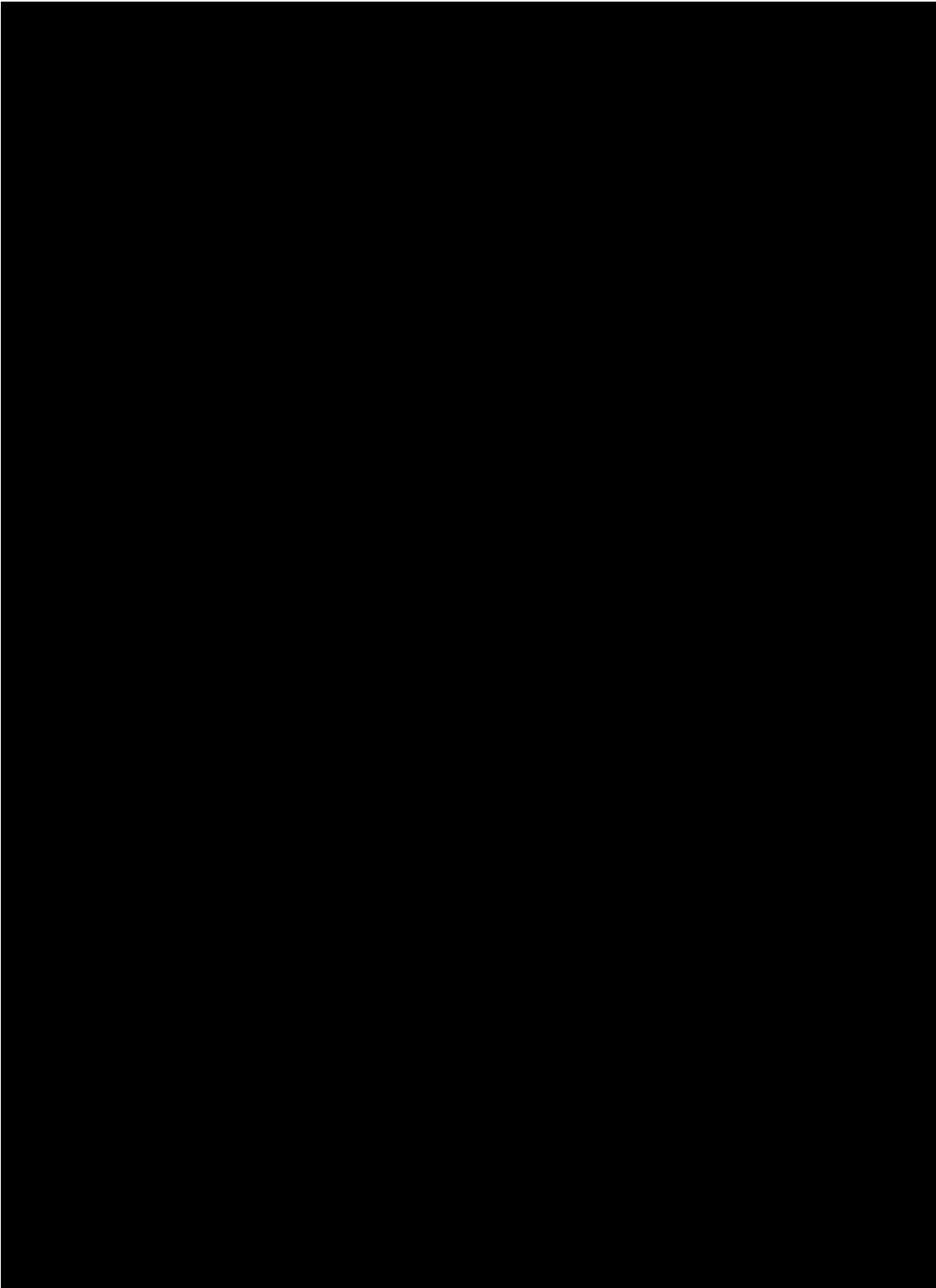
**Figure 1.10. Mitochondria dynamics.** (A) Simplified schematic of mitochondrial fusion. Mfn1/Mfn2 are found on the outer mitochondrial membrane (OMM) while Opa1 mediates fusion on the IMM. Fusion thus begins with fusing of the OMM mediated by Mfn1/2 followed by fusing of the IMM through the activity of Opa1. (B) Simplified schematic of mitochondria fission. Dynamin-related protein 1 (Drp1) and dynamin-2 (Dnm2) found on the OMM drive fission through constriction and scission, respectively, recruited by mitochondrial fission factor (Mff) and mitochondrial dynamics proteins 49 and 51 (MiD49 and MiD51). Fission can also be ER-mediated for larger mitochondrial tubules where the diameters of Drp1 and Dnm2 are not wide enough to form contractile rings.

Key players in the processes of fusion and fission are dynamin-related GTPases. The first mitochondrial fusion protein fuzzy onion (Fzo1) was originally discovered in *Drosophila* sperm cells (also found in yeast) followed by the mitochondria assembly



regulatory factor (Marf) in other cells (Hales & Fuller 1997; Santel & Fuller 2000; Koshiba et al. 2004). Mammals carry two homologues of these proteins, *Mitofusin-1* and 2 (*Mfn1* and *Mfn2*) as well as *optic atrophy 1* (*Opa1*), the latter of which is also present in *Drosophila* (Cipolat et al. 2004; Filadi et al. 2018; Ge et al. 2020). *Mfn1* and *Mfn2* are found on the OMM while *Opa1* mediates fusion on the IMM, fusion thus begins with fusing of the OMM mediated by *Mfn1/2* followed by fusing of the IMM through the activity of *Opa1* (Figure 1.10A). This occurs in three major stages, first the mitochondria are tethered to maintain proximity, followed by docking of the membranes to increase the contact surface area and, lastly, fusion of the OMM through conformational changes undergone by *Mfn1/2* (Figure 1.10A; Santel & Fuller 2000; Chen et al. 2003; Cipolat et al. 2004). In mouse embryos, knocking out *Mfn1* and 2 results in fragmented mitochondria, no detectable fusion, and a loss of membrane potential. Double homozygous mutations demonstrate a greater developmental delay compared to either single mutation indicating the need for the concerted function of both *Mfns* (Figure 1.11A-F; Chen et al. 2003; Filadi et al. 2018). The morphological changes of mitochondria in *Mfn* KO cells also affect mobility, preventing radial movement and increasing Brownian-like motion of fragmented organelles, while aggregation of mitochondria as a result of *Mfn* overexpression inhibits motility (Chen et al. 2003; Ishihara et al. 2009; Chen & Chan 2009). It is thus likely that manipulating *Mfns* could interfere with the connection between mitochondria and the MT cytoskeleton, enabling random mitochondrial movement over directed motion.





Images redacted due to copyright permissions  
Images available at source in figure legend.

**Figure 1.11. Changes in mitochondrial morphology upon mutation of fusion-fission machinery.** (A-F) (Images taken from Chen et al. 2003) Mitochondria-EYFP counterstained with rhodamine-phalloidin in mouse embryonic fibroblast (MEF) cells. (A-B) Mitochondrial morphology in wild-type MEF cells. (C-D) Mitochondria morphology in *Mfn1* mutant MEF cells (E-F) Mitochondrial morphology in *Mfn2* mutant. Arrow indicates a tubule >10µm in length. (G-H) HeLa cells transfected with GFP-siRNA for controls (cont.) or human Opa1 and cells were stained with MitoTracker (Images taken from Ishihara et al. 2006). (H) Mitochondrial network was fragmented in *Opa1* mutants. (I-N) Mitochondria visualised by GFP -tagging mitochondria in *mitochondrial genome maintenance-1 (mgm1)* mutant *Saccharomyces cerevisiae (S. cerevisiae)* cells. Mgm1 is a dynamin-like GTPase necessary for mitochondrial fusion in yeast (Images taken from Wong et al. 2000). (J-M) *mgm1* mutant cells displayed fragmented mitochondria when compared to controls (I-L). (K-N)  $\Delta$ *mgm1* mutants also displayed a fragmented mitochondrial network when compared to controls with a slightly more dramatic phenotype. Scale bars represent 2µm. (O-T) MEF cells expressing mitochondria-DsRed and YFP-tagged  $\alpha$ -tubulin (Images taken from Ishihara et al. 2009). (O-Q) *Drp1 lox/lox* MEFs. (P) In the early mitotic phase, mitochondria are fragmented and spread throughout the cytoplasm in control cells. (R-T) *Drp1*<sup>-/-</sup> MEFs. (S) Mitochondria displayed filamentous morphology and clustered leading to asymmetric division of the mitochondrial network between daughter cells (T).

Opa1 is a special dynamin-related GTPase as it has eight splice variants and exists in two forms, a long form membrane-bound molecule and a soluble short form variant lacking the transmembrane anchoring domain that plays a role in fusion (Cipolat et al. 2004; Song et al. 2007; Mishra et al. 2014; MacVicar & Langer 2016; Ge et al. 2020). Studies have shown that while OXPHOS triggers Yme1L-mediated Opa1 cleavage for fusion, stress-induced Oma1-mediated cleavage generates s-Opa1 and leads to mitochondrial fragmentation to enhance mitophagy and cell death (Baker et al. 2014; Mishra et al. 2014). In HeLa cells, deletion of *Opa1* has led to fragmented mitochondria and aberrations in the morphology of the IMM while overexpression leads to elongation of the organelle (Figure 1.11G-H; Ishihara et al. 2006). Another mitochondrial stress response is hyperfusion which relies on l-Opa1 to increase network connections to protect against the effect of stresses either through steric hindrance or maintaining ATP production (Tondera et al. 2009; Simcox et al. 2013). *Opa1* is named after the condition that develops when the gene is mutated; autosomal dominant optical atrophy, a progressive degeneration of retinal ganglia cells in the optic nerve that leads to blindness one of the number of diseases associated with mutations in mitochondrial fusion and fission machinery (Griparic et al. 2004; Davies et al. 2007; MacVicar & Langer 2016).

In humans, *Mfn2* mutations cause Charcot-Marie-Tooth type 2A (CMT2A) an inherited, sensorimotor polyneuropathy, while abnormal levels of the fission protein dynamin-related protein 1, Drp1, is associated with developmental delays, ataxia and peripheral neuropathy (Palau et al. 2009; Pareyson et al. 2015; Ueda & Ishihara 2018; Dai et al. 2020; Wei & Qian 2021; Johnson et al. 2021). Drp1 functions as a molecular scissor, polymerising and constricting around membranes to initiate fission, the formed contractile rings constrict upon GTP hydrolysis in a process similar to membrane constriction during endocytosis (Figure 1.10B; Labrousse et al. 1999; Ishihara et al. 2009; Chen & Chan 2009; Kraus & Ryan 2017; Whitley et al. 2018). Once Drp1 is recruited at the membrane and initiates constriction, Dnm2 binds transiently forming a collar-like structure to separate the sister organelles. Fission can also be ER-mediated for larger mitochondrial tubules (~300nm) where the diameters of Drp1 and Dnm2 are not wide enough to form contractile rings (Bleazard et al. 1999; Labrousse et al. 1999; Friedman et al. 2011; Korobova et al. 2013; Lee & Yoon 2014). In mammals, the tail-anchored adaptor proteins that recruit Drp1 to the membrane are mitochondrial fission factor (Mff) and mitochondrial dynamics proteins 49 and 51 (MiD49 and MiD51) (Figure 1.10B'; Gandre-Babbe & van der Bliek 2008; Palmer et al. 2011; Kraus & Ryan 2017; Whitley et al. 2018; Banerjee et al. 2021). In *Drp1* mutant mouse fibroblast cells, the mitochondrial network displays a hyperfused phenotype, similar to homozygous *Drp1* mutant mouse embryos, and an increase in density of mitochondria in the dendrites of hippocampal neurons transfected with dominant-negative *Drp1* (Figure 1.11O-T; Li et al. 2004; Ishihara et al. 2009).

Drp1 activity appears to be tightly linked to actin and its associated proteins. In MEFs and U2OS cells, Drp1 activity is enhanced by actin filaments and reduced levels of ABPs, Arp2/3 or Myosin II leads to a reduction in Drp1 levels and rate of fission, and consequentially elongation of the mitochondrial network (Ji et al. 2015; Li et al. 2015; Hatch et al. 2016; Illescas et al. 2021). Actin is also involved in ER-mediated mitochondrial fission as a pre-constriction step. The binding of ER-bound INF2 to mitochondria-anchored Spire1C initiates polymerisation of short actin filaments that tighten around the ER tubules to further constrict the dissociating mitochondria

(Friedman et al. 2011; Korobova et al. 2013; Manor et al. 2015; Kraus & Ryan 2017; Chakrabarti et al. 2018).

Actin is present in two main structures in the neuron, actin patches and actin rings. Actin patches are areas of high levels of branched actin which anchor vesicles and organelles at the base of spines. Actin rings are formed of cortical actin and spectrin which help stabilise neuronal processes and membrane proteins (Korobova & Svitkina 2010; Konietzny et al. 2017; Lavoie-Cardinal et al. 2020). In neurons, mitochondria motion is bidirectional and saltatory. 70% of organelles remain stationary at any given time as the accumulation of ATP production in cellular subcompartments needs to compensate for its low diffusion rate. Myosin V and VI most likely function as anchor proteins in *Drosophila* axons as loss of Myosin V has been shown to increase mitochondrial transport and the deletion of Myosin V and VI reduces the time mitochondria remained immobile ((Hubley et al. 1996; Pathak et al. 2010; Lewis et al. 2016; Cardanho-Ramos et al. 2020; Li et al. 2020).

In the axon of mammalian neurons, MT minus-ends are pointed towards the cell body and plus-ends towards the periphery while in dendrites, filaments are arranged with mixed polarity (Figure 5A; Morris & Hollenbeck 1995; Hollenbeck & Saxton 2005; Pilling et al. 2006; Glater et al. 2006; Mandal & Drerup 2019). Anterograde transport in the neuron moves content from the cell body to the periphery through the activity of kinesin. Mutating neuron-specific kinesin *KIF5A* and *KIF5C* in *Drosophila* larvae axons or upon overexpression of their cargo-binding domains in rat hippocampal neurons decreases anterograde transport of mitochondria In *Drosophila* neurons, the cyclic AMP/protein kinase A (cAMP/PKA) and kinesin-1 levels decline with age coinciding with an increased percentage of inactive mitochondria in aged flies (Nangaku et al. 1994; Pereira et al. 1997; Tanaka et al. 1998; Tong et al. 2007; Campbell et al. 2014; Ogawa et al. 2016; Brandt et al. 2017; Vagnoni & Bullock 2018; Henrichs et al. 2020; Serra-Marques et al. 2020; Zhao et al. 2020).

Using genetic screens and immunoprecipitation, Milton was identified as a mitochondria-specific adaptor protein that binds to kinesin-1 (Stowers et al. 2002). The N-terminal of the Milton protein binds to the C-terminal of the kinesin heavy chain for axonal transport of mitochondria to the synaptic terminals. Milton does not contain a mitochondrial import sequence or transmembrane domain suggesting the presence of another adaptor (Stowers et al. 2002; Glater et al. 2006; van Spronsen et al. 2013; Melkov et al. 2016; Fenton et al. 2021). The identification of Mitochondrial Rho GTPase (Miro) originated from a search in public DNA and protein databases for new members within the Rho GTPases family (Guo et al. 2005; Frederik et al. 2004; Klosowiak et al. 2013). Miro-like protein genes have been discovered in various eukaryotes, spanning from yeast and *Arabidopsis* to *Drosophila* and mammals, underscoring a significant level of evolutionary conservation. Mfn2 was found to interact with both Miro1/2 and mutations in *Mfn2* lead to reduced mitochondrial transport and increases the proportion of stationary mitochondria in neurons like mitochondria accumulation in the cell body in *Milton* null mutants (Stowers et al. 2002; Glater et al. 2006; Baloh et al. 2007; Misko et al. 2010; van Spronsen et al. 2013). Similarly to overexpressed *Milton* mutants, mutations in human and yeast *Miro* result in loss of anterograde transport, increase in perinuclear clustering and a decrease of mitochondria at the neuromuscular junctions (Fransson et al. 2003; Frederik et al. 2004; Russo et al. 2009; Schuler et al. 2017).

During early embryogenesis, in frogs, fish and insects, the formation of the Balbiani body (Bb) is the first stage in establishing cell polarity containing maternal determinants for germ cell fate specification and is proposed to be involved in mitochondrial segregation (Guraya 1997; Cox & Spradling 2003; Bilinski et al. 2017; Jamieson-Lucy & Mullins 2019; Yang et al. 2022). In *Drosophila* and mouse egg chambers, mitochondria originating from the NCs accumulate at the ring canals between the NCs and oocyte boundary, push into the oocyte by large-scale cytoplasmic flows, joining the population of oocyte mitochondria to form the Bb (Robinson et al. 1994; Warn et al. 1985; Pokrywka & Stephenson 1995; Quinlan 2016). In *milt<sup>92</sup>* null germline clones, only one third of the mitochondria that are normally found at the anterior for Bb formation during early oogenesis localised correctly (Cox & Spradling 2003). Other Bb-associated

organelles localise normally while mitochondria do not, indicating that Milton activity is mitochondria specific. Dhc levels are unaffected by either *milt*<sup>96</sup> or *milt*<sup>EY01559</sup> mutants suggesting that mitochondrial motion seems to be controlled by the state and number of Milton adaptors (Cox & Spradling 2006; Melkov et al. 2016). At st10 of *Drosophila* oogenesis, mitochondria localise at the posterior of the oocyte independently of the germ plasm coinciding with the MT-driven bulk cytoplasmic streaming at the initiation of late oogenesis at an observed speed of 0.4  $\mu\text{m}/\text{s}$  with similar unidirectionality and speed to other streaming organelles (Gutzeit & Koppa 1982; Serbus et al. 2005; Ganguly et al. 2012).

Direct yet transient interactions between mitochondria and endosomes/lysosomes have been observed in mammalian cells. Recent studies highlight the importance of mammalian orthologs of *Vps13*, specifically *VPS13A* and *VPS13C*, in mediating contacts between mitochondria and endosomes, the mutation of which has been associated with neurodegenerative diseases such as Parkinson's (Lesage et al. 2016; Kumar et al. 2018). Interestingly, the deletion of *VPS13A* affects lysosomal function, which is particularly significant given the recently discovered role of mitochondria in regulating lysosomal activity (Muñoz-Braceras et al. 2019). Recent findings suggest that physical contacts between endosomes and mitochondria through transient "kiss-and-run" interactions facilitate mitochondrial steroid hormone synthesis and the formation of iron-sulfur clusters by a direct transfer of iron and cholesterol from endosomes to mitochondria, a process involving the late endosome protein MLN64 (Charman et al. 2010; Miller 2013; Das et al. 2016; Hamdi et al. 2016; Braymer and Lill 2017). Additionally, lipid transport between organelles is thought to be initiated by VpS13A through interactions with Rab7 (Muñoz-Braceras et al. 2019). In turn, genetic alterations or chemical inhibition of mitochondrial activity result in impaired lysosomal acidification and activity, leading to the accumulation of enlarged endosomal/lysosomal structures (Baixauli et al. 2015; Demers-Lamarche et al. 2016). The observed cross-talk suggests a robust network of interactions between endosomes and mitochondria.

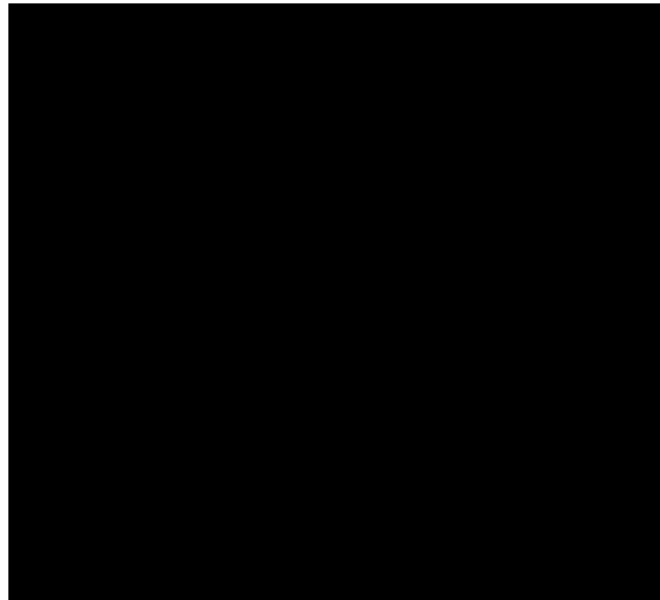
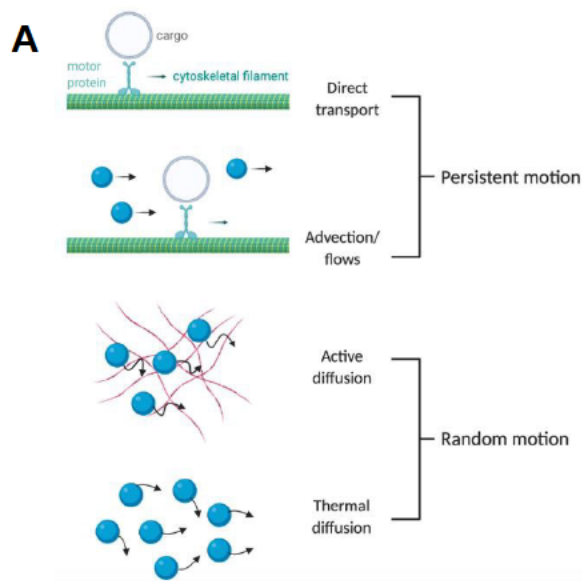
## 1.6 Characteristics of the cytoplasmic medium and the impact on molecular motion.

Molecules and organelles are transported through the cytoplasm through various methods; directed transport, advection/flows, active diffusion, and thermal diffusion (Figure 1.12A). The cytoplasmic medium is a very crowded and viscoelastic medium and due to this viscosity and macromolecular crowding, any movement of a particle would rearrange the surrounding fluid. In turn, the motion of the particle is impacted by the hydrodynamic properties of said medium. The Reynolds number ( $Re$ ) is a dimensionless quantity used in fluid dynamics to characterize flow regimes. It indicates the relative importance of inertial forces compared to viscous forces:

$$Re = \frac{vL\rho}{\eta}$$

Where  $v$  = flow speed,  $L$  = linear size scale of object,  $\rho$  = fluid density and  $\eta$  = fluid viscosity. In a typical animal cell,  $v < 100\mu m s^{-1}$  and  $L < 100\mu m$  which means the Reynolds number of cytoplasm is very low, on the order of  $10^{-2}$  to  $10^{-4}$ . This describes an environment with negligible inertial forces in comparison to viscous forces indicating viscous forces and diffusion control transport and mixing processes, enabling careful spatial organisation and signalling within cells (Purcell 1977; Happel & Brenner 1983; Ganguly et al. 2012; Koslover et al. 2016). In large oocytes like *Drosophila*, cytoskeletal motor proteins can generate significant flows of cytoplasm, or cytoplasmic streaming, through viscous drag. Streaming provides bulk circulation to transport molecules rapidly through the large oocyte cytoplasm but is most effective at larger scales and cannot as easily mix locally. Diffusion and cytoplasmic streaming thus play complementary roles in transport and mixing oocytes enabling efficient molecular localization across changing oocyte scales; streaming provides rapid bulk transport across large distances, and diffusion alone is efficient at small scales but becomes slow over long distances in large cells therefore mixing and refining local concentrations (Pickard 2003; Goldstein & van de Meent 2015; Drechsler et al. 2017).





**Figure 1.12. Motion and crowding in the cell.** (A) Cargo can undergo direct transport as motor protein cargo on cytoskeletal filaments, advection because of the viscous drag created by the translocation of motor proteins, ATP-driven active diffusion, and thermal diffusion (red strands - actin filaments). (B) A cartoon of the crowded cytoplasm in a eukaryotic cell. The image illustrates a section of the cytoplasm with an edge length of 100nm. Sizes, shapes, and number of macromolecules are approximately correct (Image taken from Ellis (2001)).

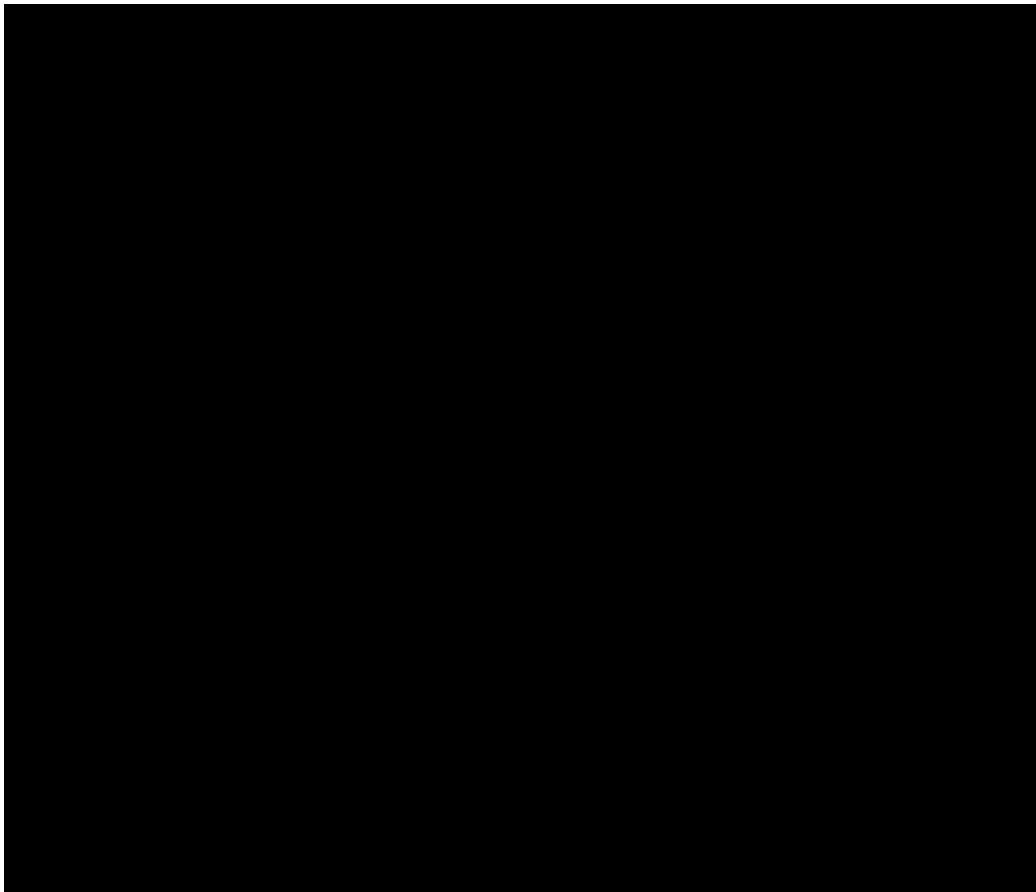
As discussed previously, in *st9 Drosophila* oocytes, MTs nucleate at the cell cortex with plus-ends pointed at the posterior creating a decreasing density gradient from the anterior to the posterior pole. This gradient creates coupled steady-state patterns of cytosolic flows and MT orientation allowing localisation of determinants by kinesin and dynein. In general, active directed transport by kinesin and dynein on MTs and cytoplasmic streaming are required for long-range transport of molecules, while diffusion, and the activity of myosin and actin, drive short-range transport (Parton et al. 2011; Trong et al. 2015; Ando et al. 2015; Barlan & Gelfand 2017; Mogre et al. 2020; Agrawal et al. 2022). The typical geometry of the cytoskeletal network allows for cooperation between the force-generating mechanisms of MTs and actin. MTs tend to be radially polarised near the nucleus and randomly oriented actin filaments are organised at the periphery, or near the cortex enabling long-runs for cargoes towards the surface and subsequent effective random walk along the periphery (Nedelec et al.

1997; Mullins et al. 1998; Fletcher & Mullins 2010; Ando et al. 2015). MTs also undergo a process called MT sliding which describes the movement of individual filaments relative to one another or the entire network relative to the actin mesh. This phenomenon is motor-driven and aids in expansion of the network and efficient transport into distal or crowded cellular regions between overlapping filaments by allowing cargo to avoid obstacles in their path (Kapitein & Hoogenraad 2015; Lu et al. 2016; Monteith et al. 2016; Guha et al. 2021).

Therefore, the spatial architecture of the cytoskeleton dictates the long-range behaviour of motor-driven cargos and efficient and precise sorting into subcellular locations. Relevant parameters to consider include the density, polarity and filament length of the cytoskeleton in question (Mizuno et al. 2007; Ando et al. 2015; Agrawal et al. 2022). Novak et al. (2009) present a computational study examining how the complex geometry of intracellular structures like cytoskeletal filaments and organelle membranes affects molecular diffusion in the cytoplasm. They model the intricate intracellular geometry using a mixture of simple obstacles like rods and disks to mimic actin and ER structures, respectively (Figure 1.13). They found that excluded volume alone can account for a 4-6-fold reduction in diffusion compared to aqueous rates, and sheet-like structures like ER membranes are more efficient barriers than rod-like cytoskeletal filaments for a given volume fraction occupied. Larger tracers were found to experience more hindrance with diffusion scaling inversely with size while small proteins are minimally obstructed. The consequences of *SpireB* overexpression in oocytes sheds light on the intricate dynamics within the cell and aligns with this model. In *SpireB*-overexpressing oocytes, the observed absence of *st9* streaming and diffusive-like dynamics suggests a potential link to the hindrance experienced by molecular diffusion (Drechsler et al. 2017). This connection emphasizes the importance of understanding how alterations in cytoskeletal dynamics can influence molecular transport within the cell.

The relationship between size and susceptibility to hindrance from macromolecular crowding has been demonstrated in the cytoplasm of *Escherichia coli* and in the

translational diffusion of microinjected FITC-dextran and Ficoll in the cytoplasm and nucleus of MDCK epithelial cells and Swiss 3T3 fibroblasts (Zimmerman & Trach 1991; Seksek et al. 1997). GFP-actin diffusion in living *Dictyostelium* cells using fluorescence correlation spectroscopy (FCS) complements Novak et al.'s computational model. Small GFP tracers were found to move ~2-5 times slower in cytoplasm when compared to dilute solution, and jasplakinolide-induced actin polymerization similarly reduced mobility in both studies, confirming the cytoskeleton's role in hindering diffusion when extensively polymerized (Engelke et al.'s 2010). Binding interactions with these obstacles can also contribute to hindered diffusion as well as viscosity in areas proximal to the imposing structures (Alberts et al. 2002; Novak et al. 2009; Engelke et al. 2010; Höfling & Franosch 2012).



**Figure 1.13. Simulated and in vivo actin filaments and ER taken from Novak (2009)** (A) Electron micrograph of actin filaments in a keratocyte (B) Long thin cylinders representing cytoskeletal filaments (C) Optical section of ER of the unfertilized sea urchin eggs (D) Random three-dimensional disks modelling ER sheets.

The motility of Rab5-positive endosomes is complex and influenced by their cellular location, involving stops, starts, and variable distances. They primarily move with an inward bias but can also move outward and bidirectionally with fast imaging revealing approximately half of Rab5-positive endosomes undergo directed motion with an average speed of  $1 - 2 \mu\text{m s}^{-1}$  and a peak observed at  $4 - 6 \mu\text{m s}^{-1}$  during a 30–50 second recording (Flores-Rodriguez et al. 2011; Zajac et al. 2013). High-resolution imaging shows a subpopulation with confined motion regulated by actin density, while the motile group displays dynein-dependent directed movement interspersed with diffusive pauses (Zajac et al. 2013). Ballistic motion simulations reveal filament arrangements near the nucleus as potential traps increasing transport time mitigated by distributing the network over more filaments with shorter length (Ando et al. 2015). Mapping the behaviour of lysosomes at microtubule intersections using a combination of single-particle tracking and super-resolution microscopy reveals that these intersections act as significant hindrances, leading to prolonged pauses in transport (Bálint et al. 2013). These obstacles are usually overcome by motor proteins through switching to the intersecting MT, maintaining the polarity of motion. The spatial overlap of microtubule and actin filaments suggests these factors contribute to interrupting directed runs of endosomes with interactions and pauses likely playing functional roles in endosomal maturation and sorting. Therefore, the movement of molecules through the crowded cytoplasm is a complex, ‘many-body’ issue. Not only are components moving in a crowded, heterogeneous space but they also interact with other molecules and structures (Figure 1.12B). Understanding the contribution of these elements helps establish biophysical principles of how cells regulate mass transport through their structural organization and provides fundamental insights into how cell structure and organization affect intercellular transport and signalling processes.

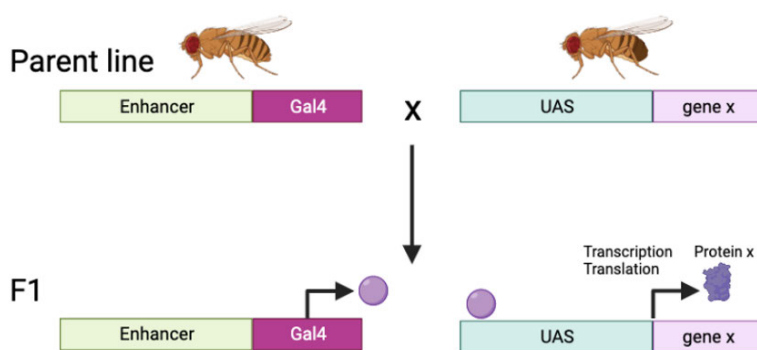
## 1.7 Research aims

The primary goal of this study is to comprehensively characterise the mechano-chemical relationship between actin and microtubule cytoskeletons and the active motion of cytoplasmic components within the cell. Specifically, I focus on analysing the motion behaviours of Rab7-positive vesicles, predominantly representing late endosomes, Rab5-positive vesicles, representing early endosomes, and mitochondria. Recognising the link between these populations of organelles as well as the interplay between organelle morphology, function, and cytoskeletal force-generation, this investigation seeks to elucidate the factors that influence system-environment interactions within the *Drosophila* oocyte. The primary hypothesis of this study posits that alterations in organelle morphology and size under conditions of fusion/fission mutation, ageing, and cytoskeletal depolymerisation will significantly influence their motility. Furthermore, it is hypothesised that these conditions will extend their impact to the motility of other organelles in the same cell beyond EEs, LEs and mitochondria, specifically vesicles as observed through DIC imaging. This hypothesis stems from the intricate interactions between endosomes, mitochondria and the cytoskeletal networks described in the previous section. Using a combination of confocal microscopy and differential dynamic microscopy, I systematically explore the impact of various conditions, including mitochondrial fusion and fission mutations, mitochondrial ageing, and the depolymerisation of actin and microtubules, on the morphology, motility, and distribution of endosomes and mitochondria in *stage 9* oocytes. This stage is chosen due to the previously established interplay between the actin and MT cytoskeletons and presence in the oocyte prior to the initiation of late oogenesis. Through this exploration, I aim to provide additional empirical evidence supporting the intricate mechanochemical relationship between cytoskeletal networks and organelle dynamics. This analysis is crucial for advancing our understanding of how physical forces govern the observed active motion of organelles and influence their function and dynamics. Despite encountering challenges, including lack of advanced imaging techniques better suited for a study of this nature and issues in the robustness of mutant studies, the data presented here offers a sturdy foundation for further, in-depth exploration.

## Chapter 2: Materials & Methods

### 2.1 Fly stocks and genetics.

Over the years, great advancements have been made in regard to genetic tools used to spatiotemporally manipulate gene expression in *Drosophila* but the UAS/Gal4 system remains as the workhorse of *Drosophila* genetics (Southall et al. 2008; Jones 2009; Barwell et al. 2017). First developed by Brand & Perrimon (1993), this binary expression system uses the yeast protein Gal4 and its upstream activating sequence (UAS). Gal4 is a transcription activating protein used as a driver of cell-specific transgenes; it binds to the *cis*-regulatory sites of the UAS to drive expression of the gene of interest attached to the UAS promoter (Fischer et al. 1988; Brand & Perrimon 1993). To express a particular gene, these components are carried in two separate lines, the driver line containing Gal4 expressed in a tissue-specific manner and the UAS reporter line which contains the gene of interest (Figure 14). Thus, the progeny parental lines will carry the 'UAS-gene' expressed in a pattern according to Gal4 tissue-specificity. Experimental applications of this system include mosaic gene expression for genetic mutant rescue, gene overexpression, RNA interference and perturbation of pathways (Brand & Perrimon 1993; Osterwalder et al. 2001; Busson & Pret 2007).



**Figure 2.1 Schematic of the *Drosophila* UAS/Gal4 system.** The driver line (left) contains Gal4, the expression of which is controlled by a tissue-specific enhancer, and the UAS reporter line (right) contains the gene of interest (gene x). Gal4 will then bind to UAS to activate transcription of gene x. Progeny will carry the UAS-gene expressed in a pattern according to Gal4 tissue-specificity.

**Table 2.1. Fly lines used and their origins.**

<b>Fly line</b>	<b>Origin</b>
<i>w</i>	<i>Daniel St.Johnston, University of Cambridge</i>
<i>w;CyO/Sco;nos-Gal4.VP16,sqh-YFP::Mito/MKRS</i>	<i>Maik Drechsler, Palacios Lab</i>
<i>w;CyO/Sco;nos-Gal4.VP16,YFP::Myc::Rab7/MKRS</i>	<i>Maik Drechsler, Palacios Lab</i>
<i>w;spir<sup>1</sup>/CyO;YFP::Myc:Rab7/MKRS</i>	<i>Maik Drechsler, Palacios Lab</i>
<i>w;Df(2L)Exel6046/CyO;TM6B/MKRS</i>	<i>Maik Drechsler, Palacios Lab</i>
<i>w/v;Sco/CyO;Khc-RNAi.GL00330/MKRS.</i>	<i>Maik Drechsler, Palacios Lab</i>
<i>w;spir<sup>1</sup>/CyO;sqh-YFP::Mito/MKRS</i>	<i>Layla al-Khatib, Palacios Lab</i>
<i>w; P{UAS-Marf-RNAi (III)} (from M. Guo)</i>	<i>Ming Guo, UCLA</i>
<i>w; P{UAS-Marf-RNAi} (GD40478)</i>	<i>Alex Whitworth, University of Cambridge</i>
<i>w; P{UAS-Drp1<sup>WT</sup>}/TM6B</i>	<i>Alex Whitworth, University of Cambridge</i>
<i>Drp1<sup>T26</sup>,cn<sup>[1]</sup>,bw<sup>[1]</sup>, speck<sup>[1]</sup>/ In(2LR) <i>Gla</i>, <i>wg</i> [<i>Gla-1</i>]</i>	<i>Alex Whitworth, University of Cambridge</i>
<i>w;YFP::Myc:Rab5 (early endosome)*</i>	<i>Bloomington Drosophila Stock Center</i>
<i>w;YFP::Myc:Rab7 (late endosome)*</i>	<i>Bloomington Drosophila Stock Center</i>
<i>w;sqh-YFP::Mito(III)*</i>	<i>Bloomington Drosophila Stock Center – BL7194</i>
<i>w;Sco/Cyo;UTRN-GFP/TM6B</i>	<i>Isabel Palacios, Palacios Lab</i>

\* *YFP::Rab5, YFP::Rab7, YFP::Mito hereafter*

Unless stated otherwise, all flies were kept on standard cornmeal agar at room temperature and all UAS/Gal4 crosses were performed at 25°C.

## 2.2 Fixed samples.

All oocytes were imaged at *st9* and dissected from 1-day old flies. Flies in microtubule depolymerisation experiments were dissected at 2 days old as they require overnight feeding with colchicine. Oocytes in ageing experiments were dissected at the desired age (20, 30 and 40 days).

***Manual dissection and fixation of egg chambers.*** Ovaries were dissected in PBS with 0.2% Tween-20 and fixed in 0.5ml of 4% paraformaldehyde (PFA) in PBS/0.2% Tween-20 for 20 minutes while rotating. Ovaries are then washed with PBS with 2% Tween-20 twice for 5 minutes each while rotating and then mounted in Vectashield mounting medium (Vectorlabs). Images were acquired on a Leica SP5 inverted confocal microscope, using a 63x/1.3 Oil DIC Plan-Neofluar objective.

***Drug treatment for microtubule depolymerisation.*** 200  $\mu\text{g ml}^{-1}$  colchicine was diluted in yeast paste and fed to female flies for 16h at 25°C. Dissection and imaging was performed as described above. The depolymerisation of microtubules was confirmed by scoring those oocytes that displayed a misplaced nucleus, a robust read-out of microtubule depolymerisation.

## 2.3 Live imaging of Rab vesicles and mitochondria.

Ovaries were dissected in a drop of halocarbon oil (Votalef 10S, VWR) on a glass coverslip and single egg chambers were separated using fine tungsten needles. Images were acquired on a Leica SP5 inverted confocal microscope, using a 63x/1.3 Oil DIC Plan-Neofluar objective. For high-resolution image series, a single plane from the middle of the oocyte was imaged at a scan speed of 50 Hz and an image resolution of 4,096 x 4,096 pixels corresponding to 1 frame/ 5.363sec (0.19 frame/sec) for 50 frames.

For analysis using differential dynamic microscopy (DDM), images were taken at a scan speed of 400 Hz and a resolution of 1024 x 512 pixels, corresponding to 1 frame/0.675 sec (1.48 frame/sec) for a total of 500 frames. The cells were illuminated by 488 nm



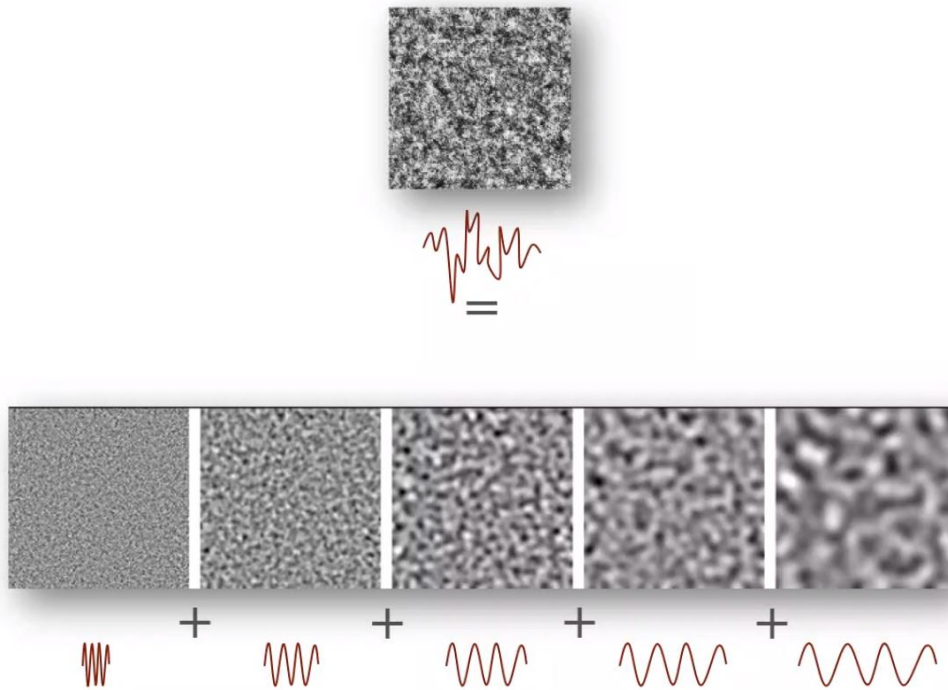
laser light and emission light was collected simultaneously using a hybrid detector at 500–550 nm (GFP), a conventional photon multiplier at 560–650 nm (vesicle auto-fluorescence) and a transmitted light detector with DIC filter set. DIC imaging introduces contrast to structures that lack contrast under brightfield microscopy.

#### 2.4 Differential dynamic microscopy.

Differential dynamic microscopy (DDM) combines principles of dynamic light scattering and microscopy to provide information about the movement and interactions of a particle in a sample. A series of images are captured over time using bright-field microscopy which are then analysed to extract information about the dynamics of the particles in question. The “differential” in DDM refers to the process of taking the differences between consecutive frames in the image sequence to observe changes in particle movements. The dynamic information is provided by analysing the fluctuations in intensity and position of particles between frames from which information such as diffusion coefficients and velocity distribution can be extracted. Previous attempts in the lab to analyse motion of particles using particle image velocimetry (PIV) proved to be inadequate. Compared to DDM, PIV has limited temporal resolution and requires single particle tracking which can be challenging in dense and crowded environments like the cytoplasm. DDM captures high-frequency dynamics with higher temporal resolution making it suitable for analysis of rapid movements in cells. The use of the Fourier domain in DDM provides spatially resolved information for analysis at different length scales therefore offering a more comprehensive picture of dynamic behaviour.

The Fourier domain is an integral part of DDM analysis, mapping spatial information from real space to reciprocal space coordinates helping visualise patterns and structures in the data. Essentially, when performing a Fourier transform, a signal is broken down into its constituting signals obtaining different images containing information relating to a specific length scale from small to large (Figure 2.2). In the context of this study this involves comparing the pixel intensity in one frame with the intensity in the next frame and calculating the correlation function. To analyse the spatial frequency of dynamic fluctuations in the images, the Fourier transform of the

intensity correlation function is taken yielding a signal power spectrum distributed across different frequencies. The peaks of this spectrum correspond to spatial frequencies relating to the size and dynamics of the particles with different modes of motion, such as advection and diffusion, contributing differently to the spectrum.



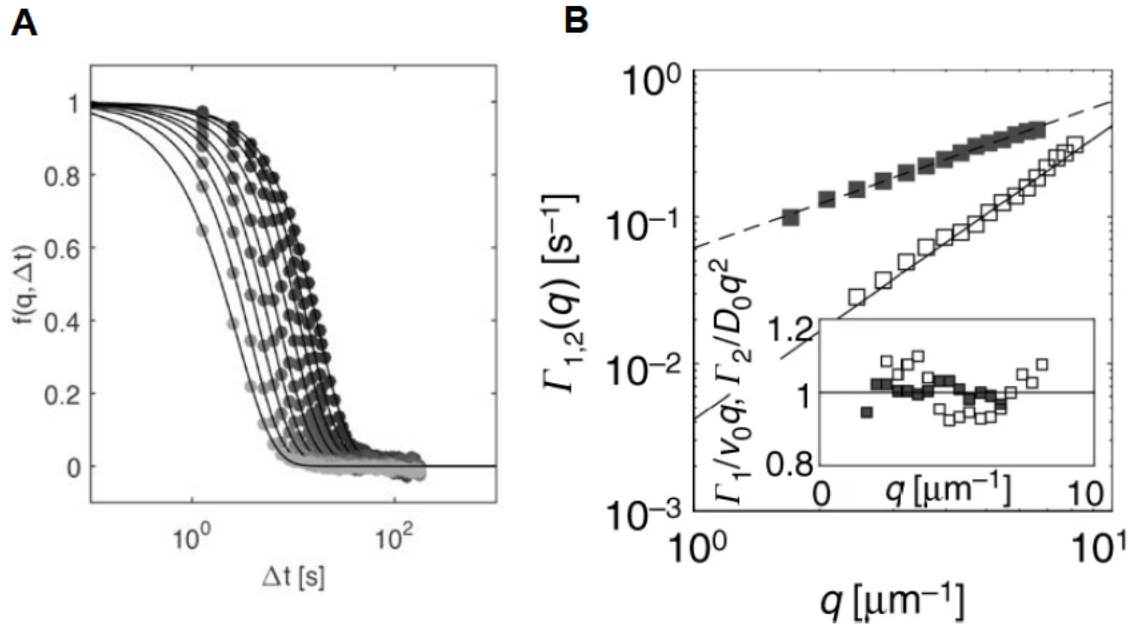
**Figure 2.2 Fourier transform decomposition.** Decomposition of an image into its constituent signals relating to their length scales. Each image describes the evolution of a system at these length scales (Image courtesy of Fabio Giavazzi).

In DDM analysis, the intermediate scattering function (ISF) denoted as  $f(q, \Delta t)$  captures the relaxation of density fluctuations with a specific wave vector  $q$  over a defined delay time  $\Delta t$  (Figure 2.3A). When considering a specific length scale, say  $2\mu m$ , the spatial frequencies associated with the dynamics at that scale are analysed. The spatial frequency, characterized by the wave vector  $q$ , is integral to Fourier transformation, allowing discernment of the rates of change  $\Gamma$  associated with the  $2\mu m$  length scale. Plotting the rate  $\Gamma$  as a function of  $q$  unveils a spectrum of spatial frequencies, providing a nuanced understanding of how different length scales

contribute to the overall dynamics of the sample. The ISF is mathematically represented by the advection-diffusion equation:

$$f(q, \Delta t) = P_0(\Gamma_1(q)\Delta t)e^{-\Gamma_2(q)\Delta t}$$

which serves as a tailored tool in this DDM model. Different types of motion such as diffusion and advection contribute differently to spatial frequencies. This equation accounts for both directional, ballistic motion with a rate of  $\Gamma_1(q)$  and random, diffusive motion with a rate of  $\Gamma_2(q)$ . The parameters  $P_0, \Gamma_1(q)$ , and  $\Gamma_2(q)$  are gleaned from experimental data, offering insights into the nature and rates of motion exhibited by vesicles or particles in the sample. In this model, each vesicle captured by DIC has the same diffusivity  $D_{ves}$  and a different velocity,  $v_{ves}$ , drawn from a probability distribution function (PDF) denoted by  $P_0$  in the above equation (Drechsler et al. 2017). The average vesicle speed is then used to determine  $\Gamma_1(q)$  and  $\Gamma_2(q)$  which describe the motion of vesicles at different spatial frequencies  $q$ , where  $\Gamma_1(q) = v_{ves}q$  accounts for directional (advective) motion and  $\Gamma_2(q) = D_{ves}q^2$  accounts for random (diffusive) motion (Figure 16B).



**Figure 2.3 Dynamic analysis of vesicle motion: ISF and decorrelation rates as a function of spatial frequency.** (A) Intermediate scattering functions (ISF)  $f(q, \Delta t)$  for different wave vectors  $q$  in the range  $1.8\mu\text{m}^{-1} < q < 8\mu\text{m}^{-1}$ . (B) Decorrelation rates  $\Gamma_1(q)$  (solid black boxes) and  $\Gamma_2(q)$  (open boxes) from the fit of the ISF plotted against the wave vector  $q$ .  $\Gamma_1(q)$ , which accounts for the ballistic contribution to the motion of the vesicles, exhibits a linear scaling  $\Gamma_1(q) = v_{ves}q$  (dashed line), while  $\Gamma_2(q)$  which describes a diffusive-like relaxation process, is well fitted to a quadratic law  $\Gamma_2(q) = D_{ves}q^2$  (continuous line).

In most of the experiments presented in this work, the effective  $q$ -range roughly corresponds to  $[2, 20] \mu\text{m}^{-1}$ . In the direct space, this corresponds to considering density fluctuations on length scales approximately between  $0.3\mu\text{m}$  and  $3\mu\text{m}$ . The interplay of spatial frequencies, represented by  $q$ , and characteristic rates  $\Gamma$  derived from Fourier transformation, unveils a spatially resolved perspective on the dynamic properties of the sample. It is worth noting that, when flow is present inside the oocyte, the velocity field exhibits some spatial heterogeneity, especially close to the cell edges. For this reason, only regions of interest (ROIs) far from these edges were considered, which were imaged long enough to guarantee that the average velocity was rather homogeneous across the field of view. For a given cell, a single ROI is typically considered of size  $118 \times 118\text{px}$  ( $28.38 \times 28.38\mu\text{m}$ ) in the anterior part of the cell.

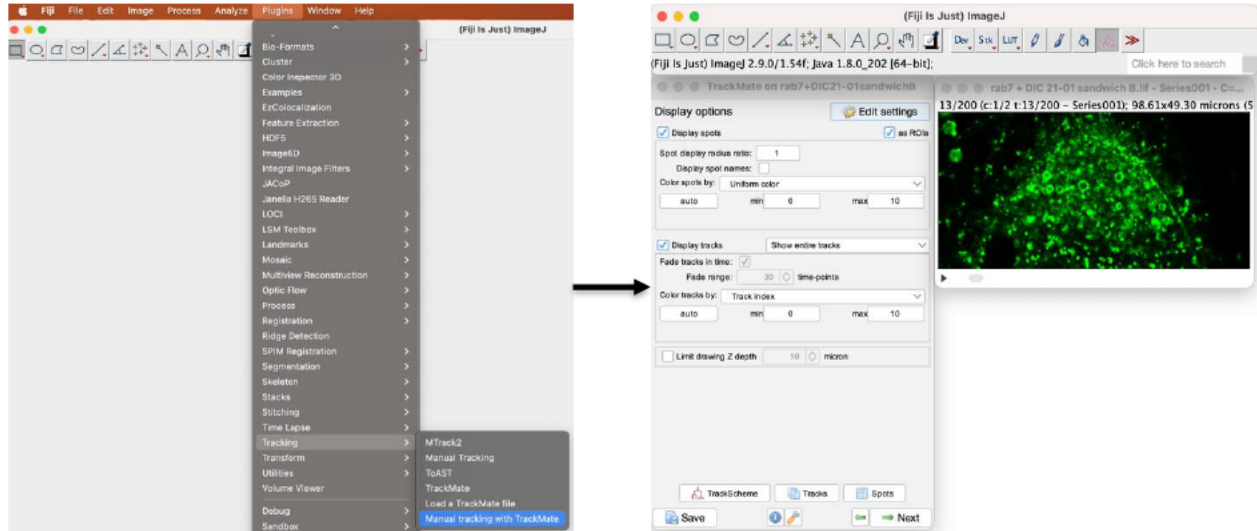
*For a more comprehensive description of DDM and its applications please refer to Cerbino et al. 2021.*

## 2.5 Manual single-particle tracking.


The TrackMate plugin on Fiji (ImageJ) was used to track Rab7 and mitochondria traveling in a directed and ballistic manner. This involves segmenting objects of interest and reconstructing their trajectory over time from the starting frame to, in this study, the frame in which the object is no longer visible.

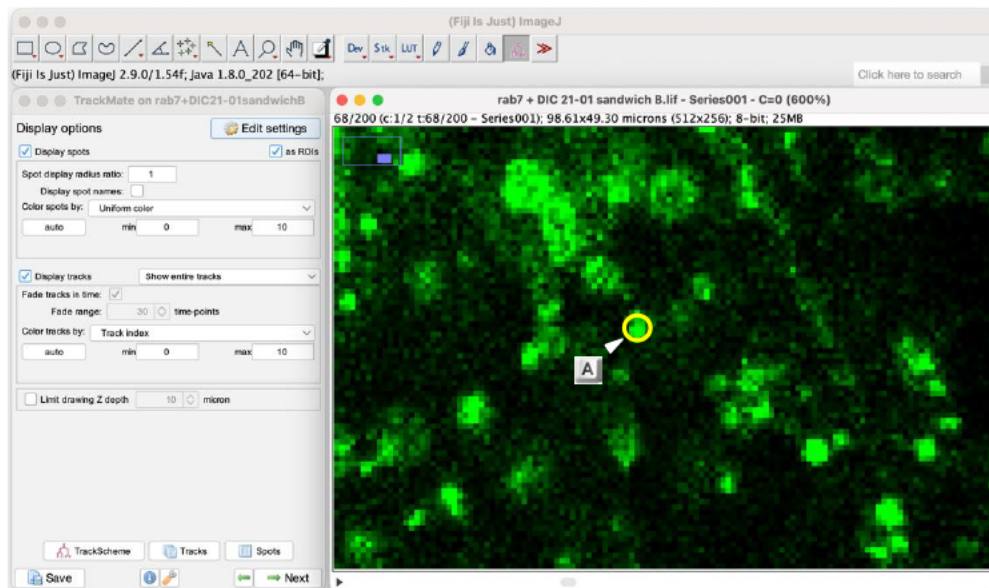
### Step 1

After launching Fiji(ImageJ), open the movie for analysis and select *Plugins > Tracking > Manual tracking with TrackMate*. A panel titled **TrackMate on [name of file]** will open next to your movie.



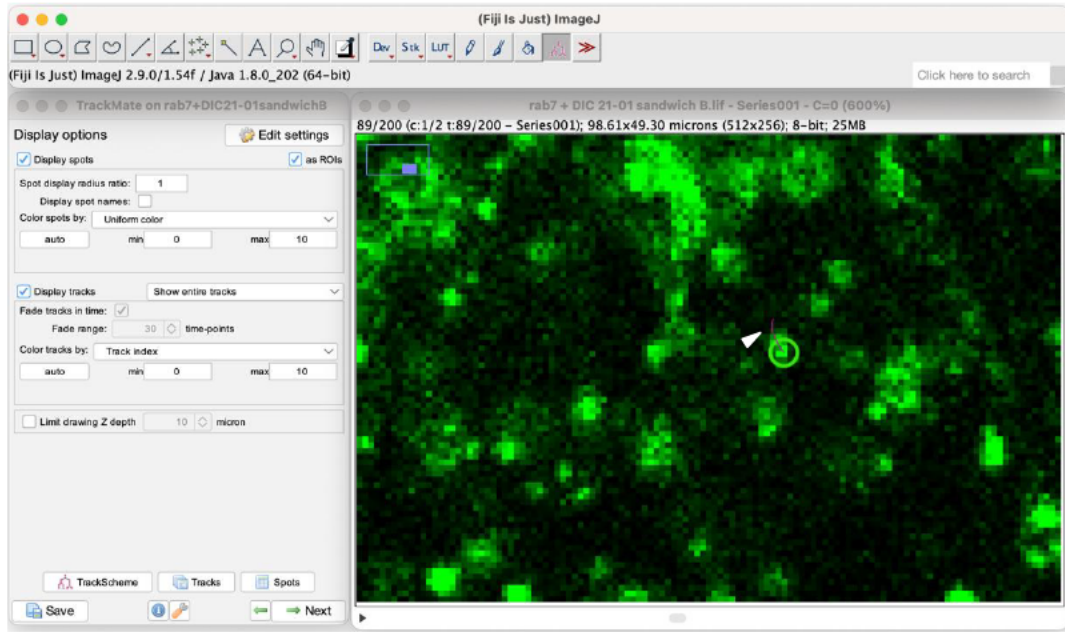
## Step 2

Select the TrackMate tool  in the Fiji(ImageJ) toolbar. Once that is selected, you can create a circle (spot) around the particle or organelle you are tracking by pressing **A** on your keyboard. To adjust the position of the spot, press **Space** with your mouse over the target spot and move the mouse accordingly. To increase the radius of the circle press **Q** with your mouse over the target spot, to decrease the radius press **E**. To delete a spot, press **D** with your mouse over the spot.



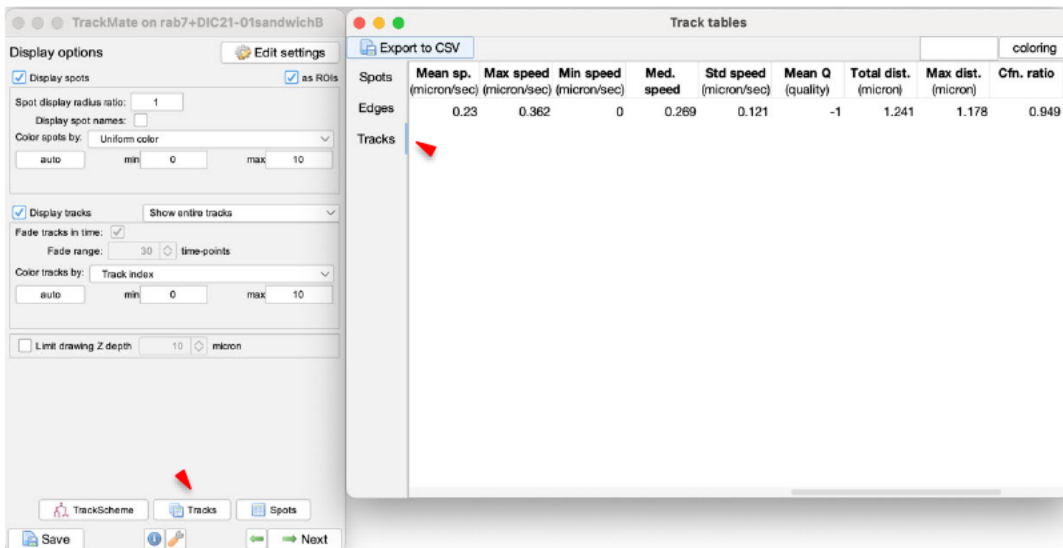
### Step 3

To track a particle over several frames, a link needs to be created. Switch on auto-linking mode by pressing **Shift** + **L** and press **A** over the particle across consecutive frames. This will link the spots creating a track (colour of the track will vary).



### Step 4

To extract information on the velocity and distance of the particle(s) you are tracking, click the **Tracks** button on the display panel. Another panel will open with three tabs: **Spots**, **Edges** and **Tracks**. Information on velocity and distance is found in the **Tracks** tab.





In this study, I extracted the mean velocity of 20-30 individual manually tracked organelles in a single cell moving in a directed and ballistic manner to determine the mean speed in  $\mu\text{m s}^{-1}$  and create a histogram of frequency vs velocity (Figure 17F & Figure 20C).

*Example raw data and qualitative analysis (using GraphPad Prism):*

Group A	
Mitochondria	
1	0.15372871867426
2	0.17061168349301
3	0.42441242661448
4	0.10736876689525
5	0.15372867531693
6	0.18980296338518
7	0.13686889438914
8	0.18362885518111
9	0.19598169624227
10	0.44561272051566
11	0.37232359048957
12	0.15885099376089
13	0.12500769229412
14	0.18971858166864
15	0.14348716468344
16	0.26284815127894
17	0.26921095686659
18	0.25675177187567
19	0.16996800276061

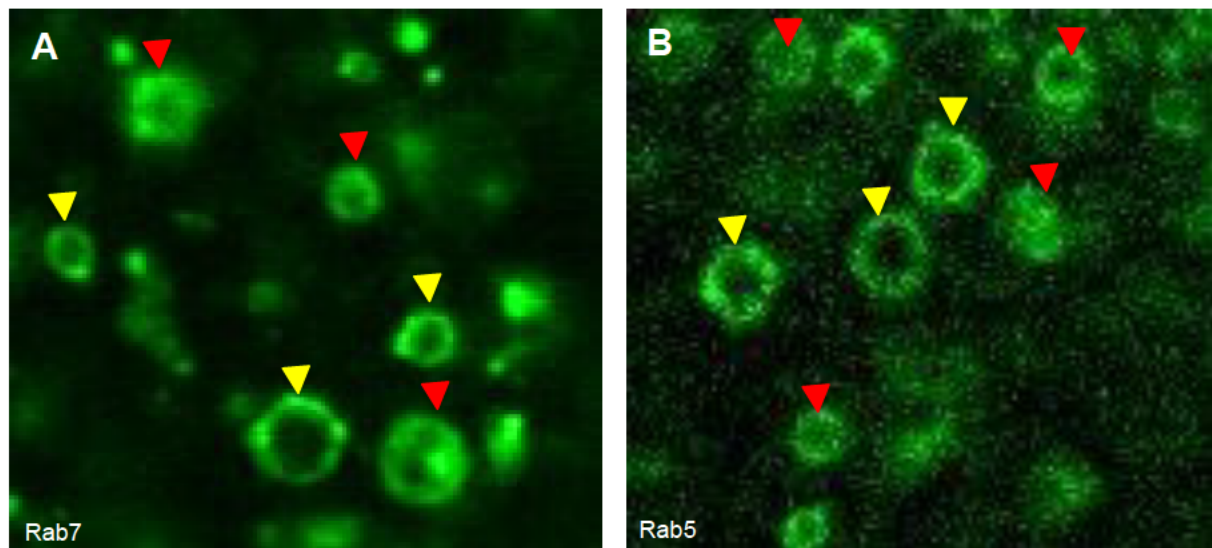
  

Histogram		A
Descriptive statistics		Mitochondria
		Y
1	Total number of values	19
2	Number of excluded values	0
3	Number of binned values	19
4		
5	Minimum	0.107368766895254
6	25% Percentile	0.153728675316928
7	Median	0.183628855181112
8	75% Percentile	0.262848151278942
9	Maximum	0.445612720515661
10		
11	Mean	0.216311174020302
12	Std. Deviation	0.0991368640986826
13	Std. Error of Mean	0.0227435564308254
14		
15	Lower 95% CI of mean	0.168528735041315
16	Upper 95% CI of mean	0.264093612999289

## 2.6 Measuring vesicle diameter.

For measurement and comparison of vesicle diameter, fluorescence and DIC images of vesicles were processed using Fiji (ImageJ). Images of DIC vesicles and YFP-tagged Rab5 and Rab7 vesicles were opened in Fiji, and the scale was set using known references. The "line" tool in Fiji was used to draw a line perpendicular to the vesicle's structure, within the membrane. After drawing the line, the measured length in pixels was recorded for each vesicle. Pixel measurements were automatically converted to micrometres using the set scale by selecting *Analyse > Measure*. In selecting vesicles for measurement, those exhibiting clear visibility of the membrane circumference were chosen for accuracy, specifically opting for vesicles with an absence of fluorescence in

the central region (Figure 2.4). The procedure was repeated for 30 randomly selected vesicles per oocyte. The average diameter and standard deviation were then calculated for each vesicle population. For comparisons between Rab5 and Rab7 vesicles a total of 60 vesicles were randomly chosen for measurement for each group and only two oocytes were selected for each experimental group due to challenges in obtaining high-resolution images of YFP::Rab5 vesicles.



**Figure 2.4. Vesicle selection process.** Representative images showcasing the criteria used for vesicle selection. Vesicles with a clearly discernible membrane circumference were prioritized for measurement. Additionally, preference was given to vesicles displaying an absence of fluorescence in the central region, as indicated by a black appearance (yellow arrowheads – selected, red arrowheads – not selected).




## 2.7 Analysing distribution of organelles under different experimental conditions.

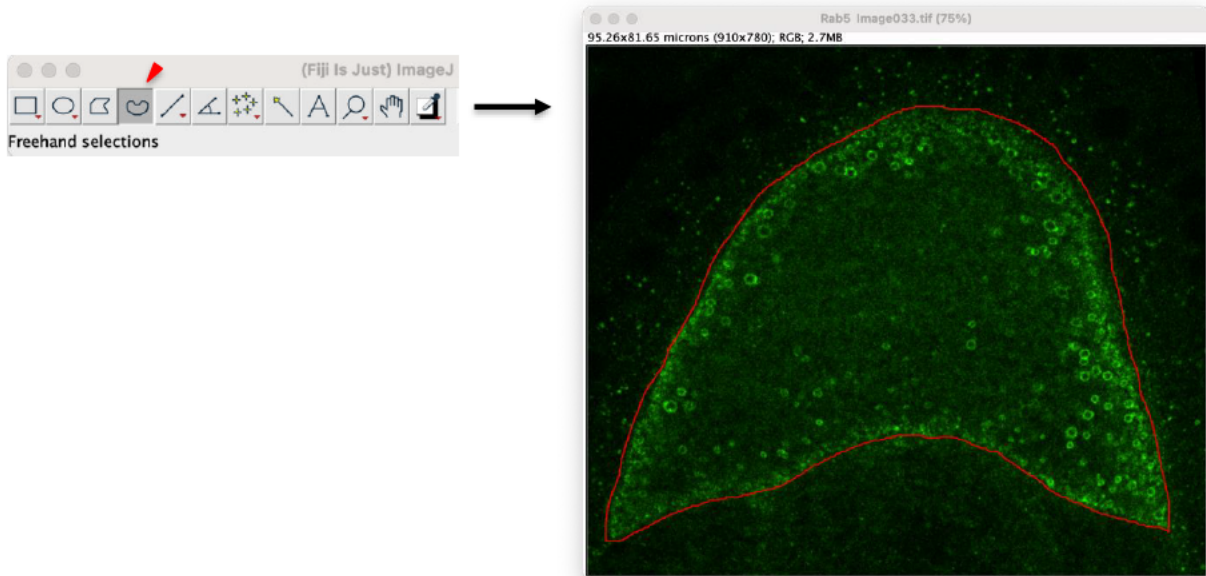
An intensity-based analysis was conducted to assess changes in the distribution of early endosomes, late endosomes, and mitochondria across the different experimental conditions. Each grayscale image was initially converted to a binary image using Otsu's thresholding method to segment the oocyte. Contours were defined based on a manually drawn region of interest (ROI) covering the entire oocyte.

To distinguish between the anterior and posterior regions, the oocyte was divided into quadrants using centroid coordinates calculated from the ROI. Morphological operations were applied to differentiate between peripheral and central regions using Python (see Section 3 of Appendix). Specifically, an erosion operation using a 3x3 kernel shrunk the oocyte mask, defining the central region as the area within this eroded mask. All masks can be found [here](#).

To establish each oocyte's centroid, intensity-weighted mean coordinates ( $X_M$ ,  $Y_M$ ) were used, accounting for non-uniform intensity distribution. This method better represents the functional centre of organelle distribution, especially in lower resolution images where individual organelles are not clearly resolved. The intensity-weighted approach gives greater weight to brighter pixels, likely representing genuine signal rather than background noise, thus providing a more reliable estimate of organelle distribution. The script used analysed average intensity values for central, peripheral, anterior, and posterior regions by computing mean pixel values within respective masks (Table 2.2). Statistical significance was assessed as described in Section 2.9. The following steps outline the image preparation process:

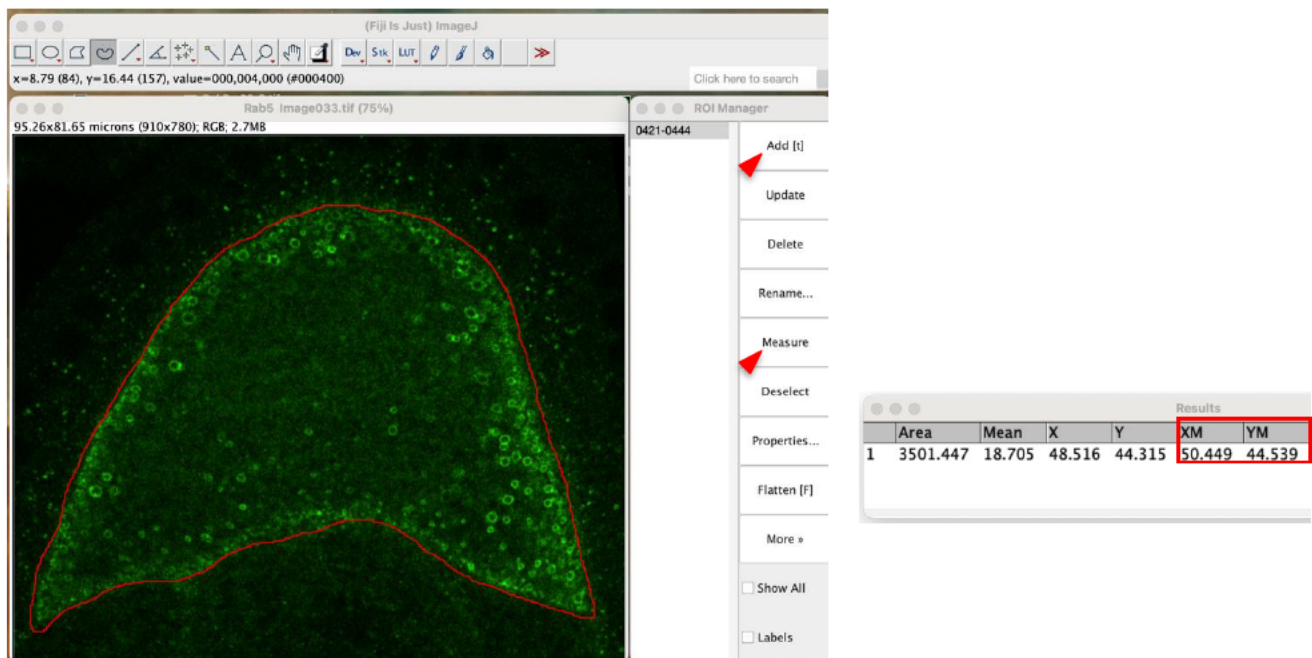
## Step 1

Open the image in Fiji (ImageJ) and manually outline the oocyte borders using *Freehand selections*  to define the region of interest (ROI) for centroid calculation.




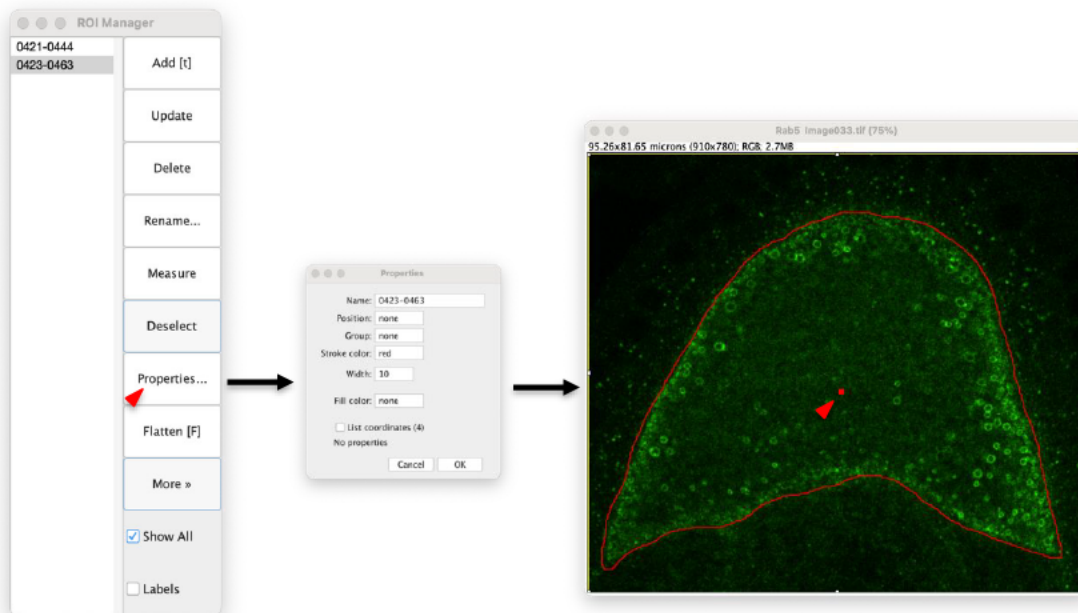
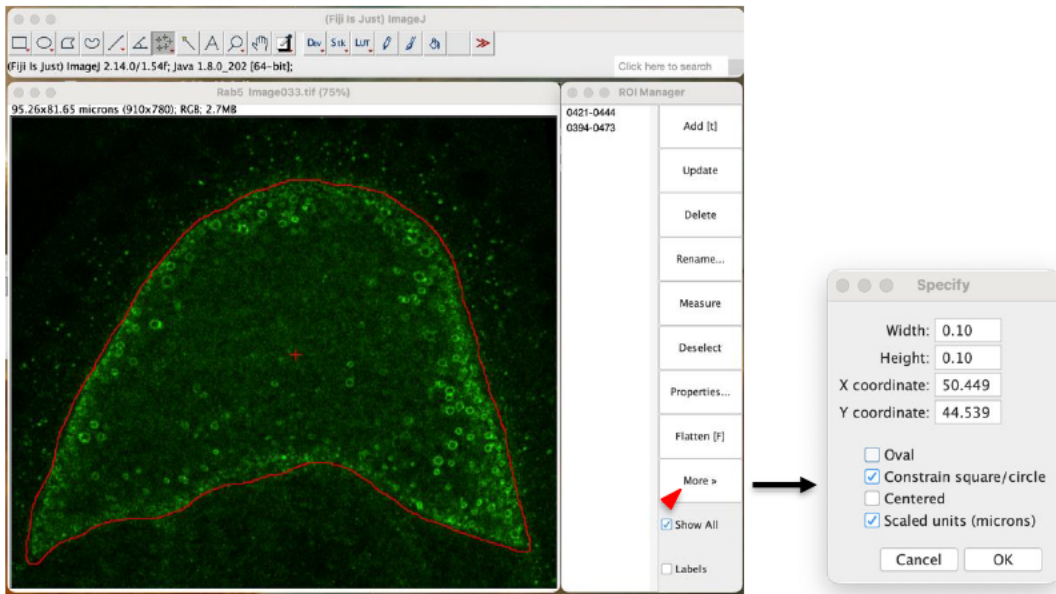
## Step 2

Access the ROI Manager via *Analyse > Tools > ROI Manager*. Add the oocyte ROI and extract the centroid coordinates by selecting **Add [t]** and then **Measure**. The results window displays a table with the XM and YM coordinates of the centroid.




### Step 3

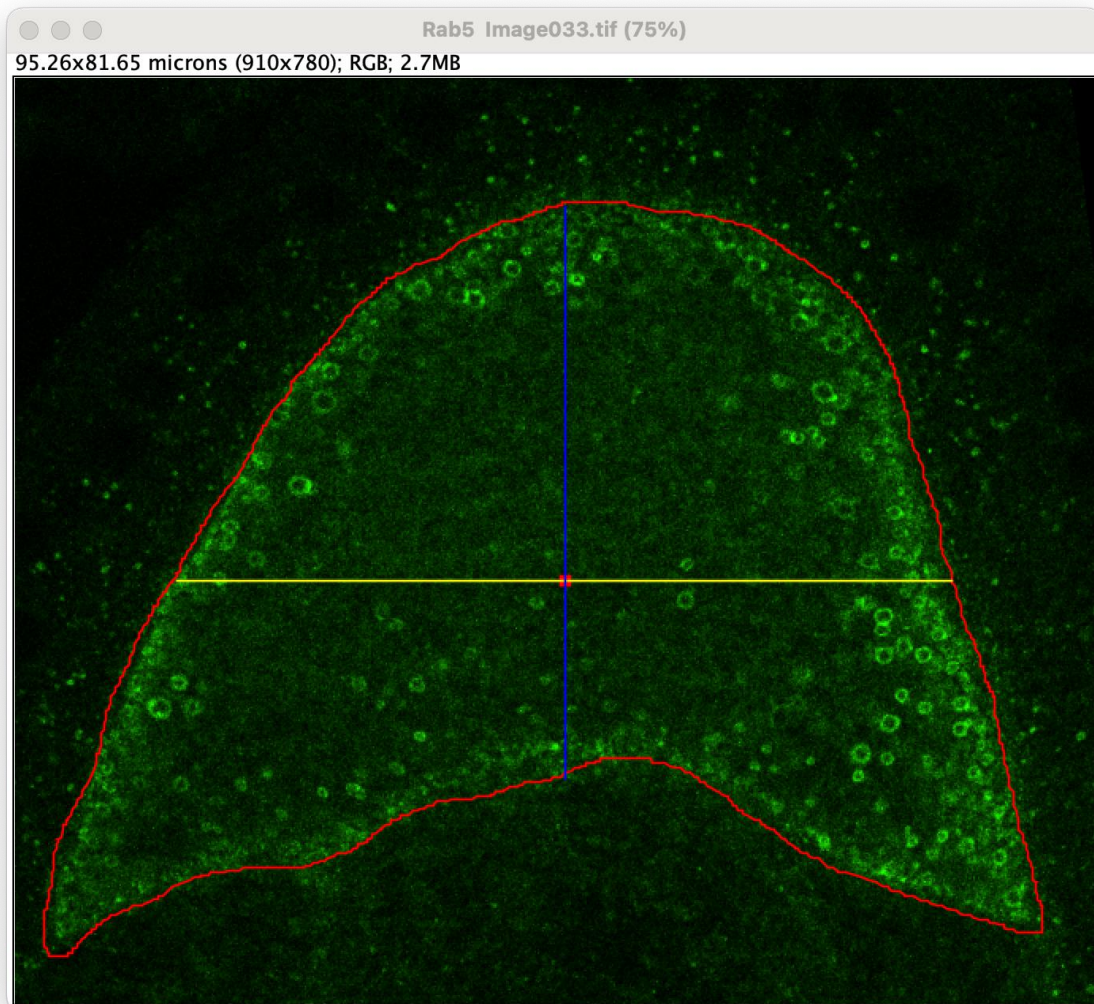
Use the *Multi-point* tool  to mark a point within the oocyte and select **Add [t]** to save. With the point selected, choose **More>>** and then **Specify** in the ROI manager. To enter the centroid coordinates from the **Results** table. The new point will be automatically added to the manager, select and adjust the appearance of the point as needed by selecting **Properties**.





#### Step 4

Draw horizontal and vertical lines through the centroid point using the *Straight line* tool  in the toolbar to divide the oocyte into quadrants clicking **Add[t]** after drawing each line. Use different colours for each ROI for the script to read the separate regions.



#### Step 5

After selecting **Flatten [F]** in the ROI Manager to embed the ROIs into the image, save the images and execute the script to extract fluorescence intensity data from each quadrant (see Section 2 of Appendix).

## 2.8 Enhancing borders of mitochondria.

Fiji (ImageJ)'s "Find Edges" function was used to enhance the visibility of edges and boundaries of mitochondria in *st9 Drosophila* oocytes . The algorithm calculates intensity gradients, emphasizing areas of rapid intensity changes and effectively highlighting the edges of objects within the image.

To use the "Find Edges" function in Fiji (ImageJ) open the image you want to process and select *Process > Find Edges*.

## 2.9 Statistical analysis.

To assess the statistical significance of differences in mean velocities and differences in distribution of organelles between each dataset, a comprehensive statistical analysis was employed using GraphPad Prism (Table 2.3). This analysis aimed to ensure the validity of comparisons and provide robust insights into the observed variations.

**Normality Tests** Before proceeding with parametric statistical tests, normality tests were conducted for each group using the Shapiro-Wilk test. This test assesses whether the distribution of velocities within each group follows a normal distribution.

**Student's t-Test or Mann-Whitney U test** Given the satisfactory outcomes of the normality test, the Student's t-test was selected to determine whether there is a statistically significant difference in mean velocities. This parametric test is appropriate for comparing means of two independent groups when normality and equal variances assumptions are met. If normality was not met, Mann-Whitney U test is used. By relying on ranks rather than raw data values, the Mann-Whitney U test allows for the examination of potential differences between groups without relying on parametric assumptions also making it suitable for small sample sizes.

The significance level  $\alpha$  for all tests was set at 0.05.

### **Example of statistical tests and reasonings**

<i>v<sub>organelle</sub></i>	Shapiro-Wilk <i>p-value</i>	Mann-Whitney U <i>p-value</i>
Rab5 – Rab7	>0.999 – 0.0006	0.8636

Rab5 *p-value* is greater than 0.05, indicating that we do not have strong evidence to reject the assumption of normality for this group while Rab7 *p-value* is lower than 0.05 indicating we have strong evidence to reject the assumption of normality for this group.

The Mann-Whitney U test was chosen due to the observed deviation from normality in the Rab7 dataset as indicated by the Shapiro-Wilk test ( $p < 0.05$ ) and the large discrepancy in sample size ( $n_{Rab5} = 3, n_{Rab7} = 9$ ).

With this *p-value* we fail to reject the null hypothesis; there is not enough statistical evidence to support the hypothesis of a significant difference between Rab5 and Rab7 velocity in the oocyte.

**Table 2.3. Statistical significance (p-value) comparisons of velocity, representing advective motion and diffusivity of experimental groups derived from Mann-Whitney U and Student's t-tests.**

	$v_{organelle}$	$v_{DIC}$	$D_{organelle}$	$D_{DIC}$
YFP:: <i>Rab5</i> <sup>1day</sup> vs YFP:: <i>Rab7</i> <sup>1day</sup>	0.8636*	-	0.01604*	-
YFP:: <i>Mito</i> <sup>1day</sup> vs YFP:: <i>Rab7</i> <sup>1day</sup>	0.001851*	0.001349	0.06253	0.2763
YFP:: <i>Mito</i> <sup>1day</sup> vs YFP:: <i>Rab5</i> <sup>1day</sup>	0.0001794	-	0.01604*	-
YFP:: <i>Mito</i> <sup>1day</sup> vs DIC <sup>YFP::<i>Mito</i></sup>	0.5279	-	0.05031*	-
YFP:: <i>Mito</i> <sup>20day</sup> vs DIC <sup>YFP::<i>Mito</i>(20day)</sup>	0.1646	-	0.6048*	-
YFP:: <i>Mito</i> <sup>30day</sup> vs DIC <sup>YFP::<i>Mito</i>(30day)</sup>	0.7304*	-	0.005205*	-
YFP:: <i>Mito</i> <sup>40day</sup> vs DIC <sup>YFP::<i>Mito</i>(40day)</sup>	0.1002	-	0.0002043	-
YFP:: <i>Rab7</i> <sup>1day</sup> vs DIC <sup>YFP::<i>Rab7</i></sup>	0.1135*	-	0.01061	-
YFP:: <i>Mito</i> <sup>1day</sup> vs YFP:: <i>Mito</i> <sup>20day</sup>	0.4944	0.03229	0.9314*	0.4363*
YFP:: <i>Mito</i> <sup>1day</sup> vs YFP:: <i>Mito</i> <sup>30day</sup>	0.9314*	0.7785	1.000*	0.6592
YFP:: <i>Mito</i> <sup>1day</sup> vs YFP:: <i>Mito</i> <sup>40day</sup>	0.003215	0.002809	0.005636*	0.008581
YFP:: <i>Mito</i> <sup>20day</sup> vs YFP:: <i>Mito</i> <sup>30day</sup>	1.000*	0.05694	0.8336	0.1903*
YFP:: <i>Mito</i> <sup>30day</sup> vs YFP:: <i>Mito</i> <sup>40day</sup>	0.002756*	0.01542	0.008344	0.03558
YFP:: <i>Mito</i> <sup>20day</sup> vs YFP:: <i>Mito</i> <sup>40day</sup>	0.00003292	0.3672	0.02708	0.002666*
YFP:: <i>Mito</i> <sup>nos-gal4</sup> vs Marf <sup>1</sup>	0.08313	0.1812*	0.008992	0.01085
YFP:: <i>Mito</i> <sup>nos-gal4</sup> vs Marf <sup>2</sup>	0.9433*	0.8329*	0.3899	0.2379
YFP:: <i>Mito</i> <sup>nos-gal4</sup> vs Drp1 <sup>1</sup>	0.4047	0.8296	0.04988*	0.02813*
YFP:: <i>Mito</i> <sup>nos-gal4</sup> vs Drp1 <sup>2</sup>	0.04435	0.1084	0.0381	0.02023
Marf <sup>1</sup> vs Marf <sup>2</sup>	0.1255*	0.01732*	0.2222	0.3636
YFP:: <i>Mito</i> <sup>spir</sup> vs YFP:: <i>Mito</i> <sup>spir/Df</sup>	0.00004241	0.001446	0.01399*	0.1645*
YFP:: <i>Mito</i> <sup>spir</sup> vs YFP:: <i>Mito</i> + colchicine	0.01869	0.02939*	0.5512	0.1636*
YFP:: <i>Mito</i> <sup>spir</sup> vs YFP:: <i>Mito</i> <sup>spir/Df</sup> + colchicine	0.05556*	0.1059*	0.2222*	0.5000*
YFP:: <i>Mito</i> <sup>spir</sup> vs DIC <sup>YFP::<i>Mito</i>/spir</sup>	0.9027	-	0.09732*	-
YFP:: <i>Mito</i> <sup>spir/Df</sup> vs DIC <sup>YFP::<i>Mito</i>/spir/Df</sup>	0.3967	-	0.01476	-
YFP:: <i>Mito</i> + colchicine vs DIC <sup>MYFP::<i>Mito</i>+colchicine</sup>	0.8857	-	0.5307	-
YFP:: <i>Mito</i> <sup>spir/Df</sup> + colchicine vs DIC <sup>YFP::<i>Mito</i>/spir/Df+colchicine</sup>	0.3333*	-	0.3333*	-
YFP:: <i>Rab7</i> <sup>spir</sup> vs YFP:: <i>Rab7</i> <sup>spir/Df</sup>	0.000666*	0.000666*	0.005457	0.03008
YFP:: <i>Rab7</i> <sup>spir</sup> vs YFP:: <i>Rab7</i> + colchicine	0.1217	0.1111*	0.3152	0.8375
YFP:: <i>Rab7</i> <sup>spir</sup> vs YFP:: <i>Rab7</i> <sup>spir/Df</sup> + colchicine	0.3434*	0.04492	0.1038*	0.8763*
YFP:: <i>Rab7</i> <sup>spir</sup> vs DIC <sup>YFP::<i>Rab7</i>/spir</sup>	0.7157	-	0.3064	-
YFP:: <i>Rab7</i> <sup>spir/Df</sup> vs DIC <sup>YFP::<i>Rab7</i>/spir/Df</sup>	0.5966*	-	0.3799	-
YFP:: <i>Rab7</i> + colchicine vs DIC <sup>YFP::<i>Rab7</i>+colchicine</sup>	0.2000*	-	0.9669	-
YFP:: <i>Rab7</i> <sup>spir/Df</sup> + colchicine + DIC <sup>YFP::<i>Rab7</i>/spir/Df+colchicine</sup>	0.8048*	-	0.4557*	-

statistically significant

## Key

\* - Mann-Whitney U test,  $v$  – velocity ( $\text{nm s}^{-1}$ ),  $D$  – diffusion coefficient ( $\times 10^{-3} \mu\text{m}^2 \text{s}^{-1}$ ), **Marf<sup>1</sup>** -  $w$ ; P{UAS-*Marf-RNAi*} (GD40478), **Marf<sup>2</sup>** -  $w$ ; P{UAS-*Marf-RNAi* (III)} , **Drp1<sup>1</sup>** -  $w$ ; P{UAS-*Drp1<sup>[WT]</sup>*}/TM6B, **Drp1<sup>2</sup>** - *Drp1<sup>[T26]</sup>,cn<sup>[1]</sup>,bw<sup>[1]</sup>,speck<sup>[1]</sup>/ln(2LR) Gla, wg [Gla-1], YFP::*[...]<sup>spir</sup>* – control , YFP::*[...]<sup>nosgal4</sup>* – control*



## Chapter 3: Results

3.1 Early endosomes, late endosomes and mitochondria exhibit a combination of advective and diffusive motion in *st9 Drosophila* oocytes with variability in rates.

**Table 3.1. DDM analysis of velocity, representing advective motion, and diffusivity of early (Rab5-positive), late (Rab7-positive) endosomes and mitochondria in *st9* wildtype oocytes**

Organelle	$v \text{ nm s}^{-1}$	$D \times 10^{-3} \mu\text{m}^2 \text{ s}^{-1}$	Genotype	$n$
EES	$8.20 \pm 0.30$	$0.97 \pm 0.40$	YFP:: <i>Rab5</i>	3
LEs	$1.84 \pm 2.94$	$3.32 \pm 2.92$	YFP:: <i>Rab7</i>	9
Mitochondria	$7.22 \pm 3.31$	$1.48 \pm 0.61$	YFP:: <i>Mito</i>	9

Values for advective and diffusive motions  $\pm$  standard deviation (SD) obtained using Con-DDM analysis in different genotypes (early endosomes – EE, late endosomes – LE, velocity –  $v$ , diffusion coefficient –  $D$ ).

To begin the investigation of intracellular dynamics in the *Drosophila* oocyte, the rates of advection and diffusion for three distinct organelle populations – Rab5-positive vesicles (Rab5 vesicles, hereafter), Rab7-positive vesicles (Rab7 vesicles, hereafter), and mitochondria – were analysed using a combination of confocal microscopy and DDM (Con-DDM). The results summarised in Table 3.1 indicate that Rab5 vesicles exhibited the highest advection rate at  $8.20 \pm 0.30 \text{ nm s}^{-1}$ , indicative of consistent directed motion of this population of vesicles ([Timelapse 1](#)). In contrast, Rab7 vesicles displayed a lower advection rate of  $1.84 \pm 2.94 \text{ nm s}^{-1}$ , coupled with a considerably larger standard deviation, suggesting more variable and less directed movement in the observed population ([Timelapse 2](#)). In comparison, mitochondria showcased a substantial advection rate of  $7.22 \pm 3.31 \text{ nm s}^{-1}$ , hinting at a directed motion that, while efficient, exhibits greater variability compared to Rab5 vesicles ([Timelapse 3](#)).

Rab7 vesicles demonstrated the highest diffusion rate at  $3.32 \pm 2.92 \times 10^{-3} \mu\text{m}^2 \text{ s}^{-1}$ . The large standard deviation implies considerable heterogeneity in the diffusive behaviour within this population, with some groups of vesicles observed in the same oocyte displaying notably higher diffusion rates than others. In contrast, Rab5 vesicles and mitochondria exhibited lower diffusion rates along with smaller standard deviations

suggesting a more uniform and predictable random motion ( $0.97 \pm 0.40 \times 10^{-3} \mu\text{m}^2 \text{s}^{-1}$  and  $1.48 \pm 0.61 \times 10^{-3} \mu\text{m}^2 \text{s}^{-1}$ , respectively). The standard deviations accompanying the rates of advective, and diffusive motion provide insights into the heterogeneity detected within each population, particularly Rab7 vesicles, demonstrating the extent of random motion of the organelles.

Statistical comparisons further revealed that the advection rates between Rab5 and Rab7 were not significantly different despite the distinct standard deviations (Table 2.2). This implies that while Rab7 vesicles exhibit more variability in the rate of advection, the overall distribution of advection rates does not significantly differ from that of Rab5 vesicles. Significant differences in advection rates were observed when comparing mitochondria to both Rab7 and Rab5 and in diffusion rates between Rab5 and Rab7 and mitochondria and Rab5, indicating variations in the diffusivity of these populations. It is crucial to interpret these findings cautiously, considering the substantial differences in sample sizes ( $n_{Rab5} = 3$ ,  $n_{Rab7} = 9$ , and  $n_{mito} = 9$ ). The smaller sample sizes may limit the generalizability of observed effects.

3.2 Integrating DIC imaging analysis with organelle-specific fluorescent imaging reveals variable and shared motion characteristics between DIC vesicles and late endosomes and mitochondria.

**Table 3.2. DDM analysis of velocity, representing advective motion, and diffusivity of DIC vesicles in the same oocytes as late (Rab7-positive) endosomes and mitochondria in *st9* wildtype oocytes.**

	$v_{org} \text{ nm s}^{-1}$	$v_{DIC} \text{ nm s}^{-1}$	$D_{org} \times 10^{-3} \mu\text{m}^2 \text{s}^{-1}$	$D_{DIC} \times 10^{-3} \mu\text{m}^2 \text{s}^{-1}$	Genotype	<i>n</i>
LEs	$1.84 \pm 2.94$	$2.73 \pm 2.58$	$3.32 \pm 2.92$	$0.98 \pm 0.49$	YFP:: <i>Rab7</i>	9
Mito	$7.22 \pm 3.31$	$8.23 \pm 3.32$	$1.48 \pm 0.61$	$0.74 \pm 0.38$	YFP:: <i>Mito</i>	9

Values for advective and diffusive motions  $\pm$  standard deviation (SD) obtained using Con-DDM analysis in different genotypes (late endosomes – LE, velocity – *v*, diffusion coefficient – *D*, organelle – *org*, DIC vesicles – *DIC*).

In the investigation preceding this study, vesicle motion was analysed using solely Differential Interference Contrast (DIC) imaging which provides a broader view of

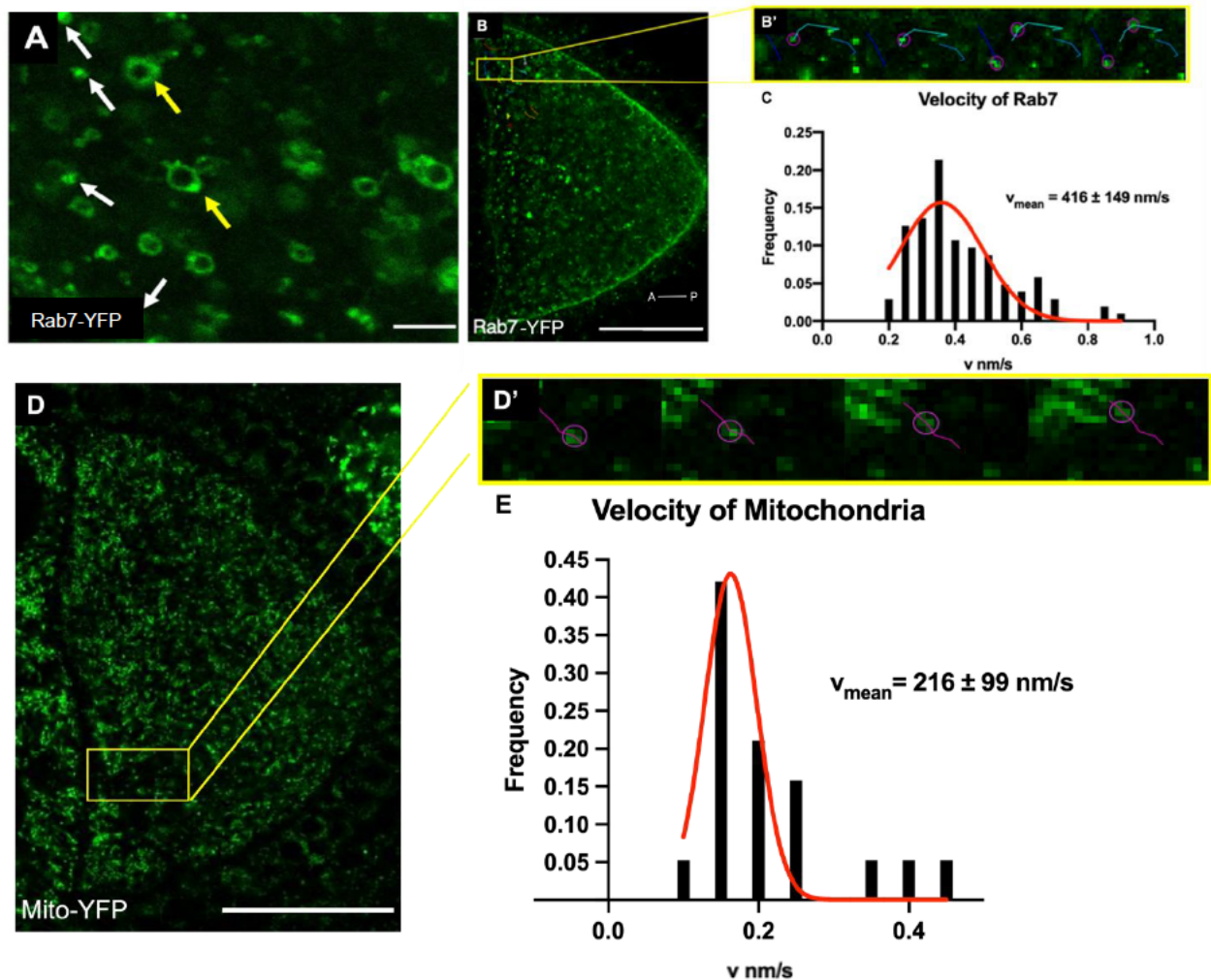
general vesicle dynamics in the oocyte without specific details about their nature (Drechsler et al. 2017). Integrating both DIC imaging with analysis of the motion of YFP-tagged organelles offers a more comprehensive understanding of organelle dynamics and how they may differ between populations, as well as validation of the imaging and analysis techniques used.

DIC vesicles were imaged and analysed in tandem with YFP-tagged Rab7 vesicles and mitochondria and results are summarised in Table 3.2. The higher advection rate of DIC vesicles compared to both mitochondria and Rab7 vesicles suggests a subset of faster moving vesicles within the general DIC vesicle population and the lower diffusion rate implies less pronounced random motion in comparison to the two organelles. The larger standard deviations for both velocity and diffusivity of DIC vesicles indicates greater variability in type of motion between detected vesicles compared to Rab7 vesicles and mitochondria, expected from the nonspecific nature of DIC imaging. Statistical analyses revealed non-significant differences in advection rates between mitochondria and DIC vesicles in the same oocyte but marginally significant differences in diffusion rates same as DIC vesicles and Rab7 vesicles (Table 2.2). Both observed and statistical findings suggest nuanced variations in the motion characteristics of organelles and DIC-detected vesicles, particularly regarding diffusive behaviour. Since DIC microscopy provides a broad and nonspecific view of various cellular components, the observed variability in motion is likely due to a composite of different structures with varying motion behaviours.

### 3.3 Analysis of individual Rab7 vesicles and mitochondria moving in directed and ballistic manner suggests transport as cargo on motors.

When examining the motion of Rab7 vesicles within the oocyte, distinct types of motion were observed among differently sized vesicles. Notably, small, spot-like vesicles exhibited ballistic and directed motion, deviating from typical advection (Figure 3.1A, white arrows; [Timelapse 4](#)). In contrast, larger Rab7-positive vesicles displayed a slower, large-scale mode of motion (Figure 3.1A, yellow arrows; [Timelapse 5](#)). Classification of vesicles based on size revealed two predominant groups: group (1) 'small' vesicles (250 – 300nm; white arrows in Figure 3.1A) showcasing strongly directed and persistent motion, and group (2) 'large' or 'donut-like' vesicles (0.5 – 2.5  $\mu\text{m}$ ; yellow arrows in Figure 3.1A) moving predominantly in an advective manner.

Single-particle tracking using the TrackMate plugin on Fiji (ImageJ) for group 1 Rab7 vesicles yielded a mean velocity of 400 – 420  $\text{nm s}^{-1}$ , close to the established average of  $340 \pm 8 \text{ nm s}^{-1}$  for kinesin in the oocyte (Figure 3.1B, coloured lines; Loiseau et al. 2010). In addition to advective and diffusive motion, mitochondria of similar size range also exhibited cargo-like motion, featuring directional and ballistic movement akin to the motion of group 1 Rab7 vesicles. The mean particle velocity of mitochondria moving in this manner fell slightly below the mentioned average velocity of kinesin, while individual measurements of ballistic velocities reached 370 – 420  $\text{nm s}^{-1}$ . A comparison of ballistic mitochondrial motion with the motion of group 1 Rab7 vesicles demonstrated a significant reduction in velocity (Table 2.2;  $216 \pm 99 \text{ nm s}^{-1}$  vs  $416 \pm 149 \text{ nm s}^{-1}$ ). This discrepancy may be attributed to the small sample size for mitochondria compared to group 1 Rab7 vesicles ( $n_{\text{mito}} = 19, n_{\text{Rab7}} = 63$ ) due to the lower observed frequency of these events along with image resolution constraints. Additionally, as discussed in Section 1.5, motor-based mitochondrial movement is highly responsive to changes in the local environment (nitric oxide and calcium levels and ADP concentration) and the cell's energy requirements in comparison to Rab7 vesicles. It is thus possible that mitochondria experience more pauses and redirection that takes them out of the field of view in 2D imaging.



**Figure 3.1. Motion and dynamics of Rab7 vesicle subgroups and mitochondria.** (A) The two predominant groups of Rab7 vesicles observed are characterised as group (1) 'small' vesicles (white arrows) showcasing strongly directed and persistent motion, and group (2) 'large' or 'donut-like' vesicles (yellow arrows) (B-B') Single particle tracking of group (1) Rab7 vesicles using ImageJ plugin TrackMate to reconstruct trajectory of vesicles and measure velocity. Scale bar represents 30 $\mu$ m (anterior - A, posterior - P). (C) Histogram presenting mean velocities of small Rab7 vesicles (nm/s) in the oocyte falling within the range of the velocity of kinesin. (D-D') Single particle tracking of mitochondria moving in directed and persistent manner. Scale bar represents 30 $\mu$ m. (E) Histogram presenting mean velocities of mitochondria (nm/s) in the oocyte. Scale bar represents 30 $\mu$ m.

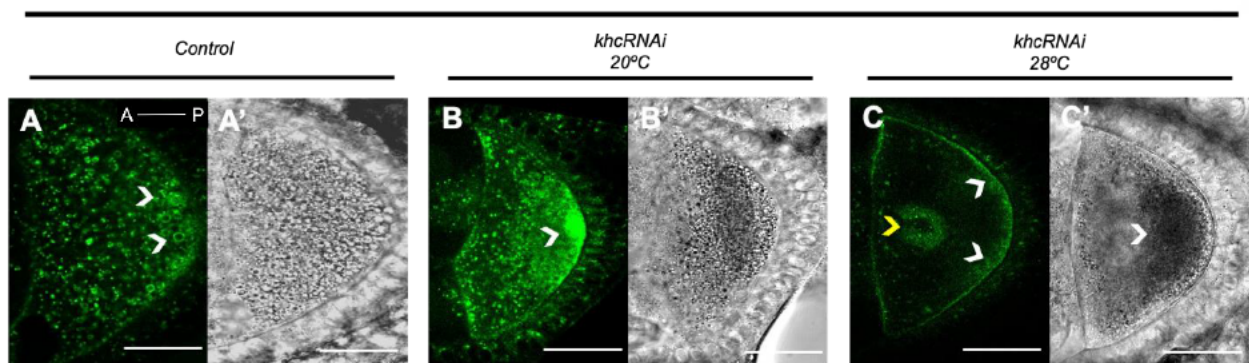
Changes in this type of directed motion, as well as large-scale flow, of endosomes and mitochondria would therefore be expected upon mutating kinesin. To test this, organelle motion was analysed in oocytes mutant for kinesin using a kinesin heavy chain RNAi (*KhcRNAi*) driven by *nos*-Gal4. The heavy chain confers kinesin's motor capability thus mutating it will impact its ability to translocate on MT filaments but not its cargo binding. Unfortunately, the experimental protocol for imaging mitochondria motion in kinesin mutants proved nonviable. Imaging and analysis of Rab7 motion was more successful although not without its own challenges. The first of these challenges was several rounds of inconsistent phenotypes despite all other variables remaining unchanged.

When flies were left to develop at room temperature (20°C), oocytes demonstrated a weak and inconsistent phenotype (approximately 3/10 oocytes in viable mutants; 30% penetrance) when flies were left to develop at room temperature (20°C; Figure 3.2B). Given that *nos*-Gal4 is a temperature sensitive driver, the effects of manipulating temperature were investigated. By immersing the fly vials in a water bath for 20h at 28°C prior to dissection and imaging, oocytes demonstrated more prominent and consistent changes in Rab7 distribution and morphology (60% penetrance). These conditions resulted in a decrease in group 2 'large' vesicles and aberrant clustering towards the centre of the oocyte although vesicles are persistently present along the cortex (Figure 3.2C). Neither advective nor diffusive motion was observed in these oocytes which can be largely attributed to the lack of kinesin-generated flows. DIC vesicles in the same oocytes demonstrated similar motion behaviour and change in size although their distribution was concentrated at the posterior of the oocyte in contrast to Rab7 vesicles (Figure 3.2C'). Accurately measuring changes in DIC vesicle diameter presented a challenge throughout this study as it was very difficult to discern the membranes of individual vesicles due to low resolution and crowding. To overcome this limitation in future investigations, the implementation of super-resolution microscopy and machine-learning segmentation tools could provide enhanced spatial resolution and more accurate measurements of vesicle morphology.



Due to the low resolution of timelapse images, it is difficult to conclusively analyse the extent to which *KhcRNAi* interrupts motion in the cell therefore further investigation into motion data at higher resolution for this experimental condition is required. Despite the absence of detectable advection and diffusion in DDM analysis, a few ‘cargo-like’ motion events were detected in the anterior region in the 28°C condition, similar in motion and speed as group 1 Rab7 vesicles and mitochondria discussed above, although at much lower frequency ( $n = 8; v = 403 \pm 67 \text{ nm s}^{-1}$ ; [Timelapse 6](#)). While this hints at interesting trends, including possible compensation by dynein to maintain coordinated regulation of opposite-end motors as discussed in Section 1.3, the limited sample size makes it crucial to interpret the results with caution. Further investigation with a larger sample would provide insight into the dynamic interplay between Rab7 vesicle motion and motor proteins. Unfortunately, attempts at observing changes in Rab7 distribution and motion in oocytes lacking both motor proteins were unsuccessful. Using *w/v; Dhc - RNAi. GL00543/CyO; Khc - RNAi. GL00330/MKRS* flies resulted in significant developmental issues in the oocytes making it very challenging to image live cells. Had it been successful, the experiment also held the promise of providing valuable information about the relationship between kinesin and dynein within organelle transport highlighting the need for future investigations.

### ***Rab7.YFP***



**Figure 3.2. Changes in distribution of Rab7 vesicles in oocytes mutant for kinesin.** (A) YFP-tagged Rab7 vesicles in control oocyte. Rab7 vesicles in control oocytes vary in size from small vesicles (diffraction limited, 250-300nm) to larger ‘donut-like’ vesicles (diameter 0.5-2.5  $\mu\text{m}$ ). Vesicle distribution here is widespread in the oocyte with a higher density of larger endosomes towards the posterior at the location of MT plus ends (white arrowheads) (anterior – A, posterior - P). (A') DIC vesicles in the same control oocyte. Sizes vary similarly to Rab7 vesicles and are also widely distributed across the oocyte. (B) YFP-tagged Rab7 vesicles in *KhcRNAi*

background developed at 25°C. There is a distinct lack of large vesicles in this condition and a ‘cloud’ of YFP concentrated at the posterior of the oocyte which may be an accumulation of stationary Rab7 vesicles (white arrowhead). **(B’)** DIC vesicles in the same oocyte. Vesicles here do not display abnormal distribution but there is an observable reduction in size when compared to vesicles in A’. **(C)** YFP-tagged Rab7 vesicles in *KhcRNAi* background developed at 28°C. Here we see a drastic difference in vesicle distribution and size. Small endosomes are concentrated along the cortex (white arrowheads) and in a small area in the middle of the oocyte towards the anterior (yellow arrowhead). No group 2 Rab7 vesicles are visible. **(C’)** DIC vesicles in the same oocyte. In addition to vesicles being concentrated along the cortex, vesicles accumulate at the posterior and are absent in the centre and towards the anterior of the oocyte (white arrowhead). Scale bar represents 20µm.

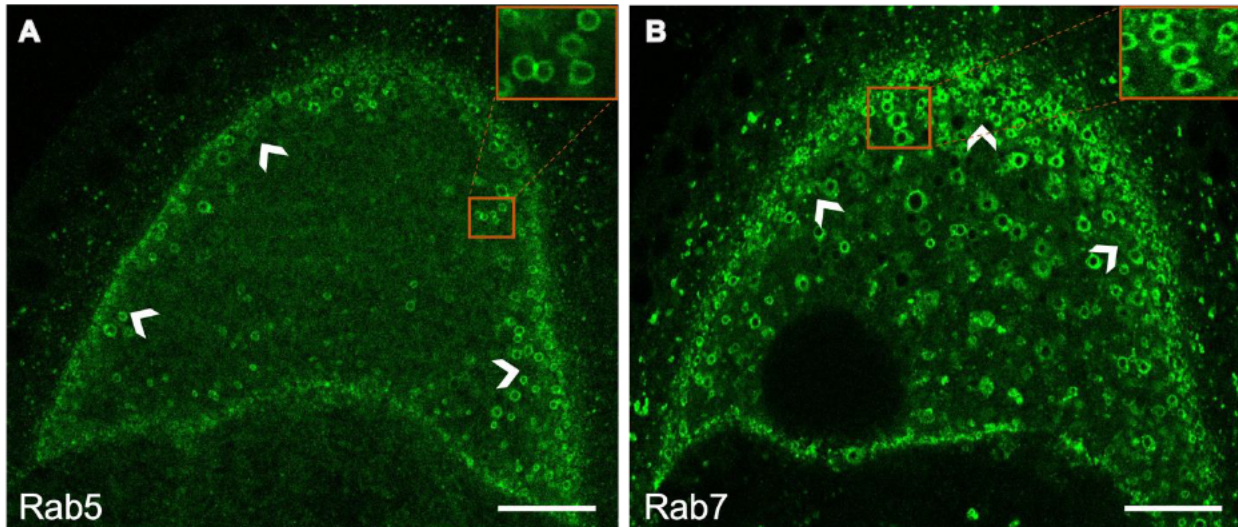
### 3.4 Distribution and morphology of early endosomes, late endosomes, and mitochondria in *st9 Drosophila* oocytes and age-related morphological changes of the mitochondrial network.

In *st9 Drosophila* oocytes, distinct patterns emerge in the distribution of Rab5 and Rab7 vesicles. More specifically, Rab5 vesicles are notably concentrated near the cortex (Figure 3.3A, white arrowheads) whereas Rab7 vesicles display a more dispersed distribution throughout the cytoplasm, with a pronounced density along the posterior cortex (Figure 3.3B). Additionally, Rab7 vesicles have a significantly larger average diameter of  $0.923 \pm 0.42 \mu\text{m}$  compared to  $0.482 \pm 0.12 \mu\text{m}$  for Rab5 vesicles. Relative fluorescence intensity analysis revealed a 55% higher central intensity in Rab7 compared to Rab5 with differences approaching significance, along with a 32% higher peripheral intensity ( $p = 0.0545$  and  $p = 0.157$ , respectively). The central versus peripheral intensity for Rab7 vesicles differed by 8%, whereas for Rab5, this difference was 32% suggesting notable trends that warrant further investigation despite the lack of statistical significance (Table 3.3).

As discussed in Section 1.3, at this stage in oogenesis, MT plus-end orientation exhibits a global posterior bias. Accordingly, the concentration of Rab7 at the posterior of the oocyte may be due to transport as cargo on kinesin and the viscous drag created by kinesin translocation towards the MT plus-ends. Rab5 is associated with early endosomes moving from the membrane into the oocyte and is involved in cortical actin remodelling during endocytosis which may explain the concentration of Rab5 vesicles



along the cortex. Additionally, as mentioned in Section 1.6, Rab5-positive vesicle motion exhibits a general inward bias confined by actin density.



**Figure 3.3.** YFP-tagged Rab5 and Rab7 vesicle distribution in *st9* wildtype oocytes. (A) YFP-tagged Rab5 vesicles. Distribution of Rab5 vesicles is concentrated mainly along the cortex of the oocyte (white arrows). (B) YFP-tagged Rab7 vesicles. Rab7 vesicles are distributed extensively within the cytoplasm, exhibiting a significant concentration cortically and at the posterior of the oocyte (white arrows). Scale bar represents 10µm.

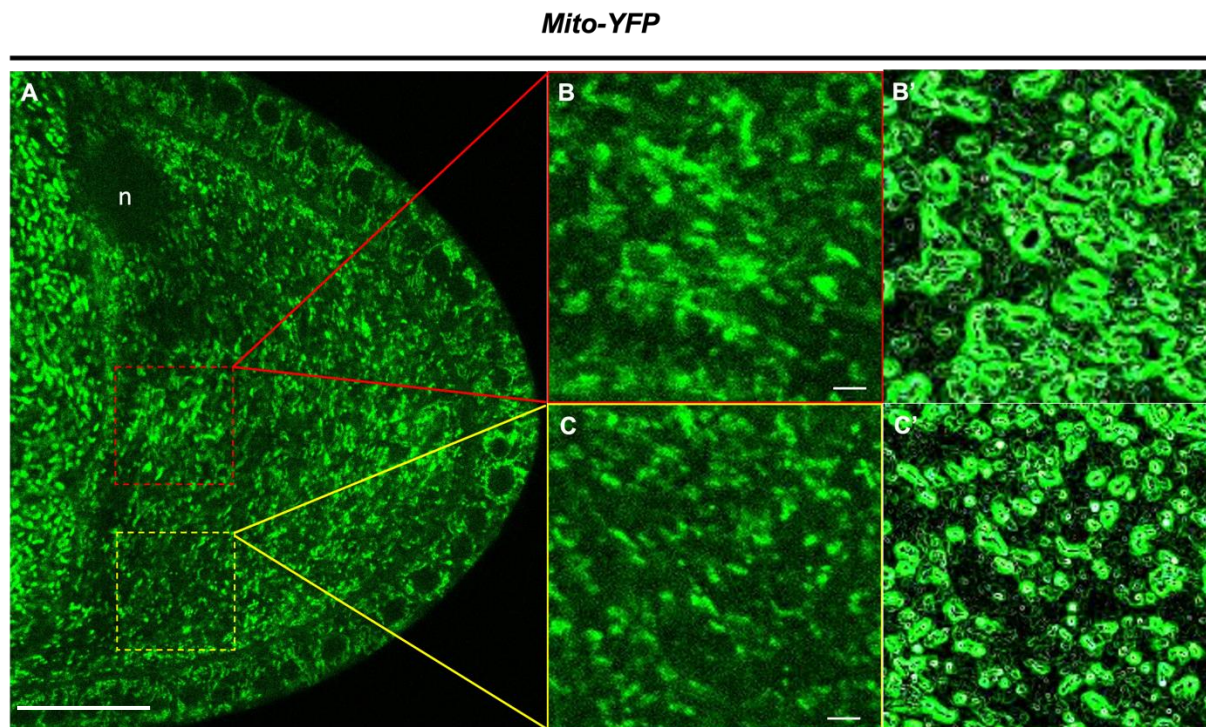
**Table 3.3. Mean and standard deviation of central and peripheral fluorescent intensity of Rab5 and Rab7 vesicles in wildtype oocytes.**

	Central Intensity	Peripheral Intensity	Genotype	<i>n</i>
Mean	29.90	41.62	YFP:: <i>Rab5</i> <sup>1day</sup>	4
SD	10.48	12.47		
Mean	52.82	57.64	YFP:: <i>Rab7</i> <sup>1day</sup>	4
SD	16.12	15.42		

Values for intensity measured in arbitrary units (AU) using Python script found in Appendix.

The mitochondrial network in *st9* oocytes exhibited a distinctive pattern compared to Rab5 and Rab7 vesicles. Unlike these vesicles, there were no discernible areas of low concentration within the mitochondrial network (Figure 3.4A). The network spans the entire cytoplasm of the oocyte, showcasing morphological diversity with organelles ranging from small, discrete tubules (referred to as punctate) to more complex,

interconnected tubular clusters (Figure 3.4B-C'). An attempt was made to quantitatively compare the lengths of mitochondria in these two distinct groups but the low resolution of captured images made it difficult to accurately discern the membrane from background noise. As discussed in Section 1.5, mitochondrial dynamics are regulated by factors beyond motor proteins. These include energetic demands, stress levels, calcium concentration, and others, collectively maintaining the delicate balance of fusion and fission. Impairment of fusion and fission machinery or changes in the balance, whether directly through mutations or indirectly as a stress response, results in aberrant mitochondrial morphology, impacting distribution and motility. One factor that initiates the mitochondrial stress-response and alters morphology and motility of the network is ageing.



**Figure 3.4. Variable morphology of the mitochondrial network in wildtype *st9* oocytes.** (A) YFP-tagged mitochondria in *st9* oocytes. A closer look at the different morphologies displayed by mitochondria in the same cell. Scale bar represents 20 $\mu$ m. (B) Magnified image of mitochondria with interconnected tubular mitochondria. (B') Enhanced edges of mitochondria with filamentous morphology using the Fiji (ImageJ) "Find Edges" function. (C) Magnified image of punctate mitochondria. Scale bar represents 10 $\mu$ m. (C') Enhanced edges of punctate mitochondria using the Fiji (ImageJ) "Find Edges" function.

To investigate the morphological impact of ageing and the subsequent effects on motility discussed in the following section, flies were aged for 20, 30, and 40 days and oocytes imaged for mitochondria ( $n = 9$ ). Mitochondria in oocytes at 1 and 20 days old display comparable morphology (Figure 3.5A-B). At 30 days, which is approximately half the average lifespan of *Drosophila*, filamentous aggregates begin to accumulate in the middle of the oocyte and towards the cortex (Figure 3.5C, yellow arrowheads) and are depleted near the posterior region of the oocyte (Figure 3.5C, white arrowheads). In 40-day old oocytes, this phenotype appears more severe in the posterior with larger regions seemingly void of mitochondria and an increase in number and size of the filamentous aggregates (Figure 3.5D, white arrowheads). Nevertheless, fluorescence intensity analysis revealed only a 5% difference in intensity at the posterior between control and 30-day-old oocytes. Comparatively, 30-day-old samples exhibited a 30% higher intensity centrally, although this difference did not reach statistical significance ( $p = 0.340$ ). Surprisingly, a 16% decrease in intensity at the posterior was observed in 40-day-old oocytes compared to controls likely impacted by the difference in image resolution between the two ( $p = 0.120$ ), with the latter showing a 10% lower intensity compared to 30-day-old ( $p = 0.643$ ; Table 3.4). These phenotypic aberrations are concomitant with changes in motility of mitochondria, suggesting a strong link between morphology and motility, and, subsequently, distribution of the organelle. DIC imaging was employed in conjunction with fluorescent imaging in all following experiments to investigate whether alterations in experimental conditions exerted broader effects on the overall cytoplasmic content or if the observed impacts were confined solely to mitochondria.



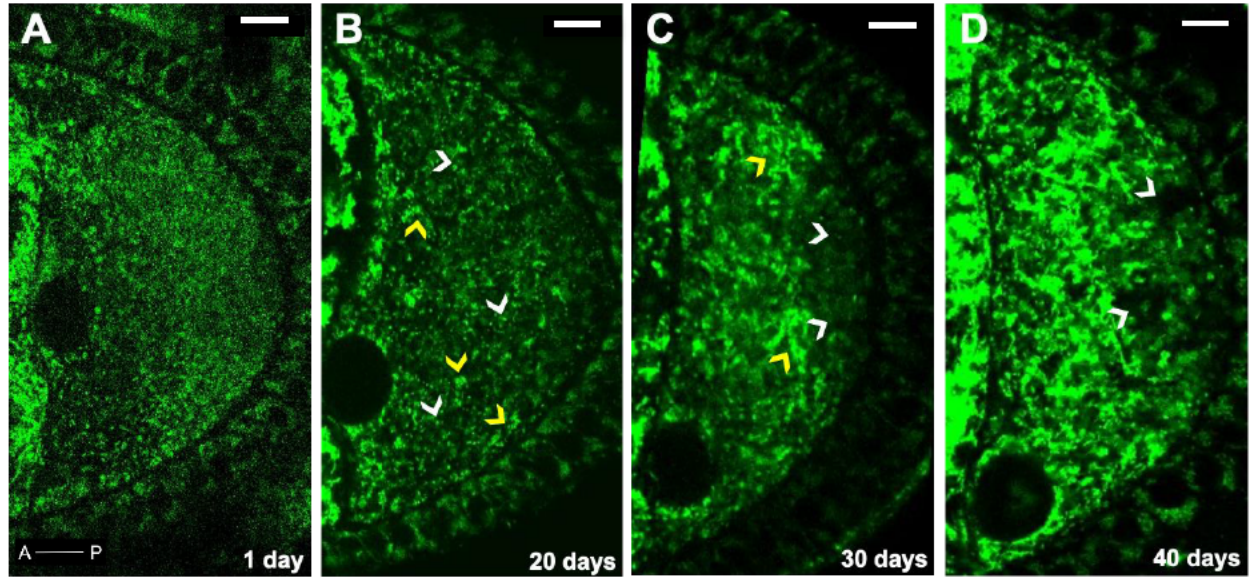


Figure 3.5. Age-related morphological changes of YFP-tagged mitochondria in *st9* oocytes. (A) 1-day old control oocyte. (anterior – A, posterior – P) (B) 20-day old oocyte. Mitochondrial morphology is comparable to wildtype in variation and distribution, demonstrating a mix of clustered (yellow arrowheads) and punctate (white arrowheads) organelles traversing the entirety of the cytoplasm. (C) After 30 days, we observe aggregates of filamentous mitochondria in the centre and near the cortex (yellow arrowheads) and fewer punctate structures as well as a depletion in the posterior of the oocyte (white arrowheads). This phenotype is even more dramatic after 40 days (D) with strongly visible domains lacking mitochondria in the posterior (white arrowheads) and an increase in filamentous aggregates (yellow arrowheads). Scale bar represents 10µm.

**Table 3.4. Mean and standard deviation of anterior and posterior fluorescent intensity of mitochondria in control, 30 day old, and 40 day old oocytes.**

		Anterior intensity	Posterior intensity	Genotype	<i>n</i>
1-day	Mean	78.50	85.29	YFP:: <i>Mito</i> <sup>1day</sup>	3
	SD	14.48	14.18		
30-day	Mean	106.41	80.53	YFP:: <i>Mito</i> <sup>30day</sup>	3
	SD	42.27	28.30		
40-day	Mean	82.38	72.27	YFP:: <i>Mito</i> <sup>40day</sup>	3
	SD	5.88	3.85		

Values for intensity measured in arbitrary units (AU) using Python script found in Appendix.

### 3.5 Ageing adversely affects mitochondrial motility in *st9 Drosophila* oocytes.

**Table 3.5. DDM analysis of velocity, representing advective motion, and diffusivity of mitochondria at different ages (1, 20, 30 and 40 days old).**

	$v_{org} \text{ nm s}^{-1}$	$v_{DIC} \text{ nm s}^{-1}$	$D_{org} \mu\text{m}^2 \text{ s}^{-1} \times 10^{-3}$	$D_{DIC} \mu\text{m}^2 \text{ s}^{-1} \times 10^{-3}$	Genotype	<i>n</i>
1-day	7.22 ± 3.31	8.23 ± 3.32	1.48 ± 0.61	0.74 ± 0.38	YFP::Mito	9
20-day	6.37 ± 1.46	4.63 ± 3.19	1.55 ± 0.86	1.37 ± 1.03	YFP::Mito	9
30-day	6.84 ± 4.26	7.48 ± 3.39	1.42 ± 0.63	0.68 ± 0.44	YFP::Mito	9
40-day	2.72 ± 1.22	3.59 ± 0.86	0.76 ± 0.23	0.30 ± 0.16	YFP::Mito	9

Values for advective and diffusive motions ± standard deviation (SD) obtained using Con-DDM analysis in different genotypes (velocity – *v*, diffusion coefficient – *D*, organelle – *org*, DIC vesicles – *DIC*).

The analysis of age-related changes in mitochondrial motion reveals that there are no significant differences in advection or diffusion rates when comparing mitochondrial motion in 1-day and 20-day oocytes, suggesting relatively stable motion characteristics between these ages (Table 2.2; [Timelapse 7](#); [Timelapse 8](#)). Likewise, mitochondria at 1-day and 30-day ([Timelapse 9](#)) exhibit no significant differences in advection and diffusion rates however, mitochondria in 40-day oocytes ([Timelapse 10](#)) demonstrate a significant decrease in both advection and diffusion rates compared to 1-day, suggesting adverse age-related effects on both directed and random motion behaviours. Similarly, comparing motion of mitochondria at 20-day and 40-day revealed significant differences in both advection and diffusion rates, indicating distinct motion characteristics during this period as was the case when comparing mitochondria at 30-day and 40-day. The significant differences observed in motion between the 40-day group and the other time points suggest that mitochondrial dynamics undergo substantial alterations as the oocyte ages from 30 days to 40 days. However, the lack of significant differences in motion between the earlier time points (1 – day vs 20 – day, 20 – day vs 30 – day, and 1 – day vs 30 – day) indicates that these changes are not linear and may be more pronounced in the later stages of ageing. The transitional

periods between 1-day and 20-day, as well as 20-day and 30-day, may involve subtle adjustments in mitochondrial motion undetected at this imaging resolution.

In the investigation of DIC vesicle dynamics across different ageing conditions, several noteworthy patterns emerge. When comparing DIC vesicles at 1-day with 20-day, significant differences are observed in advection and no significant differences in diffusion rates, indicating some variation in motion behaviour during this ageing period. When comparing DIC vesicles at 1-day and 30-day, no significant differences are found in advection or diffusion rates while DIC vesicles at 1-day and 40-day note significant differences in both advection and diffusion rates, highlighting substantial changes in motion behaviour during this ageing period in line with the changes in mitochondrial motion behaviour. When comparing mitochondria and DIC vesicle velocity and diffusion in the same aged oocyte, no significant differences were noted except for marginal statistically significant differences in diffusion rates at 1-, 30- and 40-day (Table 2.2). This statistical analysis suggests some variations in the way ageing impacts the motion behaviours of these populations in the same cell.

The qualitative observation of mitochondrial hyperfusion in aged oocytes coupled with results showing a decrease in mitochondrial and DIC vesicle motility over time suggests a compelling relationship between organelle size and dynamics and their motility within the cell. The observed hyperfusion, characterized by the fusion of individual mitochondria into larger interconnected networks, suggests larger and more interconnected mitochondria may experience a decrease in their ability to navigate through the cellular environment. This subsequently creates hindrance for other organelles significantly affecting their motility within the oocyte cytoplasm and interactions with other cellular structures. To explore the intricate interplay between mitochondrial dynamics, size, and motility further, the balance of fusion and fission processes was manipulated to uncover potential causative relationships.

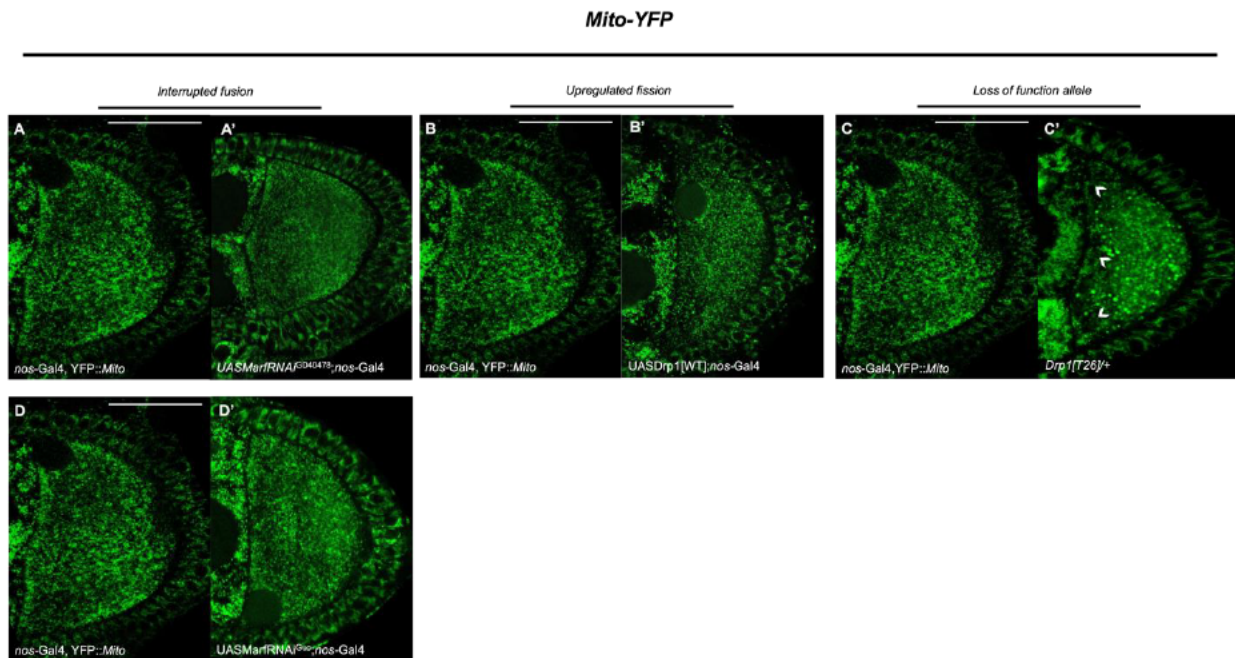
### 3.6 Perturbing the balance of mitochondrial fusion and fission using *Marf* and *Drp1* mutants affects morphology and distribution of mitochondria in *st9 Drosophila* oocytes.

As we observed in wildtype *st9* oocytes, mitochondrial morphology ranges from separate punctate structures to longer filamentous networks (Figure 3.4). This variability is attributed to mitochondrial dynamics involving processes of fusion and fission. The aim of this experiment is to investigate the relationship between mitochondrial dynamics and distribution and the subsequent effect on motility when these dynamics are altered. Mitochondrial fusion was interrupted using two *Marf* RNAi's (*UASMarfRNAi<sup>GD40478</sup>*; *nos-Gal4.YFP::Mito* and *UASMarfRNAi<sup>Guo</sup>*; *nos-Gal4.YFP::Mito*) to enhance the reliability and generalisability of the observed outcomes particularly due to the inconsistent results obtained when originally solely using *UASMarfRNAi<sup>GD40478</sup>*; *nos-Gal4.YFP::Mito*. A loss of function *Drp1* mutant (*Drp1<sup>[T26]</sup>*) allele was used as severe reductions in *Drp1* lead to lethality. The presence of *nos-Gal4* has been noted to have an impact on cytoplasmic flows in the absence of any mutation therefore the experimental control is *nos-Gal4.YFP::Mito* rather than *YFP::Mito* (Drechsler et al. 2017).

In conditions where fusion was interrupted in *UASMarfRNAi<sup>GD40478</sup>*; *nos-Gal4* and *UASMarfRNAi<sup>Guo</sup>*; *nos-Gal4*, the mitochondrial network in mutants appear more fragmented and punctate compared to controls ( $n_{GD} = 6, n_{Guo} = 5$ ; Figure 3.6A'&D'). Similarly, in the upregulated fission conditions of *UASDrp1[WT]*; *nos-Gal4* mutant oocytes, mitochondria appear more fragmented than wildtype controls and both interrupted fusion mutants ( $n = 8$ ; Figure 3.6B'). With fission processes interrupted, mutant oocytes heterozygous for the *Drp1<sup>[T26]</sup>* loss of function allele display a more dramatic phenotypic change and are less evenly distributed when compared to wildtype ( $n = 10$ ). Filamentous mitochondria in these mutants located near the anterior cortex appear thicker (Figure 3.6C', white arrowheads) than controls while the bulk of the cytoplasm contains globular organelle structures (Figure 3.6C'). The distribution analysis results indicate a general decrease in mitochondrial intensity across the oocyte when comparing controls to mutant conditions (Table 3.6). Specifically, changes in

central distribution between controls and mutants demonstrated an 83% decrease in *UASMarfRNAi<sup>GD40478</sup>; nos-Gal4*, 43% decrease in *UASMarfRNAi<sup>Guo</sup>; nos-Gal4* oocytes, 62% in *UASDrp1[WT]; nos-Gal4* and most notably a 101% decrease in *Drp1<sup>[T26]</sup>* mutants. Similar differences were observed in the peripheral, anterior, and posterior regions of mutant oocytes compared to controls, all of which reached statistical significance except for *UASMarfRNAi<sup>Guo</sup>* (Appendix 3).

To further understand the implications of mutating fusion and fission processes on distribution and effects on the spatial relationships of organelles, the use of 3D imaging techniques and machine learning segmentation tools to measure the differences in thickness and length of the filamentous structures would be beneficial. In the same manner as age-related morphological changes impacting the rates of motion of mitochondria, the phenotypic changes observed in these mutants accompany changes in organelle motility.



**Figure 3.6. Fusion and fission mutants affect mitochondrial morphology and distribution.** (A,B,C,D) YFP-tagged mitochondria in control oocytes. Mitochondria in control oocytes vary in size from punctate to longer, filamentous organelles that may be undergoing either fission, fusion, or tethering (anterior – A, posterior – P). (A',D') YFP-tagged mitochondria in *UASMarfRNAi<sup>GD40478</sup>; nos-Gal4* and *UASMarfRNAi<sup>Guo</sup>; nos-Gal4* genetic background, respectively, where fusion is interrupted. Mitochondria in the Marf mutants appear more fragmented and punctate when compared to controls and have a cloudy



appearance. (B') YFP-tagged mitochondria in *UASDrp1[WT]; nos-Gal4* genetic background where fission is upregulated. Similarly, mitochondria in these oocytes appear more punctate and fragmented. (C') YFP-tagged mitochondria in oocytes heterozygous for the *Drp1<sup>T26</sup>* loss-of-function fission allele displaying largely globular morphology, concentrated at the posterior while filamentous mitochondria in the anterior appear thicker than controls (white arrowheads). Scale bar represents 30 $\mu$ m.

**Table 3.6. Mean and standard deviation of central, peripheral, anterior and posterior fluorescent intensities of mitochondria in oocytes mutant for Marf and Drp1.**

	Central Intensity	Peripheral Intensity	Anterior Intensity	Posterior Intensity	Genotype	<i>n</i>
Control						
<b>Mean</b>	79.72	73.44	72.26	77.93	<i>nos-Gal4.</i>	3
<b>SD</b>	24.73	24.33	19.74	30.15	<i>YFP::Mito</i>	
Interrupted fusion						
<b>Mean</b>	32.74	35.51	32.99	33.52	<i>UASMarfRNA<sup>GD4</sup></i>	3
<b>SD</b>	6.52	7.28	5.95	7.391	<i>0478; nos-Gal4. YFP::Mito</i>	
Interrupted fusion						
<b>Mean</b>	51.17	51.58	50.22	55.27	<i>UASMarfRNA<sup>Guo</sup>; nos-Gal4. YFP::Mito</i>	3
<b>SD</b>	7.96	12.28	7.63	12.65		
Increased fission						
<b>Mean</b>	42.01	36.99	37.28	39.67	<i>UASDrp1<sup>WT</sup>; nos-Gal4. YFP::Mito</i>	3
<b>SD</b>	4.40	2.90	2.057	7.349		
Fission allele						
<b>Mean</b>	26.06	27.27	25.72	27.76	<i>Drp1<sup>T26</sup>; nos-Gal4. YFP::Mito</i>	3
<b>SD</b>	1.16	2.81	1.093	2.093		

Values for intensity measured in arbitrary units (AU) using Python script found in Section 3 of Appendix.

3.7 Perturbing the balance of mitochondrial fusion and fission using *Marf* and *Drp1* mutants reduces advective and diffusive motion of mitochondria and DIC vesicles in *st9 Drosophila* oocytes.

**Table 3.7. DDM analysis of velocity, representing advective motion, and diffusivity of mitochondria in interrupted fusion and fission conditions.**

	$v_{org} \text{ nm s}^{-1}$	$v_{DIC} \text{ nm s}^{-1}$	$D_{org} \mu\text{m}^2 \text{ s}^{-1} \times 10^{-3}$	$D_{DIC} \mu\text{m}^2 \text{ s}^{-1} \times 10^{-3}$	Genotype	<i>n</i>
Control	13.87 ± 7.50	12.73 ± 5.21	1.69 ± 0.84	1.01 ± 0.34	<i>nos-Gal4</i> . <i>YFP::Mito</i>	8
Interrupted fusion	5.20 ± 2.26	4.90 ± 1.31	0.67 ± 0.35	0.45 ± 0.40	<i>UASMarfRNAi<sup>GD</sup><sub>40478</sub></i> ; <i>nos-Gal4</i> . <i>YFP::Mito</i>	6
Interrupted fusion	6.61 ± 1.57	6.99 ± 1.51	1.32 ± 0.99	0.85 ± 0.57	<i>UASMarfRNAi<sup>Guo</sup></i> ; <i>nos-Gal4</i> . <i>YFP::Mito</i>	5
Increased fission	8.21 ± 5.09	9.35 ± 4.84	1.23 ± 0.80	0.71 ± 0.44	<i>UASDrp1<sup>WT</sup></i> ; <i>nos-Gal4</i> . <i>YFP::Mito</i>	8
Fission allele	5.18 ± 2.29	4.72 ± 2.83	0.36 ± 0.21	0.30 ± 0.40	<i>Drp1<sup>T269/+</sup></i> ; <i>nos-Gal4</i> . <i>YFP::Mito</i>	10

Values for advective and diffusive motions ± standard deviation (SD) obtained using Con-DDM analysis in different genotypes (velocity – *v*, diffusion coefficient – *D*, organelle – *org*, DIC vesicles – *DIC*).

The subsequent investigation delves into the analysis of mitochondrial motion under manipulated fusion and fission conditions. The rates of mitochondrial velocity and diffusion under various fusion and fission mutant conditions are summarised in Table 3.4. The values reveal distinct alterations in both advection and diffusion compared to the control ([Timelapse 11](#)). Mitochondria in the first downregulated fusion mutant *UASMarfRNAi<sup>GD40478</sup>* show a significant reduction in advection and a significant decrease in diffusion compared to the control, indicating a notable impact on both directed and random motion in the absence of Marf (Table 2.2; [Timelapse 12](#)). The second downregulated fusion mutation *UASMarfRNAi<sup>Guo</sup>*, also displays a reduction in advection and diffusion compared to controls but these changes failed to reach statistical significance ([Timelapse 13](#)). Upregulating fission using *UASDrp1[WT]* results in a decrease in both advection and diffusion compared to controls with marginal significance

between diffusion rates ([Timelapse 14](#)). Notably, the loss of function fission allele *Drp1<sup>T26/+</sup>* demonstrates a significant decrease in both advection and diffusion ([Timelapse 15](#)). These findings suggest that manipulating the balance of fusion and fission events has distinct effects on mitochondrial motility, with the loss of function fission mutation showing the most pronounced alterations in both directed and random motion when compared to controls. The comparison of advective and diffusive rates between the two down-regulated fusion mutations reveals no statistically significant differences in motion. These consistent decreases in both advective and diffusive motion across the two mutations suggest that downregulation of fusion events results in impairment of mitochondrial mobility within the cell. The statistical comparison between the mutations further supports the notion that the observed effects are consistent and likely related to the downregulated fusion events.

The advection rates for DIC vesicles in mitochondria mutants did not show significant differences compared to the control, suggesting that the manipulations in mitochondrial fusion and fission did not have a substantial impact on the advection of these vesicles (Table 2.2). In contrast, diffusion rates of DIC vesicles in *UASMarfRNAi<sup>GD40478</sup>* and both *Drp1* mutants displayed a significant decrease when compared to controls, suggesting that alterations in mitochondrial fusion and fission events may influence the diffusive behaviour of these vesicles. While advection remains relatively unchanged, significant differences in diffusion rates indicate that manipulating mitochondrial fusion and fission events can impact the random motion of DIC vesicles in the oocyte. The dynamic interaction between endosomes and mitochondria described in Section 1.5 plays a crucial role in shaping mitochondrial function and morphology. Although difficult to quantify under these imaging conditions, DIC vesicle morphology appears altered in mutants compared to controls in line with previous data demonstrating changes in endosomal size when mitochondrial function is altered ([Timelapse 11](#) vs [Timelapse 12](#) & [Timelapse 13](#)). Endosomes, as central hubs for intracellular trafficking, are intricately involved in the transport and delivery of proteins and lipids to mitochondria. Given that DIC vesicles comprise vesicles originating from endosomes, the observed changes in the motion patterns in mitochondria fusion and fission mutants may, in part, be attributed to

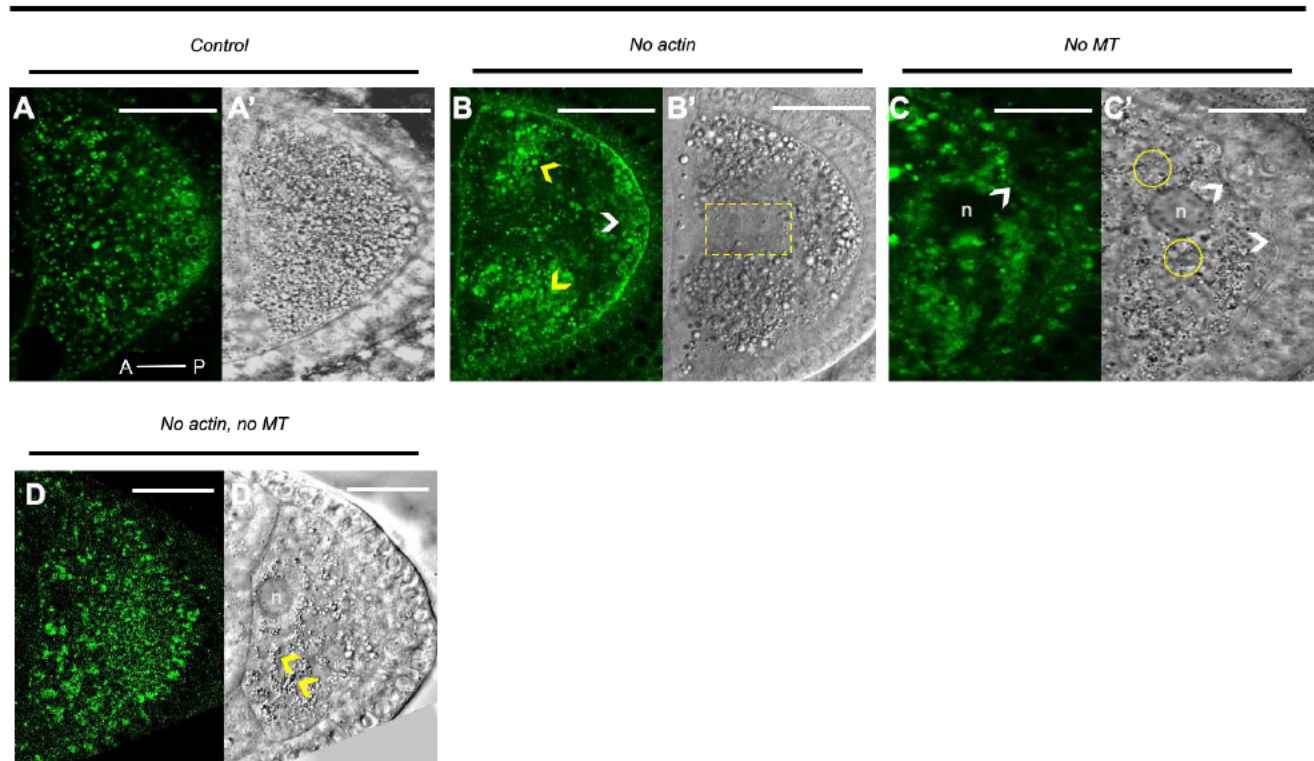
alterations in the processes involving endosomes, impacting the coordinated exchange of cellular cargo. The observed changes underscore the complexity of the interconnected pathways of mitochondrial dynamics and their intricate association with endosomes in the *Drosophila* oocyte.

As these changes in the motion characteristics of DIC vesicles hint at disruptions in the interplay between endosomes and mitochondria, perturbing the cytoskeletal network demonstrates how alterations in cellular infrastructure impact the intricate orchestration of organelle motion, contributing to the understanding of their collaborative interactions.

### 3.8 Depolymerising microtubules and the actin mesh affects the distribution and morphology of late endosomes and mitochondria in *st9 Drosophila* oocyte.

Due to the critical roles of the cytoskeletal network in endosome maturation, manipulating MT and actin cytoskeletons has a profound impact on the morphology and distribution of late endosomes in the oocyte. The absence of the actin mesh alters the distribution and morphology of Rab7 and DIC vesicles, resulting in large regions of the cytosol devoid of vesicles and aberrant accumulations at the anterior and posterior corners ( $n = 10$ ). Additionally, there is a reduction in group 2 Rab7 vesicles quantified using the selection process described in Section 2.6 ( $n_{no\ actin} = 6$  vs  $n_{control} = 30$ ; Figure 3.7B-B'). In the absence of MTs, both Rab7 and DIC vesicles are significantly affected, with the formation of large cloudy aggregates throughout the oocyte and warping of the anterior membrane ( $n = 4$ ; Figure 3.7C-C', white arrowheads). Under no actin and no MT conditions, Rab7 vesicle borders become indistinct, forming merged clusters around the posterior pole, while DIC vesicles in the same oocyte appear predominantly smaller than those in the control and no actin conditions, with irregular and aberrant clustering observed across different oocytes ( $n = 7$ ; Figure 3.7D-D', white arrowheads and yellow circles, respectively).

## *Rab7.YFP*



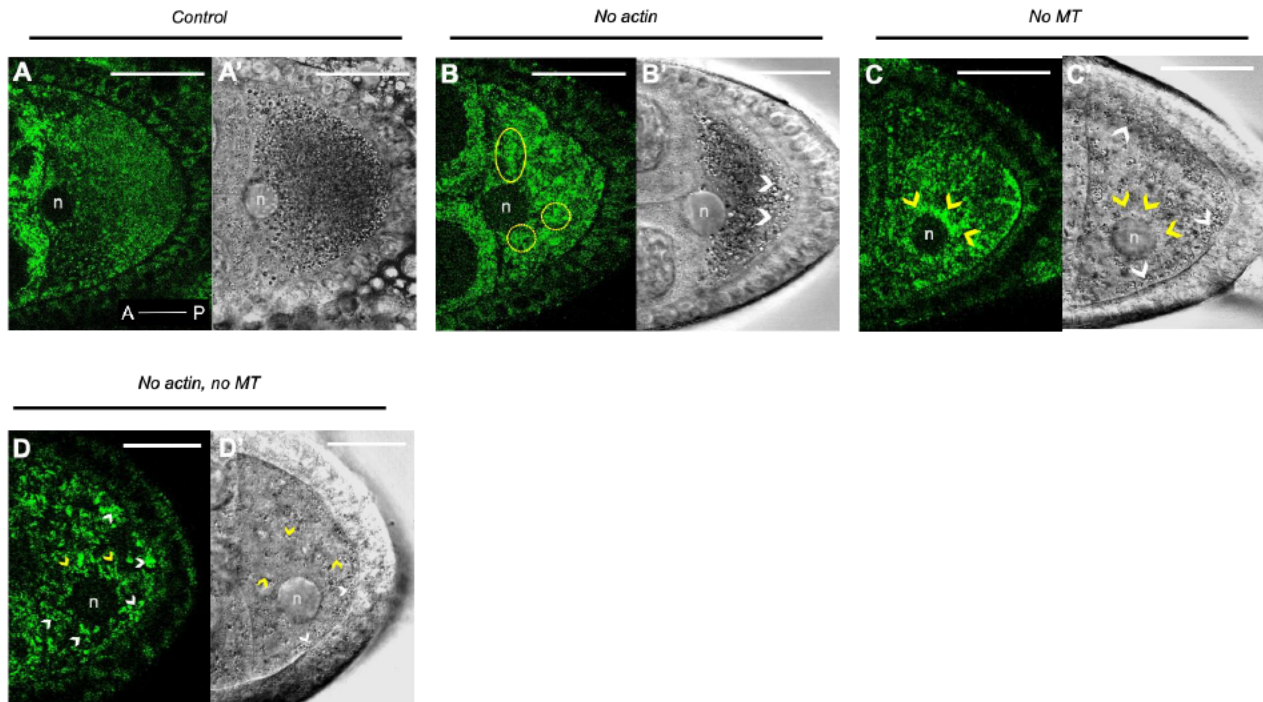
**Figure 3.7. Absence of MT and actin cytoskeletons affect motion, morphology and distribution of Rab7 and DIC vesicles.** (A) YFP-tagged Rab7 vesicles in control oocytes. Rab7 vesicles in control oocytes vary in size from punctate, small vesicles (diffraction limited, 250-300nm) to larger 'donut-like' vesicles (0.5-2.5  $\mu\text{m}$ ) (anterior – A, posterior - P). (A') DIC vesicles in the same control oocyte. Sizes vary similarly to Rab7 vesicles. (B) YFP-tagged Rab7 vesicles in the absence of the actin mesh. Vesicle morphology in this condition is not affected as much as distribution; vesicles are concentrated to the right and left posteriorly (yellow arrowheads) and close to the cortex anteriorly (white arrow head) (B') DIC vesicles in the same oocyte as B. Distribution of these vesicles reflects that of Rab7 vesicles with even fewer vesicles concentrated in the middle (yellow square). (C) YFP-tagged Rab7 vesicles in the absence of the MT cytoskeleton, indicated by the displaced nucleus (n). In this condition, individual Rab7 vesicles are very difficult to discern, instead they form cloudy aggregates spanning the oocyte with a few scattered bright fluorescent dots that resemble the small vesicles we observe in control and no actin oocytes. The cortical membrane of these oocytes is also affected by the absence of MTs particularly anteriorly where the membrane seems to cave in (white arrowheads). (C') DIC vesicles in the same oocyte as C. Distribution of DIC vesicles reflects that of Rab7 vesicles in this condition. Individual vesicles are visible but appear smaller when compared to control DIC vesicles. Vesicles also fail to accumulate in regions near the nucleus (yellow circles) (D) YFP-tagged Rab7 vesicles in the absence of both actin and MT cytoskeletons. In this condition, the borders of individual vesicles are hard to discern, similarly to the no MT condition, and form merged clusters near the posterior of the oocyte (white arrowheads). (D') DIC vesicles in the same oocyte as D. Larger DIC vesicles (white arrowheads) are scarce particularly when compared to control and no actin conditions and the smaller vesicles are concentrated in clusters

predominantly in one area near the posterior (yellow arrowhead) unlike the other conditions where DIC vesicles are found both posteriorly and anteriorly despite changes in distribution. Scale bar represents 30 $\mu$ m.

Similarly, mitochondria exhibit alterations in morphology and distribution upon manipulation of the actin and MT cytoskeletons. In wildtype oocytes, mitochondria display variable morphologies, including punctate and tubular structures, or filamentous networks as seen in Figure 3.4. In the absence of the actin mesh, mitochondria form distinct aggregates across the cytoplasm, accompanied by changes in size and distribution of DIC vesicles, which appear absent from the very posterior pole ( $n = 8$ ; Figure 3.8B-B', yellow circles and white arrowheads, respectively). MT depolymerization leads to perinuclear clustering of mitochondria and the formation of filamentous networks near the cortex and posterior tip while DIC vesicles in the same conditions are largely absent perinuclearly ( $n = 4$ ; Figure 3.8C-C', yellow and white arrowheads, respectively). In the absence of both cytoskeletal networks, mitochondria exhibit a largely branched morphology, clustered near the nucleus and cortex, while DIC vesicles in the same oocyte are sparser in the bulk of the cytosol, aggregating along the cortex ( $n = 2$ ; Figure 3.8D-D', yellow and white arrowheads, respectively). Unfortunately, analysing DIC distribution proved to be difficult due to image parameters but in examining the distribution of mitochondria in oocytes with compromised cytoskeletal networks, the central distribution in control oocytes was 8% lower compared to conditions lacking actin ( $p = 0.756$ ). Conversely, when compared to conditions lacking microtubules, the central distribution was 14% higher in control oocytes ( $p = 0.566$ ). Notably, control oocytes exhibited a 32% higher central distribution of mitochondria compared to conditions lacking both actin and microtubules ( $p = 0.135$ ). Regarding peripheral distribution, control oocytes showed a 2% lower intensity compared to conditions lacking actin ( $p = 0.883$ ), and a 12-15% higher intensity compared to conditions lacking microtubules and both cytoskeletal components ( $p = 0.116, 0.426$ ; Table 3.7). Although not reaching statistical significance, these observed differences suggest complex interactions between mitochondrial distribution and the cytoskeleton, warranting further investigation.



### Mito.YFP



**Figure 3.8. Absence of MT and actin cytoskeletons affect morphology and distribution of mitochondria and DIC vesicles.** (A) YFP-tagged mitochondria in control oocyte. In this condition, mitochondria morphology is varied displaying both filamentous and punctate organelles (anterior – A, posterior – P). (A') DIC vesicles in the same control oocyte. (B) YFP-tagged mitochondria in the absence of the actin mesh. The lack of the mesh results in distribution of organelles in distinct clusters across the cytoplasm (yellow circles). (B') DIC vesicles in the same oocyte as B. DIC vesicle size and distribution differs when compared to controls, particularly absent near the posterior cortex (white arrowheads). (C) YFP-tagged mitochondria in the absence of the MT cytoskeleton, indicated by the displaced nucleus (n). In this condition, mitochondria display perinuclear clustering and longer filaments near the cortex and towards the posterior tip of the oocyte (yellow arrowheads). (C') DIC vesicles in the same oocyte as C. The distribution of DIC vesicles is more dramatically affected than in no actin conditions failing to accumulate in several regions of the oocyte particularly near the nucleus (yellow arrows) and clustering in a thin line around the cortex (white arrowheads). Individual vesicles are visible but are decreased in size when compared to control DIC vesicles. (D) YFP-tagged mitochondria in the absence of both actin and MT cytoskeletons. In this condition, mitochondria display branched morphology (yellow arrowheads) and cluster in aggregates near the nucleus and cortex (white arrowheads). (D') DIC vesicles in the same oocyte as D. Vesicles are even more sparse in the absence of both cytoskeletons compared to B' and C' (yellow arrowheads) but display highest concentration near the cortex (white arrowheads). Scale bar represents 30µm.

**Table 3.8. Mean and standard deviation of cortical fluorescent intensities of mitochondria in control oocytes and oocytes in conditions with compromised cytoskeletal networks**

	Central intensity	Peripheral intensity	Genotype	<i>n</i>
Control				
	<b>Mean</b> 114.6	89.55	<i>spire</i> <sup>+</sup> ; YFP:: <i>Mito</i>	3
	<b>SD</b> 36.99	23.02		
No actin				
	<b>Mean</b> 124.4	76.62	<i>spire</i> /Df(2L)Exel6046; YFP:: <i>Mito</i>	3
	<b>SD</b> 35.75	41.5		
No MT				
	<b>Mean</b> 99.36	83.93	<i>spire</i> <sup>+</sup> ; YFP:: <i>Mito</i> + colchicine	3
	<b>SD</b> 20.28	24.76		
No actin, no MT				4
	<b>Mean</b> 82.60	86.56	<i>spire</i> /Df(2L)Exel6046; YFP:: <i>Rab7</i> + colchicine	
	<b>SD</b> 2.09	7.79		

Values for intensity measured in arbitrary units (AU) using Python script found in Section 2 of Appendix.

The presented data suggests a crucial interplay between the MT and actin networks and the distribution and morphology of organelles within the *Drosophila* oocyte. Further analysis on the perinuclear distribution changes in these conditions would be an interesting avenue, one highlighted by initial observations of perinuclear clustering of mitochondria. Further analysis was hindered by limitations in sample size ( $n = 1$  per condition) and inadequate image resolution but future investigations would benefit from a method involving radial profiling and more precise masking of the perinuclear area. Nevertheless, these findings collectively suggest that the integrity and functionality of cytoskeletal elements play a critical role in determining the spatial organization and structural characteristics of organelles within the oocyte. These pronounced effects underscore the intricate relationship between cytoskeletal integrity and organelle organization in the *Drosophila* oocyte, setting the stage for a detailed analysis of how both the structural integrity and function of cytoskeletons influence the dynamic motility of the organelles.



### 3.9 Absence of microtubules and actin mesh impedes advective and diffusive motion of late endosomes, DIC vesicles and mitochondria.

**Table 3.9. DDM analysis of velocity, representing advective motion, and diffusivity of late (Rab7-positive) endosomes and mitochondria in conditions with compromised cytoskeletal networks.**

LE	$v_{org} \text{ nm s}^{-1}$	$v_{DIC} \text{ nm s}^{-1}$	$D_{org} \mu\text{m}^2\text{s}^{-1}\times 10^{-3}$	$D_{DIC} \mu\text{m}^2\text{s}^{-1}\times 10^{-3}$	Genotype	n
Wildtype	1.84 ± 2.94	2.73 ± 2.58	3.32 ± 2.92	0.98 ± 0.49	YFP:: <i>Rab7</i>	9
Control	5.53 ± 4.15	6.39 ± 2.94	2.44 ± 0.93	1.79 ± 0.95	<i>spire</i> <sup>+/+</sup> ; YFP:: <i>Rab7</i>	5
No actin	29.93 ± 18.45	27.62 ± 16.20	0.29 ± 0.30	0.44 ± 0.46	<i>spire</i> /Df(2L)Exel6 046; YFP:: <i>Rab7</i>	10
No MT	1.88 ± 1.09	3.48 ± 1.69	1.89 ± 0.58	1.91 ± 0.72	<i>spire</i> <sup>+/+</sup> ; YFP:: <i>Rab7</i> + colchicine	4
No actin, No MT	6.55 ± 13.11	2.53 ± 2.50	3.40 ± 6.80	2.45 ± 2.78	<i>spire</i> /Df(2L)Exel6 046; YFP:: <i>Rab7</i> + colchicine	7
Mito	$v_{org} \text{ nm s}^{-1}$	$v_{DIC} \text{ nm s}^{-1}$	$D_{org} \mu\text{m}^2\text{s}^{-1}\times 10^{-3}$	$D_{DIC} \mu\text{m}^2\text{s}^{-1}\times 10^{-3}$	Genotype	n
Wildtype	7.22 ± 3.31	8.23 ± 3.32	1.48 ± 0.61	0.74 ± 0.38	YFP:: <i>Mito</i>	9
Control	9.36 ± 4.94	8.84 ± 3.82	1.12 ± 0.58	0.44 ± 0.68	<i>spire</i> <sup>+/+</sup> ; YFP:: <i>Mito</i>	7
No actin	37.96 ± 14.60	32.46 ± 10.10	0.35 ± 0.63	1.17 ± 0.71	<i>spire</i> /Df(2L)Exel 6046; YFP:: <i>Mito</i>	8
No MT	1.40 ± 1.64	0.92 ± 1.39	1.79 ± 0.82	1.31 ± 1.20	<i>spire</i> <sup>+/+</sup> ; YFP:: <i>Mito</i> + colchicine	4
No actin, No MT	0.04 ± 0.03	0.96 ± 0.88	0.57 ± 0.04	0.44 ± 0.14	<i>spire</i> /Df(2L)Exel 6046; YFP:: <i>Mito</i> + colchicine	2

Values for advective and diffusive motions ± standard deviation (SD) obtained using Con-DDM analysis in different genotypes (velocity –  $v$ , diffusion coefficient –  $D$ , organelle – <sub>org</sub>, DIC vesicles – <sub>DIC</sub>).

To elucidate the influence of the actin and microtubule cytoskeletons on organelle dynamics, motion data of late endosomes, mitochondria, and DIC vesicles was gathered under the depolymerised cytoskeleton conditions. To investigate cytoplasmic content motion in the absence of the actin mesh, a *spire* mutant was used. To depolymerise

microtubules, flies were subjected to an overnight treatment with colchicine, a microtubule-depolymerizing drug, and oocytes with a displaced nucleus, a readout for microtubule depolymerization, were imaged. For the condition lacking both actin and microtubules, *spire* mutant flies were fed colchicine in the same manner. The results are summarised in Table 3.5.

In comparison to the control group, the absence of the actin cytoskeleton significantly increases advection and decreases diffusion of Rab7 vesicles and mitochondria (Table 2.2; [Timelapse 16](#); [Timelapse 17](#)). The absence of the microtubule cytoskeleton leads to statistically significant decreases in advection for mitochondria. For Rab7 vesicles, the rate of advection decreases slightly and there were no significant changes in the rate of diffusion for either organelle ([Timelapse 18](#); [Timelapse 19](#)). The absence of both actin and microtubule cytoskeletons results in minimal advection and diffusion for mitochondria compared to control ([Timelapse 20](#)). It is challenging to definitively attribute this reduction in detectable motion observed in the absence of both cytoskeletons to the effects of cytoskeletal perturbation due to challenge associated with obtaining high-resolution timelapse images for accurate analysis. Additionally, the low sample size for this condition ( $n = 2$ ) further warrants for future investigations with larger sample sizes and refined imaging techniques. Under the same conditions, Rab7 vesicles demonstrated an increase in both advection and diffusion in the absence of both cytoskeletons compared to the control. The elevated Rab7 motion detected in oocytes lacking both actin and microtubule cytoskeletons is most likely attributed to the excessive noise present in the time-lapse imaging sequences ([Timelapse 20](#)). Despite DDM being designed to amplify the signal-to-noise ratio, certain noise components persisted in the denoised images. Thus, the heightened noise levels could contribute to the observed higher values of advection and diffusion in the mutant group, potentially confounding the interpretation of motion changes. Additionally, the movement of DIC vesicles mirrored the patterns observed for both mitochondria and Rab7 vesicles across all experimental conditions, exhibiting no significant differences except for the increased diffusion of DIC vesicles in YFP::*Mito* oocytes lacking actin.

## Chapter 4: Discussion

4.1 Dynamic variations in distribution, advection and diffusion rates among organelle populations in *Drosophila* oocytes and implications of fluorescent tagging on Rab7.

The comparison of Con-DDM motion data for early endosomes, late endosomes and mitochondria analysis highlights variations in advection and diffusion rates among the three organelle populations (Table 3.1). The data reveals that Rab5 vesicles representing EEs exhibit the highest and most consistent advective motion, while Rab7 vesicles predominantly representing LEs show a lower and more variable advection rate across oocytes. LEs demonstrate the highest diffusion rates with considerable heterogeneity while EEs show lower and more uniform diffusion rates in comparison. Additionally, Rab5 vesicles, which showed a concentrated distribution near the cortex where actin accumulates, while Rab7 vesicles display a more widespread distribution throughout the cytoplasm most likely interacting more with MTs, in line with their function in the endocytic pathway.

By studying these distribution patterns and their correlation with cytoskeletal elements, we can gain insights into how Rab5 and Rab7 vesicles utilize different cytoskeletal networks for force generation, movement, and spatial organization within the cell. This understanding is crucial for unravelling the mechanisms underlying organelle dynamics and their contributions to cellular function and organisation. Mitochondria display a substantial advection rate with greater variability than EEs and lower diffusion rates than LEs. Mitochondria are large organelles that need to move at rapid rates over longer distances in the cell in response to physiological and environmental signals and require other proteins for anchoring and docking resulting in slower accumulation, mixing and temporal response of organelles. This makes diffusion an inefficient mode of transport. Thus, advective forces and motor-driven transport are the predominant and more efficient type of motion for the rapid localisation of mitochondria to distal sites in large cells.

Additionally, most Rab7 vesicles in this study were characterised by a significantly larger size compared to Rab5 vesicles, showcasing a two-fold increase in diameter (Figure 3.3;  $0.923 \pm 0.42 \mu\text{m}$  vs.  $0.482 \pm 0.12 \mu\text{m}$ ). This size difference is consistent with the general trend observed in LEs, which tend to be larger than early endosomes due to the high number of ILVs, exceeding 30 compared to 1-8 in EEs (Huotari & Helenius, 2011). Under the hypothesis that size affects the speed and type of motion undergone by an organelle and considering the parameters that influence the motion of an object in a crowded environment like the oocyte cytoplasm, it is expected that the larger the vesicle, the more susceptible it will be to hindrance from cytoskeletal structures leading to lower rates of diffusion, and thus the more reliant it will be on large-scale cytoplasmic flows and cargo transport. These results therefore are contrary to the initially hypothesised relationship between organelle size and motion characteristics.

Comparing YFP::*Rab7* oocytes to other control groups presents differences in motion behaviour and morphology of DIC vesicles. DIC vesicles in GFP::*UTRN*, *w-* and YFP::*Mito* oocytes demonstrate similar morphology and size, averaging at  $0.23\mu\text{m}$ ,  $0.19\mu\text{m}$ ,  $0.30\mu\text{m}$  respectively ( $n = 12$ ) while the average diameter of DIC vesicles in YFP::*Rab7* oocytes is  $0.51\mu\text{m}$  ( $n = 16$ ) (Figure 4.1; yellow arrowheads). The motion behaviour of DIC vesicles in these groups, particularly advection, is summarised in Table 4.1. The dramatic reduction in velocity suggests that the fluorescent tagging of Rab7 may be adversely affecting the motility of Rab7-positive vesicles and interacting organelles.

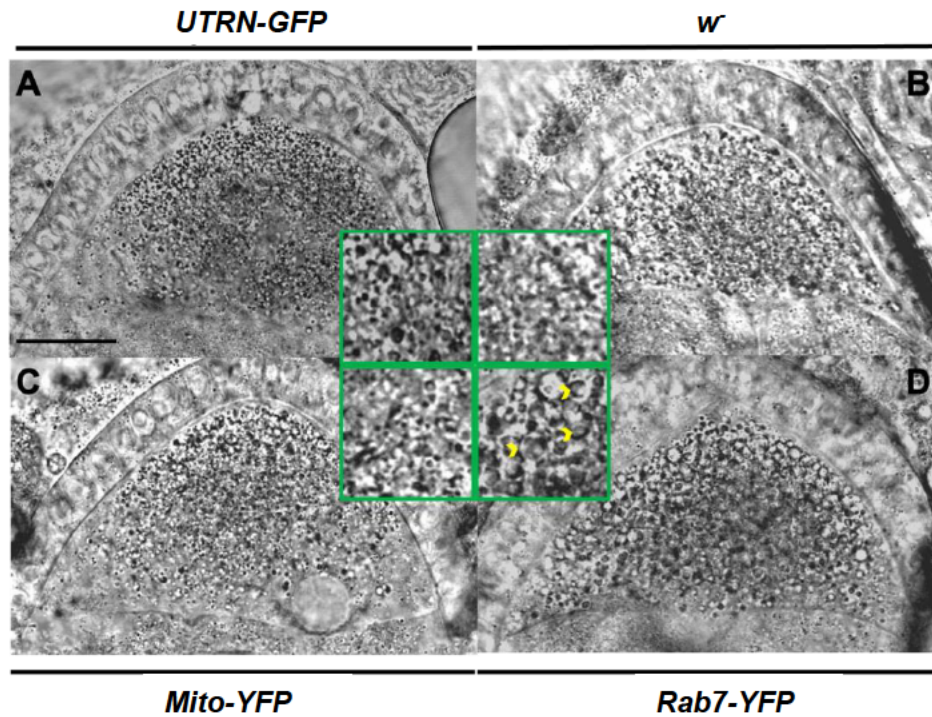


Figure 4.1 DIC vesicles in *Rab7-YFP* oocytes differ in morphology when compared to *w*-, *Mito-YFP* and *GFP::UTRN* backgrounds. (A-C) DIC image of vesicles in *GFP::UTRN*, *w* and *YFP::Mito* oocytes. Vesicles here display more homogenous morphology and size averaging at  $0.23\mu\text{m}$ ,  $0.19\mu\text{m}$ ,  $0.30\mu\text{m}$  respectively ( $n=12$ ). (D) DIC image of vesicles in *YFP::Rab7* oocytes average at  $0.51\mu\text{m}$  in diameter ( $n=16$ ). Scale bar represents  $30\mu\text{m}$ .

The presence of a fluorescent tag on Rab7 could introduce various factors influencing interactions with cellular components, potentially leading to morphological changes in DIC vesicles and alterations in motion behaviour. These factors may include changes in the molecular size and structure of Rab7 due to the tag, steric hindrance affecting its normal conformation and interactions, tag-induced aggregation, and altered expression levels. Unfortunately, constraints in imaging equipment prevented confirmation of the tag's impact by imaging DIC vesicles in *YFP::Rab5* oocytes during this study. Further investigation is crucial, considering minute differences between sensitivity, function, and localization of the two Rabs are likely to influence observed effects.

Alternatively, the process of introducing a fluorescent tag to Rab7 may result in quantitative differences in expression levels. Overexpression could overwhelm normal regulatory mechanisms governing vesicle formation, transport, and fusion, triggering

stress pathways or altered signalling cascades that influence vesicle morphology and overall cellular homeostasis. Techniques such as Western blotting can provide insights into the relative abundance of the tagged protein. Additionally, tagging and imaging Rab7 with a different fluorescent protein would help differentiate effects caused by Rab7 itself and those induced by the specific tag. Localization studies and functional assays, supplemented by 3D imaging or super-resolution microscopy, would offer more detailed information about vesicle morphology. Further investigation into these aspects is essential to clarify the confounding results regarding size and motility observed in this study and reconcile the large discrepancies in different genotypes (Table 4.1). An added layer of complexity is the fact that Rab5 and Rab7 are also markers of early and late phagosomes, respectively (Sturgill-Koszyck et al. 1996; Vieira et al. 2003; Harrison et al. 2003). In order to more accurately describe and compare the motion behaviour of EEs and LEs in the *Drosophila* oocyte, clearer differentiation between the two populations is needed. A potential avenue is the use of dual or triple image cross correlation spectroscopy which would allow for visualisation of multiple markers on the same endosome to confirm its nature (Semrau et al. 2011; Shearer & Peterson 2019).

**Table 4.1. DDM analysis of velocity, representing advective motion, and diffusivity of DIC vesicles in control oocyte groups.**

	$v_{DIC} \text{ nm s}^{-1}$	$D_{DIC} \times 10^{-3} \mu\text{m}^2 \text{ s}^{-1}$	Genotype	<i>n</i>
Rab7	2.73 ± 2.58	0.98 ± 0.49	YFP:: <i>Rab7</i>	9
Mito	8.23 ± 3.32	0.74 ± 0.38	YFP:: <i>Mito</i>	9
Control	7.00 ± 0.80	1.06 ± 0.29	GFP:: <i>UTRN</i>	9
Control	5.66 ± 5.31	0.27 ± 0.22	w-	9

Values for advective and diffusive motions ± standard deviation (SD) obtained using Con-DDM analysis in different genotypes (velocity – *v*, diffusion coefficient – *D*, DIC vesicles – *DIC*).

Using intensity-based analysis for organelle distribution provides a robust starting point, but it's not without drawbacks, largely due to human error and limitations in spatial resolution. Radial distribution analysis offers more detailed spatial information but requires higher and more consistent image quality to be effective. Higher resolution,

consistent image acquisition combined with machine learning algorithms for automated segmentation and quantification techniques like radial profiling would enhance the analysis. CellProfiler and Ilastik are two powerful tools that can significantly improve this process. Despite these issues, this method effectively identifies gross changes in distribution patterns, particularly when dealing with low-resolution images and datasets with varying parameters. It also allows for easier normalization between different images.

#### 4.2 Impact of ageing and disrupting the fusion-fission equilibrium on mitochondrial motion and organelle distribution.

In aged oocytes, the mitochondrial network adopted a hyperfused appearance. The enlargement of mitochondria has also been observed in aged *Drosophila* and mouse muscle cells where longitudinal sections of aged mouse skeletal muscles using TEM shows a dramatic increase in average area, perimeter and Feret's diameter of mitochondria (Leduc-Gaudet et al. 2015; Chalmers et al. 2016; Chen et al. 2020). In rat cerebral resistance arteries, fewer mitochondria in aged myocytes are observed to undergo any type of motion compared to mitochondria in young myocytes, which exhibit both directed and diffusive motility (Chalmers et al. 2016). Thus, the hyperfused phenotype and motion data in the aged conditions of this study suggest that the decrease in motility is partially due to increase in size of the network and likely its susceptibility to steric hindrance. This is likely due to a change in the balance of fusion and fission, a characteristic identified in aged rat myocytes where the elevation in the Mfn2 to Drp1 ratio suggests an increase in fusion and/or a decrease in fission (Leduc-Gaudet et al. 2015). Additionally, the substantial decrease in motion behaviour of DIC vesicles during the 1 to 40 day ageing period is in line with the changes in mitochondrial motion behaviour. This similarity is also noted in the significant decrease in DIC vesicle diffusion rates in fusion and fission mutants compared to controls. These results are in line with the research discussed in Section 1.5, where alterations in mitochondrial activity in mouse T-lymphocytes result in impaired endolysosomal dynamics and morphology (Baixauli et al. 2015; Demers-Lamarche et al. 2016). Additionally, hyperfused network can have the same impact on motility as an overexpressed

cytoskeletal network by increasing tortuosity and steric hindrance. Combined with the observed changes in distribution between anterior and posterior regions of the oocyte as the oocytes ages, this data underscores the intricate relationship between mitochondrial dynamics and functional adaptability in the oocyte and its impact on endosomal motility.

An intriguing avenue for further exploration is to investigate the influence of ageing on the oocyte cytoskeleton. Previous studies have documented gradual changes in the expression levels of cytoskeletal filaments in ageing cells. For example, an increase in F-actin has been observed in ageing *Drosophila* brains and dermal fibroblasts. Notably, reducing F-actin levels in ageing *Drosophila* neurons has been shown to decelerate brain ageing and enhance health span in an autophagy-dependent manner (Schmid et al. 2023). Additionally, studies have reported the overexpression of MTs in ageing sensory axons in human skin (Schulze et al. 2012; Metzner et al. 2022). Investigations on human cells have indicated that the cytoskeleton undergoes age-dependent stiffening in human epithelial cells, fibroblasts, and cardiomyocytes, contributing to the mechanical rigidity of cells (Lieber et al. 2004; Berdyevva et al. 2005; Dulińska-Molak et al. 2014). Consequently, the distinctive alterations in the mechanical characteristics of aging cells likely lead to deficiencies in mechanosensation and mechanotransduction. Parameters such as density, polarity, and filament length of the cytoskeleton, as highlighted in Section 1.6, contribute to cellular dynamics and motility (Mizuno et al. 2007; Ando et al. 2015; Agrawal et al. 2022). Given the significant changes in the motion behaviour of organelles observed in conditions with altered cytoskeletal networks in this study, both the spatial architecture and functionality of the cytoskeleton are relevant to the motion of cytoplasmic components.

The opposing processes of mitochondrial fusion and fission are continuous and must remain in balance to maintain a healthy and homogenous population of organelles for cellular function and survival. In this study, interruption of fusion and upregulation of fission lead to a more fragmented network, while a fission loss-of-function mutation resulted in the formation of globular organelle structures in the cytoplasm (Figure 3.6).



In instances of downregulated fusion and upregulated fission, both advective and diffusive motion of mitochondria significantly decrease though based on the relationship between size and motion behaviour as well as previous research discussed in Section 1.5 demonstrating an increase of Brownian-like motion in fusion mutant MEFs and U2OS cells, diffusive motion of mitochondria would be expected to increase (Table 3.4; Chen et al. 2003; Ishihara et al. 2009; Chen & Chan 2009). Combined with the changes in distribution, these results suggest that the disruption of the fusion and fission events is the dominant influence on the mobility of mitochondria likely through alterations in interactions with fusion-fission associated proteins and organelles.

In addition to fission, Drp1 plays a role in mitophagy and apoptosis (Kageyama et al. 2014; Tong et al. 2020). Thus, the clearance of unhealthy organelles may be disrupted in *Drp1* mutants, resulting in the accumulation of abnormal mitochondria. Additionally, based on the literature discussed in Section 1.5, the lack of Drp1 in the oocytes may impact ER-mitochondrial interactions which aids in maintain the balance of fusion-fission. In the context of hereditary spastic paraplegia (HSP) subtype SPG61, characterized by mutations in the ER-shaping protein Arl6IP1, knockdown of *Arl6IP1* leads to decreased Drp1 levels leading to impaired ER-mitochondrial contacts and compromised mitochondrial load in the distal ends of long motor neurons. Restoring mitochondrial fission through the overexpression of wild-type *Drp1* enhances ER-mitochondrial contacts, re-establishing mitochondrial load within axons, and partially mitigating locomotor defects (Fowler et al. 2020). Marf is also required for the transport of mitochondria on MTs through the binding of the adaptor proteins Miro and Milton as is observed in axons of cultured dorsal root ganglion neurons and cerebellar dendrites of Purkinje cells (Chen et al. 2007; Misko et al. 2010; Sandoval et al. 2014). A loss of mitochondrial membrane potential in *Mfn1/2* mutant mouse embryos provides further insight into the factors that affect mitochondria motion behaviour and understanding the factor influencing motion characteristics (Chen et al. 2003; Filadi et al. 2018). Although both *Drp1* and *Marf* loss impair mitochondrial trafficking, a detailed comparison of the phenotypes linked to the loss of *Drosophila* Drp1 or Marf would be valuable, as their suggested mechanisms for impairing transport appear to be distinct.

### 4.3 Exploring the role of kinesin in mitochondrial and endosomal dynamic and implications for cellular organization and function of the *Drosophila* oocyte.

MT motor proteins are crucial in mitochondrial dynamic processes of fusion and fission and binding of mitochondria with LEs and lysosomes. Motor-driven transport is necessary for bringing organelles from different regions into proximity, in turn regulating the spatial organisation of metabolic processes in the cell. In this study, the mean particle velocity of LEs moving in a ballistic and directed manner was  $416 \pm 149 \text{ nm s}^{-1}$  while mitochondria moved in this manner at a speed of  $216 \pm 99 \text{ nm s}^{-1}$  compared to the known average speed of  $340 \pm 8 \text{ nm s}^{-1}$  for kinesin in the oocyte (Loiseau et al. 2010). To understand the details of the dynamic relationship between Rab7 and kinesin, employing co-immunoprecipitation (Co-IP) assays will allow for the examination of the direct association between these proteins as well as co-localisation studies with Rab7 motor protein-binding complexes, RILP and FHF. Similarly, the use of Proximity Ligation Assays (PLA) would help visualize the spatial proximity of kinesin and Rab7 at the single-molecule level within the cellular context of the oocyte. Distribution of Rab7 vesicles in *KhcRNAi* oocytes was severely altered with a distinct accumulation along the cortex and near the posterior end. Assessing motion behaviour of Rab7 in a more reliable kinesin mutant supplemented by functional assays for endosomal trafficking would offer a more comprehensive picture of the role of kinesin in Rab7 vesicle motility, structure and function.

Kinesin-driven transport significantly influences mitochondrial dynamics, regulating the turnover of damaged organelles and their transport to metabolically demanding regions (Wang & Schwarz 2009; Vagnoni & Bullock 2018; Kruppa et al. 2021). The limited number and reduced velocity of mitochondria exhibiting ballistic motion observed by 2D imaging may be attributed to frequent pauses and redirection, taking them out of the field of view. Although unable to directly observe the impact of kinesin RNAi on mitochondrial motion, future investigations hold promise due to the close association between mitochondrial dynamics and motor-driven transport. Notably, the reduction in

membrane potential, often seen in aged cells, triggers the dissociation of kinesin from microtubules through the PINK1/Parkin pathway, leading to Miro adaptor degradation (Shneyer et al. 2017; López-Doménech et al. 2018). Understanding the reliance of mitochondrial motor-driven transport on Milton adaptors and motors in oocytes by measuring Dhc and Khc levels in Milton/Miro mutants, can clarify the impact of motor protein alterations on mitochondrial motion. Additionally, investigating differences in membrane potential loss due to Mfn1/2 mutations, as observed in mouse embryos, and age-related changes using techniques like Flicker-assisted Localization Microscopy (FaLM) in conjunction with DDM analysis, could provide insights into shared molecular mechanisms contributing to cellular decline through mitochondrial dysfunction in both aged and fusion-fission mutant backgrounds. This comparative approach can help enhance our understanding of the complex interplay between genetic factors, ageing, and mitochondrial function.

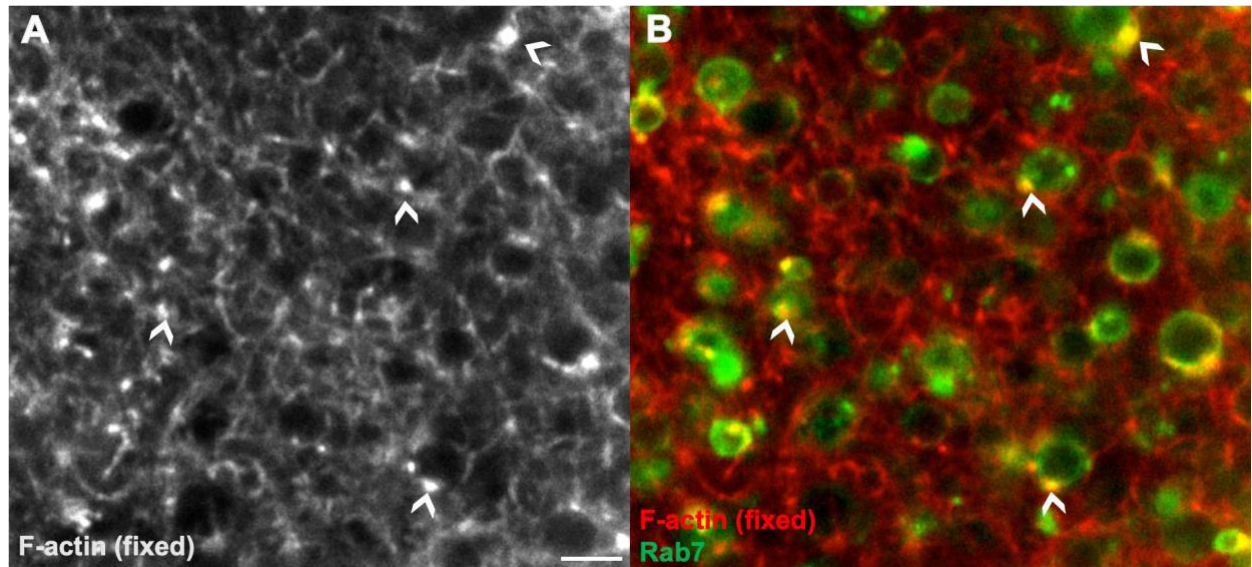
#### 4.4 The role of microtubule-driven motion and actin-mediated forces in *Drosophila* oocyte organelle dynamics.

This study identifies two primary driving forces governing organelle movement in the oocyte: ballistic and persistent motion driven by MT-generated cytoplasmic flows and active diffusion regulated by both MTs and actin. The motion patterns of DIC vesicles align with those of mitochondria and LEs under wildtype and cytoskeleton-depleted conditions (Table 3.5). This shared motion behaviour, along with the effects of cytoskeletal alterations on LEs, DIC vesicles, and mitochondria, reinforces an interplay between endosomes and mitochondria reliant on cytoskeletal integrity and mutual interactions. Notably, Rab7, a key player in mitochondria-lysosome contact, has been linked to mitochondrial morphology and dynamics through interactions with Drp1 (Wong et al. 2018; Gu et al. 2022). These findings highlight that mitochondrial morphology and motility is influenced by dynamic machinery, motor proteins, and the endosomal pathway. Further investigation by reducing Rab7 using a dominant-negative mutation and observing its effects on mitochondrial dynamics and motion would help illuminate the relationship between the two populations.

Actin networks exhibit both viscous and elastic characteristics, where at low concentrations of actin filaments in buffer the solution behaves as a viscous liquid while at high levels of actin filaments, the resulting network behaves as an elastic solid. This is regulated by myosin motor activity creating tension in the network and uncoordinated contractile pulses that lead to random walks of tracer particles (Brangwynne et al. 2009). The organisation and activity of the actin mesh is not only necessary for direct interactions with other organelles but the generation of forces for global cell function. On a larger scale, actin force fluctuations are necessary for cell division and migration. When actin-based cytoskeletal forces are disrupted by the depolymerisation of the network or removal of myosin activity, the active fluctuating forces in the cell are reduced (Guo et al. 2014). This can negatively impact cell health as large-scale diffusive transport of cytoplasmic components is interrupted, the function of which is dependent on their ability to move through the cytoplasm and establish gradients for signalling. Furthermore, the activity of myosin has been shown to regulate microtubule diffusivity, impacting on transport of bound cargoes (Gittes et al. 1993; Brangwynne et al. 2008; Brangwynne et al. 2009).

The actin mesh plays a central role in shaping the cytoplasmic environment, creating a network of obstacles that alters the tortuosity and length-scale of vesicles navigating the oocyte. The increased large-scale advective movement in its absence results in the clustering of Rab7-positive vesicles at distal oocyte ends, mirroring cytoplasmic dynamics observed during late oogenesis, suggesting actin's regulatory role in MT force generation. During meiosis in the mouse oocyte, Rab7 interacts with actin-nucleating factors, including Arp2/3 and WASP, playing a crucial role in actin and mitochondrial dynamics, impacting spindle migration and mitochondrial segregation (Gautreau et al. 2014; Pan et al. 2020). The reciprocal relationship between endosomes and actin extends to Arp2/3-mediated actin nucleation from the endosomal membrane via the WASH complex (Duleh & Welch 2010; Tyrell et al. 2016; Fokin & Gautreau 2021). While contact sites between Rab7 vesicles and the actin mesh were observed in *st9 Drosophila* oocytes in a supplementary experiment to this study, further exploration is

necessary to confirm the presence of actin nucleators, such as Spire and Arp2/3, at the endosomal membrane (Figure 4.2).



**Figure 4.2 Contact sites of F-actin and Rab7 vesicles (Image courtesy of Maik Drechsler) 4(A)** Actin mesh in white stained with phalloidin **(B)** Actin mesh in red stained with phalloidin, Rab7-positive vesicles in green. Sites of colocalisation are associated with filaments from the mesh suggesting potential actin nucleation from the vesicular membrane (white arrowheads). Scale bar represents 10 $\mu$ m.

In the absence of actin, both LEs and mitochondria experience increased advection and decreased diffusion (Table 3.5). Microtubule depletion reduces advection for LEs, DIC vesicles, and mitochondria without significantly affecting diffusion rates. Specifically, the lack of microtubules leads to substantial cloudy aggregates for LEs and DIC vesicles, while combined microtubule and actin absence results in merged LE clusters and smaller, anteriorly clustered DIC vesicles (Figure 3.7). Simultaneously, mitochondria aggregate without actin and cluster perinuclearly upon microtubule depolymerization (Figure 3.8). Complete cytoskeletal absence results in branched mitochondria near the nucleus and cortex. The findings underscore the pivotal role of cytoskeletal elements in organelle dynamics, determining spatial organization, and influencing structural characteristics.

To deepen the understanding of the intricate interplay between cytoplasmic F-actin and mitochondria in oocytes, an exploration into the colocalization of these organelles in wildtype and mutant backgrounds can offer valuable information on the relationship between the two structures. Clustering of mitochondria in the absence of the actin mesh could very likely be due to the relationship between actin and Drp1. Previous studies found reduced Drp1 levels and function, and elongation of mitochondria when levels of ABPs, Arp2/3 and Myosin II are decreased (Ji et al. 2015; Li et al. 2015; Hatch et al. 2016; Illescas et al. 2021). Measuring Drp1 levels in oocytes lacking the actin mesh would help uncover whether the observed phenotype is due to interrupted fission due to diminished Drp1. Additionally, the tagging of ABPs during the dynamic motion of these organelles presents a compelling avenue for investigation. In yeast, ER-mediated fission initiates F-actin polymerisation through the binding of ER-anchored INF2 and mitochondria membrane-anchored Spire1C assisting in outer membrane constriction and recruitment of Drp1 by myosin II (Korobova et al. 2013; Manor et al. 2015; Chakrabarti et al. 2017). In *Drosophila* embryonic epidermis, wound healing is impeded by mutations in *Drp1* through a reduction in F-actin levels (Cooper et al. 1988; García-Bartolomé et al. 2020; Ponte et al. 2020). Disruptions in F-actin not only affect mitochondrial morphology through fission but also trigger a stress response, impacting oxidative phosphorylation regulators (Cooper et al. 1988; García-Bartolomé et al. 2020). Actin polymerisation on the outer membrane also triggers a spike in mitochondrial  $Ca^{2+}$  enhancing OXPHOS with actin and ABPs involved in OXPHOS also implicated in mitochondrial disorders such as OXPHOS system deficiency and Alzheimer's (Antequera et al. 2009; Marín-Buera et al. 2015; García-Bartolomé et al. 2017; Chakrabarti et al. 2017). Exploring this relationship further will shed light on how alterations in mitochondrial dynamics, specifically through the disruption of fusion and fission events, influence the intricate dance between cytoplasmic F-actin and organelle motion.

## Chapter 5: Conclusion

In conclusion, this study offers an examination of organelle dynamics within the intricate cellular landscape of the *Drosophila* oocyte. The findings presented in this study contribute to unravelling the intricate interplay of various factors that influence the motion behaviour and morphology of organelles. The identification of size-related patterns challenges preconceived notions and opens avenues for further exploration into the complex relationship between factors at play in organelle motion behaviour. Moreover, the study sheds light on the impact of microtubules and actin on organelle dynamics. The interconnected roles of these structural components in shaping organelle distribution and morphology underscore the pivotal role of the cytoskeleton in cellular processes. The role of Rab7 in mitochondrial dynamics and its implications for mitochondrial morphology further emphasize the intricate relationships that dictate cellular functionality.

Investigation into these interactions hold significant implications for disease research, particularly in the understanding and potential treatment of mitochondrial disorders and neurodegenerative diseases. Mitochondrial disorders often manifest with aberrations in mitochondrial size and morphology. The observed alterations in mitochondrial dynamics and morphology in this study, particularly the hyperfused phenotype in aged oocytes, are similar to features observed in neuropathy such as CMT2A (Ueda & Isihara 2018; Chen et al. 2023). Moreover, the relationship between Rab7 and mitochondrial dynamics adds a layer of relevance to neurodegenerative diseases where disturbances in endosomal-lysosomal pathways have been implicated such as CMT2B (Schiavon et al. 2021; Gu et al. 2022; Wong et al. 2023). Furthermore, the impact of cytoskeletal elements on organelle behaviour has broader implications for diseases involving cytoskeletal abnormalities, particularly MTs, such as Alzheimer's, amyotrophic lateral sclerosis and various tauopathies (Williamson & Cleveland 1999; Heutink 2000; Varidaki et al. 2018; Congdon & Sigurdsson 2018). Actin and associated proteins involved in oxidative phosphorylation (OXPHOS), as highlighted in this study, have been implicated in mitochondrial disorders. Understanding these molecular interactions

could potentially unveil new therapeutic targets for diseases marked by disrupted organelle dynamics. The identified molecular interactions, alterations in organelle dynamics, and their implications for cellular health provide a foundation for future studies aimed at unravelling the intricate mechanisms underlying organelle motion and the relevance to various diseases.



## References

- Agrawal A, Scott ZC, Koslover EF. (2022) Morphology and Transport in Eukaryotic Cells. *Annu Rev Biophys.* **51**(9) pp.247-266. doi: 10.1146/annurev-biophys-111121-103956.
- Ahmed WW, Fodor É, Almonacid M, Bussonnier M, Verlhac MH, Gov N, Visco P, van Wijland F, Betz T (2018) Active Mechanics Reveal Molecular-Scale Force Kinetics in Living Oocytes. *Biophys J.* **114**(7) pp. 1667-79. doi: 10.1016/j.bpj.2018.02.009.
- Alberti S. (2015) Don't Go with the Cytoplasmic Flow. *Dev Cell.* **34**(4) pp. 381-2. doi: 10.1016/j.devcel.2015.08.004.
- Alberts B, Johnson A, Lewis J, Raff M, Roberts K, and Walter P. (2002) Transport from the Trans Golgi Network to the Cell Exterior: Exocytosis. *Molecular Biology of the Cell.* **4**.
- Alim K, Andrew N, Pringle A, Brenner MP. (2017) Mechanism of signal propagation in *Physarum polycephalum*. *Proc Natl Acad Sci USA.* **114**(20) pp. 5136-5141. doi: 10.1073/pnas.1618114114.
- Alim K. (2018) Fluid flows shaping organism morphology. *Philos Trans R Soc Lond B Biol Sci.* **373**(1747) pp. 20170112. doi: 10.1098/rstb.2017.0112.
- Allan V. (2014) Cell biology. One, two, three, cytoplasmic dynein is go! *Science* **345** (6194) pp. 271–272. doi: 10.1126/science.1257245

Ally S, Larson AG, Barlan K, Rice SE, Gelfand VI. (2009) Opposite-polarity motors activate one another to trigger cargo transport in live cells. *J Cell Biol.* **187**(7) pp. 1071-82. doi: 10.1083/jcb.200908075.

Almonacid M, Ahmed WW, Bussonnier M, Mailly P, Betz T, Voituriez R, Gov NS, Verlhac MH. (2016) Active diffusion positions the nucleus in mouse oocytes. *Nat Cell Biol.* **17**(4) pp. 470-9. doi: 10.1038/ncb3131.

Anand R, Wai T, Baker MJ, Kladt N, Schauss AC, Rugarli E, Langer T. (2014) The i-AAA protease YME1L and OMA1 cleave OPA1 to balance mitochondrial fusion and fission. *J Cell Biol.* **204**(6) pp. 919-29. doi: 10.1083/jcb.201308006.

Ando D, Korabel N, Huang KC, Gopinathan A. (2015) Cytoskeletal Network Morphology Regulates Intracellular Transport Dynamics. *Biophys J.* **109**(8) pp. 1574-82. doi: 10.1016/j.bpj.2015.08.034.

Antequera D, Vargas T, Ugalde C, Spuch C, Molina JA, Ferrer I, Bermejo-Pareja F, Carro E. (2009) Cytoplasmic gelsolin increases mitochondrial activity and reduces Abeta burden in a mouse model of Alzheimer's disease. *Neurobiol Dis.* **36**(1):42-50. doi: 10.1016/j.nbd.2009.06.018.

Aniento F, Emans N, Griffiths G, Gruenberg J. (1993) Cytoplasmic dynein-dependent vesicular transport from early to late endosomes. *J Cell Biol.* **123**(6 Pt 1) pp. 1373-87. doi: 10.1083/jcb.123.6.1373.

Arduíno DM, Esteves AR, Cortes L, Silva DF, Patel B, Grazina M, Swerdlow RH, Oliveira CR, Cardoso SM. (2012) Mitochondrial metabolism in Parkinson's disease impairs quality control autophagy by hampering microtubule-dependent traffic. *Hum Mol Genet.* **21**(21) pp. 4680-702. doi: 10.1093/hmg/dds309.

Aspengren S, Hedberg D, Sköld HN, Wallin M. (2009) New insights into melanosome transport in vertebrate pigment cells. *Int Rev Cell Mol Biol.* **272** pp. 245-302. doi: 10.1016/S1937-6448(08)01606-7.

Baixauli F, Acín-Pérez R, Villarroya-Beltrí C, Mazzeo C, Nuñez-Andrade N, Gabandé-Rodríguez E, Ledesma MD, Blázquez A, Martín MA, Falcón-Pérez JM, Redondo JM, Enríquez JA, Mittelbrunn M. (2015) Mitochondrial Respiration Controls Lysosomal Function during Inflammatory T Cell Responses. *Cell Metab.* **22**(3) pp. 485-98. doi: 10.1016/j.cmet.2015.07.020.

Baker MJ, Lampe PA, Stojanovski D, Korwitz A, Anand R, Tatsuta T, Langer T. (2014) Stress-induced OMA1 activation and autocatalytic turnover regulate OPA1-dependent mitochondrial dynamics. *EMBO J.* **33**(6) pp. 578-93. doi: 10.1002/emboj.201386474.

Baloh RH, Schmidt RE, Pestronk A, Milbrandt J. (2007) Altered axonal mitochondrial transport in the pathogenesis of Charcot-Marie-Tooth disease from mitofusin 2 mutations. *J Neurosci.* **27**(2) pp. 422-30. doi: 10.1523/JNEUROSCI.4798-06.2007.

Bancaud A, Huet S, Daigle N, Mozziconacci J, Beaudouin J, Ellenberg J. (2009) Molecular crowding affects diffusion and binding of nuclear proteins in heterochromatin and reveals the fractal organization of chromatin. *EMBO J.* **28**(24) pp. 3785-98. doi: 10.1038/emboj.2009.340

Banerjee R, Kumar A, Satpati P, Nagotu S. (2021) Mimicking human Drp1 disease-causing mutations in yeast Dnm1 reveals altered mitochondrial dynamics. *Mitochondrion.* **59** pp. 283-295. doi: 10.1016/j.mito.2021.06.009.

Banks RA, Galstyan V, Lin HJ, Hirokawa S, Ierokomos A, Ross TD, Bryant Z, Thomson M, Phillips R (2021). Motor processivity and speed determine structure

and dynamics of microtubule-motor assemblies. *Biorxiv*. doi:  
10.1101/2021.10.22.465381

Baravalle G, Schober D, Huber M, Bayer N, Murphy RF, Fuchs R. (2005)  
Transferrin recycling and dextran transport to lysosomes is differentially affected by  
bafilomycin, nocodazole, and low temperature. *Cell Tissue Res*. **320**(1) pp. 99-113.  
doi: 10.1007/s00441-004-1060-x.

Bardsley A, McDonald K, Boswell RE. (1993) Distribution of tudor protein in the  
*Drosophila* embryo suggests separation of functions based on site of localization.  
*Development*. **119**(1) pp. 207-19. doi: 10.1242/dev.119.1.207.

Barkus RV, Klyachko O, Horiuchi D, Dickson BJ, Saxton WM. (2008) Identification of  
an axonal kinesin-3 motor for fast anterograde vesicle transport that facilitates  
retrograde transport of neuropeptides. *Mol Biol Cell*. **19**(1) pp. 274-83. doi:  
10.1091/mbc.E07-03-0261.

Barlan K, Gelfand VI. (2017) Microtubule-Based Transport and the Distribution,  
Tethering, and Organization of Organelles. *Cold Spring Harb Perspect Biol*. **9**(5).  
doi: 10.1101/cshperspect.a025817.

Baum B, Li W, Perrimon N. (2000) A cyclase-associated protein regulates actin and  
cell polarity during *Drosophila* oogenesis and in yeast. *Curr Biol*. **10**(16) pp. 964-73.  
doi: 10.1016/s0960-9822(00)00640-0.

Bayer N, Schober D, Prchla E, Murphy RF, Blaas D, Fuchs R. (1998) Effect of  
bafilomycin A1 and nocodazole on endocytic transport in HeLa cells: implications for  
viral uncoating and infection. *J Virol*. **72**(12) pp. 9645-55. doi:  
10.1128/JVI.72.12.9645-9655.

Bear, J. (1988) Dynamics of fluids in porous media. *Dover publications*.

- Becalska AN, Gavis ER. (2009) Lighting up mRNA localization in *Drosophila* oogenesis. *Development*. **136**(15) pp. 2493-503. doi: 10.1242/dev.032391.
- Behnia R, Munro S. (2005) Organelle identity and the signposts for membrane traffic. *Nature*. **438**(7068) pp. 597-604. doi: 10.1038/nature04397.
- Berdyeva TK, Woodworth CD, Sokolov I. (2005) Human epithelial cells increase their rigidity with ageing in vitro: direct measurements. *Phys Med Biol*. **50**(1):81-92. doi: 10.1088/0031-9155/50/1/007.
- Berrak Ugur, Kuchuan Chen, Hugo J. Bellen. (2016) *Drosophila* tools and assays for the study of human diseases. *Dis Model Mech*. **9**(3) pp. 235–244. doi: 10.1242/dmm.023762.
- Bieling P, Laan L, Schek H, Munteanu EL, Sandblad L, Dogterom M, Brunner D, Surrey T. (2007) Reconstitution of a microtubule plus-end tracking system in vitro. *Nature*. **450**(7172) pp.1100-5. doi: 10.1038/nature06386.
- Birgisdottir ÁB, Johansen T. (2020) Autophagy and endocytosis - interconnections and interdependencies. *J Cell Sci*. **133**(10):jcs228114. doi: 10.1242/jcs.228114.
- Bleazard W, McCaffery JM, King EJ, Bale S, Mozdy A, Tieu Q, Nunnari J, Shaw JM. (1999) The dynamin-related GTPase Dnm1 regulates mitochondrial fission in yeast. *Nat Cell Biol*. **1**(5) pp. 298-304. doi: 10.1038/13014.
- Boldogh IR, Pon LA. (2006) Interactions of mitochondria with the actin cytoskeleton. *Biochim Biophys Acta*. **1763**(5-6) pp. 450-62. doi: 10.1016/j.bbamcr.2006.02.014.
- Bonifacino JS, Neefjes J. (2017) Moving and positioning the endolysosomal system. *Curr Opin Cell Biol*. **47** pp. 1-8. doi: 10.1016/j.ceb.2017.01.008.

Borg M, Bakke O, Progida C. (2014) A novel interaction between Rab7b and actomyosin reveals a dual role in intracellular transport and cell migration. *J Cell Sci.* **127**(Pt 22) pp. 4927-39. doi: 10.1242/jcs.155861.

Boswell RE, Mahowald AP. (1985) tudor, a gene required for assembly of the germ plasm in *Drosophila melanogaster*. *Cell.* **43**(1) pp. 97-104. doi: 10.1016/0092-8674(85)90015-7.

Bove J, Vaillancourt B, Kroeger J, Hepler PK, Wiseman PW, Geitmann A. (2008) Magnitude and direction of vesicle dynamics in growing pollen tubes using spatiotemporal image correlation spectroscopy and fluorescence recovery after photobleaching. *Plant Physiol.* **147**(4) pp. 1646-58. doi: 10.1104/pp.108.120212.

Bradley AO, Vizcarra CL, Bailey HM, Quinlan ME. (2020) Spire stimulates nucleation by Cappuccino and binds both ends of actin filaments. *Mol Biol Cell.* **31**(4) pp. 273-286. . doi: 10.1091/mbc.E19-09-0550.

Brandt T, Mourier A, Tain LS, Partridge L, Larsson NG, Kühlbrandt W. (2017) Changes of mitochondrial ultrastructure and function during ageing in mice and *Drosophila* 2017 *eLife.* 6:e24662. doi: 10.7554/eLife.24662.

Brangwynne CP, Koenderink GH, Mackintosh FC, Weitz DA. (2008) Nonequilibrium microtubule fluctuations in a model cytoskeleton. *Phys Rev Lett.* **100**(11) pp. 118104. doi: 10.1103/PhysRevLett.100.118104.

Brangwynne CP, Koenderink GH, MacKintosh FC, Weitz DA. (2009) Intracellular transport by active diffusion. *Trends Cell Biol.* **19**(9) pp. 423-7. doi: 10.1016/j.tcb.2009.04.004

Brendza RP, Serbus LR, Duffy JB, Saxton WM. (2000) A function for kinesin I in the posterior transport of oskar mRNA and Staufen protein. *Science.* **289**(5487) pp. 2120-2. doi: 10.1126/science.289.5487.2120.

Brendza RP, Serbus LR, Saxton WM, Duffy JB. (2002) Posterior localization of dynein and dorsal-ventral axis formation depend on kinesin in *Drosophila* oocytes. *Curr Biol.* **12**(17):1541-5. doi: 10.1016/s0960-9822(02)01108-9.

Bresnick AR. (1999) Molecular mechanisms of nonmuscle myosin-II regulation. *Curr Opin Cell Biol.* **11**(1) pp. 26-33. doi: 10.1016/s0955-0674(99)80004-0.

Bressloff PC, Newby JM. (2013) Stochastic models of intracellular transport. *Rev. Mod. Phys.* **85**(1) pp. 135-196. doi: 10.1103/RevModPhys.85.135

Briane V, Vimond M, Kervrann C. (2020) An overview of diffusion models for intracellular dynamics analysis. *Brief Bioinform.* **21**(4) pp. 1136-1150. doi: 10.1093/bib/bbz052.

Bright NA, Gratian MJ, Luzio JP. (2005) Endocytic delivery to lysosomes mediated by concurrent fusion and kissing events in living cells. *Curr Biol.* 2005 **15**(4) pp.360-5. doi: 10.1016/j.cub.2005.01.049.

Brown CL, Maier KC, Stauber T, Ginkel LM, Wordeman L, Vernos I, Schroer TA. (2005) Kinesin-2 is a motor for late endosomes and lysosomes. *Traffic.* **6**(12) pp. 1114-24. doi: 10.1111/j.1600-0854.2005.00347.x.

Bucci C, Thomsen P, Nicoziani P, McCarthy J, van Deurs B. (2000) Rab7: a key to lysosome biogenesis. *Mol Biol Cell.* **11**(2) pp. 467-80. doi: 10.1091/mbc.11.2.467.

Burgess SA, Walker ML, Sakakibara H, Oiwa K, Knight PJ. (2004) The structure of dynein-c by negative stain electron microscopy. *J Struct Biol.* 146(1-2) pp. 205-16. doi: 10.1016/j.jsb.2003.10.005.

Busson, D., Pret, AM. (2007) GAL4/UAS Targeted Gene Expression for Studying *Drosophila* Hedgehog Signalling. *Methods In Molecular Biology.* **397**. doi: 10.1007/978-1-59745-516-9\_13

Cabukusta B, Neefjes J. Mechanisms of lysosomal positioning and movement. *Traffic.* **19**(10) pp. 761-769. doi: 10.1111/tra.12587.

- Cai D, Verhey KJ, Meyhöfer E. (2007) Tracking single Kinesin molecules in the cytoplasm of mammalian cells. *Biophys J.* **92**(12) pp. 4137-44. doi: 10.1529/biophysj.106.100206.
- Campbell PD, Shen K, Sapio MR, Glenn TD, Talbot WS, Marlow FL. (2014) Unique function of Kinesin Kif5A in localization of mitochondria in axons. *J Neurosci.* 2014 **34**(44) pp. 14717-32. doi: 10.1523/JNEUROSCI.2770-14.2014.
- Cardanho-Ramos C, Faria-Pereira A, Morais VA. (2020) Orchestrating mitochondria in neurons: Cytoskeleton as the conductor. *Cytoskeleton (Hoboken).* **77**(3-4) pp. 65-75. doi: 10.1002/cm.21585.
- Cardoso SM, Esteves AR, Arduíno DM. (2012) Mitochondrial metabolic control of microtubule dynamics impairs the autophagic pathway in Parkinson's disease. *Neurodegener Dis.* **10**(1-4) pp. 38-40. . doi: 10.1159/000332601.
- Carlier MF, Laurent V, Santolini J, Melki R, Didry D, Xia GX, Hong Y, Chua NH, Pantaloni D. (1997) Actin depolymerizing factor (ADF/cofilin) enhances the rate of filament turnover: implication in actin-based motility. *J Cell Biol.* 136(6) pp. 1307-22. doi: 10.1083/jcb.136.6.1307. PMID: 9087445.
- Chada SR, Hollenbeck PJ. (2004) Nerve growth factor signaling regulates motility and docking of axonal mitochondria. *Curr Biol.* **14**(14) pp. 1272-6. doi: 10.1016/j.cub.2004.07.027.
- Chakrabarti R, Ji WK, Stan RV, de Juan Sanz J, Ryan TA, Higgs HN. (2018) INF2-mediated actin polymerization at the ER stimulates mitochondrial calcium uptake, inner membrane constriction, and division. *J Cell Biol.* **217**(1) pp. 251-268. doi: 10.1083/jcb.201709111
- Chalmers S, Saunter CD, Girkin JM & McCarron JG. (2015) Flicker-assisted localization microscopy reveals altered mitochondrial architecture in hypertension. *Scientific Reports.* **5**, 16875.



Chalmers, S., Saunter, C.D., Girkin, J.M. and McCarron, J.G. (2016), Age decreases mitochondrial motility and increases mitochondrial size in vascular smooth muscle. *J Physiol.* **594**: 4283-4295. doi: 10.1113/JP271942.

Chang YC, Wu JW, Wang CW, Jang AC. (2020) Hippo Signaling-Mediated Mechano- transduction in Cell Movement and Cancer Metastasis. *Front Mol Biosci.* **6**(157) doi: 10.3389/fmolb.2019.00157.

Chen H, Chan DC. (2009) Mitochondrial dynamics--fusion, fission, movement, and mitophagy--in neurodegenerative diseases. *Hum Mol Genet.* **18**(R2) pp.169-76. doi: 10.1093/hmg/ddp326.

Chen H, Detmer SA, Ewald AJ, Griffin EE, Fraser SE, Chan DC. (2003) Mitofusins Mfn1 and Mfn2 coordinately regulate mitochondrial fusion and are essential for embryonic development. *J Cell Biol.* **160**(2) pp.189-200. doi: 10.1083/jcb.200211046.

Chen H, McCaffery JM, Chan DC. (2007) Mitochondrial fusion protects against neurodegeneration in the cerebellum. *Cell.* **130**(3) pp. 548-62. doi: 10.1016/j.cell.2007.06.026.

Chen Y, Csordás G, Jowdy C, Schneider TG, Csordás N, Wang W, Liu Y, Kohlhaas M, Meiser M, Bergem S, Nerbonne JM, Dorn GW 2nd, Maack C. (2012) Mitofusin 2-containing mitochondrial-reticular microdomains direct rapid cardiomyocyte bioenergetic responses via interorganelle Ca(2+) crosstalk. *Circ Res.* **111**(7) pp. 863-75. doi: 10.1161/CIRCRESAHA.112.266585.

Chen Y, Yu L. (2018) Development of Research into Autophagic Lysosome Reformation. *Mol Cells.* **41**(1) pp. 45-49. doi: 10.14348/molcells.2018.2265.

Cho J, Hur JH, Walker DW. (2011) The role of mitochondria in Drosophila aging. *Exp Gerontol.* **46**(5) pp. 331-4. doi: 10.1016/j.exger.2010.08.010.

Christensen JR, Kendrick AA, Truong JB, Aguilar-Maldonado A, Adani V, Dzieciatkowska M, Reck-Peterson SL. (2021) Cytoplasmic dynein-1 cargo diversity

is mediated by the combinatorial assembly of FTS-Hook-FHIP complexes. *Elife*. **10**:e74538. doi: 10.7554/eLife.74538.

Christoforidis S, Miaczynska M, Ashman K, Wilm M, Zhao L, Yip SC, Waterfield MD, Backer JM, Zerial M. (1999) Phosphatidylinositol-3-OH kinases are Rab5 effectors. *Nat Cell Biol*. **1**(4) pp. 249-52. doi: 10.1038/12075.

Cipolat S, Martins de Brito O, Dal Zilio B, Scorrano L. (2004) OPA1 requires mitofusin 1 to promote mitochondrial fusion. *Proc Natl Acad Sci USA*. **101**(45) pp. 15927-32. . doi: 10.1073/pnas.0407043101.

Clark I, Giniger E, Ruohola-Baker H, Jan LY, Jan YN. (1994) Transient posterior localization of a kinesin fusion protein reflects anteroposterior polarity of the *Drosophila* oocyte. *Curr Biol*. **4**(4) pp. 289-300. doi: 10.1016/s0960-9822(00)00068-3.

Clark IE, Jan LY, Jan YN. (1997) Reciprocal localization of Nod and kinesin fusion proteins indicates microtubule polarity in the *Drosophila* oocyte, epithelium, neuron and muscle. *Development*. **124**(2) pp. 461-70. doi: 10.1242/dev.124.2.461.

Cohen RS. (2002) Oocyte patterning: dynein and kinesin, inc. *Curr Biol*. **12**(23) pp. R797-9. doi: 10.1016/s0960-9822(02)01310-6.

Congdon EE, Sigurdsson EM. (2018) Tau-targeting therapies for Alzheimer disease. *Nat Rev Neurol*. **14**(7):399-415. doi: 10.1038/s41582-018-0013-z.

Costantini LM, Snapp EL. (2013) Fluorescent proteins in cellular organelles: serious pitfalls and some solutions. *DNA Cell Biol*. **32**(11) pp. 622-7. doi: 10.1089/dna.2013.2172.

Cox RT, Spradling AC. (2003) A Balbiani body and the fusome mediate mitochondrial inheritance during *Drosophila* oogenesis. *Development*. **130**(8) pp. 1579-90. doi: 10.1242/dev.00365.

Cox RT, Spradling AC. (2006) Milton controls the early acquisition of mitochondria by *Drosophila* oocytes. *Development*. **133**(17) pp. 3371-7. doi: 10.1242/dev.02514.

Craig R, Woodhead JL. (2006) Structure and function of myosin filaments. *Curr Opin Struct Biol*. **16**(2) pp. 204-12. doi: 10.1016/j.sbi.2006.03.006.

Crimella C, Baschiroto C, Arnoldi A, Tonelli A, Tenderini E, Airoidi G, Martinuzzi A, Trabacca A, Losito L, Scarlato M, Benedetti S, Scarpini E, Spinicci G, Bresolin N, Bassi MT. (2012) Mutations in the motor and stalk domains of KIF5A in spastic paraplegia type 10 and in axonal Charcot-Marie-Tooth type 2. *Clin Genet*. **82**(2) pp. 157-64. doi: 10.1111/j.1399-0004.2011.01717.x.

Dahlggaard K, Raposo AA, Niccoli T, St Johnston D. (2007) Capu and Spire assemble a cytoplasmic actin mesh that maintains microtubule organization in the *Drosophila* oocyte. *Dev Cell*. **13**(4) pp. 539-53. doi: 10.1016/j.devcel.2007.09.003.

Daniolos A, Lerner AB, Lerner MR. (1990) Action of light on frog pigment cells in culture. *Pigment Cell Res*. **3**(1) pp. 38-43. doi: 10.1111/j.1600-0749.1990.tb00260.x.

Daumke O, Roux A. (2017) Mitochondrial Homeostasis: How Do Dimers of Mitofusins Mediate Mitochondrial Fusion? *Curr Biol*. **27**(9) pp. R353-R356. doi: 10.1016/j.cub.2017. 03.024.

Davies KM, Anselmi C, Wittig I, Faraldo-Gómez JD, Kühlbrandt W. (2012) Structure of the yeast F1Fo-ATP synthase dimer and its role in shaping the mitochondrial cristae. *Proc Natl Acad Sci USA*. **109**(34) pp. 13602-7. doi: 10.1073/pnas.1204593109.

Davies VJ, Hollins AJ, Piechota MJ, Yip W, Davies JR, White KE, Nicols PP, Boulton ME, Votruba M. (2007) Opa1 deficiency in a mouse model of autosomal dominant optic atrophy impairs mitochondrial morphology, optic nerve structure and visual function. *Hum Mol Genet*. **16**(11) pp. 1307-18.

Demers-Lamarche J, Guillebaud G, Tlili M, Todkar K, Bélanger N, Grondin M, Nguyen AP, Michel J, Germain M. (2016) Loss of Mitochondrial Function Impairs Lysosomes. *J Biol Chem.* **291**(19) pp. 10263-76. doi: 10.1074/jbc.M115.695825.

Desai A, Mitchison TJ. (1997) Microtubule polymerisation dynamics. *Annual Review of Cell and Developmental Biology.* **13**:1 pp. 83-117. doi: 10.1146/annurev.cellbio.13.1.83.

DeWitt MA, Chang AY, Combs PA, Yildiz A. (2012) Cytoplasmic dynein moves through uncoordinated stepping of the AAA+ ring domains. *Science.* **335**(6065) pp. 221-5. doi: 10.1126/science.1215804.

Dickinson DJ, Schwager F, Pintard L, Gotta M, Goldstein B. (2017) A Single-Cell Biochemistry Approach Reveals PAR Complex Dynamics during Cell Polarization. *Dev Cell.* **42**(4) pp. 416-434. doi: 10.1016/j.devcel.2017.07.024.

Dienstbier M, Boehl F, Li X, Bullock SL. (2009) Egalitarian is a selective RNA-binding protein linking mRNA localization signals to the dynein motor. *Genes Dev.* **23**(13) pp. 1546-58. doi: 10.1101/gad.531009.

Dix JA, Verkman AS. (2008) Crowding effects on diffusion in solutions and cells. *Annu Rev Biophys.* **37** pp. 247-63. doi: 10.1146/annurev.biophys.37.032807.125824.

Dodson MW, Zhang T, Jiang C, Chen S, Guo M. (2012) Roles of the Drosophila LRRK2 homolog in Rab7-dependent lysosomal positioning. *Hum Mol Genet.* **21**(6) pp. 1350-63. doi: 10.1093/hmg/ddr573.

Doerflinger H, Benton R, Torres IL, Zwart MF, St Johnston D. (2006) Drosophila Anterior-Posterior Polarity Requires Actin-Dependent PAR-1 Recruitment to the Oocyte Posterior. *Current Biology.* **16**(11) pp. 1090-1095. doi: 10.1016/j.cub.2006.04.001.

Dominguez R, Holmes KC. (2011) Actin structure and function. *Annu Rev Biophys.* **40** pp. 169-86. doi: 10.1146/annurev-biophys-042910-155359.

- Donaldson JG, Porat-Shliom N, Cohen LA. (2009) Clathrin-independent endocytosis: a unique platform for cell signaling and PM remodeling. *Cell Signal.* **21**(1) pp. 1-6. doi: 10.1016/j.cellsig.2008.06.020.
- Drechsler M, Lang LF, Al-Khatib L, Dirks H, Burger M, Schönlieb CB, Palacios IM. (2020) Optical flow analysis reveals that Kinesin-mediated advection impacts the orientation of microtubules in the *Drosophila* oocyte. *Mol Biol Cell.* **31**(12) pp. 1246-1258. doi: 10.1091/mbc.E19-08-0440.
- Driskell OJ, Mironov A, Allan VJ, Woodman PG. (2007) Dynein is required for receptor sorting and the morphogenesis of early endosomes. *Nat Cell Biol.* **9**(1) pp. 113-20. doi: 10.1038/ncb1525.
- Duleh SN, Welch MD. (2010) WASH and the Arp2/3 complex regulate endosome shape and trafficking. *Cytoskeleton (Hoboken).* **67**(3) pp. 193-206. doi: 10.1002/cm.20437.
- Dulińska-Molak I, Pasikowska M, Pogoda K, Lewandowska M, Eris I, Lekka M. (2014) Age-Related Changes in the Mechanical Properties of Human Fibroblasts and Its Prospective Reversal After Anti-Wrinkle Tripeptide Treatment. *Int J Pept Res Ther.* **20**(1):77-85. doi: 10.1007/s10989-013-9370-z.
- Duncan JE, Warrior R. (2002) The cytoplasmic dynein and kinesin motors have interdependent roles in patterning the *Drosophila* oocyte. *Curr Biol.* **12**(23) pp. 1982-91. doi: 10.1016/s0960-9822(02)01303-9.
- Elkin SR, Lakoduk AM, Schmid SL. (2016) Endocytic pathways and endosomal trafficking: a primer. *Wien Med Wochenschr.* **166**(7-8) pp. 196-204. doi: 10.1007/s10354 -016-0432-7.
- Ellis RJ. (2001) Macromolecular crowding: an important but neglected aspect of the intracellular environment. *Curr Opin Struct Biol.* **11**(1) pp. 114-9. doi: 10.1016/s0959-440x(00)00172-x.

Encarnação M, Espada L, Escrevente C, Mateus D, Ramalho J, Michelet X, Santarino I, Hsu VW, Brenner MB, Barral DC, Vieira OV. (2016) A Rab3a-dependent complex essential for lysosome positioning and plasma membrane repair. *J Cell Biol.* **213**(6) pp. 631-40. doi: 10.1083/jcb.201511093.

Ephrussi A, Dickinson LK, Lehmann R. (1991) Oskar organizes the germ plasm and directs localization of the posterior determinant nanos. *Cell.* **66**(1) pp. 37-50. doi: 10.1016/0092-8674(91)90137-n.

Erdélyi M, Michon AM, Guichet A, Glotzer JB, Ephrussi A. (1995) Requirement for Drosophila cytoplasmic tropomyosin in oskar mRNA localization. *Nature.* **377**(6549) pp. 524-7. doi: 10.1038/377524a0.

Eskelinen EL, Saftig P. (2009) Autophagy: a lysosomal degradation pathway with a central role in health and disease. *Biochim Biophys Acta.* **1793**(4) pp. 664-73. doi: 10.1016/j.bbamcr.2008.07.014.

Esteves AR, Gozes I, Cardoso SM. (2014) The rescue of microtubule-dependent traffic recovers mitochondrial function in Parkinson's disease. *Biochim Biophys Acta.* **1842**(1) pp. 7-21. doi: 10.1016/j.bbadis.2013.10.003.

Falguières T, Luyet PP, Bissig C, Scott CC, Velluz MC, Gruenberg J. (2008) In vitro budding of intraluminal vesicles into late endosomes is regulated by Alix and Tsg101. *Mol Biol Cell.* **19**(11) pp. 4942-55. doi: 10.1091/mbc.e08-03-0239.

Farkhondeh A, Niwa S, Takei Y, Hirokawa N. (2015) Characterizing KIF16B in neurons reveals a novel intramolecular "stalk inhibition" mechanism that regulates its capacity to potentiate the selective somatodendritic localization of early endosomes. *J Neurosci.* **35**(12) pp. 5067-86. doi: 10.1523/JNEUROSCI.4240-14.2015.

Fenton, A.R., Jongens, T.A. & Holzbaur, E.L.F. (2021) Mitochondrial adaptor TRAK2 activates and functionally links opposing kinesin and dynein motors. *Nat Commun.* **12** (4578). doi: 10.1038/s41467-021-24862-7.

Ferramosca A, Provenzano SP, Coppola L, Zara V. (2012) Mitochondrial respiratory efficiency is positively correlated with human sperm motility. *Urology*. **79**(4) pp. 809-14. doi: 10.1016/j.urology.2011.12.042.

Filadi R, Pendin D, Pizzo P. (2018) Mitofusin 2: from functions to disease. *Cell Death Dis*. **9**(3) pp. 330. doi: 10.1038/s41419-017-0023-6.

Fletcher DA, Mullins RD. (2010) Cell mechanics and the cytoskeleton. *Nature*. **463**(7280) pp. 485-92. doi: 10.1038/nature08908.

Fletcher GC, Elbediwy A, Khanal I, Ribeiro PS, Tapon N, Thompson BJ. (2015) The Spectrin cytoskeleton regulates the Hippo signalling pathway. *EMBO J*. **34**(7) pp. 940-54. doi: 10.15252/emj.201489642.

Fowler PC, Byrne DJ, Blackstone C, O'Sullivan NC. (2020) Loss of the Mitochondrial Fission GTPase Drp1 Contributes to Neurodegeneration in a *Drosophila* Model of Hereditary Spastic Paraplegia. *Brain Sci*. **10**(9):646. doi: 10.3390/brainsci10090646.

Fransson A, Ruusala A, Aspenström P. (2003) Atypical Rho GTPases have roles in mitochondrial homeostasis and apoptosis. *J Biol Chem*. **278**(8) pp. 6495-502. doi: 10.1074/jbc.M208609200.

Frederick RL, McCaffery JM, Cunningham KW, Okamoto K, Shaw JM. (2004) Yeast Miro GTPase, Gem1p, regulates mitochondrial morphology via a novel pathway. *J Cell Biol*. **167**(1) pp. 87-98. doi: 10.1083/jcb.200405100.

Friedman JR, Lackner LL, West M, DiBenedetto JR, Nunnari J, Voeltz GK. (2011) ER tubules mark sites of mitochondrial division. *Science*. **334**(6054) pp. 358-62. doi: 10.1126/science.1207385.

Friedman JR, Nunnari J. (2014) Mitochondrial form and function. *Nature*. **505**(7483) pp. 335-43. doi: 10.1038/nature12985.

Galletta BJ, Cooper JA. (2009) Actin and endocytosis: mechanisms and phylogeny. *Curr Opin Cell Biol.* **21**(1) pp. 20-7. doi: 10.1016/j.ceb.2009.01.006.

Gandre-Babbe S, van der Blik AM. (2008) The novel tail-anchored membrane protein Mff controls mitochondrial and peroxisomal fission in mammalian cells. *Mol Biol Cell.* **19**(6) pp. 2402-12. doi: 10.1091/mbc.e07-12-1287.

Ganguly S, Williams LS, Palacios IM, Goldstein RE. (2012) Cytoplasmic streaming in *Drosophila* oocytes varies with kinesin activity and correlates with the microtubule cytoskeleton architecture. *Proc Natl Acad Sci USA.* **109** pp.15109–15114. doi: 10.1073/pnas.1203575109.

García-Bartolomé A, Peñas A, Illescas M, Bermejo V, López-Calcerrada S, Pérez-Pérez R, Marín-Buera L, Domínguez-González C, Arenas J, Martín MA, Ugalde C. (2020) Altered Expression Ratio of Actin-Binding Gelsolin Isoforms Is a Novel Hallmark of Mitochondrial OXPHOS Dysfunction. *Cells.* **9**(9) pp.1922. doi: 10.3390/cells9091922.

García-Bartolomé A, Peñas A, Marín-Buera L, Lobo-Jarne T, Pérez-Pérez R, Morán M, Arenas J, Martín MA, Ugalde C. (2017) Respiratory chain enzyme deficiency induces mitochondrial location of actin-binding gelsolin to modulate the oligomerization of VDAC complexes and cell survival. *Hum Mol Genet.* **26**(13):2493-2506. doi: 10.1093/hmg/ddx144.

Gautreau A, Oguievetskaia K, Ungermann C. (2014) Function and regulation of the endosomal fusion and fission machineries. *Cold Spring Harb Perspect Biol.* **6**(3):a016832. doi: 10.1101/cshperspect.a016832.

Ge Y, Shi X, Boopathy S, McDonald J, Smith AW, Chao LH. (2020) Two forms of Opa1 cooperate to complete fusion of the mitochondrial inner-membrane. *Elife.* **9**:e50973. doi: 10.7554/eLife.50973.



Geitmann A, Nebenführ A. (2015) Navigating the plant cell: intracellular transport logistics in the green kingdom. *Mol Biol Cell*. **26**(19) pp. 3373-8. doi:10.1091/mbc.E14-10-1482.

Gheorghe DM, Aghamohammadzadeh S, Smaczynska-de Rooij II, Allwood EG, Winder SJ, Ayscough KR. (2008) Interactions between the yeast SM22 homologue Scp1 and actin demonstrate the importance of actin bundling in endocytosis. *J Biol Chem*. **283**(22) pp. 15037-46. doi: 10.1074/jbc.M710332200.

Gigant B, Wang W, Dreier B, Jiang Q, Pecqueur L, Plückthun A, Wang C, Knossow M. (2013) Structure of a kinesin-tubulin complex and implications for kinesin motility. *Nat Struct Mol Biol*. **20**(8) pp. 1001-7. doi: 10.1038/nsmb.2624.

Gillooly DJ, Morrow IC, Lindsay M, Gould R, Bryant NJ, Gaullier JM, Parton RG, Stenmark H. (2000) Localization of phosphatidylinositol 3-phosphate in yeast and mammalian cells. *EMBO J*. **19**(17) pp. 4577-88. doi: 10.1093/emboj/19.17.4577.

Gittes F, Mickey B, Nettleton J, Howard J. (1993) Flexural rigidity of microtubules and actin filaments measured from thermal fluctuations in shape. *J Cell Biol*. **120**(4) pp. 923-34. doi: 10.1083/jcb.120.4.923.

Glater EE, Megeath LJ, Stowers RS, Schwarz TL. (2006) Axonal transport of mitochondria requires Milton to recruit kinesin heavy chain and is light chain independent. *J Cell Biol*. **173**(4) pp. 545-57. doi: 10.1083/jcb.200601067.

Godec A, Metzler R. (2015) Signal focusing through active transport. *Phys Rev E Stat Nonlin Soft Matter Phys*. **92**(1) pp. 010701. doi: 10.1103/PhysRevE.92.010701.

Gold VA, Brandt T, Cavellini L, Cohen MM, Ieva R, van der Laan M. (2017) Analysis of Mitochondrial Membrane Protein Complexes by Electron Cryo-tomography. *Methods Mol Biol*. **1567** pp. 315-336. doi: 10.1007/978-1-4939-6824-4\_19.

Goldman CH, Neiswender H, Veeranan-Karmegam R, Gonsalvez GB. (2019) The Egalitarian binding partners Dynein light chain and Bicaudal-D act sequentially to

link mRNA to the Dynein motor. *Development*. **146**(15): dev176529. doi: 10.1242/dev.176529.

Goldstein RE, Tuval I, van de Meent JW. (2008) Microfluidics of cytoplasmic streaming and its implications for intracellular transport. *Proc Natl Acad Sci USA*. **105**(10) pp. 3663-7. doi: 10.1073/pnas.0707223105.

Gouspillou G, Bourdel-Marchasson I, Rouland R, Calmettes G, Biran M, Deschodt-Arsac V, Miraux S, Thiaudiere E, Pasdois P, Detaille D, Franconi JM, Babot M, Trézéguet V, Arsac L, Diolez P. (2014) Mitochondrial energetics is impaired in vivo in aged skeletal muscle. *Aging Cell*. **13**(1) pp. 39-48. doi: 10.1111/accel.12147.

Graef M, Nunnari J. (2011) Mitochondria regulate autophagy by conserved signalling pathways. *EMBO J*. **30**(11) pp. 2101-14. doi: 10.1038/emboj.2011.104.

Grant BD, Donaldson JG. (2009) Pathways and mechanisms of endocytic recycling. *Nat Rev Mol Cell Biol*. **10**(9) pp. 597-608. doi: 10.1038/nrm2755.

Griparic L, van der Wel NN, Orozco IJ, Peters PJ, van der Bliek AM. (2004) Loss of the intermembrane space protein Mgm1/OPA1 induces swelling and localized constrictions along the lengths of mitochondria. *J Biol Chem*. **279**(18) pp. 18792-8. doi: 10.1074/jbc.M400920200.

Gruenberg J, Griffiths G, Howell KE. (1989) Characterization of the early endosome and putative endocytic carrier vesicles in vivo and with an assay of vesicle fusion in vitro. *J Cell Biol*. **108**(4) pp. 1301-16. doi: 10.1083/jcb.108.4.1301.

Gu, Y, Guerra, F, Hu M, Pope A, Sung K, Yang W, Jetha S, Shoff TA, Gunatilake T, Dahlkamp O, Shi LZ, Manganeli F, Nolano M, Zhou Y, Ding J, Bucci C, Wu C. (2022) Mitochondria dysfunction in Charcot Marie Tooth 2B Peripheral Sensory Neuropathy. *Commun Biol*. **5** (717). doi: 10.1038/s42003-022-03632-1.

Guha S, Patil A, Muralidharan H, Baas PW. (2021) Mini-review: Microtubule sliding in neurons. *Neurosci Lett*. **753**:135867. doi: 10.1016/j.neulet.2021.135867.

- Guilgur LG, Prudencio P, Sobral D, Liszekova D, Rosa A, Martinho RG. (2014) Requirement for highly efficient pre-mRNA splicing during *Drosophila* early embryonic development. *Elife* **3**: e02181. doi: 10.7554/eLife.02181.
- Guo M, Ehrlicher AJ, Jensen MH, Renz M, Moore JR, Goldman RD, Lippincott-Schwartz J, Mackintosh FC, Weitz DA. (2014) Probing the stochastic, motor-driven properties of the cytoplasm using force spectrum microscopy. *Cell*. **158**(4) pp. 822-832. doi: 10.1016/j.cell.2014.06.051.
- Guo X, Macleod GT, Wellington A, Hu F, Panchumarthi S, Schoenfield M, Marin L, Charlton MP, Atwood HL, Zinsmaier KE. (2005) The GTPase dMiro is required for axonal transport of mitochondria to *Drosophila* synapses. *Neuron*. **47**(3) pp. 379-93. doi: 10.1016/j.neuron.2005.06.027.
- Guraya SS. (1979) Recent advances in the morphology, cytochemistry, and function of Balbiani's vitelline body in animal oocytes. *Int Rev Cytol*. **59** pp. 249-321. doi: 10.1016/s0074-7696(08)61664-2.
- Gutzeit HO, Koppa R. (1982) Time-lapse film analysis of cytoplasmic streaming during late oogenesis of *Drosophila*. *Development*. **67** (1) pp. 101–111. Doi: 10.1242/dev.67. 1.101.
- Hales KG, Fuller MT. (1997) Developmentally regulated mitochondrial fusion mediated by a conserved, novel, predicted GTPase. *Cell*. **90**(1) pp. 121-9. doi: 10.1016/s0092 -8674(00)80319-0.
- Hancock WO. (2014) Bidirectional cargo transport: moving beyond tug of war. *Nat Rev Mol Cell Biol*. **15**(9) pp. 615-28. doi: 10.1038/nrm3853.
- Happel J and Brenner H. (1983) Low Reynolds Number Hydrodynamics: With Special Applications to Particulate Media. *Springer (Berlin)*. **1**.
- Harada A, Takei Y, Kanai Y, Tanaka Y, Nonaka S, Hirokawa N. (1998) Golgi vesiculation and lysosome dispersion in cells lacking cytoplasmic dynein. *J Cell Biol*. **141**(1) pp. 51-9. doi: 10.1083/jcb.141.1.51.

Harrison RE, Bucci C, Vieira OV, Schroer TA, Grinstein S. (2003) Phagosomes fuse with late endosomes and/or lysosomes by extension of membrane protrusions along microtubules: role of Rab7 and RILP. *Mol Cell Biol.* **23**(18):6494-506. doi: 10.1128/MCB.23.18.6494-6506.2003.

Hatch AL, Ji WK, Merrill RA, Strack S, Higgs HN. (2016) Actin filaments as dynamic reservoirs for Drp1 recruitment. *Mol Biol Cell.* **27**(20) pp. 3109-3121. doi: 10.1091/mbc.E16-03-0193.

Havlin S and Ben-Avraham D. (1987) Diffusion in disordered media. *Adv. Phys.* **36** pp. 695–798. doi: 10.1080/00018738700101072.

He L, Wang X, Montell DJ. (2011) Shining light on Drosophila oogenesis: live imaging of egg development. *Curr Opin Genet Dev.* **21**(5) pp. 612-9. doi:10.1016/j.gde.2011.08. 011.

Helenius A, Mellman I, Wall D, Hubbard A. (1983) Endosomes. *Trends in Biochemical Sciences.* **8**(7) pp. 245-250. doi: 10.1016/0968- 0004(83)90350-X.

Henrichs, V., Grycova, L., Barinka, C. Nahacka Z, Neuzil J, Diez S, Rohlena J, Braun M, Lansky Z. (2020) Mitochondria-adaptor TRAK1 promotes kinesin-1 driven transport in crowded environments. *Nat Commun.* **11**(3123). doi: 10.1038/ s41467-020-16972-5.

Hermann GJ, Shaw JM. (1998) Mitochondrial dynamics in yeast. *Annu Rev Cell Dev Biol.* **14** pp. 265-303. doi: 10.1146/annurev.cellbio.14.1.265.

Hessvik NP, Llorente A. (2018) Current knowledge on exosome biogenesis and release. *Cell Mol Life Sci.* **75**(2) pp. 193-208. doi: 10.1007/s00018-017-2595-9.

Heutink P. (2000) Untangling tau-related dementia. *Hum Mol Genet.* **9**(6):979-86. doi: 10.1093/hmg/9.6.979.

Hirokawa N. (1998) Kinesin and dynein superfamily proteins and the mechanism of organelle transport. *Science.* **279**(5350):519-26. doi: 10.1126/science.279.5350.519.

Hirose K, Akimaru E, Akiba T, Endow SA, Amos LA. (2006) Large conformational changes in a kinesin motor catalyzed by interaction with microtubules. *Mol Cell*. **23**(6) pp. 913-23. doi: 10.1016/j.molcel.2006.07.020.

Hoepfner S, Severin F, Cabezas A, Habermann B, Runge A, Gillooly D, Stenmark H, Zerial M. (2005) Modulation of receptor recycling and degradation by the endosomal kinesin KIF16B. *Cell*. **121**(3) pp. 437-50. doi: 10.1016/j.cell.2005.02.017.

Hollenbeck PJ, Saxton WM. (2005) The axonal transport of mitochondria. *J Cell Sci*. **118**(Pt 23) pp. 5411-9. doi: 10.1242/jcs.02745

Holubcová Z, Howard G, Schuh M. (2013) Vesicles modulate an actin network for asymmetric spindle positioning. *Nat Cell Biol*. **15**(8) pp. 937-47. doi: 10.1038/ncb2802.

Holy TE, Leibler S. (1994) Dynamic instability of microtubules as an efficient way to search in space. *Proc Natl Acad Sci USA*. **91**(12) pp. 5682-5. doi: 10.1073/pnas.91.12.5682.

Hong W, Takshak A, Osunbayo O, Kunwar A, Vershinin M. (2016) The Effect of Temperature on Microtubule-Based Transport by Cytoplasmic Dynein and Kinesin-1 Motors. *Biophys J*. **111**(6) pp. 1287-1294. doi: 10.1016/j.bpj.2016.08.006.

Horio T, Hotani H. (1986) Visualization of the dynamic instability of individual microtubules by dark-field microscopy. *Nature*. **321**(6070) pp. 605-7. doi: 10.1038/321605a0.

Hu YB, Dammer E, Ren RJ, Wang G. (2015) The endosomal-lysosomal system: from acidification and cargo sorting to neurodegeneration. *Transl Neurodegener*. **4**(18). doi: 10.1186/s40035-015-0041-1.

Hubley MJ, Locke BR, Moerland TS. (1996) The effects of temperature, pH, and magnesium on the diffusion coefficient of ATP in solutions of physiological ionic strength. *Biochim Biophys Acta*. **1291**(2) pp. 115-21. doi: 10.1016/0304-4165(96)00053-0.

Huotari J, Helenius A. (2011) Endosome maturation. *EMBO J.* **30**(17) pp. 3481-500. doi: 10.1038/emboj.2011.286.

Hurd TR, Herrmann B, Sauerwald J, Sanny J, Grosch M, Lehmann R. (2016) Long Oskar Controls Mitochondrial Inheritance in *Drosophila melanogaster*. *Dev Cell.* **39**(5) pp. 560-571. doi: 10.1016/j.devcel.2016.11.004.

Illescas M, Peñas A, Arenas J, Martín MA, Ugalde C. (2021) Regulation of Mitochondrial Function by the Actin Cytoskeleton. *Front Cell Dev Biol.* **9** pp. 795-838. doi: 10.3389/fcell.2021.795838.

Illukkumbura R, Bland T, Goehring NW. (2020) Patterning and polarization of cells by intracellular flows. *Curr Opin Cell Biol.* **62** pp. 123-134. doi: 10.1016/j.ceb.2019.10.005.

Ishihara N, Fujita Y, Oka T, Mihara K. (2006) Regulation of mitochondrial morphology through proteolytic cleavage of OPA1. *EMBO J.* **25**(13) pp. 2966-77. doi:10.1038/sj. emboj.7601184.

Ishihara N, Nomura M, Jofuku A, Kato H, Suzuki SO, Masuda K, Otera H, Nakanishi Y, Nonaka I, Goto Y, Taguchi N, Morinaga H, Maeda M, Takayanagi R, Yokota S, Mihara K. (2009) Mitochondrial fission factor Drp1 is essential for embryonic development and synapse formation in mice. *Nat Cell Biol.* **11**(8) pp. 958-66. doi: 10.1038/ncb1907.

J A Cooper, D J Loftus, C Frieden, J Bryan, E L Elson. (1988) Localization and mobility of gelsolin in cells.. *J Cell Biol.* **106** (4) pp. 1229–1240. doi: 10.1083/jcb.106.4.1229

Jacinto A, Baum B. (2003) Actin in development. *Mech Dev.* **120**(11) pp. 1337-49. doi: 10.1016/j.mod.2003.06.006

Jacomin, AC., Fauvarque, MO. & Taillebourg, E. (2016) A functional endosomal pathway is necessary for lysosome biogenesis in *Drosophila* . *BMC Cell Biol.* **17**(36) doi: 10.1186/s12860-016-0115-7.

Jaiswal JK, Rivera VM, Simon SM. (2009) Exocytosis of post-Golgi vesicles is regulated by components of the endocytic machinery. *Cell*. **137**(7) pp. 1308-19. doi: 10.1016/j.cell.2009.04.064.

Januschke J, Gervais L, Dass S, Kaltschmidt JA, Lopez-Schier H, St Johnston D, Brand AH, Roth S, Guichet A. (2002) Polar transport in the *Drosophila* oocyte requires Dynein and Kinesin I cooperation. *Curr Biol*. **12**(23) pp. 1971-81. doi: 10.1016/s0960-9822(02)01302-7.

Jennings BH. (2011) *Drosophila* – a versatile model in biology & medicine. *Materials Today*. **14**(5) pp.190-195. doi: 10.1016/S1369-7021(11)70113-4.

Jensen RE, Johnson AE. (2001) Opening the door to mitochondrial protein import. *Nat Struct Biol*. **8**(12) pp. 1008-10. doi: 10.1038/nsb1201-1008.

Ji WK, Hatch AL, Merrill RA, Strack S, Higgs HN. (2015) Actin filaments target the oligomeric maturation of the dynamin GTPase Drp1 to mitochondrial fission sites. *Elife*. **4**:e11553. doi: 10.7554/eLife.11553.

Johnson DE, Ostrowski P, Jaumouillé V, Grinstein S. (2016) The position of lysosomes within the cell determines their luminal pH. *J Cell Biol*. **212**(6) pp. 677-92. doi: 10.1083/jcb.201507112.

Jongsma ML, Berlin I, Wijdeven RH, Janssen L, Janssen GM, Garstka MA, Janssen H, Mensink M, van Veelen PA, Spaapen RM, Neefjes J. (2016) An ER-Associated Pathway Defines Endosomal Architecture for Controlled Cargo Transport. *Cell*. **166**(1) pp. 152-66. doi: 10.1016/j.cell.2016.05.078.

Joubert F, Puff N. (2021) Mitochondrial Cristae Architecture and Functions: Lessons from Minimal Model Systems. *Membranes (Basel)*. **11**(7) pp. 465. doi: 10.3390/membranes11070465.

Jovic M, Sharma M, Rahajeng J, Caplan S. (2010) The early endosome: a busy sorting station for proteins at the crossroads. *Histol Histopathol*. **25**(1) pp. 99-112. doi: 10.14670/HH-25.99.

Kageyama Y, Hoshijima M, Seo K, Bedja D, Sysa-Shah P, Andrabi SA, Chen W, Höke A, Dawson VL, Dawson TM, Gabrielson K, Kass DA, Iijima M, Sesaki H. (2014) Parkin-independent mitophagy requires Drp1 and maintains the integrity of mammalian heart and brain. *EMBO J.* **33**(23):2798-813. doi: 10.15252/embj.201488658.

Kaksonen M, Sun Y, Drubin DG. (2003) A pathway for association of receptors, adaptors, and actin during endocytic internalization. *Cell.* **115**(4) pp. 475-87. doi: 10.1016/s0092-8674(03)00883-3.

Kanaan NM, Pigino GF, Brady ST, Lazarov O, Binder LI, Morfini GA. (2013) Axonal degeneration in Alzheimer's disease: when signaling abnormalities meet the axonal transport system. *Exp Neurol.* **246** pp. 44-53. doi: 10.1016/j.expneurol.2012.06.003.

Kang JS, Tian JH, Pan PY, Zald P, Li C, Deng C, Sheng ZH. (2008) Docking of axonal mitochondria by syntaphilin controls their mobility and affects short-term facilitation. *Cell.* **132**(1) pp. 137-48. doi: 10.1016/j.cell.2007.11.024.

Kapitein LC, Hoogenraad CC. (2015) Building the Neuronal Microtubule Cytoskeleton. *Neuron.* **87**(3) pp. 492-506. doi: 10.1016/j.neuron.2015.05.046.

Katzmann DJ, Odorizzi G, Emr SD. (2002) Receptor downregulation and multivesicular-body sorting. *Nat Rev Mol Cell Biol.* **3**(12) pp. 893-905. doi: 10.1038/nrm973.

Kemphues KJ, Priess JR, Morton DG, Cheng N. (1988) Identification of genes required for cytoplasmic localization in early *C. elegans* embryos. *Cell.* **5**(3), pp. 311-320. doi: 10.1016/S0092-8674(88)80024-2.

Khuc Trong P, Doerflinger H, Dunkel J, St Johnston D, Goldstein RE. (2015) Cortical microtubule nucleation can organise the cytoskeleton of *Drosophila* oocytes to define the anteroposterior axis. *Elife.* **4**:e06088. doi: 10.7554/eLife.06088.

King S, Schroer T. (2000) Dynactin increases the processivity of the cytoplasmic dynein motor. *Nat Cell Biol.* **2** pp. 20–24. doi: 10.1038/71338.



Kjeken R, Egeberg M, Habermann A, Kuehnel M, Peyron P, Floetenmeyer M, Walther P, Jahraus A, Defacque H, Kuznetsov SA, Griffiths G. (2004) Fusion between phagosomes, early and late endosomes: a role for actin in fusion between late, but not early endocytic organelles. *Mol Biol Cell*. **15**(1) pp. 345-58. doi: 10.1091/mbc.e03-05-0334.

Klosowiak JL, Focia PJ, Chakravarthy S, Landahl EC, Freymann DM, Rice SE. (2013) Structural coupling of the EF hand and C-terminal GTPase domains in the mitochondrial protein Miro. *EMBO Rep*. **14**(11) pp. 968-74. doi: 10.1038/embor.2013.151.

Kohlhaas M, Maack C. (2013) Calcium release microdomains and mitochondria. *Cardiovasc Res*. **98**(2) pp. 259-68. doi: 10.1093/cvr/cvt032.

Konietzny A, Bär J, Mikhaylova M. (2017) Dendritic Actin Cytoskeleton: Structure, Functions, and Regulations. *Front Cell Neurosci*. **11**(147). doi: 10.3389/fncel.2017.00147.

Korobova F, Ramabhadran V, Higgs HN. (2013) An actin-dependent step in mitochondrial fission mediated by the ER-associated formin INF2. *Science*. **339**(6118) pp. 464-7. doi: 10.1126/science.1228360.

Korobova F, Svitkina T. (2010) Molecular architecture of synaptic actin cytoskeleton in hippocampal neurons reveals a mechanism of dendritic spine morphogenesis. *Mol Biol Cell*. **21**(1) pp. 165-76. doi: 10.1091/mbc.e09-07-0596.

Korolchuk VI, Saiki S, Lichtenberg M, Siddiqi FH, Roberts EA, Imarisio S, Jahreiss L, Sarkar S, Futter M, Menzies FM, O'Kane CJ, Deretic V, Rubinsztein DC. (2011) Lysosomal positioning coordinates cellular nutrient responses. *Nat Cell Biol*. **13**(4) pp. 453-60. doi: 10.1038/ncb2204.

Koshiba T, Detmer SA, Kaiser JT, Chen H, McCaffery JM, Chan DC. (2004) Structural basis of mitochondrial tethering by mitofusin complexes. *Science*. **305**(5685) pp. 858-62. doi: 10.1126/science.1099793.

Koslover EF, Chan CK, Theriot JA. (2016) Disentangling Random Motion and Flow in a Complex Medium. *Biophys J.* **110**(3) pp. 700-709. doi: 10.1016/j.bpj.2015.11.008.

Kraus F, Ryan MT. (2017) The constriction and scission machineries involved in mitochondrial fission. *J Cell Sci.* **130**(18) pp. 2953-2960. doi: 10.1242/jcs.199562.

Krishnan K, Moens PDJ. (2009) Structure and functions of profilins. *Biophys Rev.* **1**(2) pp. 71-81. doi: 10.1007/s12551-009-0010-y.

Kruppa AJ, Buss F. (2021) Motor proteins at the mitochondria-cytoskeleton interface. *J Cell Sci.* **134**(7);jcs226084. doi: 10.1242/jcs.226084.

Kugler JM, Lasko P. (2009) Localization, anchoring and translational control of oskar, gurken, bicoid and nanos mRNA during *Drosophila* oogenesis. *Fly (Austin).* **3**(1) pp. 15-28. doi: 10.4161/fly.3.1.7751.

Kühlbrandt, W. (2015) Structure and function of mitochondrial membrane protein complexes. *BMC Biol.* **13**(89). doi: 10.1186/s12915-015-0201-x.

Labrousse AM, Zappaterra MD, Rube DA, van der Bliek AM. (1999) *C. elegans* dynamin-related protein DRP-1 controls severing of the mitochondrial outer membrane. *Mol Cell.* **4**(5) pp. 815-26. doi: 10.1016/s1097-2765(00)80391-3.

Langemeyer L, Fröhlich F, Ungermann C. (2018) Rab GTPase Function in Endosome and Lysosome Biogenesis. *Trends Cell Biol.* **28**(11) pp. 957-970. doi: 10.1016/j.tcb. 2018.06.007.

Lasko PF, Ashburner M. (1990) Posterior localization of vasa protein correlates with, but is not sufficient for, pole cell development. *Genes Dev.* **4**(6) pp. 905-21. doi:10.1101 /gad.4.6.905.

Lavoie-Cardinal F, Bilodeau A, Lemieux M, Gardner MA, Wiesner T, Laramée G, Gagné C, De Koninck P. (2020) Neuronal activity remodels the F-actin based

submembrane lattice in dendrites but not axons of hippocampal neurons. *Sci Rep.* **10**(1):11960. doi: 10.1038/s41598-020-68180-2.

Leduc-Gaudet JP, Picard M, St-Jean Pelletier F, Sgarioto N, Auger MJ, Vallée J, Robitaille R, St-Pierre DH, Gouspillou G. (2015) Mitochondrial morphology is altered in atrophied skeletal muscle of aged mice. *Oncotarget.* **6**(20) pp. 17923-37. doi: 10.18632/oncotarget.4235.

Lei Y, Warrior R. (2000) The *Drosophila* Lissencephaly1 (DLis1) gene is required for nuclear migration. *Dev Biol.* **226**(1) pp. 57-72. doi: 10.1006/dbio.2000.9848.

Lewis TL Jr, Turi GF, Kwon SK, Losonczy A, Polleux F. (2016) Progressive Decrease of Mitochondrial Motility during Maturation of Cortical Axons In Vitro and In Vivo. *Curr Biol.* **26**(19) pp. 2602-2608. doi: 10.1016/j.cub.2016.07.064.

Li M, McGrail M, Serr M, Hays TS. (1994) *Drosophila* cytoplasmic dynein, a microtubule motor that is asymmetrically localized in the oocyte. *J Cell Biol.* **126**(6) pp. 1475-94. doi: 10.1083/jcb.126.6.1475.

Li S, Xiong GJ, Huang N, Sheng ZH. (2020) The cross-talk of energy sensing and mitochondrial anchoring sustains synaptic efficacy by maintaining presynaptic metabolism. *Nat Metab.* **2**(10) pp. 1077-1095. doi: 10.1038/s42255-020-00289-0.

Li S, Xu S, Roelofs BA, Boyman L, Lederer WJ, Sesaki H, Karbowski M. (2015) Transient assembly of F-actin on the outer mitochondrial membrane contributes to mitochondrial fission. *J Cell Biol.* **208**(1) pp. 109-23. doi: 10.1083/jcb.201404050.

Lieber SC, Aubry N, Pain J, Diaz G, Kim SJ, Vatner SF. (2004) Aging increases stiffness of cardiac myocytes measured by atomic force microscopy nanoindentation. *Am J Physiol Heart Circ Physiol.* **287**(2):H645-51. doi: 10.1152/ajpheart.00564.2003.

Ligon LA, Tokito M, Finklestein JM, Grossman FE, Holzbaur EL. (2004) A direct interaction between cytoplasmic dynein and kinesin I may coordinate motor activity. *J Biol Chem.* **279**(18) pp. 19201-8. doi: 10.1074/jbc.M313472200.

Lin C, Schuster M, Guimaraes SC, Ashwin P, Schrader M, Metz J, Hacker C, Gurr SJ, Steinberg G. (2016) Active diffusion and microtubule-based transport oppose myosin forces to position organelles in cells. *Nat Commun.* **7**:11814. doi: 10.1038/ncomms 11814.

Lin MY, Cheng XT, Tammineni P, Xie Y, Zhou B, Cai Q, Sheng ZH. (2017) Releasing Syntaphilin Removes Stressed Mitochondria from Axons Independent of Mitophagy under Pathophysiological Conditions. *Neuron.* **94**(3) pp. 595-610. doi: 10.1016/j.neuron. 2017.04.004.

Ling SC, Fahrner PS, Greenough WT, Gelfand VI. (2004) Transport of Drosophila fragile X mental retardation protein-containing ribonucleoprotein granules by kinesin-1 and cytoplasmic dynein. *Proc Natl Acad Sci USA.* **101**(50) pp. 17428-33. doi: 10.1073/pnas. 0408114101.

Lipshitz HD, Smibert CA. (2000) Mechanisms of RNA localization and translational regulation. *Curr Opin Genet Dev.* **10**(5) pp. 476-88. doi: 10.1016/s0959-437x(00)00116-7.

Liu G, Sanghavi P, Bollinger KE, Perry L, Marshall B, Roon P, Tanaka T, Nakamura A, Gonsalvez GB. (2015) Efficient Endocytic Uptake and Maturation in Drosophila Oocytes Requires Dynamin/p50. *Genetics.* **201**(2) pp. 631-49. doi: 10.1534/genetics.115. 180018.

Liu X, Weaver D, Shirihai O, Hajnóczky G. (2009) Mitochondrial 'kiss-and-run': interplay between mitochondrial motility and fusion-fission dynamics. *EMBO J.* **28**(20) pp. 3074-89. doi: 10.1038/emboj.2009.255.

Llorca O, Martín-Benito J, Ritco-Vonsovici M, Grantham J, Hynes GM, Willison KR, Carrascosa JL, Valpuesta JM. (2000) Eukaryotic chaperonin CCT stabilizes actin and tubulin folding intermediates in open quasi-native conformations. *EMBO J.* **19**(22) pp. 5971-9. doi: 10.1093/emboj/19.22.5971.

Loiseau P, Davies T, Williams LS, Mishima M, Palacios IM. (201) *Drosophila* PAT1 is required for Kinesin-1 to transport cargo and to maximize its motility.

*Development*. **137**(16) pp. 2763-72. doi: 10.1242/dev.048108.

López-Doménech G, Covill-Cooke C, Ivankovic D, Halff EF, Sheehan DF, Norkett R, Birsa N, Kittler JT. (2018) Miro proteins coordinate microtubule- and actin-dependent mitochondrial transport and distribution. *EMBO J*. **37**(3) pp. 321-336. doi: 10.15252/emboj.201696380.

Lu B, Vogel H. (2009) *Drosophila* models of neurodegenerative diseases. *Annu Rev Pathol*. **4** pp. 315-42. doi: 10.1146/annurev.pathol.3.121806.151529.

Lu W, Lakonishok M, Serpinskaya AS, Gelfand VI. (2022) A novel mechanism of bulk cytoplasmic transport by cortical dynein in *Drosophila* ovary. *Elife*. **11**:e75538. doi: 10.7554/eLife.75538.

Lu W, Winding M, Lakonishok M, Wildonger J, Gelfand VI. (2016) Microtubule-microtubule sliding by kinesin-1 is essential for normal cytoplasmic streaming in *Drosophila* oocytes. *Proc Natl Acad Sci USA*. **113**(34) pp. 4995-5004. doi: 10.1073/pnas.1522424113.

Luzio JP, Pryor PR, Bright NA. (2007) Lysosomes: fusion and function. *Nat Rev Mol Cell Biol*. **8**(8) pp. 622-32. doi: 10.1038/nrm2217.

Ma X, Liu K, Li J, Li H, Li J, Liu Y, Yang C, Liang H. (2018) A non-canonical GTPase interaction enables ORP1L-Rab7-RILP complex formation and late endosome positioning. *J Biol Chem*. **293**(36) pp. 14155-14164. doi: 10.1074/jbc.RA118.001854.

MacDougall N, Clark A, MacDougall E, Davis I. (2003) *Drosophila* gurken (TGF $\alpha$ ) mRNA localizes as particles that move within the oocyte in two dynein-dependent steps. *Dev Cell*. **4**(3) pp. 307-19. doi: 10.1016/s1534-5807(03)00058-3.

Mach JM, Lehmann R. (1997) An Egalitarian-BicaudalD complex is essential for oocyte specification and axis determination in *Drosophila*. *Genes Dev*. **11**(4) pp. 423-35. doi: 10.1101/gad.11.4.423.

MacVicar T, Langer T. (2016) OPA1 processing in cell death and disease - the long and short of it. *J Cell Sci.* **129**(12) pp. 2297-306. doi: 10.1242/jcs.159186.

Mallik R, Carter B, Lex S, King SJ, Gross SP. (2004) Cytoplasmic dynein functions as a gear in response to load. *Nature.* **427** pp. 649–652. doi: 10.1038/nature02293.

Mandal A, Drerup CM. (2019) Axonal Transport and Mitochondrial Function in Neurons. *Frontiers in Cellular Neuroscience.* **13**. doi: 10.3389/fncel.2019.00373.

Manor U, Bartholomew S, Golani G, Christenson E, Kozlov M, Higgs H, Spudich J, Lippincott-Schwartz J. (2015) A mitochondria-anchored isoform of the actin-nucleating spire protein regulates mitochondrial division. *Elife.* **4**:e08828. doi: 10.7554/eLife.08828.

Manseau L, Calley J, Phan H. (1996) Profilin is required for posterior patterning of the *Drosophila* oocyte. *Development.* **122**(7) pp. 2109-16. doi: 10.1242/dev.122.7.2109.

Manseau LJ, Schüpbach T. (1989) *cappuccino* and *spire*: two unique maternal-effect loci required for both the anteroposterior and dorsoventral patterns of the *Drosophila* embryo. *Genes Dev.* **3**(9) pp. 1437-52. doi: 10.1101/gad.3.9.1437.

Marín-Buera L, García-Bartolomé A, Morán M, López-Bernardo E, Cadenas S, Hidalgo B, Sánchez R, Seneca S, Arenas J, Martín MA, Ugalde C. (2015) Differential proteomic profiling unveils new molecular mechanisms associated with mitochondrial complex III deficiency. *J Proteomics.* **113**:38-56. doi: 10.1016/j.jprot.2014.09.007.

Martin M, Iyadurai SJ, Gassman A, Gindhart JG Jr, Hays TS, Saxton WM. (1999) Cytoplasmic dynein, the dynactin complex, and kinesin are interdependent and essential for fast axonal transport. *Mol Biol Cell.* **10**(11) pp. 3717-28. doi: 10.1091/mbc.10.11.3717.

Marx A, Hoenger A, Mandelkow E. (2009) Structures of kinesin motor proteins. *Cell Motil Cytoskeleton.* **66**(11) pp. 958-66. doi: 10.1002/cm.20392.

Maxfield FR, Yamashiro DJ. (1987) Endosome acidification and the pathways of receptor-mediated endocytosis. *Adv Exp Med Biol.* **225** pp.189-98. doi: 10.1007/978-1-4684-5442-0\_16.

Maza NA, Schiesser WE, Calvert PD. (2019) An intrinsic compartmentalization code for peripheral membrane proteins in photoreceptor neurons. *J Cell Biol.* **218**(11) pp. 3753-3772. doi: 10.1083/jcb.201906024.

McKenney RJ, Huynh W, Tanenbaum ME, Bhabha G, Vale RD. (2014) Activation of cytoplasmic dynein motility by dynactin-cargo adapter complexes. *Science.* **345**(6194) pp. 337-41. doi: 10.1126/science.1254198.

Mehta AD, Rock RS, Rief M, Spudich JA, Mooseker MS, Cheney RE. (1999) Myosin-V is a processive actin-based motor. *Nature.* **400**(6744) pp. 590-3. doi: 10.1038/23072.

Melkov A, Baskar R, Alcalay Y, Abdu U. (2016) A new mode of mitochondrial transport and polarized sorting regulated by Dynein, Milton and Miro. *Development.* **143**(22) pp. 4203-4213. doi: 10.1242/dev.138289.

Mellman I. Endocytosis and molecular sorting. (1996) *Annu Rev Cell Dev Biol.* **12** pp. 575-625. doi: 10.1146/annurev.cellbio.12.1.575.

Mesaki K, Tanabe K, Obayashi M, Oe N, Takei K. (2011) Fission of tubular endosomes triggers endosomal acidification and movement. *PLoS One.* **6**(5):e19764. doi: 10.1371/journal.pone.0019764.

Metzner K, Darawsha O, Wang M, Gaur N, Cheng Y, Rödiger A, Frahm C, Witte OW, Perocchi F, Axer H, Grosskreutz J, Brill MS. (2022) Age-dependent increase of cytoskeletal components in sensory axons in human skin. *Front Cell Dev Biol.* **10**:965382. doi: 10.3389/fcell.2022.965382

Miller KE, Sheetz MP. (2004) Axonal mitochondrial transport and potential are correlated. *J Cell Sci.* **117**(Pt 13) pp. 2791-804. doi: 10.1242/jcs.01130.

Milton SG, Knutson VP. (1990) Comparison of the function of the tight junctions of endothelial cells and epithelial cells in regulating the movement of electrolytes and macromolecules across the cell monolayer. *J Cell Physiol.* **144**(3) pp. 498-504. doi: 10.1002/jcp.1041440318.

Miragoli M, Sanchez-Alonso JL, Bhargava A, Wright PT, Sikkel M, Schobesberger S, Diakonov I, Novak P, Castaldi A, Cattaneo P, Lyon AR, Lab MJ, Gorelik J. (2016) Microtubule-Dependent Mitochondria Alignment Regulates Calcium Release in Response to Nanomechanical Stimulus in Heart Myocytes. *Cell Rep.* **14**(1) pp. 140-151. doi: 10.1016/j.celrep.2015.12.014.

Mirzoyan Z, Sollazzo M, Allocca M, Valenza AM, Grifoni D, Bellosta P. (2019) *Drosophila melanogaster*: A Model Organism to Study Cancer. *Frontiers in Genetics.* **10**. doi: 10.3389/fgene.2019.00051.

Mishra P, Carelli V, Manfredi G, Chan DC. (2014) Proteolytic cleavage of Opa1 stimulates mitochondrial inner membrane fusion and couples fusion to oxidative phosphorylation. *Cell Metab.* **19**(4) pp. 630-41. doi: 10.1016/j.cmet.2014.03.011.

Mishra P, Chan DC. (2014) Mitochondrial dynamics and inheritance during cell division, development and disease. *Nat Rev Mol Cell Biol.* **15**(10) pp. 634-46. doi: 10.1038/nrm3877.

Mishra P, Chan DC. (2016) Metabolic regulation of mitochondrial dynamics. *J Cell Biol.* **212**(4) pp. 379-87. doi: 10.1083/jcb.201511036.

Misko A, Jiang S, Wegorzewska I, Milbrandt J, Baloh RH. (2010) Mitofusin 2 is necessary for transport of axonal mitochondria and interacts with the Miro/Milton complex. *J Neurosci.* **30**(12) pp. 4232-40. doi: 10.1523/JNEUROSCI.6248-09.2010.

Mitchison T, Kirschner M. (1984) Dynamic instability of microtubule growth. *Nature.* **312**(5991) pp. 237-42. doi: 10.1038/312237a0.

Miyazono Y, Hirashima S, Ishihara N, Kusukawa J, Nakamura K, Ohta K. (2018) Uncoupled mitochondria quickly shorten along their long axis to form indented



spheroids, instead of rings, in a fission-independent manner. *Sci Rep.* **8**(350). doi: 10.1038/s41598-017-18582-6.

Mizuno D, Tardin C, Schmidt CF, Mackintosh FC. (2007) Nonequilibrium mechanics of active cytoskeletal networks. *Science.* **315**(5810) pp. 370-3. doi: 10.1126/science.1134404.

Mogre SS, Brown AI, Koslover EF. (2020) Getting around the cell: physical transport in the intracellular world. *Phys Biol.* **17**(6):061003. doi: 10.1088/1478-3975/aba5e5.

Mogre SS, Christensen JR, Reck-Peterson SL, Koslover EF. (2021) Optimizing microtubule arrangements for rapid cargo capture. 2021. *Biophys. J.* **120**(22) pp. 4918–31. doi: 10.1016/j.bpj.2021.10.020.

Mogre SS, Koslover EF. (2018) Multimodal transport and dispersion of organelles in narrow tubular cells. *Phys Rev E.* **97**(4-1):042402. doi: 10.1103/PhysRevE.97.042402.

Monteith CE, Brunner ME, Djagaeva I, Bielecki AM, Deutsch JM, Saxton WM. (2016) A Mechanism for Cytoplasmic Streaming: Kinesin-Driven Alignment of Microtubules and Fast Fluid Flows. *Biophys J.* **110**(9): pp. 2053-65. doi: 10.1016/j.bpj.2016.03.036.

Moore AS, Holzbaur ELF. (2018) Mitochondrial-cytoskeletal interactions: dynamic associations that facilitate network function and remodeling. *Curr Opin Physiol.* **3** pp. 94-100. doi: 10.1016/j.cophys.2018.03.003.

Moore AS, Wong YC, Simpson CL, Holzbaur EL. (2016) Dynamic actin cycling through mitochondrial subpopulations locally regulates the fission-fusion balance within mitochondrial networks. *Nat Commun.* **7** pp. 128-86. doi: 10.1038/ncomms12886.

Mooren OL, Galletta BJ, Cooper JA. (2012) Roles for actin assembly in endocytosis. *Annu Rev Biochem.* **81** pp. 661-86. doi: 10.1146/annurev-biochem-060910-094416.

Morris RL, Hollenbeck PJ. (1995) Axonal transport of mitochondria along microtubules and F-actin in living vertebrate neurons. *J Cell Biol.* **131**(5) pp. 1315–1326. doi: 10.1083/jcb.131.5.1315

Moughamian AJ, Osborn GE, Lazarus JE, Maday S, Holzbaur EL. (2013) Ordered recruitment of dynactin to the microtubule plus-end is required for efficient initiation of retrograde axonal transport. *J Neurosci.* **33**(32) pp. 13190-203. doi: 10.1523/JNEUROSCI.0935-13.2013.

Mullins RD, Heuser JA, Pollard TD. (1998) The interaction of Arp2/3 complex with actin: nucleation, high affinity pointed end capping, and formation of branching networks of filaments. *Proc Natl Acad Sci USA.* **95**(11) pp. 6181-6. doi: 10.1073/pnas.95.11.6181.

Mullock BM, Bright NA, Fearon CW, Gray SR, Luzio JP. (1998) Fusion of lysosomes with late endosomes produces a hybrid organelle of intermediate density and is NSF dependent. *J Cell Biol.* **140**(3) pp. 591-601. doi: 10.1083/jcb.140.3.591.

Murray JT, Panaretou C, Stenmark H, Miaczynska M, Backer JM. (2002) Role of Rab5 in the recruitment of hVps34/p150 to the early endosome. *Traffic.* **3**(6) pp. 416-27. doi: 10.1034/j.1600-0854.2002.30605.x.

Najafi M, Maza NA, Calvert PD. (2011) Steric volume exclusion sets soluble protein concentrations in photoreceptor sensory cilia. *Proc Natl Acad Sci USA.* **109**(1) pp. 203-8. doi: 10.1073/pnas.1115109109.

Nakata T, Hirokawa N. (1995) Point mutation of adenosine triphosphate-binding motif generated rigor kinesin that selectively blocks anterograde lysosome membrane transport. *J Cell Biol.* **131**(4) pp. 1039-53. doi: 10.1083/jcb.131.4.1039.

Nangaku M, Sato-Yoshitake R, Okada Y, Noda Y, Takemura R, Yamazaki H, Hirokawa N. (1994) KIF1B, a novel microtubule plus end-directed monomeric motor protein for transport of mitochondria. *Cell.* **79**(7) pp. 1209-20. doi: 10.1016/0092-8674(94)90012-4.

Nath S, Bananis E, Sarkar S, Stockert RJ, Sperry AO, Murray JW, Wolkoff AW. (2007) Kif5B and Kifc1 interact and are required for motility and fission of early endocytic vesicles in mouse liver. *Mol Biol Cell*. **18**(5) pp. 1839-49. doi: 10.1091/mbc.e06-06-0524.

Navarro C, Puthalakath H, Adams JM, Strasser A, Lehmann R. (2004) Egalitarian binds dynein light chain to establish oocyte polarity and maintain oocyte fate. *Nat Cell Biol*. **6**(5) pp. 427-35. doi: 10.1038/ncb1122.

Nedelec, F. J., Surrey, T., Maggs, A. C. & Leibler, S. (1997) Self-organization of microtubules and motors. *Nature*. **389** pp. 305–308. doi: 10.1038/38532.

Nielsen E, Severin F, Backer JM, Hyman AA, Zerial M. (1999) Rab5 regulates motility of early endosomes on microtubules. *Nat Cell Biol*. **1**(6) pp. 376-82. doi: 10.1038/14075.

Oberhofer A, Reithmann E, Spieler P, Stepp WL, Zimmermann D, Schmid B, Frey E, Ökten Z. (2020) Molecular underpinnings of cytoskeletal cross-talk. *Proc Natl Acad Sci USA*. **117**(8) pp. 3944-3952. doi: 10.1073/pnas.1917964117.

Oeding SJ, Majstrowicz K, Hu XP, Schwarz V, Freitag A, Honnert U, Nikolaus P, Bähler M. (2018) Identification of Miro1 and Miro2 as mitochondrial receptors for myosin XIX. *J Cell Sci*. **131**(17):jcs219469. doi: 10.1242/jcs.219469.

Ogawa F, Murphy LC, Malavasi EL, O'Sullivan ST, Torrance HS, Porteous DJ, Millar JK. (2016) NDE1 and GSK3 $\beta$  Associate with TRAK1 and Regulate Axonal Mitochondrial Motility: Identification of Cyclic AMP as a Novel Modulator of Axonal Mitochondrial Trafficking. *ACS Chem Neurosci*. **7**(5) pp. 553-64. doi: 10.1021/acchemneuro.5b00255.

Osterwalder T, Yoon KS, White BH, and Keshishian H. (2001) A conditional tissue-specific transgene expression system using inducible GAL4. *PNAS*. **98**(22) pp. 12596-12601. doi/10.1073/pnas.221303298

Otera H, Wang C, Cleland MM, Setoguchi K, Yokota S, Youle RJ, Mihara K. (2010) Mff is an essential factor for mitochondrial recruitment of Drp1 during mitochondrial fission in mammalian cells. *J Cell Biol.* **191**(6) pp. 1141-58. doi: 10.1083/jcb.201007152.

Paavilainen VO, Bertling E, Falck S, Lappalainen P. Regulation of cytoskeletal dynamics by actin-monomer-binding proteins. (2004) *Trends Cell Biol.* **14**(7) pp. 386-94. doi: 10.1016/j.tcb.2004.05.002.

Palau F, Estela A, Pla-Martín D, Sánchez-Piris M. (2009) The role of mitochondrial network dynamics in the pathogenesis of Charcot-Marie-Tooth disease. *Adv Exp Med Biol.* **652** pp. 129-37. doi: 10.1007/978-90-481-2813-6\_9.

Palmer CS, Osellame LD, Laine D, Koutsopoulos OS, Frazier AE, Ryan MT. (2011) MiD49 and MiD51, new components of the mitochondrial fission machinery. *EMBO Rep.* **12**(6) pp. 565-73. doi: 10.1038/embor.2011.54.

Pan ZN, Pan MH, Sun MH, Li XH, Zhang Y, Sun SC. (2020) RAB7 GTPase regulates actin dynamics for DRP1-mediated mitochondria function and spindle migration in mouse oocyte meiosis. *FASEB J.* **34**(7) pp. 9615-9627. doi: 10.1096/fj.201903013R.

Parent CA. (2004) Making all the right moves: chemotaxis in neutrophils and Dictyostelium. *Curr Opin Cell Biol.* **16**(1) pp. 4-13. doi: 10.1016/j.ceb.2003.11.008.

Pareyson D, Saveri P, Sagnelli A, Piscosquito G. (2015) Mitochondrial dynamics and inherited peripheral nerve diseases. *Neurosci Lett.* **596** pp. 66-77. doi: 10.1016/j.neulet.2015.04.001.

Parton RM, Hamilton RS, Ball G, Yang L, Cullen CF, Lu W, Ohkura H, Davis I. (2011) A PAR-1-dependent orientation gradient of dynamic microtubules directs posterior cargo transport in the Drosophila oocyte. *J Cell Biol.* **194**(1) pp.121-35. doi: 10.1083/jcb.201103160.

Pathak D, Sepp KJ, Hollenbeck PJ. (2010) Evidence That Myosin Activity Opposes Microtubule-Based Axonal Transport of Mitochondria. *Journal of Neuroscience*. **30**(26) pp. 8984-8992. doi: 10.1523/JNEUROSCI.1621-10.2010.

Pechlivanis M, Samol A, Kerkhoff E. (2009) Identification of a short Spir interaction sequence at the C-terminal end of formin subgroup proteins. *J Biol Chem*. **284**(37) pp. 25324-33. doi: 10.1074/jbc.M109.030320.

Pegoraro AF, Janmey P, Weitz DA. (2017) Mechanical Properties of the Cytoskeleton and Cells. *Cold Spring Harb Perspect Biol*. **9**(11): a022038. doi: 10.1101/cshperspect. a022038.

Pekkurnaz G, Trinidad JC, Wang X, Kong D, Schwarz TL. (2014) Glucose regulates mitochondrial motility via Milton modification by O-GlcNAc transferase. *Cell*. **158**(1) pp. 54-68. doi: 10.1016/j.cell.2014.06.007.

Pereira AJ, Dalby B, Stewart RJ, Doxsey SJ, Goldstein LS. (1997) Mitochondrial association of a plus end-directed microtubule motor expressed during mitosis in *Drosophila*. *J Cell Biol*. **136**(5) pp. 1081-90. doi: 10.1083/jcb.136.5.1081.

Pfanner N, Meijer M. (1997) The Tom and Tim machine. *Curr Biol*. **7**(2) pp. R100-3. doi: 10.1016/s0960-9822(06)00048-0.

Pfender S, Kuznetsov V, Pleiser S, Kerkhoff E, Schuh M. (2011) Spire-type actin nucleators cooperate with Formin-2 to drive asymmetric oocyte division. *Curr Biol*. **21**(11) pp. 955-60. doi: 10.1016/j.cub.2011.04.029.

Pieuchot L, Lai J, Loh RA, Leong FY, Chiam KH, Stajich J, Jedd G. (2015) Cellular Subcompartments through Cytoplasmic Streaming. *Dev Cell*. **34**(4) pp. 410-20. doi: 10.1016/j.devcel.2015.07.017.

Pilling AD, Horiuchi D, Lively CM, Saxton WM. (2006) Kinesin-1 and Dynein Are the Primary Motors for Fast Transport of Mitochondria in *Drosophila* Motor Axons. *Molecular Biology of the Cell*. **17**(4) pp. 2057-2068. doi: 10.1091/mbc.e05-06-0526.

Piomboni P, Focarelli R, Stendardi A, Ferramosca A, Zara V. (2012) The role of mitochondria in energy production for human sperm motility. *Int J Androl.* **35**(2) pp. 109-24. doi: 10.1111/j.1365-2605.2011.01218.x.

Podinovskaia M, Spang A. The Endosomal Network: Mediators and Regulators of Endosome Maturation. (2018) *Prog Mol Subcell Biol.* **57** pp. 1-38. doi: 10.1007/978-3-319-96704-2\_1.

Pokrywka NJ, Stephenson EC. (1991) Microtubules mediate the localization of bicoid RNA during Drosophila oogenesis. *Development.* **113**(1) pp. 55-66. doi: 10.1242/dev. 113.1.55.

Pokrywka NJ, Stephenson EC. (1995) Microtubules are a general component of mRNA localization systems in Drosophila oocytes. *Dev Biol.* **167**(1) pp. 363-70. doi: 10.1006/ dbio.1995.1030.

Pollard TD, Blanchoin L, Mullins RD. (2000) Molecular mechanisms controlling actin filament dynamics in nonmuscle cells. *Annu Rev Biophys Biomol Struct.* **29** pp. 545-76. doi: 10.1146/annurev.biophys.29.1.545.

Pollard TD, Borisy GG. (2003) Cellular motility driven by assembly and disassembly of actin filaments. *Cell.* **112**(4) pp. 453-65. doi: 10.1016/s0092-8674(03)00120-x.

Ponte S, Carvalho L, Gagliardi M, Campos I, Oliveira PJ, Jacinto A. (2020) Drp1-mediated mitochondrial fission regulates calcium and F-actin dynamics during wound healing. *Biol Open.* **9**(5):bio048629. doi: 10.1242/bio.048629.

Poulton JS, Deng WM. (2007) Cell–cell communication and axis specification in the Drosophila oocyte. *Developmental Biology.* **311**(1) pp. 1-10. doi: 10.1016/j.ydbio.2007. 08.030.

Pruyne D, Evangelista M, Yang C, Bi E, Zigmund S, Bretscher A, Boone C. (2002) Role of formins in actin assembly: nucleation and barbed-end association. *Science.* **297** (5581) pp. 612-5. doi: 10.1126/science.1072309.

- Purcell E M. (1977) Life at low Reynolds number. *Am. J. Phys.* **45** pp. 3-11
- Qualmann B, Kessels MM. (2009) New players in actin polymerization- WH2-domain- containing actin nucleators. *Trends Cell Biol.* **19**(6) pp. 276-85. doi: 10.1016/j.tcb.2009. 03.004.
- Quinlan ME, Heuser J, Kerkhoff E, Mullins RD. (2005) *Drosophila* Spire is an actin nucleation factor. *Nature.* **433** pp, 382–388. doi : 10.1038/nature03241.
- Quinlan ME. (2013) Direct interaction between two actin nucleators is required in *Drosophila* oogenesis. *Development.* **140**(21) pp. 4417-25. doi: 10.1242/dev.097337.
- Quinlan ME. (2016) Cytoplasmic Streaming in the *Drosophila* Oocyte. *Annu Rev Cell Dev Biol.* **32** pp. 173-195. doi: 10.1146/annurev-cellbio-111315-125416.
- Quintero OA, DiVito MM, Adikes RC, Kortan MB, Case LB, Lier AJ, Panaretos NS, Slater SQ, Rengarajan M, Feliu M, Cheney RE. (2009) Human Myo19 is a novel myosin that associates with mitochondria. *Curr Biol.* **19**(23) pp. 2008-13. doi: 10.1016/j.cub. 2009.10.026.
- Riechmann V, Ephrussi A. (2001) Axis formation during *Drosophila* oogenesis. *Curr Opin Genet Dev.* **11**(4) pp. 374-83. doi: 10.1016/s0959-437x(00)00207-0.
- Rivero F, Cvrcková F. (2007) Origins and evolution of the actin cytoskeleton. *Adv Exp Med Biol.* **607** pp. 97-110. doi: 10.1007/978-0-387-74021-8\_8.
- Roberts AJ, Kon T, Knight PJ, Sutoh K, Burgess SA. (2013) Functions and mechanics of dynein motor proteins. *Nat Rev Mol Cell Biol.* **14**(11) pp. 713-26. doi: 10.1038/ nrm3667.
- Roberts AJ, Malkova B, Walker ML, Sakakibara H, Numata N, Kon T, Ohkura R, Edwards TA, Knight PJ, Sutoh K, Oiwa K, Burgess SA. (2012) ATP-driven remodeling of the linker domain in the dynein motor. *Structure.* **20**(10) pp. 1670-80. doi: 10.1016/j.str. 2012.07.003.

Robinson DN, Cant K, Cooley L. (1994) Morphogenesis of *Drosophila* ovarian ring canals. *Development*. **120**(7) pp. 2015-25. doi: 10.1242/dev.120.7.2015.

Rocha N, Kuijl C, van der Kant R, Janssen L, Houben D, Janssen H, Zwart W, Neefjes J. (2009) Cholesterol sensor ORP1L contacts the ER protein VAP to control Rab7- RILP-p150 Glued and late endosome positioning. *J Cell Biol*. **185**(7) pp. 1209-25. doi: 10.1083/jcb.200811005.

Russo GJ, Louie K, Wellington A, Macleod GT, Hu F, Panchumarthi S, Zinsmaier KE. (2009) *Drosophila* Miro Is Required for Both Anterograde and Retrograde Axonal Mitochondrial Transport. *Journal of Neuroscience*. **29**(17) pp. 5443-55. doi: 10.1523/JNEUROSCI.5417-08.2009

Sakato M, King SM. (2004) Design and regulation of the AAA+ microtubule motor dynein. *J Struct Biol*. **146**(1-2) pp. 58-71. doi: 10.1016/j.jsb.2003.09.026.

Samaj J, Baluska F, Voigt B, Schlicht M, Volkmann D, Menzel D. (2004) Endocytosis, actin cytoskeleton, and signaling. *Plant Physiol*. **135**(3) pp. 1150-61. doi: 10.1104/pp. 104.040683.

Samaj J, Ovecka M, Hlavacka A, Lecourieux F, Meskiene I, Lichtscheidl I, Lenart P, Salaj J, Volkmann D, Bögre L, Baluska F, Hirt H. (2002) Involvement of the mitogen-activated protein kinase SIMK in regulation of root hair tip growth. *EMBO J*. **21**(13) pp. 3296-306. doi: 10.1093/emboj/cdf349.

Sandoval H, Yao CK, Chen K, Jaiswal M, Donti T, Lin YQ, Bayat V, Xiong B, Zhang K, David G, Charng WL, Yamamoto S, Duraine L, Graham BH, Bellen HJ. (2014) Mitochondrial fusion but not fission regulates larval growth and synaptic development through steroid hormone production. *Elife*. **3**:e03558. doi: 10.7554/eLife.03558.

Sanghavi P, Liu G, Veeranan-Karmegam R, Navarro C, Gonsalvez GB. (2016) Multiple Roles for Egalitarian in Polarization of the *Drosophila* Egg Chamber. *Genetics*. **203**(1) pp. 415-32. doi: 10.1534/genetics.115.184622.



Santel A, Fuller MT. (2001) Control of mitochondrial morphology by a human mitofusin. *J Cell Sci.* **114**(Pt 5) pp. 867-74. doi: 10.1242/jcs.114.5.867.

Sato O, Sakai T, Choo YY, Ikebe R, Watanabe TM, Ikebe M. (2022) Mitochondria-associated myosin 19 processively transports mitochondria on actin tracks in living cells. *J Biol Chem.* **298**(5):101883. doi: 10.1016/j.jbc.2022.101883.

Satoh T, Nakafuku M, Kaziro Y. (1992) Function of Ras as a molecular switch in signal transduction. *J Biol Chem.* **267**(34) pp. 24149-52.

Scaife RM, Margolis RL. (1997) The role of the PH domain and SH3 binding domains in dynamin function. *Cell Signal.* **9**(6) pp. 395-401. doi: 10.1016/s0898-6568(97)00041-7.

Schiavon CR, Shadel GS, Manor U. (2021) Impaired Mitochondrial Mobility in Charcot-Marie-Tooth Disease. *Front Cell Dev Biol.* **9**:624823. doi: 10.3389/fcell.2021.624823.

Schmid ET, Schinaman JM, Williams KS, Walker DW. (2023) Accumulation of F-actin drives brain aging and limits healthspan in *Drosophila*. *Res Sq [Preprint]*. rs.3.rs-3158290. doi: 10.21203/rs.3.rs-3158290/v1.

Schmidt H, Zalyte R, Urnavicius L, Carter AP. (2015) Structure of human cytoplasmic dynein-2 primed for its power stroke. *Nature.* **518**(7539) pp. 435-438. doi: 10.1038/nature14023.

Schnorrer F, Bohmann K, Nüsslein-Volhard C. (2000) The molecular motor dynein is involved in targeting swallow and bicoid RNA to the anterior pole of *Drosophila* oocytes. *Nat Cell Biol.* **2**(4) pp. 185-90. doi: 10.1038/35008601.

Schroer TA. (2004) Dynactin. *Annu Rev Cell Dev Biol.* **20** pp. 759-79. doi: 10.1146/annurev.cellbio.20.012103.094623.

Schuchardt I, Assmann D, Thines E, Schuberth C, Steinberg G. (2005) Myosin-V, Kinesin-1, and Kinesin-3 cooperate in hyphal growth of the fungus *Ustilago maydis*. *Mol Biol Cell*. **16**(11) pp. 5191-201. doi: 10.1091/mbc.e05-04-0272.

Schuh M. (2011) An actin-dependent mechanism for long-range vesicle transport. *Nat Cell Biol*. **13**(12) pp.1431-6. doi: 10.1038/ncb2353.

Schuler MH, Lewandowska A, Caprio GD, Skillern W, Upadhyayula S, Kirchhausen T, Shaw JM, Cunniff B. (2017) Miro1-mediated mitochondrial positioning shapes intracellular energy gradients required for cell migration. *Mol Biol Cell*. **28**(16) pp. 2159-2169. doi: 10.1091/mbc.E16-10-0741.

Schwarz TL. (2013) Mitochondrial trafficking in neurons. *Cold Spring Harb Perspect Biol*. **5**(6):a011304. doi: 10.1101/cshperspect.a011304.

Scott ZC, Brown AI, Mogre SS, Westrate LM, Koslover EF. (2021) Diffusive search and trajectories on tubular networks: a propagator approach. *Eur Phys J E Soft Matter*. **44**(6) pp. 80. doi: 10.1140/epje/s10189-021-00083-0.

Sept D. (2007) Microtubule Polymerization: One Step at a Time. *Current Biology*. **17**(17) pp. R764-R766. doi: 10.1016/j.cub.2007.07.002.

Serbus LR, Cha BJ, Theurkauf WE, Saxton WM. (2005) Dynein and the actin cytoskeleton control kinesin-driven cytoplasmic streaming in *Drosophila* oocytes. *Development*. **132**(16) pp. 3743-52. doi: 10.1242/dev.01956.

Serra-Marques A, Martin M, Katrukha EA, Grigoriev I, Peeters CA, Liu Q, Hooikaas PJ, Yao Y, Solianova V, Smal I, Pedersen LB, Meijering E, Kapitein LC, Akhmanova A. (2020) Concerted action of kinesins KIF5B and KIF13B promotes efficient secretory vesicle transport to microtubule plus ends. *Elife*. **9**:e61302. doi: 10.7554/eLife.61302.

Sesaki H, Southard SM, Yaffe MP, Jensen RE. (2003) Mgm1p, a dynamin-related GTPase, is essential for fusion of the mitochondrial outer membrane. *Mol Biol Cell*. **14**(6) pp. 2342-56. doi: 10.1091/mbc.e02-12-0788.

Seydoux G, Strome S. (1999) Launching the germline in *Caenorhabditis elegans*: regulation of gene expression in early germ cells. *Development*. **126**(15) pp. 3275–3283. doi: 10.1242/dev.126.15.3275.

Shearer LJ, Petersen NO. (2019) Distribution and Co-localization of endosome markers in cells. *Heliyon*. **5**(9):e02375. doi: 10.1016/j.heliyon.2019.e02375.

Shen L and Chen Z. (2007) Critical review of the impact of tortuosity on diffusion *Chem. Eng. Sci.* **62** pp. 3748–55. doi: 10.1016/j.ces.2007.03.041

Sheng ZH, Cai Q. (2012) Mitochondrial transport in neurons: impact on synaptic homeostasis and neurodegeneration. *Nat Rev Neurosci.* **13**(2) pp. 77-93. doi: 10.1038/nrn3156.

Shepard KA, Yaffe MP. (1999) The yeast dynamin-like protein, Mgm1p, functions on the mitochondrial outer membrane to mediate mitochondrial inheritance. *J Cell Biol.* **144**(4) pp. 711-20. doi: 10.1083/jcb.144.4.711.

Shneyer BI, Ušaj M, Henn A. (2016) Myo19 is an outer mitochondrial membrane motor and effector of starvation-induced filopodia. *J Cell Sci.* **129**(3) pp. 543-56. doi: 10.1242/jcs.175349.

Shneyer BI, Ušaj M, Wiesel-Motiuk N, Regev R, Henn A. (2017) ROS induced distribution of mitochondria to filopodia by Myo19 depends on a class specific tryptophan in the motor domain. *Sci Rep.* **7**(1) pp. 11577. . doi: 10.1038/s41598-017-11002-9.

Short B. (2013) Syntaphilin puts the brakes on axonal mitochondria. *J Cell Biol.* **202**(2) pp. 183. doi: 10.1083/jcb.2022if.

Shulman JM, Benton R, St Johnston D. (2000) The *Drosophila* Homolog of *C. elegans* PAR-1 Organizes the Oocyte Cytoskeleton and Directs oskar mRNA Localization to the Posterior Pole. *Cell.* **101**(4) pp. 377-388. doi: 10.1016/S0092-8674(00)80848-X.

Simcox EM, Reeve A, Turnbull D. (2013) Monitoring mitochondrial dynamics and complex I dysfunction in neurons: implications for Parkinson's disease. *Biochem Soc Trans.* **41**(6) pp. 1618-24. doi: 10.1042/BST20130189.

Simionescu M, Gafencu A, Antohe F. (2002) Transcytosis of plasma macromolecules in endothelial cells: a cell biological survey. *Microsc Res Tech.* **57**(5) pp. 269-88. doi: 10.1002/jemt.10086.

Simons M, Wang M, McBride OW, Kawamoto S, Yamakawa K, Gdula D, Adelstein RS, Weir L. (1991) Human nonmuscle myosin heavy chains are encoded by two genes located on different chromosomes. *Circ Res.* **69**(2) pp. 530-9. doi: 10.1161/01.res.69.2.530.

Skjeldal FM, Haugen LH, Mateus D, Frei DM, Rødseth AV, Hu X, Bakke O. (2021) De novo formation of early endosomes during Rab5-to-Rab7a transition. *J Cell Sci.* **134**(8):jcs254185. doi: 10.1242/jcs.254185.

Sladewski TE, Billington N, Ali MY, Bookwalter CS, Lu H, Kremontsova EB, Schroer TA, Trybus KM. (2018) Recruitment of two dyneins to an mRNA-dependent Bicaudal D transport complex. *Elife.* **7**:e36306. doi: 10.7554/eLife.36306.

Slepchenko BM, Semenova I, Zaliapin I, Rodionov V. (2007) Switching of membrane organelles between cytoskeletal transport systems is determined by regulation of the microtubule-based transport. *J Cell Biol.* **179**(4) pp. 635-41. doi: 10.1083/jcb.200705146.

Snider J, Thibault G, Houry WA. (2008) The AAA+ superfamily of functionally diverse proteins. *Genome Biol.* **9**(4) pp. 216. doi: 10.1186/gb-2008-9-4-216.

Song Z, Chen H, Fiket M, Alexander C, Chan DC. (2007) OPA1 processing controls mitochondrial fusion and is regulated by mRNA splicing, membrane potential, and Yme1L. *J Cell Biol.* **178**(5) pp. 749-55. doi: 10.1083/jcb.200704110.

Splinter D, Razafsky DS, Schlager MA, Serra-Marques A, Grigoriev I, Demmers J, Keijzer N, Jiang K, Poser I, Hyman AA, Hoogenraad CC, King SJ, Akhmanova A.

(2012) BICD2, dynactin, and LIS1 cooperate in regulating dynein recruitment to cellular structures. *Mol Biol Cell*. **23**(21) pp. 4226-41. doi: 10.1091/mbc.E12-03-0210.

St Johnston D. (1995) The intracellular localization of messenger RNAs. *Cell*. **81**(2) pp. 161-70. doi: 10.1016/0092-8674(95)90324-0.

Steinhauer J, Kalderon D. (2006) Microtubule polarity and axis formation in the *Drosophila* oocyte. *Dev Dyn*. **235**(6) pp. 1455-68. doi: 10.1002/dvdy.20770.

Storrie B, Desjardins M. (1996) The biogenesis of lysosomes: is it a kiss and run, continuous fusion and fission process? *Bioessays*. **18**(11) pp. 895-903. doi: 10.1002/bies.950181108.

Stowers RS, Megeath LJ, Górska-Andrzejak J, Meinertzhagen IA, Schwarz TL. (2002) Axonal transport of mitochondria to synapses depends on milton, a novel *Drosophila* protein. *Neuron*. **36**(6) pp. 1063-77. doi: 10.1016/s0896-6273(02)01094-2.

Sturgill-Koszycki S, Schaible UE, Russell DG. (1996) Mycobacterium-containing phagosomes are accessible to early endosomes and reflect a transitional state in normal phagosome biogenesis. *EMBO J*. **15**(24):6960-8.

Stürmer K, Baumann O, Walz B. (1995) Actin-dependent light-induced translocation of mitochondria and ER cisternae in the photoreceptor cells of the locust *Schistocerca gregaria*. *J Cell Sci*. **108** ( Pt 6) pp. 2273-83. doi: 10.1242/jcs.108.6.2273.

Svitkina T. (2018) The Actin Cytoskeleton and Actin-Based Motility. *Cold Spring Harb Perspect Biol*. **10**(1):a018267. doi: 10.1101/cshperspect.a018267.

Sweeney HL, Holzbaur ELF. (2018) Motor Proteins. *Cold Spring Harb Perspect Biol*. **10**(5):a021931. doi: 10.1101/cshperspect.a021931.

Tanaka Y, Kanai Y, Okada Y, Nonaka S, Takeda S, Harada A, Hirokawa N. (1998) Targeted disruption of mouse conventional kinesin heavy chain, kif5B, results in abnormal perinuclear clustering of mitochondria. *Cell*. **93**(7) pp. 1147-58. doi: 10.1016/s0092-8674(00)81459-2.

Tetsuya H, Takashi M. (2014) The role of dynamic instability in microtubule organization. *Frontiers in Plant Science*. **5**. doi: 10.3389/fpls.2014.00511.

Tetzlaff MT, Jäckle H, Pankratz MJ. (1996) Lack of *Drosophila* cytoskeletal tropomyosin affects head morphogenesis and the accumulation of oskar mRNA required for germ cell formation. *EMBO J*. **15**(6) pp. 1247-54. doi: 10.1002/j.1460-2075.1996.tb00466.x.

Theurkauf WE. (1994) Microtubules and cytoplasm organization during *Drosophila* oogenesis. *Dev Biol*. **165**(2):352-60. doi: 10.1006/dbio.1994.1258.

Theurkauf WE, Smiley S, Wong ML, Alberts BM. (1992) Reorganization of the cytoskeleton during *Drosophila* oogenesis: implications for axis specification and intercellular transport. *Development*. **115**(4) pp. 923-36. doi: 10.1242/dev.115.4.923.

Tilokani L, Nagashima S, Paupe V, Prudent J. (2018) Mitochondrial dynamics: overview of molecular mechanisms. *Essays Biochem*. **62**(3) pp. 341-360. doi: 10.1042/EBC201 70104.

Todkar K, Chikhi L, Germain M. (2019) Mitochondrial interaction with the endosomal compartment in endocytosis and mitochondrial transfer. *Mitochondrion*. **49** pp. 284-288. doi: 10.1016/j.mito.2019.05.003.

Tondera D, Grandemange S, Jourdain A, Karbowski M, Mattenberger Y, Herzig S, Da Cruz S, Clerc P, Raschke I, Merkwirth C, Ehse S, Krause F, Chan DC, Alexander C, Bauer C, Youle R, Langer T, Martinou JC. (2009) SLP-2 is required for stress-induced mitochondrial hyperfusion. *EMBO J*. **28**(11) pp.1589-600. doi: 10.1038/emboj.2009.89.

Tong M, Zablocki D, Sadoshima J. (2020) The role of Drp1 in mitophagy and cell death in the heart. *J Mol Cell Cardiol.* **142**:138-145. doi: 10.1016/j.yjmcc.2020.04.015.

Tuma P, Hubbard AL. (2003) Transcytosis: crossing cellular barriers. *Physiol Rev.* **83**(3) pp. 871-932. doi: 10.1152/physrev.00001.2003.

Twig G, Elorza A, Molina AJ, Mohamed H, Wikstrom JD, Walzer G, Stiles L, Haigh SE, Katz S, Las G, Alroy J, Wu M, Py BF, Yuan J, Deeney JT, Corkey BE, Shirihai OS. (2008) Fission and selective fusion govern mitochondrial segregation and elimination by autophagy. *EMBO J.* **27**(2) pp. 433-46. doi: 10.1038/sj.emboj.7601963.

Ueda E, Ishihara N. (2018) Mitochondrial hyperfusion causes neuropathy in a fly model of CMT2A. *EMBO Rep.* **19**(8):e46502. doi: 10.15252/embr.201846502.

Vagnoni A, Bullock SL. (2018) A cAMP/PKA/Kinesin-1 Axis Promotes the Axonal Transport of Mitochondria in Aging Drosophila Neurons. *Curr Biol.* **28**(8) pp. 1265-1272. doi: 10.1016/j.cub.2018.02.048.

Vallee RB, Bloom GS. (1991) Mechanisms of Fast and Slow Axonal Transport. *Annual Review of Neuroscience.* **14**:1 pp. 59-92. doi : 10.1146/annurev.ne.14.030191.000423.

Vallee RB, Tai CY (2002) The Role of Dynein in Disease. *In Molecular Motors.* **1** pp.497-509. doi: 10.1002/3527601503.ch20.

Van Blerkom J. (1991) Microtubule mediation of cytoplasmic and nuclear maturation during the early stages of resumed meiosis in cultured mouse oocytes. *Proc Natl Acad Sci USA.* **88**(11) pp. 5031-5. doi: 10.1073/pnas.88.11.5031.

van der Kant R, Fish A, Janssen L, Janssen H, Krom S, Ho N, Brummelkamp T, Carette J, Rocha N, Neefjes J. (2013) Late endosomal transport and tethering are coupled processes controlled by RILP and the cholesterol sensor ORP1L. *J Cell Sci.* **126**(Pt 15) pp. 3462-74. doi: 10.1242/jcs.129270.

van Deurs B, Holm PK, Kayser L, Sandvig K. (1995) Delivery to lysosomes in the human carcinoma cell line HEp-2 involves an actin filament-facilitated fusion between mature endosomes and preexisting lysosomes. *Eur J Cell Biol.* **66**(4) pp. 309-23.

van Eeden FJ, Palacios IM, Petronczki M, Weston MJ, St Johnston D. (2001) Barentsz is essential for the posterior localization of oskar mRNA and colocalizes with it to the posterior pole. *J Cell Biol.* **154**(3) pp. 511-23. doi: 10.1083/jcb.200105056.

van Spronsen M, Mikhaylova M, Lipka J, Schlager MA, van den Heuvel DJ, Kuijpers M, Wulf PS, Keijzer N, Demmers J, Kapitein LC, Jaarsma D, Gerritsen HC, Akhmanova A, Hoogenraad CC. (2013) TRAK/Milton motor-adaptor proteins steer mitochondrial trafficking to axons and dendrites. *Neuron.* **77**(3) pp. 485-502. doi: 10.1016/j.neuron.2012.11.027.

Vanlandingham PA, Ceresa BP. (2009) Rab7 regulates late endocytic trafficking downstream of multivesicular body biogenesis and cargo sequestration. *J Biol Chem.* **284**(18) pp. 12110-24. doi: 10.1074/jbc.M809277200.

Varidaki A, Hong Y, Coffey ET. (2018) Repositioning Microtubule Stabilizing Drugs for Brain Disorders. *Front Cell Neurosci.* **12**:226. doi: 10.3389/fncel.2018.00226.

Verstreken P, Ly CV, Venken KJ, Koh TW, Zhou Y, Bellen HJ. (2005) Synaptic mitochondria are critical for mobilization of reserve pool vesicles at Drosophila neuromuscular junctions. *Neuron.* **47**(3) pp. 365-78. doi: 10.1016/j.neuron.2005.06.018.

Vicente-Manzanares M, Ma X, Adelstein RS, Horwitz AR. (2009) Non-muscle myosin II takes Centre stage in cell adhesion and migration. *Nat. Rev. Mol. Cell Biol.* **10** pp. 778–790. doi : 10.1038/nrm2786.

Vieira OV, Bucci C, Harrison RE, Trimble WS, Lanzetti L, Gruenberg J, Schreiber AD, Stahl PD, Grinstein S. (2003) Modulation of Rab5 and Rab7 recruitment to



phagosomes by phosphatidylinositol 3-kinase. *Mol Cell Biol.* **23**(7):2501-14. doi: 10.1128/MCB.23.7.2501-2514.2003.

Vizcarra CL, Kreutz B, Rodal AA, Toms AV, Lu J, Zheng W, Quinlan ME, Eck MJ. (2011) Structure and function of the interacting domains of Spire and Fmn-family formins. *Proc Natl Acad Sci USA.* **108** pp. 11884–11889. doi: 10.1073/pnas.110570310.

Vogel F, Bornhövd C, Neupert W, Reichert AS. (2006) Dynamic subcompartmentalization of the mitochondrial inner membrane. *J Cell Biol.* **175**(2) pp. 237-47. doi: 10.1083/jcb.200605138.

Vonderheit A, Helenius A. (2005) Rab7 associates with early endosomes to mediate sorting and transport of Semliki forest virus to late endosomes. *PLoS Biol.* **3**(7):e233. doi: 10.1371/journal.pbio.0030233

Walter WJ, Brenner B, Steffen W. (2010) Cytoplasmic dynein is not a conventional processive motor. *J Struct Biol.* **170**(2) pp. 266-9. doi: 10.1016/j.jsb.2009.11.011.

Wang S, Xiao W, Shan S, Jiang C, Chen M, Zhang Y, Lü S, Chen J, Zhang C, Chen Q, Long M. (2012) Multi-patterned dynamics of mitochondrial fission and fusion in a living cell. *PLoS One.* **7**(5):e19879. doi: 10.1371/journal.pone.0019879.

Wang ZH, Clark C, Geisbrecht ER. (2016) Analysis of mitochondrial structure and function in the *Drosophila* larval musculature. *Mitochondrion.* **26** pp. 33-42. doi: 10.1016/j.mito.2015.11.005.

Warn RM, Gutzeit HO, Smith L, Warn A. (1985) F-actin rings are associated with the ring canals of the *Drosophila* egg chamber. *Exp Cell Res.* **157**(2) pp. 355-63. doi: 10.1016/0014-4827(85)90120-x.

Waterman-Storer CM, Karki SB, Kuznetsov SA, Tabb JS, Weiss DG, Langford GM, Holzbaur EL. (1997) The interaction between cytoplasmic dynein and dynactin is required for fast axonal transport. *Proc Natl Acad Sci USA.* **94**(22) pp. 12180-5. doi: 10.1073/pnas.94.22.12180.

- Weasner BM, Zhu J, Kumar JP. (2017) FLPing Genes On and Off in *Drosophila*. *Methods Mol Biol.* **1642** pp. 195-209. doi: 10.1007/978-1-4939-7169-5\_13.
- Weill U, Krieger G, Avihou Z, Milo R, Schuldiner M, Davidi D. (2019) Assessment of GFP Tag Position on Protein Localization and Growth Fitness in Yeast. *J Mol Biol.* **431**(3) pp. 636-641. doi: 10.1016/j.jmb.2018.12.004.
- Weiss M, Elsner M, Kartberg F, Nilsson T. (2004) Anomalous subdiffusion is a measure for cytoplasmic crowding in living cells. *Biophys J.* **87**(5) pp. 3518-24. doi: 10.1529/biophysj.104.044263.
- Welz T, Kerkhoff E. (2019) Exploring the iceberg: Prospects of coordinated myosin V and actin assembly functions in transport processes. *Small GTPases.* **10**(2) pp. 111-121. doi: 10.1080/21541248.2017.
- Whitley BN, Lam C, Cui H, Haude K, Bai R, Escobar L, Hamilton A, Brady L, Tarnopolsky MA, Dengle L, Picker J, Lincoln S, Lackner LL, Glass IA, Hoppins S. (2018) Aberrant Drp1-mediated mitochondrial division presents in humans with variable outcomes. *Hum Mol Genet.* **27**(21) pp. 3710-3719. doi: 10.1093/hmg/ddy287.
- Williams LS, Ganguly S, Loiseau P, Ng BF, Palacios IM. (2013) The auto-inhibitory domain and ATP-independent microtubule-binding region of Kinesin heavy chain are major functional domains for transport in the *Drosophila* germline. *Development.* **141**(1) pp. 176-86. doi: 10.1242/dev.097592.
- Williamson TL, Cleveland DW. (1999) Slowing of axonal transport is a very early event in the toxicity of ALS-linked SOD1 mutants to motor neurons. *Nat Neurosci.* **2**(1):50-6. doi: 10.1038/4553.
- Wong ED, Wagner JA, Gorsich SW, McCaffery JM, Shaw JM, Nunnari J. (2000) The dynamin-related GTPase, Mgm1p, is an intermembrane space protein required for maintenance of fusion competent mitochondria. *J Cell Biol.* **151**(2) pp. 341-52. doi: 10.1083/jcb.151.2.341.

Wong YC, Ysselstein D, Krainc D. (2018) Mitochondria-lysosome contacts regulate mitochondrial fission via RAB7 GTP hydrolysis. *Nature*. **554**(7692) pp. 382-386. doi: 10.1038/nature25486.

Woodman PG, Futter CE. (2008) Multivesicular bodies: co-ordinated progression to maturity. *Curr Opin Cell Biol*. **20**(4) pp. 408-14. doi: 10.1016/j.ceb.2008.04.001.

Wu X, Tanwar PS, Raftery LA. (2008) Drosophila follicle cells: morphogenesis in an eggshell. *Semin Cell Dev Biol*. **19**(3) pp. 271-82. doi: 10.1016/j.semcdb.2008.01.004.

Xiang X, Qiu R, Yao X, Arst HN Jr, Peñalva MA, Zhang J. (2015) Cytoplasmic dynein and early endosome transport. *Cell Mol Life Sci*. **72**(17) pp. 3267-80. doi: 10.1007/s 00018-015-1926-y.

Xu J, Camfield R, Gorski SM. (2018) The interplay between exosomes and autophagy - partners in crime. *J Cell Sci*. **131**(15):jcs215210. doi: 10.1242/jcs.215210.

Xu J, Vanderzalm PJ, Ludwig M, Su T, Tokamov SA, Fehon RG. (2018) Yorkie Functions at the Cell Cortex to Promote Myosin Activation in a Non-transcriptional Manner. *Dev Cell*. **46**(3) pp. 271-284. doi: 10.1016/j.devcel.2018.06.017.

Xu P, Johnson TL, Stoller-Conrad JR, Schulz RA. (2012) Spire, an actin nucleation factor, regulates cell division during Drosophila heart development. *PLoS One*. **7**(1):e30565. doi: 10.1371/journal.pone.0030565.

Yang C, Dominique GM, Champion MM, Huber PW. (2022) Remnants of the Balbiani body are required for formation of RNA transport granules in *Xenopus* oocytes. *iScience*. **25**(3):103878. doi: 10.1016/j.isci.2022.103878.

Yang L, Long Q, Liu J, Tang H, Li Y, Bao F, Qin D, Pei D, Liu X. (2015) Mitochondrial fusion provides an 'initial metabolic complementation' controlled by mtDNA. *Cell Mol Life Sci*. **72**(13) pp. 2585-98. doi: 10.1007/s00018-015-1863-9.

Yao A, Jin S, Li X, Liu Z, Ma X, Tang J, Zhang YQ. (2011) *Drosophila* FMRP regulates microtubule network formation and axonal transport of mitochondria. *Hum Mol Genet.* **20**(1) pp. 51-63. doi: 10.1093/hmg/ddq431.

Yao X, Zhang J, Zhou H, Wang E, Xiang X. (2012) In vivo roles of the basic domain of dynactin p150 in microtubule plus-end tracking and dynein function. *Traffic.* **13**(3) pp. 375-87. doi: 10.1111/j.1600-0854.2011.01312.x.

Zerial M, McBride H. (2001) Rab proteins as membrane organizers. *Nat Rev Mol Cell Biol.* **2**(2) pp. 107-17. doi: 10.1038/35052055.

Zhang J, Schulze KL, Hiesinger PR, Suyama K, Wang S, Fish M, Acar M, Hoskins RA, Bellen HJ, Scott MP. (2007) Thirty-one flavours of *Drosophila* rab proteins. *Genetics.* **176**(2) pp.1307-22. doi: 10.1534/genetics.106.066761.

Zhao J, Fok AHK, Fan R, Kwan PY, Chan HL, Lo LH, Chan YS, Yung WH, Huang J, Lai CSW, Lai KO. (2020) Specific depletion of the motor protein KIF5B leads to deficits in dendritic transport, synaptic plasticity and memory. *Elife.* **9**:e53456. doi: 10.7554/eLife. 53456.

Zajac AL, Goldman YE, Holzbaur EL, Ostap EM. (2013) Local cytoskeletal and organelle interactions impact molecular-motor- driven early endosomal trafficking. *Curr Biol.* **23**(13) pp. 1173-80. doi: 10.1016/j.cub.2013.05.015.

Zhao T, Graham OS, Raposo A, St Johnston D. (2012) Growing microtubules push the oocyte nucleus to polarize the *Drosophila* dorsal-ventral axis. *Science.* **336**(6084) pp. 999-1003. doi: 10.1126/science.1219147.

Zigmond SH. (1974) Mechanisms of sensing chemical gradients by polymorphonuclear leukocytes. *Nature.* **249**(456) pp. 450-2. doi: 10.1038/249450a0.

Zimyanin V, Lowe N, St Johnston D. (2007) An Oskar-Dependent Positive Feedback Loop Maintains the Polarity of the *Drosophila* Oocyte. *Current Biology.* **17**(4) pp. 353-359. doi: 10.1016/j.cub.2006.12.044.



# Appendix

## Section 1. List of Timelapse movies.

<i>Title</i>	<i>Description</i>
<a href="#">Timelapse 1</a>	Timelapse image series of YFP-tagged Rab5 vesicles Playback speed 15fps, 1,024 x 1,024 pixels, 50 frames
<a href="#">Timelapse 2</a>	Timelapse image series of YFP-tagged Rab7 vesicles (left panel) and DIC vesicles (right panel) in the same oocyte Playback speed 15fps, 512 x 256 pixels, 100 frames
<a href="#">Timelapse 3</a>	Timelapse image series of YFP-tagged mitochondria (left panel) and DIC vesicles (right panel) in the same 1-day old oocyte Playback speed 15fps, 1024 x 512 pixels, 500 frames
<a href="#">Timelapse 4</a>	Timelapse image series of YFP-tagged 'group 1' Rab7 vesicles Playback speed 15fps, 512 X 256 pixels, 100 frames
<a href="#">Timelapse 5</a>	Timelapse image series of YFP-tagged 'group 2' Rab7 vesicles Playback speed 15fps, 512 x 256 pixels, 100 frames
<a href="#">Timelapse 6</a>	Timelapse image series of YFP-tagged Rab7 vesicles (left panel) and DIC vesicles (right panel) in the same oocyte in <i>KhcRNAi</i> genetic background (28°C) Playback speed 15fps, 1024 x 512 pixels, 272 frames
<a href="#">Timelapse 7</a>	Timelapse image series of YFP-tagged mitochondria (left panel) and DIC vesicles (right panel) in the same 1-day old oocyte Playback speed 15fps, 1024 x 512 pixels, 500 frames
<a href="#">Timelapse 8</a>	Timelapse image series of YFP-tagged mitochondria (left panel) and DIC vesicles (right panel) in the same 20-day oocyte Playback speed 15fps, 1024 x 512 pixels, 500 frames
<a href="#">Timelapse 9</a>	Timelapse image series of YFP-tagged mitochondria (left panel) and DIC vesicles (right panel) in the same 30-day oocyte Playback speed 15fps, 1024 x 512 pixels, 500 frames
<a href="#">Timelapse 10</a>	Timelapse image series of YFP-tagged mitochondria (left panel) and DIC vesicles (right panel) in the same 40-day oocyte Playback speed 15fps, 1024 x 512 pixels, 500 frames
<a href="#">Timelapse 11</a>	Timelapse image series of YFP-tagged mitochondria (left panel) and DIC vesicles (right panel) in the same <i>nosGal4</i> , mito control oocyte Playback speed 15fps, 1024 x 512 pixels, 500 frames
<a href="#">Timelapse 12</a>	Timelapse image series of YFP-tagged mitochondria (left panel) and DIC vesicles (right panel) in the same <i>UASMarfRNAiGD40478</i> oocyte Playback speed 15fps, 1024 x 512 pixels, 500 frames
<a href="#">Timelapse 13</a>	Timelapse image series of YFP-tagged mitochondria (left panel) and DIC vesicles (right panel) in the same <i>UASMarfRNAi<sup>Guo</sup></i> oocyte Playback speed 15fps, 1024 x 512 pixels, 500 frames
<a href="#">Timelapse 14</a>	Timelapse image series of YFP-tagged mitochondria in <i>UASDrp1[WT] mutant oocytes</i> Playback speed 15fps, 256 x 385 pixels, 50 frames

<a href="#">Timelapse 15</a>	Timelapse image series of YFP-tagged mitochondria in <i>Drp1<sup>T26/+</sup> mutant oocytes</i> Playback speed 15fps, 256 x 385 pixels, 50 frames
<a href="#">Timelapse 16</a>	Timelapse image series of YFP-tagged Rab7 (left panel) and DIC vesicles (right panel) in the same 1-day old <i>spire;YFP::Rab7</i> mutant oocyte Playback speed 15fps, 1024 x 512 pixels, 500 frames
<a href="#">Timelapse 17</a>	Timelapse image series of YFP-tagged mitochondria (left panel) and DIC vesicles (right panel) in the same 1-day <i>spire;YFP::Mito</i> mutant oocyte Playback speed 15fps, 1024 x 512 pixels, 500 frames
<a href="#">Timelapse 18</a>	Timelapse image series of YFP-tagged mitochondria (left panel) and DIC vesicles (right panel) in the same 1-day old colchicine-treated <i>YFP::Mito</i> oocyte Playback speed 15fps, 1024 x 512 pixels, 500 frames
<a href="#">Timelapse 19</a>	Timelapse image series of YFP-tagged Rab7 (left panel) and DIC vesicles (right panel) in the same 1-day old colchicine-treated <i>YFP::Rab7</i> oocyte Playback speed 15fps, 1024 x 512 pixels, 500 frames
<a href="#">Timelapse 20</a>	Timelapse image series of YFP-tagged mitochondria (left panel) and DIC vesicles (right panel) in the same 1-day old colchicine-treated <i>spire;YFP::Mito</i> oocyte Playback speed 15fps, 1024 x 512 pixels, 500 frames

## Section 2. Raw data - centroid coordinates

	Area	Mean	X	Y	XM	XY
1 YFP:: <i>Rab5</i> <sup>1day</sup>	5163.928	67.186	69.121	47.108	70.719	45.305
2 YFP:: <i>Rab5</i> <sup>1day</sup>	4082.513	82.106	71.663	55.585	74.07	54.282
3 YFP:: <i>Rab5</i> <sup>1day</sup>	2334.968	125.983	51.067	46.28	52.223	48.755
4 YFP:: <i>Rab5</i> <sup>1day</sup>	2429.604	43.99	50.151	46.024	48.707	48.811
5 YFP:: <i>Rab7</i> <sup>1day</sup>	3377.899	42.276	71.281	39.936	67.369	40.377
6 YFP:: <i>Rab7</i> <sup>1day</sup>	2239.716	65.638	52.546	45.388	52.982	45.714
7 YFP:: <i>Rab7</i> <sup>1day</sup>	4350.973	75.344	65.209	52.009	66.813	52.478
8 YFP:: <i>Rab7</i> <sup>1day</sup>	5331.658	74.037	67.068	58.149	68.663	60.978
9 YFP:: <i>Mito</i> <sup>1day</sup>	448	22.663	273.5	245	0	0
10 YFP:: <i>Mito</i> <sup>1day</sup>	280	35.708	282	224.5	0	0
11 YFP:: <i>Mito</i> <sup>1day</sup>	72379	27.744	252.346	212.724	259.697	209.191
12 YFP:: <i>Mito</i> <sup>30day</sup>	7970.113	85.793	74.415	61.009	71.366	60.649
13 YFP:: <i>Mito</i> <sup>30day</sup>	4021.756	62.671	52.506	54.954	52.41	54.315
14 YFP:: <i>Mito</i> <sup>30day</sup>	4116.139	86.112	65.644	68.243	66.353	66.663
15 YFP:: <i>Mito</i> <sup>40day</sup>	4182.067	79.008	62.733	64.626	62.813	65.614
16 YFP:: <i>Mito</i> <sup>40day</sup>	5453.229	105.475	61.113	63.148	60.329	61.024
17 YFP:: <i>Mito</i> <sup>40day</sup>	4810.81	61.779	68.604	68.7	70.689	67.507
18 YFP:: <i>Mito</i> <sup>nos-gal4</sup>	2580.854	56.631	47.366	47.581	47.331	47.38
19 YFP:: <i>Mito</i> <sup>nos-gal4</sup>	992913	24.735	1067.499	1031.457	1066.985	1030.889
20 YFP:: <i>Mito</i> <sup>nos-gal4</sup>	46503	27.311	215.352	191.244	213.055	185.495
21 YFP:: <i>Mito</i> <sup>nos-gal4</sup>	4052.833	57.138	60.191	55.558	61.216	52.676
22 Marf <sup>1</sup>	6406.89	53.626	64.72	67.52	63.567	65.436
23 Marf <sup>1</sup>	5822.301	22.586	113.289	66.499	112.648	69.687
24 Marf <sup>1</sup>	1204029	15.353	1104.316	1080.559	1071.556	1033.992
25 Marf <sup>2</sup>	3221031	16.443	1790.821	1825.043	1736.548	1777.199
26 Marf <sup>2</sup>	3987.654	73.521	68.932	51.247	69.875	49.876
27 Marf <sup>2</sup>	2789.123	98.765	55.432	47.654	54.321	48.123
28 Marf <sup>2</sup>	4567.89	59.876	63.21	57.89	64.567	56.789
29 Drp <sup>1</sup>	3456.789	81.234	59.876	52.345	61.234	53.456
30 Drp <sup>1</sup>	5678.901	69.012	72.345	59.012	73.456	58.901
31 Drp <sup>1</sup>	2345.678	112.345	53.21	45.678	54.321	47.89
32 Drp <sup>1</sup>	4321.098	57.89	66.789	54.321	67.89	55.432
33 Drp <sup>1</sup> <sup>2</sup>	3210.987	95.678	58.901	49.012	59.012	50.123
34 Drp <sup>1</sup> <sup>2</sup>	5432.109	71.234	70.123	61.234	71.234	62.345
35 Drp <sup>1</sup> <sup>2</sup>	2901.234	87.654	54.567	46.789	55.678	48.901



36 YFP:: <i>Mito</i> <sup>spir</sup>	4789.012	63.21	67.89	56.789	68.901	57.89
37 YFP:: <i>Mito</i> <sup>spir</sup>	3678.901	79.012	61.234	53.456	62.345	54.567
38 YFP:: <i>Mito</i> <sup>spir</sup>	5123.456	68.901	69.012	58.901	70.123	59.012
39 YFP:: <i>Mito</i> <sup>spir/Df</sup>	2567.89	102.345	52.345	45.123	53.456	46.234
40 YFP:: <i>Mito</i> <sup>spir/Df</sup>	4456.789	65.432	65.678	55.678	66.789	56.789
41 YFP:: <i>Mito</i> <sup>spir/Df</sup>	3345.678	83.456	60.123	51.234	61.234	52.345
42 YFP:: <i>Mito</i> + colchicine	5234.567	72.345	71.234	60.123	72.345	61.234
43 YFP:: <i>Mito</i> + colchicine	2678.901	94.567	53.456	46.567	54.567	47.678
44 YFP:: <i>Mito</i> + colchicine	4678.901	67.89	68.901	57.89	69.012	58.901
45 YFP:: <i>Mito</i> <sup>spir/Df</sup> + colchicine	3789.012	76.789	62.345	54.567	63.456	55.678
46 YFP:: <i>Mito</i> <sup>spir/Df</sup> + colchicine	5345.678	70.123	70.987	59.876	71.098	60.987
47 YFP:: <i>Mito</i> <sup>spir/Df</sup> + colchicine	2456.789	108.901	51.234	44.567	52.345	45.678
48 YFP:: <i>Mito</i> <sup>spir/Df</sup> + colchicine	4234.567	61.234	64.567	53.456	65.678	54.567
49 YFP:: <i>Rab7</i> <sup>spir</sup>	3567.89	89.012	59.012	50.123	60.123	51.234
50 YFP:: <i>Rab7</i> <sup>spir</sup>	5567.89	74.567	73.456	62.345	74.567	63.456
51 YFP:: <i>Rab7</i> <sup>spir</sup>	2789.012	97.89	54.567	47.89	55.678	49.012
52 YFP:: <i>Rab7</i> <sup>spir/Df</sup>	4901.234	66.789	69.876	58.901	70.987	59.012
53 YFP:: <i>Rab7</i> <sup>spir/Df</sup>	3901.234	78.901	63.456	55.678	64.567	56.789
54 YFP:: <i>Rab7</i> <sup>spir/Df</sup>	5789.012	71.098	72.345	61.234	73.456	62.345

Section 3. Raw data – fluorescent intensity measurements, p-values, graphs and Python script analysis.

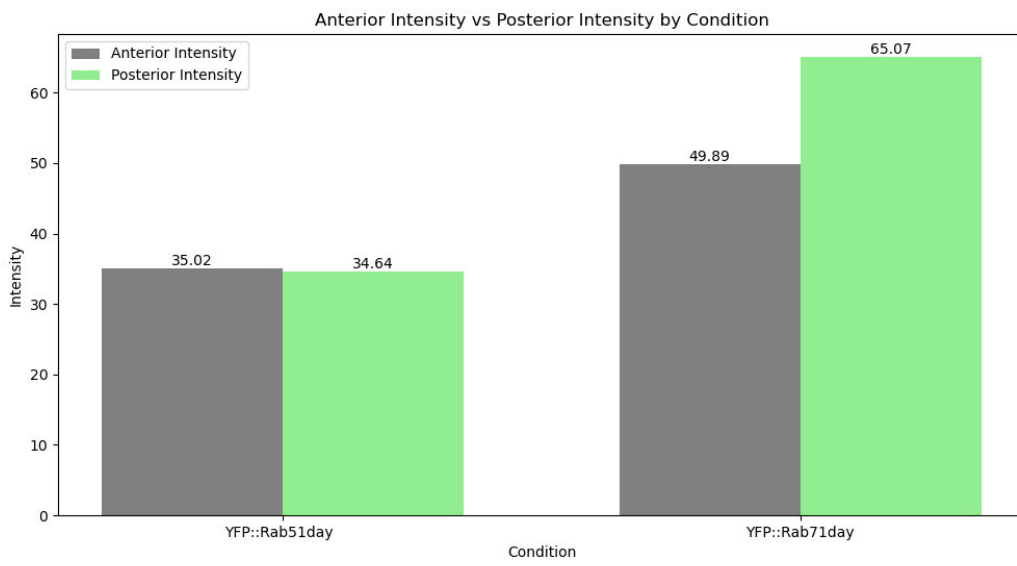
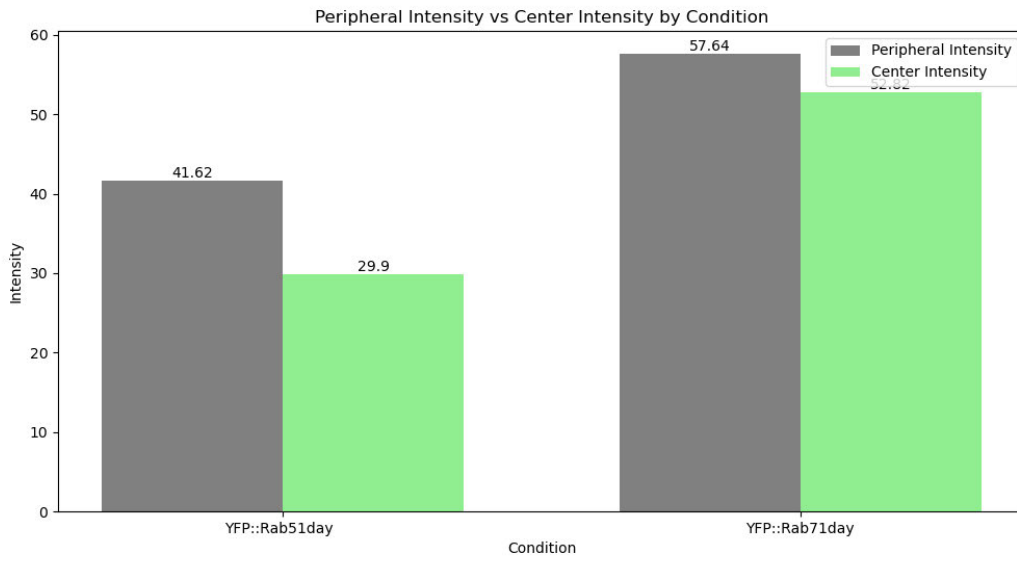
	Center Intensity	Peripheral Intensity	Left Mask	Right Mask	Anterior Mask	Posterior Mask	Top Left Mask	Top Right Mask	Bottom Left Mask	Bottom Right Mask
1 YFP:: <i>Rab</i> 5 <sup>1</sup> day	45.2402 846	59.80837 13	53.2384 962	48.8157 391	50.8586 265	51.9480 169	52.406 8742	48.7460 897	54.6802 351	48.9140 08
2 YFP:: <i>Rab</i> 5 <sup>1</sup> day	23.1052 057	32.73145 43	26.4340 91	28.5779 284	26.8952 902	28.1381 741	26.604 8218	27.0910 527	26.3288 6	29.9082 19
3 YFP:: <i>Rab</i> 5 <sup>1</sup> day	23.2129 931	34.35949 08	28.1773 318	27.9274 892	27.6719 966	28.3584 251	28.556 4855	27.2332 064	27.8975 456	28.7057 408
4 YFP:: <i>Rab</i> 5 <sup>1</sup> day	28.0476 166	39.59085 73	31.0132 034	33.4611 147	33.1331 662	31.6189 727	31.953 8511	34.1460 224	30.3729 957	32.9021 498
5 YFP:: <i>Rab</i> 7 <sup>1</sup> day	71.3557 352	80.15656 02	70.8004 761	89.4917 198	84.1370 8	74.4129 913	83.705 8701	84.8418 625	59.3813 422	92.5248 551
6 YFP:: <i>Rab</i> 7 <sup>1</sup> day	55.5875 331	53.19378 93	54.9724 25	52.5400 823	67.1645 327	46.0969 505	68.856 0289	65.8995 48	47.8586 555	44.5612 782
7 YFP:: <i>Rab</i> 7 <sup>1</sup> day	52.1836 038	52.03205 36	52.9963 223	50.9684 537	62.4035 912	47.2351 491	62.539 1575	62.2307 785	48.2808 978	46.0591 747
8 YFP:: <i>Rab</i> 7 <sup>1</sup> day	32.1381 589	45.17451 17	35.4226 694	40.1248 609	46.5563 773	31.8042 368	42.921 6133	50.0451 314	29.7081 63	33.5531 779
9 YFP:: <i>Mito</i> 1day	70.2531 712	72.56233 66	66.8230 013	75.9596 928	72.3153 273	71.3749 976	71.205 7256	73.3572 571	63.2881 138	77.7110 664
10 YFP:: <i>Mito</i> 1day	80.3260 381	72.71387 25	74.0996 667	75.2542 536	83.1345 374	68.9592 504	83.591 3039	82.4780 632	66.4713 502	71.3585 633
11 YFP:: <i>Mito</i> 1day	118.975 632	91.99410 18	91.7525 363	101.311 108	100.428 717	95.1514 792	91.838 8193	109.224 071	91.7107 846	98.1030 942
12 YFP:: <i>Mito</i> 30day	139.407 58	131.0053 97	127.555 4	137.562 305	99.9420 167	144.427 742	96.442 2269	104.026 356	140.128 781	148.463 117
13 YFP:: <i>Mito</i> 30day	57.0222 152	58.47116 1	60.4964 512	55.3102 472	48.0505 97	60.8806 915	51.262 8151	43.9811 866	62.9684 901	58.2858 412

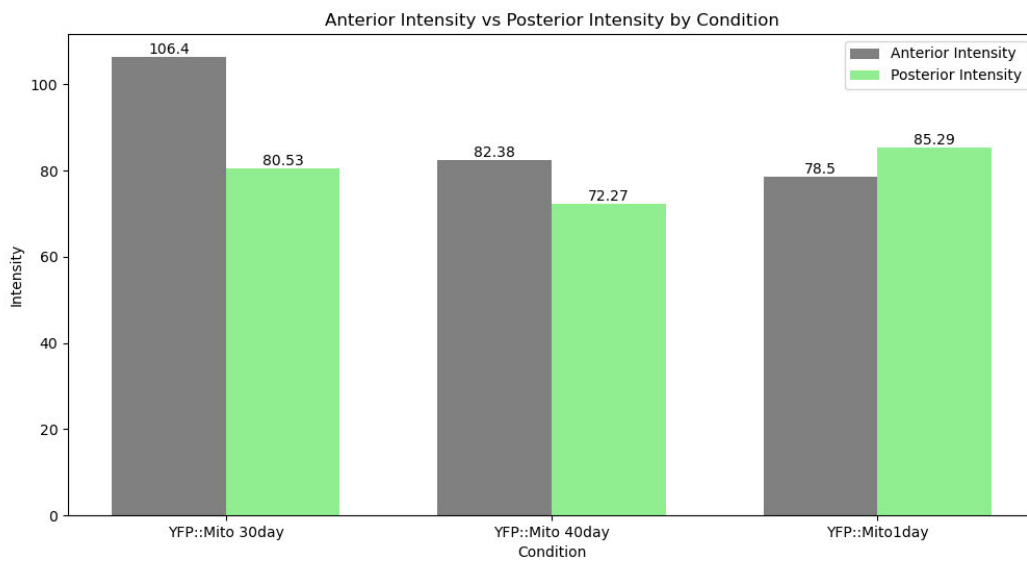
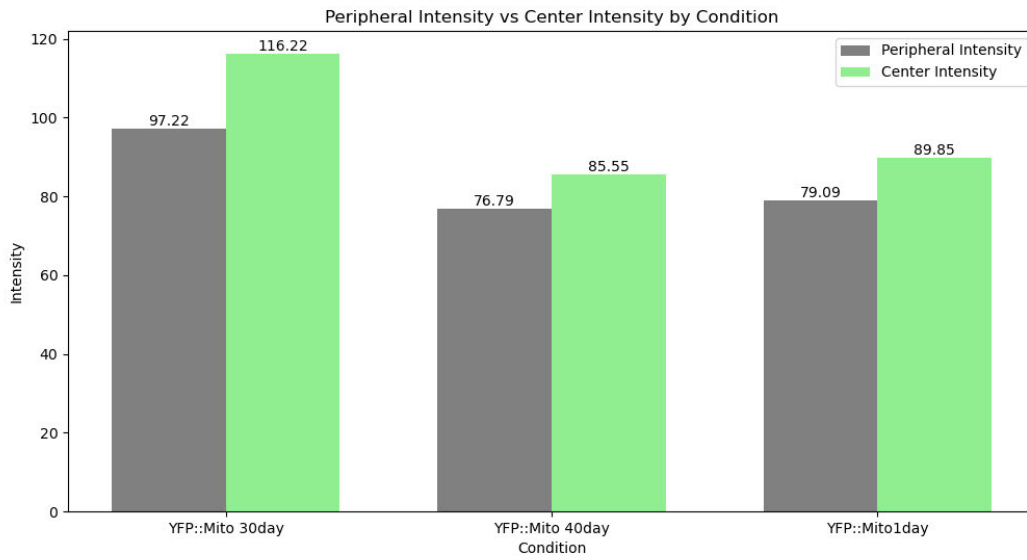
14 YFP:: <i>Mito</i> 30day	152.225 933	102.1842 46	115.262 097	101.949 396	93.5842 91	113.891 927	80.415 7169	103.159 869	130.346 209	101.402 434
15 YFP:: <i>Mito</i> 40day	82.8397 38	74.48630 2	73.8975 21	76.3999 64	72.6949 07	75.9476 84	71.257 703	73.9456 7299	74.6702 1962	77.2259 7281
16 YFP:: <i>Mito</i> 40day	86.3388 58	77.39371 0	75.4368 77	84.4463 25	68.2295 52	87.4838 57	66.069 955	70.1197 86	80.9413 83	93.9438 61
17 YFP:: <i>Mito</i> 40day	87.4576 15	78.49714 9	78.0236 08	83.8806 85	75.8937 15	83.7046 45	72.909 851	78.5178 95	80.5290 24	86.6771 84
18 YFP:: <i>Mito</i> nos-gal4	45.2309 434	40.30701 13	37.3453 418	44.9177 86	44.7153 041	40.0554 599	40.340 7855	47.7437 18	35.8695 425	43.3398 068
19 YFP:: <i>Mito</i> nos-gal4	97.5308 572	85.73154 95	99.3465 709	79.8103 909	95.3179 757	87.3849 146	106.40 6195	80.1070 01	94.0210 922	79.6195 319
20 YFP:: <i>Mito</i> nos-gal4	78.3430 07	71.42252 73	72.7227 218	72.9775 175	74.9292 999	72.0762 253	73.193 7856	77.6447 549	72.5097 543	71.6492 185
21 YFP:: <i>Mito</i> nos-gal4	97.7891 254	96.30696 43	102.316 999	91.3462 839	106.646 555	89.5883 217	113.60 2867	99.8016 687	94.1671 925	84.6389 633
22 Marf <sup>1</sup>	37.0185 6514	36.89697 864	36.8599 5849	36.9859 2923	38.6538 1236	35.8214 0875	36.256 8707	42.3074 053	37.3201 271	34.3234 463
23 Marf <sup>1</sup>	25.2328 663	27.61481 29	25.6177 609	26.1858 768	25.0471 837	26.1441 889	25.340 9017	24.6165 222	25.7170 217	26.5542 254
24 Marf <sup>1</sup>	35.9589 037	41.98075 26	36.4453 602	37.4957 207	36.8530 758	36.9980 265	38.258 2483	35.6645 666	35.7931 029	38.4057 64
25 Marf <sup>2</sup>	52.5967 512	55.61759 48	51.8558 572	54.6844 74	60.3579 521	51.7114 722	60.612 7671	60.0281 498	49.5751 403	53.6890 676
26 Marf <sup>2</sup>	50.5622 265	44.06827 93	49.9947 446	48.4565 154	45.8196 699	50.5406 974	49.091 9357	43.0273 891	50.3682 117	50.6868 646
27 Marf <sup>2</sup>	60.4333 217	66.98049 78	63.3690 011	60.3870 695	70.7879 134	58.5273 639	76.967 8046	65.0975 211	58.4617 347	58.5912 093
28 Marf <sup>2</sup>	41.0740 48	39.65470 09	39.2926 722	42.4439 164	44.1199 906	40.0356 485	44.862 6622	43.0649 48	37.9210 648	42.3272 539
29 Drp1 <sup>1</sup>	47.6919 74	34.96223 26	36.6184 27	36.0897 725	38.4105 822	35.5438 151	40.873 1653	35.7024 607	34.7968 557	36.2278 561
30 Drp1 <sup>1</sup>	40.3665 371	35.47732 53	35.6188 874	35.9627 175	31.7069 511	37.2173 383	31.275 0086	32.0864 881	37.1621 006	37.2631 739
31 Drp1 <sup>1</sup>	37.2562 554	36.23799 99	38.2225 229	35.8996 159	39.0446 585	36.1724 258	40.663 9035	37.1591 026	37.0004 61	35.3843 082
32 Drp1 <sup>1</sup>	42.7332 607	41.26297 74	40.9336 155	44.0747 504	49.4993 049	40.1861 702	48.945 5471	50.1937 557	37.7396 529	42.3524 298
33 Drp1 <sup>2</sup>	24.7231 716	24.81383 72	25.0189 621	24.4652 534	25.4205 06	24.4593 294	25.828 8781	25.0478 106	24.7027 719	24.2088 714

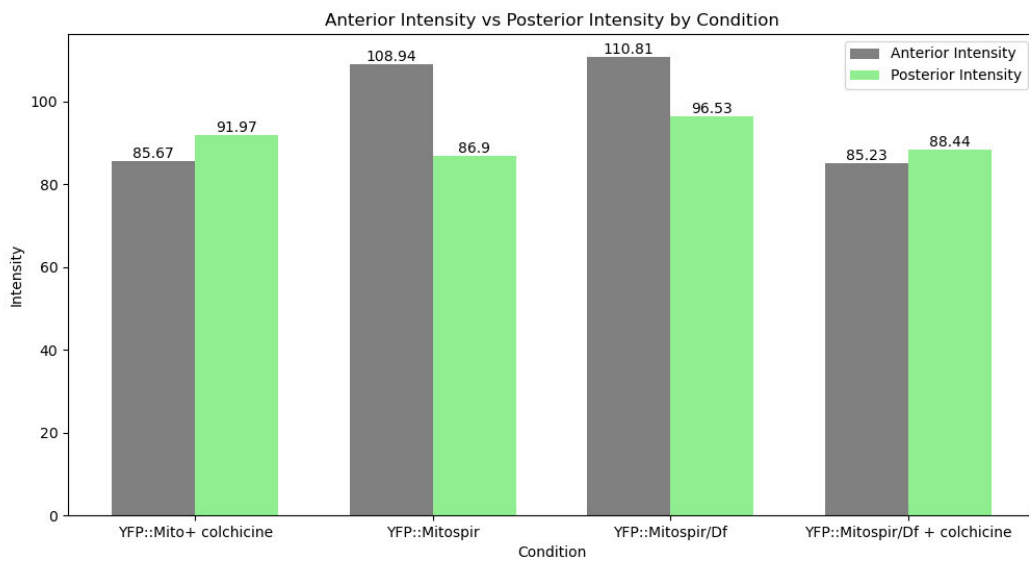
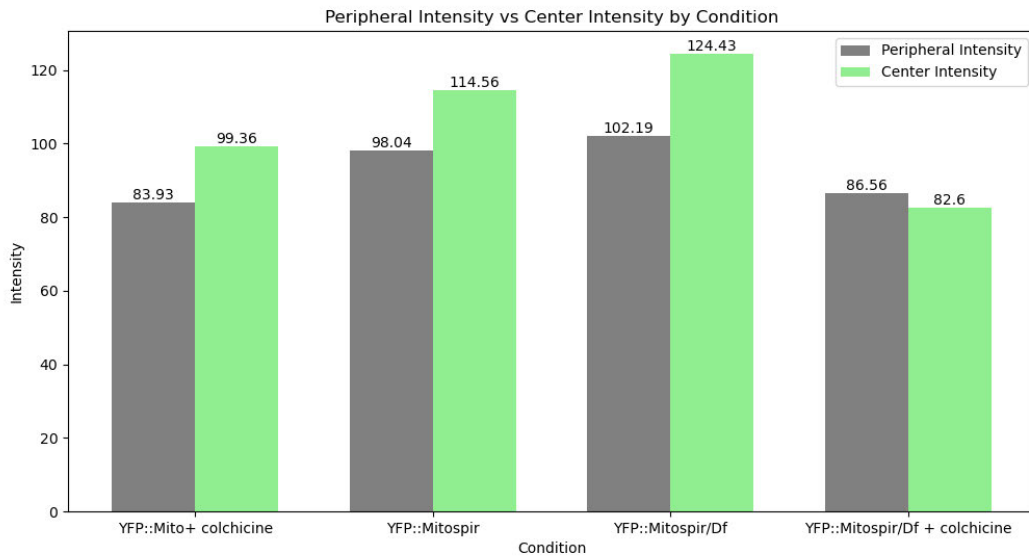
34 Drp1 <sup>2</sup>	26.7389 674	30.32000 07	28.4923 134	25.6068 341	29.4591 269	26.4156 678	29.911 123	28.7742 556	27.9015 363	24.4628 982
35 Drp1 <sup>2</sup>	26.7265 713	26.67861 31	27.1837 751	26.2324 225	28.3925 709	26.2757 352	27.141 5459	29.8361 717	27.1956 282	25.3558 87
36 YFP:: <i>Mito</i> spir	145.844 48	125.9254 51	136.286 042	125.859 361	101.655 087	143.587 516	110.46 7781	92.4895 197	147.266 518	139.822 852
37 YFP:: <i>Mito</i> spir	124.093 345	111.8736 58	120.585 057	111.531 989	98.4959 909	127.590 466	106.70 7216	89.4879 716	130.152 159	125.084 286
38 YFP:: <i>Mito</i> spir	73.7329 557	56.31339 79	60.2995 123	53.7008 134	60.5436 591	55.6535 782	58.802 8837	62.7318 148	61.1085 987	48.8729 542
39 YFP:: <i>Mito</i> spir/Df	162.928 205	129.6401 14	136.445 57	126.639 074	133.577 476	131.132 985	130.41 6128	136.206 565	137.734 992	123.969 604
40 YFP:: <i>Mito</i> spir/Df	118.103 396	101.9252 18	108.886 019	99.1887 411	82.7302 646	111.280 854	88.506 653	77.1724 817	116.095 541	106.771 065
41 YFP:: <i>Mito</i> spir/Df	92.2687 021	74.99478 98	83.0493 703	83.1683 053	73.2696 727	90.0134 69	69.435 2379	77.1691 872	92.0614 904	87.6585 028
42 YFP:: <i>Mito</i> + colchicine	121.279 766	103.8873 13	101.479 967	111.898 318	112.330 006	105.688 036	103.40 3408	118.085 298	100.767 222	109.293 155
43 YFP:: <i>Mito</i> + colchicine	95.5346 917	56.21948 09	60.5931 254	71.2667 659	61.2669 479	68.4490 692	56.022 5729	68.1389 948	64.1156 473	73.3453 112
44 YFP:: <i>Mito</i> + colchicine	81.2601 539	91.69312 36	89.0859 306	89.3705 087	102.306 904	82.8833 512	101.48 7985	102.992 019	84.0195 963	81.5468 149
45 YFP:: <i>Mito</i> spir/Df + colchicine	83.0346 976	95.20060 07	96.8570 282	90.1393 116	104.917 076	89.0559 149	120.41 7745	86.3796 629	86.6599 5	91.5630 723
46 YFP:: <i>Mito</i> spir/Df + colchicine	81.6156 754	80.90088 53	85.1406 595	76.7006 591	68.8526 994	85.7815 02	64.763 6037	73.3429 284	93.3717 125	77.9715 623
47 YFP:: <i>Mito</i> spir/Df + colchicine	85.3090 625	91.01876 14	84.6435 778	95.1540 859	92.4178 623	89.4690 795	83.337 3837	104.256 405	85.0526 687	93.2714 696

48 YFP:: <i>Mito</i> <i>spir/Df</i> + colchicine	80.4592 485	79.10196 32	82.7165 072	75.9562 852	87.5805 91	76.6236 465	83.689 8691	92.5677 267	82.3406 662	71.2728 103
49 YFP:: <i>Rab</i> <i>7<sup>spir</sup></i>	68.7156 759	61.28484 03	64.5005 355	60.9038 432	67.9171 608	60.0739 845	68.282 6461	67.4114 384	62.1141 36	58.2482 617
50 YFP:: <i>Rab</i> <i>7<sup>spir</sup></i>	94.8365 53	112.3217 85	109.786 682	102.162 337	102.342 789	108.739 802	103.34 2615	101.312 131	114.358 834	102.782 73
51 YFP:: <i>Rab</i> <i>7<sup>spir</sup></i>	91.3883 503	100.0396 86	94.3708 024	103.470 26	115.965 349	92.1678 327	115.77 2403	116.254 854	86.2209 597	99.4804 214
52 YFP:: <i>Rab</i> <i>7<sup>spir/Df</sup></i>	31.0538 012	30.89656 13	29.9803 326	32.1365 201	31.8298 761	30.5718 834	28.809 2202	34.6399 294	30.4195 091	30.7771 384
53 YFP:: <i>Rab</i> <i>7<sup>spir/Df</sup></i>	118.284 493	86.02818 26	90.4371 034	95.3563 179	95.4706 159	91.8021 57	81.914 4259	105.075 674	95.3062 204	88.9278 861
54 YFP:: <i>Rab</i> <i>7<sup>spir/Df</sup></i>	125.425 057	102.1325 35	109.447 928	103.966 925	99.8782 988	110.581 533	110.83 7536	89.0738 046	108.657 487	112.489 937

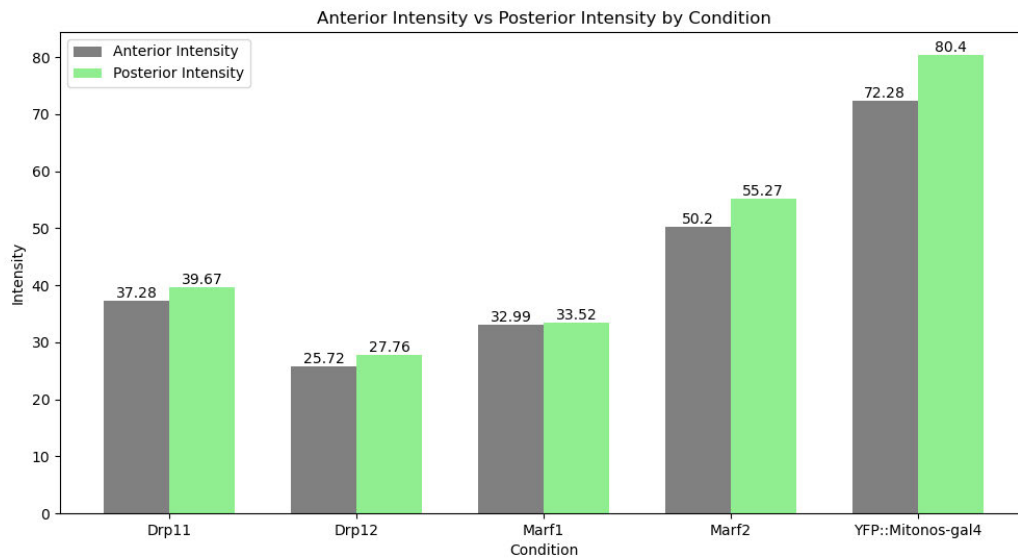
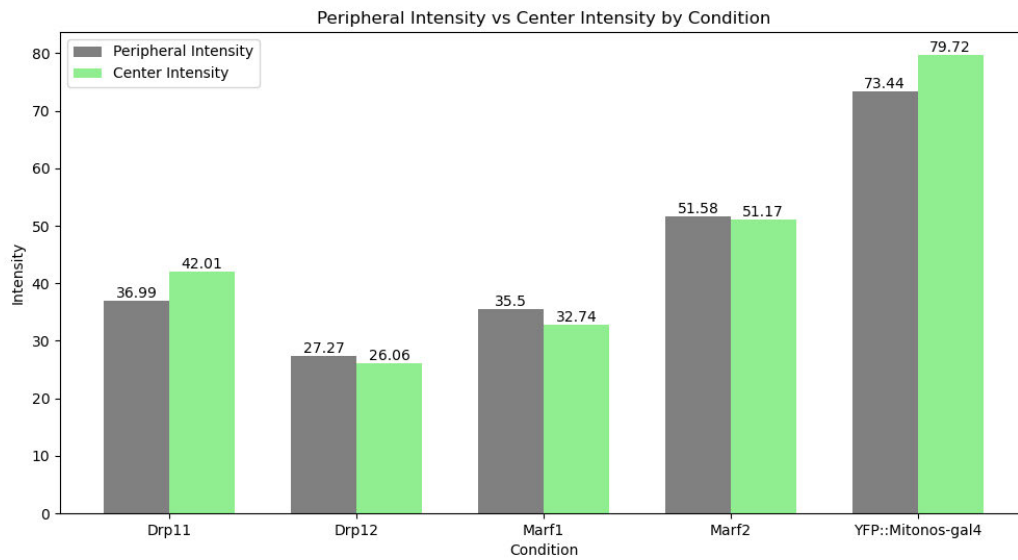
<b>p-value</b>	<b>Central</b>	<b>Peripheral</b>	<b>Anterior</b>	<b>Posterior</b>
Control vs <i>UASMarfRNA<sup>iGD40478</sup></i>	0.0257	0.0506	0.0361	0.0359
Control vs <i>UASMarfRNA<sup>iGuo</sup>; nos-Gal4. YFP::<i>Mito</i></i>	0.073	0.1597	0.1166	0.1446
Control vs <i>UASDrp1<sup>[WT]</sup>; nos-Gal4. YFP::<i>Mito</i></i>	0.0239	0.0248	0.0225	0.0275
Control vs <i>Drp1<sup>[T26]<sup>+/+</sup>; nos-Gal4. YFP::<i>Mito</i></sup></i>	0.0145	0.0242	0.0184	0.0222
<i>p-values calculated using method described in Section 2.9.</i>				











```

import cv2
import numpy as np
import pandas as pd
import matplotlib.pyplot as plt
import os

# Define the output directory
output_dir = '/Users/kirstenebanks/Oocyte image analysis 2'

# Ensure the output directory exists
os.makedirs(output_dir, exist_ok=True)

# Function to segment the image and identify the oocyte based on a manually drawn ROI
def segment_image_from_roi(image, image_name, output_dir):
    # Convert the image to grayscale if it is not already
    if len(image.shape) == 3:
        gray_image = cv2.cvtColor(image, cv2.COLOR_BGR2GRAY)
    else:
        gray_image = image

    # Extract the red channel (assuming the ROI is drawn in red)
    red_channel = image[:, :, 2]

    # Threshold the red channel to create a binary mask of the ROI
    _, binary_roi = cv2.threshold(red_channel, 100, 255, cv2.THRESH_BINARY)

    # Find contours of the ROI
    contours, _ = cv2.findContours(binary_roi, cv2.RETR_EXTERNAL,
cv2.CHAIN_APPROX_SIMPLE)

    # Assume the largest contour is the oocyte ROI
    oocyte_contour = max(contours, key=cv2.contourArea)

    # Create a mask for the oocyte
    oocyte_mask = np.zeros_like(gray_image)
    cv2.drawContours(oocyte_mask, [oocyte_contour], -1, color=255, thickness=cv2.FILLED)

    # Define the periphery mask
    kernel = np.ones((3, 3), np.uint8)
    eroded_mask = cv2.erode(oocyte_mask, kernel, iterations=50) # Increased iterations for
larger periphery
    peripheral_mask = oocyte_mask - eroded_mask

    # Create the center mask

```

```

center_mask = eroded_mask

# Function to create region masks
def create_region_masks(image, oocyte_contour):
    height, width = image.shape[:2]
    center_x, center_y = width // 2, height // 2

    oocyte_mask = np.zeros((height, width), dtype=np.uint8)
    cv2.drawContours(oocyte_mask, [oocyte_contour], -1, color=255, thickness=cv2.FILLED)

    left_mask = np.zeros_like(oocyte_mask)
    right_mask = np.zeros_like(oocyte_mask)
    left_mask[:, :center_x] = 255
    right_mask[:, center_x:] = 255
    left_mask = cv2.bitwise_and(left_mask, oocyte_mask)
    right_mask = cv2.bitwise_and(right_mask, oocyte_mask)

    anterior_mask = np.zeros_like(oocyte_mask)
    posterior_mask = np.zeros_like(oocyte_mask)
    anterior_mask[:center_y, :] = 255
    posterior_mask[center_y:, :] = 255
    anterior_mask = cv2.bitwise_and(anterior_mask, oocyte_mask)
    posterior_mask = cv2.bitwise_and(posterior_mask, oocyte_mask)

    top_left_mask = cv2.bitwise_and(left_mask, anterior_mask)
    top_right_mask = cv2.bitwise_and(right_mask, anterior_mask)
    bottom_left_mask = cv2.bitwise_and(left_mask, posterior_mask)
    bottom_right_mask = cv2.bitwise_and(right_mask, posterior_mask)

    return {
        "left_mask": left_mask,
        "right_mask": right_mask,
        "anterior_mask": anterior_mask,
        "posterior_mask": posterior_mask,
        "top_left_mask": top_left_mask,
        "top_right_mask": top_right_mask,
        "bottom_left_mask": bottom_left_mask,
        "bottom_right_mask": bottom_right_mask
    }

region_masks = create_region_masks(image, oocyte_contour)

plt.figure(figsize=(12, 8))
plt.subplot(2, 4, 1)

```

```

plt.title('Left Mask')
plt.imshow(region_masks["left_mask"], cmap='gray')
plt.subplot(2, 4, 2)
plt.title('Right Mask')
plt.imshow(region_masks["right_mask"], cmap='gray')
plt.subplot(2, 4, 3)
plt.title('Anterior Mask')
plt.imshow(region_masks["anterior_mask"], cmap='gray')
plt.subplot(2, 4, 4)
plt.title('Posterior Mask')
plt.imshow(region_masks["posterior_mask"], cmap='gray')
plt.subplot(2, 4, 5)
plt.title('Top Left Quadrant')
plt.imshow(region_masks["top_left_mask"], cmap='gray')
plt.subplot(2, 4, 6)
plt.title('Top Right Quadrant')
plt.imshow(region_masks["top_right_mask"], cmap='gray')
plt.subplot(2, 4, 7)
plt.title('Bottom Left Quadrant')
plt.imshow(region_masks["bottom_left_mask"], cmap='gray')
plt.subplot(2, 4, 8)
plt.title('Bottom Right Quadrant')
plt.imshow(region_masks["bottom_right_mask"], cmap='gray')
plt.tight_layout()
plt.show()

# Save the masks as image files
base_filename = os.path.join(output_dir, os.path.splitext(image_name)[0])
cv2.imwrite(f'{base_filename}_oocyte_mask.tif', oocyte_mask)
cv2.imwrite(f'{base_filename}_peripheral_mask.tif', peripheral_mask)
cv2.imwrite(f'{base_filename}_center_mask.tif', center_mask)

for key, mask in region_masks.items():
    cv2.imwrite(f'{base_filename}_{key}.tif', mask)

return center_mask > 0, peripheral_mask > 0, region_masks

# Function to calculate the average intensity of a masked area in an image
def calculate_intensity(image, mask):
    masked_image = cv2.bitwise_and(image, image, mask=mask.astype(np.uint8))

    # Ensure mask is boolean before applying it
    masked_image = np.where(mask[..., None], masked_image, 0)

```

```
# Calculate mean intensity considering only non-zero pixels
intensity = np.mean(masked_image[masked_image != 0])
```

```
return intensity
```

```
# List of image file paths (replace these with actual paths to your images)
```

```
images = [  
    '/Users/kirstenebanks/new set/Mito 1 day old 1-1.tif',  
    '/Users/kirstenebanks/new set/Mito 1 day old 2-1.tif',  
    '/Users/kirstenebanks/new set/Mito 1 day old 3-1.tif',  
    '/Users/kirstenebanks/new set/Mito 30 day old 1-1.tif',  
    '/Users/kirstenebanks/new set/Mito 30 day old 2-1.tif',  
    '/Users/kirstenebanks/new set/Mito 30 day old 3-1.tif',  
    '/Users/kirstenebanks/new set/Mito 40 day old 1-1.tif',  
    '/Users/kirstenebanks/new set/Mito 40 day old 2-1.tif',  
    '/Users/kirstenebanks/new set/Mito 40 day old 3-1.tif',  
    '/Users/kirstenebanks/new set/Mito drp1 overexp 1-1.tif',  
    '/Users/kirstenebanks/new set/Mito drp1 overexp 2-1.tif',  
    '/Users/kirstenebanks/new set/Mito marf gd 1-1.tif',  
    '/Users/kirstenebanks/new set/Mito no actin 1-1.tif',  
    '/Users/kirstenebanks/new set/Mito no actin 2-1.tif',  
    '/Users/kirstenebanks/new set/Mito no actin 3-1.tif',  
    '/Users/kirstenebanks/new set/Mito no cytoskeleton 1-1.tif',  
    '/Users/kirstenebanks/new set/Mito no cytoskeleton 2-1.tif',  
    '/Users/kirstenebanks/new set/Mito no cytoskeleton 3-1.tif',  
    '/Users/kirstenebanks/new set/Mito no cytoskeleton 4-1.tif',  
    '/Users/kirstenebanks/new set/Mito no MT 1-1.tif',  
    '/Users/kirstenebanks/new set/Mito no MT 2-1.tif',  
    '/Users/kirstenebanks/new set/Mito no MT 3-1.tif',  
    '/Users/kirstenebanks/new set/Mito nos gal4 control 1-1.tif',  
    '/Users/kirstenebanks/new set/Mito nos gal4 control 2 -1.tif',  
    '/Users/kirstenebanks/new set/Mito nos gal4 control 3-1.tif',  
    '/Users/kirstenebanks/new set/Mito nos gal4 control 4-1.tif',  
    '/Users/kirstenebanks/new set/Mito spire control 1-1.tif',  
    '/Users/kirstenebanks/new set/Mito spire control 2-1.tif',  
    '/Users/kirstenebanks/new set/Mito spire control 3-1.tif',  
    '/Users/kirstenebanks/new set/Rab5 Image007 selected.tif',  
    '/Users/kirstenebanks/new set/Rab5 Image033 selected.tif',  
    '/Users/kirstenebanks/new set/Rab5 Image044 selected.tif',  
    '/Users/kirstenebanks/new set/Rab5 Image056 selected.tif',  
    '/Users/kirstenebanks/new set/Rab7 no actin 1-1.tif',  
    '/Users/kirstenebanks/new set/Rab7 no actin 2-1.tif',  
    '/Users/kirstenebanks/new set/Rab7 no actin 3-1.tif',  
    '/Users/kirstenebanks/new set/Rab7 Series002-2.tif',
```

```

/Users/kirstenebanks/new set/Rab7 Series003-2.tif',
/Users/kirstenebanks/new set/rab7 Series004-1.tif',
/Users/kirstenebanks/new set/Rab7 Series005-2.tif',
/Users/kirstenebanks/new set/Rab7 spire control 1-1.tif',
/Users/kirstenebanks/new set/Rab7 spire control 2-1.tif',
/Users/kirstenebanks/new set/Rab7 spire control 3-1.tif',
/Users/kirstenebanks/new set/Mito drp1 allele 1-1.jpg',
/Users/kirstenebanks/new set/Mito drp1 allele 2-1.jpg',
/Users/kirstenebanks/new set/Mito drp1 allele 3-1.jpg',
/Users/kirstenebanks/new set/Mito drp1 overexp 3-1.jpg',
/Users/kirstenebanks/new set/Mito drp1 overexp 4-1.jpg',
/Users/kirstenebanks/new set/Mito marf gd 3-1.jpg',
/Users/kirstenebanks/new set/Mito marf gd 4-1.jpg',
/Users/kirstenebanks/new set/Mito marf guo 1-1.jpg',
/Users/kirstenebanks/new set/Mito marf guo 2-1.jpg',
/Users/kirstenebanks/new set/Mito marf guo 3-1.jpg',
/Users/kirstenebanks/new set/Mito marf guo 4-1.jpg',
/Users/kirstenebanks/new set/Mito_DIC no cytoskeleton 1-1.tif',
/Users/kirstenebanks/new set/Mito_DIC no cytoskeleton 2-1.tif',
/Users/kirstenebanks/new set/Mito_DIC no cytoskeleton 3-1.tif',
/Users/kirstenebanks/new set/Mito_DIC no cytoskeleton 4-1.tif',
/Users/kirstenebanks/new set/Mito_DIC no MT 1-1.tif',
/Users/kirstenebanks/new set/Mito_DIC no MT 2-1.tif',
/Users/kirstenebanks/new set/Mito_DIC no MT 3-1.tif',
]

data = []

# Process each image
for image_path in images:
    image_name = os.path.splitext(os.path.basename(image_path))[0] # Extract image name
    without extension
    image = cv2.imread(image_path) # Load the image in color
    if image is not None:
        mask_center, mask_peripheral, region_masks = segment_image_from_roi(image,
image_name, output_dir)
        center_intensity = calculate_intensity(image, mask_center)
        peripheral_intensity = calculate_intensity(image, mask_peripheral)

        # Calculate intensities for the regions
        region_intensities = {region: calculate_intensity(image, mask) for region, mask in
region_masks.items()}

    # Append all intensities to the data list

```

```
        data.append([image_name, center_intensity, peripheral_intensity] +
list(region_intensities.values()))
    else:
        print(f"Could not load image at path: {image_path}")

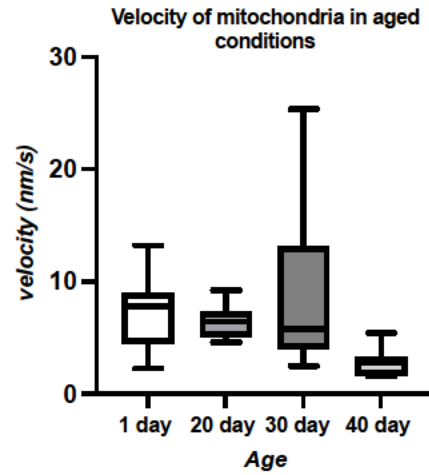
# Define the column names for the DataFrame
columns = ['File Name', 'Center Intensity', 'Peripheral Intensity'] + list(region_masks.keys())

# Create a DataFrame and save it to an Excel file
df = pd.DataFrame(data, columns=columns)
output_excel_path = os.path.join(output_dir, 'intensity_data.xlsx')
df.to_excel(output_excel_path, index=False)

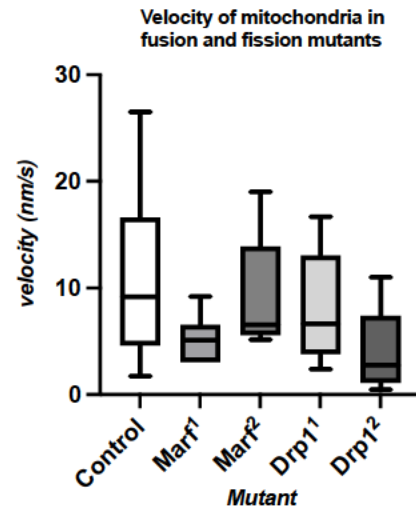
print(f"Intensity data saved to {output_excel_path}")
```

Section 4. Raw data – DDM values of velocity ( $nm s^{-1}$ ) and diffusivity ( $\mu m^{-2} s^{-1} \times 10^{-3}$ ) for each oocyte, respective box plots and single-particle tracking velocities from which mean  $\pm$  SD was calculated and compared.

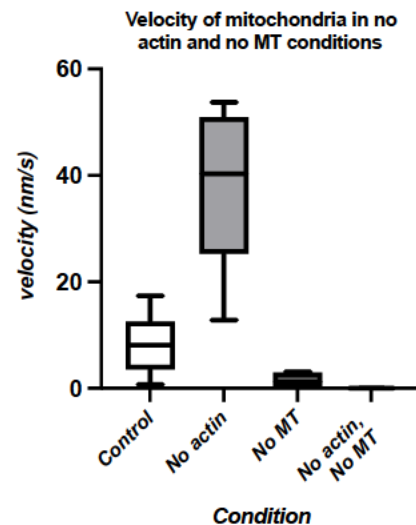
		Velocity ( $nm s^{-1}$ )			
		1 day	20 day	30 day	40 day
Mitochondria		7.0147	7.4738	2.4690	1.5710
		5.7514	4.8810	25.3642	2.8171
		13.2209	4.5542	15.3164	2.9205
		7.9185	9.1925	10.9052	1.6329
		8.4858	6.833	6.6529	3.5005
		9.4605	5.2517	4.5326	5.3813
		7.8034	7.0530	5.7711	2.8438
		3.1135	5.7130	5.7187	2.2358
		2.2261	6.3784	3.3801	1.5529



		Velocity ( $nm s^{-1}$ )				
		<i>nosGal4</i>	<i>Marf1</i>	<i>Marf2</i>	<i>Drp1<sup>1</sup></i>	<i>Drp1<sup>2</sup></i>
Mitochondria		17.0000	5.6700	19.0000	13.9000	8.6200
		5.8200	9.2100	6.5300	16.7000	11.0000
		8.7700	5.1800	8.8100	3.1700	3.2300
		26.5000	3.0500	5.1600	2.3800	6.9900
		9.6000	3.0400	5.9500	6.6100	2.8800
		15.5000	5.0600		5.6600	0.8540
		1.7300			10.6000	1.1900
		4.1800			6.6400	0.4580
						1.4800
						2.6600

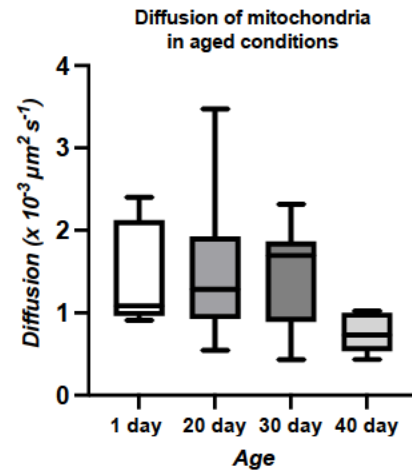


		Velocity ( $nm s^{-1}$ )			
		<i>spire</i> (ctrl)	<i>spire</i>	+ colchicine	<i>spire</i> + colchicine
Mitochondria		17.4000	44.3000	3.1500	0.0188
		3.5200	51.6000	0.00169	0.0604
		0.7290	36.4000	2.4400	
		12.6000	12.8000	0.00108	
		8.3600	53.7000		
		6.1200	22.6000		
		8.1400	49.1000		
			33.2000		

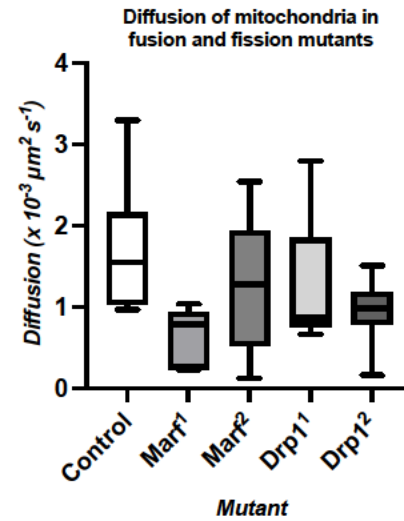




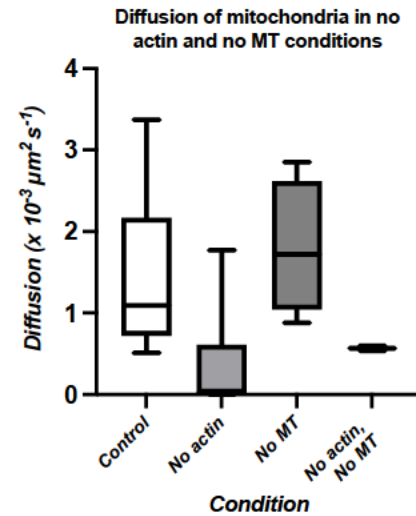
Diffusion ( $\mu\text{m}^2\text{s}^{-1} \times 10^{-3}$ )				
Mitochondria	1 day	20 day	30 day	40 day
	1.0845	0.5462	0.4329	1.0194
	2.4003	1.9664	1.8499	0.7325
	0.9757	1.6489	1.0439	0.6008
	1.9728	1.8859	2.3196	0.4342
	1.6616	0.8129	1.6969	0.6929
	2.2740	1.0396	1.8768	0.471
	0.9092	1.2590	0.7366	0.9133
	1.0520	3.4762	1.7819	0.981
	0.9485	1.2865	1.5043	1.0231



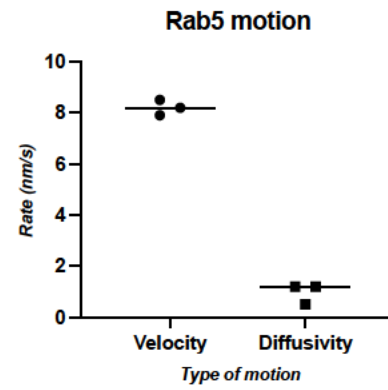
Diffusion ( $\mu\text{m}^2\text{s}^{-1} \times 10^{-3}$ )					
Mitochondria	<i>nosGal4</i>	<i>Marf</i> <sup>1</sup>	<i>Marf</i> <sup>2</sup>	<i>Drp1</i> <sup>1</sup>	<i>Drp1</i> <sup>2</sup>
	3.3000	0.2330	0.9260	0.7540	0.1650
	1.4900	0.7280	1.3500	0.8600	0.6320
	1.6200	0.2380	0.1240	2.1600	1.1800
	1.0300	0.9070	2.5400	0.7660	0.8950
	1.0400	0.8500	1.2800	2.8000	0.8320
	1.6700	1.0400		0.9540	0.8420
	0.9700			0.8820	1.0700
	2.3300			0.6660	1.5100
					1.2000
					1.1500



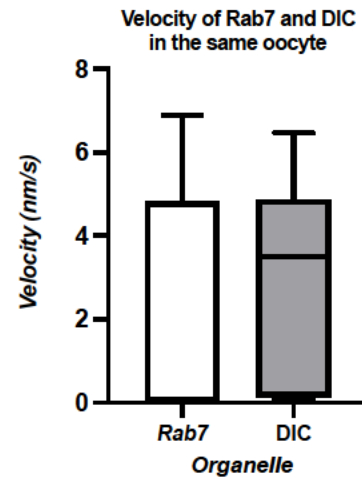
Diffusion ( $\mu\text{m}^2\text{s}^{-1} \times 10^{-3}$ )				
Mitochondria	<i>spire</i> (ctrl)	<i>spire</i>	+ colchicine	<i>spire</i> + colchicine
	0.7210	0.00701	2.8500	0.6000
	1.0900	0.0252	0.8830	0.5390
	3.3700	1.7700	1.9200	
	2.1700	0.7450	1.5200	
	0.5120	0.0325	2.8500	
	1.3100	0.2140		
	0.9360			
	0.7210			



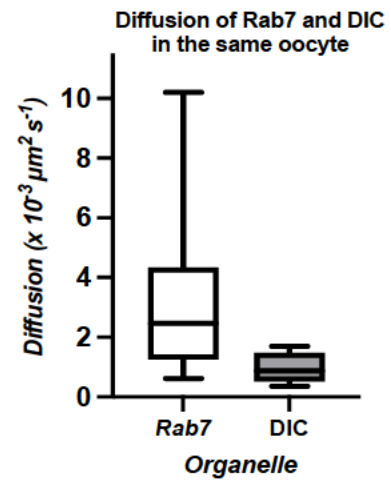
Rab5	Velocity ( $nm\ s^{-1}$ )	Diffusion ( $\mu m^{-2}\ s^{-1} \times 10^{-3}$ )
	1 day	1 day
	8.200	0.500
	7.900	1.200
	8.500	1.200



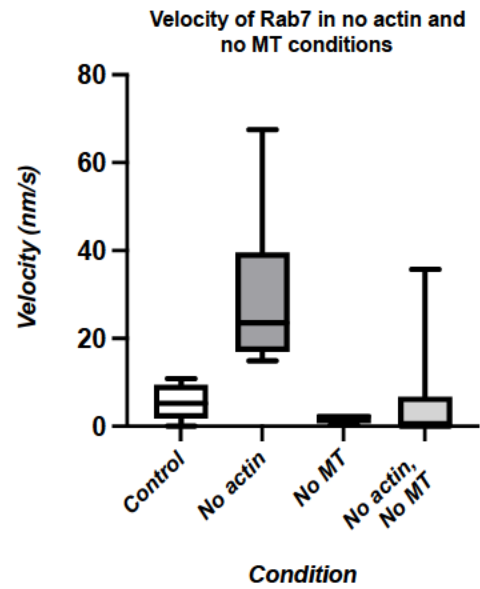
Rab7	Velocity ( $nm\ s^{-1}$ )	Diffusion ( $\mu m^{-2}\ s^{-1} \times 10^{-3}$ )
	1 day	1 day
	6.8900	2.4100
	3.81e-011	10.2000
	0.0000137	5.0500
	0.0000128	3.6200
	0.00748	2.4700
	3.1100	1.4800
	0.000324	3.0100
	6.5300	0.6140
	0.0159	1.0200



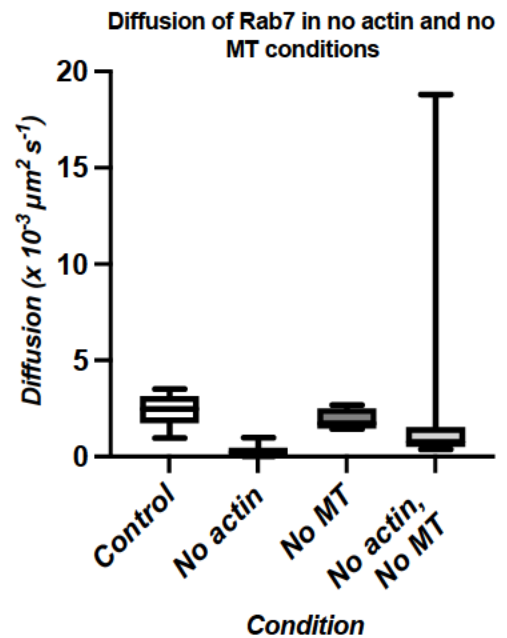
Rab7 - DIC	Velocity ( $nm\ s^{-1}$ )	Diffusion ( $\mu m^{-2}\ s^{-1} \times 10^{-3}$ )
	1 day	1 day
	6.4700	0.3580
	5.2400	1.1200
	0.2140	1.4200
	0.1670	1.7000
	4.3100	0.7620
	3.5000	0.8760
	0.0995	1.5400
	4.5000	0.4200
	0.0918	0.6110



Rab7	Velocity ( $nm\ s^{-1}$ )			
	<i>spire</i> (ctrl)	<i>spire</i>	+ colchicine	<i>spire</i> + colchicine
	3.5500	26.5000	2.5600	0.0651
	8.0800	15.4000	1.9100	0.0217
	10.8000	33.3000	0.3290	0.000337
	0.0028	21.0000	2.7300	4.18e-07
	5.2300	26.1000		3.24
		17.5000		35.7
		18.6000		6.79
		14.9000		
		67.5000		
		58.5000		

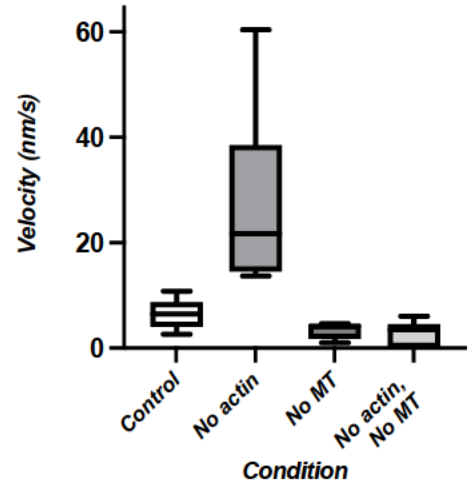


Rab7	Diffusion ( $\mu m^{-2}\ s^{-1} \times 10^{-3}$ )			
	<i>spire</i> (ctrl)	<i>spire</i>	+ colchicine	<i>spire</i> + colchicine
	2.7800	0.000875	1.4700	0.5130
	2.4800	0.3190	1.4300	1.2700
	3.5100	0.1630	2.6800	18.8000
	2.4800	0.0394	1.9900	0.5780
	0.9640	0.0610		0.7650
		0.2760		1.5200
		0.5380		0.3790
		0.4280		
		0.9800		
		0.0782		



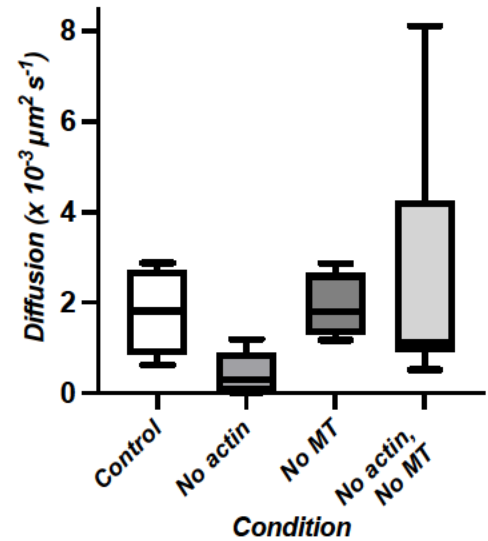
Rab7 - DIC	Velocity ( $nm\ s^{-1}$ )			
	<i>spire</i> (ctrl)	<i>spire</i>	+ colchicine	<i>spire</i> + colchicine
	5.4100	24.8000	4.6400	0.00338
	6.4600	14.4000	0.9770	3.5500
	10.8000	34.5000	4.2100	0.0292
2.6400	18.7000	4.0900	0.00779	
6.6600	26.1000		3.5100	
	14.6000		6.0300	
	18.4000		4.6000	
	13.7000			
	60.4000			
	50.6000			

Velocity of DIC vesicles in YFP::*Rab7* oocytes in no actin and no MT conditions



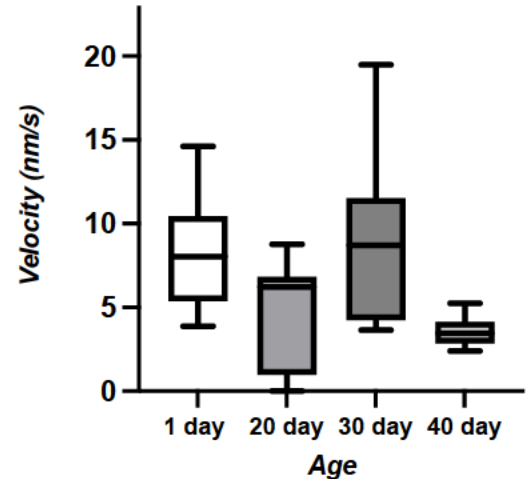
Rab7 - DIC	Diffusion ( $\mu m^2\ s^{-1} \times 10^{-3}$ )			
	<i>spire</i> (ctrl)	<i>spire</i>	+ colchicine	<i>spire</i> + colchicine
	1.8200	0.4250	1.1700	0.5240
	2.5600	0.0174	1.6300	1.3300
	2.8700	0.0220	2.8600	4.2400
1.1000	0.0890	1.9900	0.9380	
0.6220	0.0243		0.9260	
	1.1900		8.1000	
	0.6040		1.1100	
	0.1690			
	0.8160			
	1.0900			

Diffusivity of DIC vesicles in YFP::*Rab7* oocytes in no actin and no MT conditions

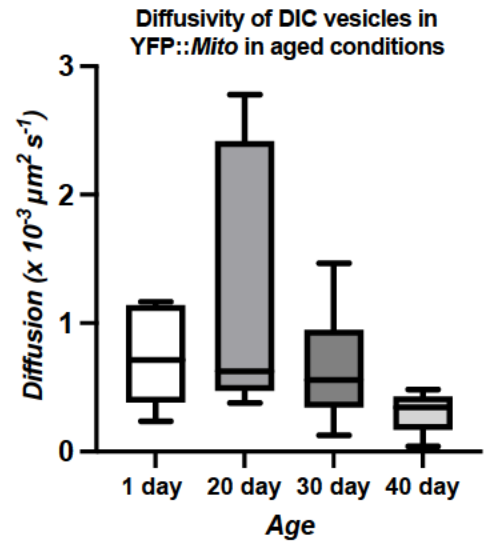


Mitochondria - DIC	Velocity ( $nm\ s^{-1}$ )			
	1 day	20 day	30 day	40 day
	8.0358	8.7610	3.6492	2.8533
	11.1384	1.5113	19.4844	4.1782
	14.6205	0.4105	10.1892	3.8035
	9.7824	6.2106	11.8005	2.4104
	8.1337	6.8528	11.2426	4.1054
	7.7271	4.7859	3.9276	5.242
	6.077	6.3657	5.7594	3.4506
	3.8728	0.0034	8.7129	3.4129
4.6798	6.7970	4.5445	2.8532	

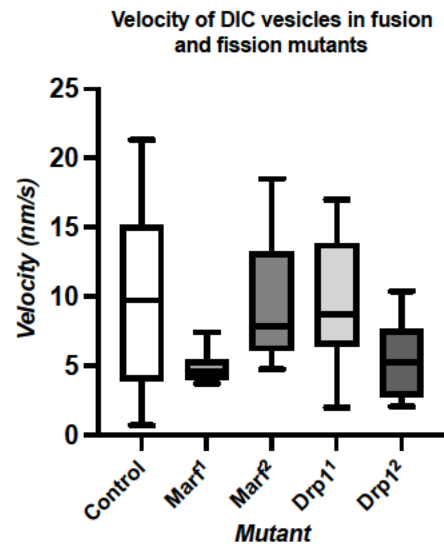
Velocity of DIC vesicles in YFP::*Mito* in aged conditions



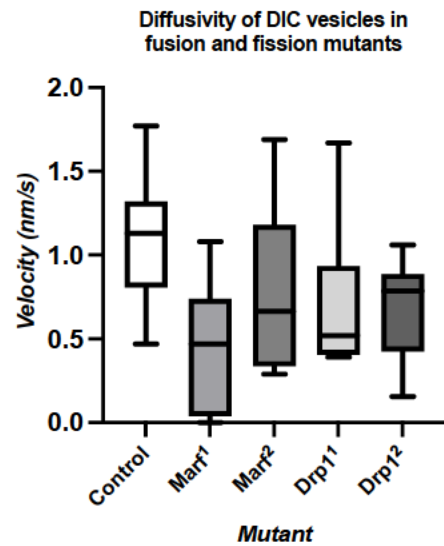
Diffusion ( $\mu\text{m}^2 \text{s}^{-1} \times 10^{-3}$ )				
Mitochondria - DIC	1 day	20 day	30 day	40 day
	0.5135	0.4810	0.1271	0.4233
	1.1658	2.1349	0.4588	0.191
	0.2672	2.6372	0.5566	0.2163
	1.0212	2.1940	0.9032	0.0423
	1.1145	0.3799	0.7383	0.3444
	1.1663	0.4595	1.4672	0.1476
	0.7139	0.6001	0.2419	0.4847
	0.4943	2.7786	0.4449	0.4337
	0.2373	0.6255	0.994	0.4233



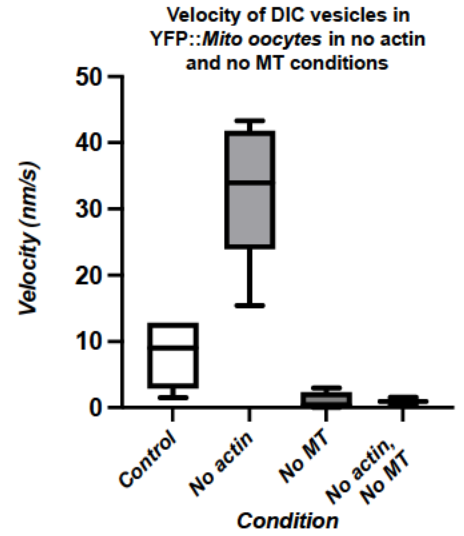
Mitochondria - DIC	Velocity ( $\text{nm s}^{-1}$ )				
	<i>nosGal4</i>	<i>Marf1</i>	<i>Marf2</i>	<i>Drp11</i>	<i>Drp12</i>
	16.1000	4.6300	18.5000	15.1000	8.4400
	9.7900	7.4200	7.8400	17.0000	10.4000
	6.9700	4.8400	7.9200	6.3400	6.4000
	21.3000	4.6200	4.7500	2.0000	7.4000
	9.6900	4.1100	7.4500	9.3500	2.7900
	12.5000	3.7200		6.6700	2.7900
	0.7120			10.2000	3.9800
	2.8900			8.1400	4.5200
					2.0700
					5.940



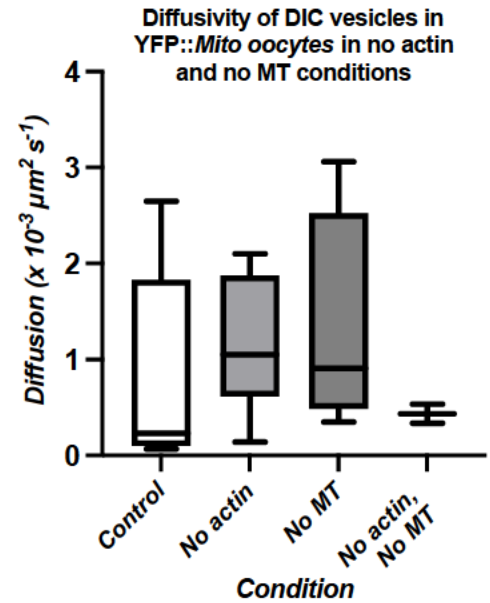
Mitochondria - DIC	Diffusion ( $\mu\text{m}^2 \text{s}^{-1} \times 10^{-3}$ )				
	<i>nosGal4</i>	<i>Marf1</i>	<i>Marf2</i>	<i>Drp11</i>	<i>Drp12</i>
	1.3400	0.000124	0.2890	0.3950	0.1560
	0.7210	0.5710	0.6640	0.4680	0.8700
	1.1200	0.0510	0.6710	1.0100	0.3490
	1.1400	0.3690	1.6900	0.7140	0.9420
	0.4700	0.6250	0.3820	1.6700	0.8090
	1.2600	1.0800		0.5710	0.4770
	1.0600			0.3900	0.8090
	1.7700			0.4340	0.4490
					1.0600
					0.7610



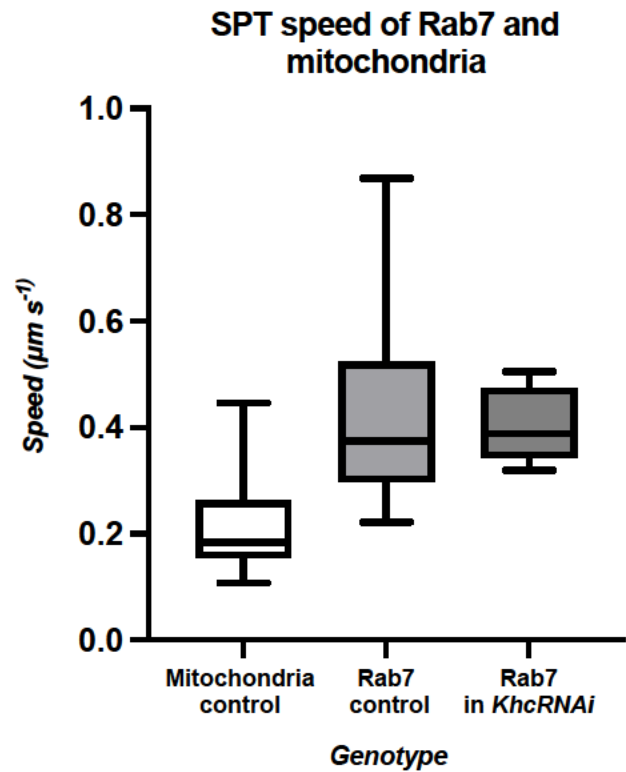
Mitochondria - DIC	Velocity ( $nm\ s^{-1}$ )			
	<i>spire</i> (ctrl)	<i>spire</i>	+ colchicine	<i>spire</i> + colchicine
	12.8000	41.9000	0.0394	1.5800
	6.3400	41.3000	0.4820	0.3350
	1.5000	27.1000	2.9800	
12.8000	15.4000	0.1850		
	9.0400	43.3000		
	2.9100	22.8000		
	9.1200	35.4000		
		32.5000		



Mitochondria - DIC	Diffusion ( $\mu m^{-2}\ s^{-1} \times 10^{-3}$ )			
	<i>spire</i> (ctrl)	<i>spire</i>	+ colchicine	<i>spire</i> + colchicine
	0.2880	0.5940	3.0600	0.3360
	0.0670	1.8900	0.3480	0.5340
	2.6500	1.2300	0.8950	
0.1270	0.1380	0.9200		
	0.0973	1.8300		
	1.8300	0.8740		
	0.2300	2.1000		
		0.6800		



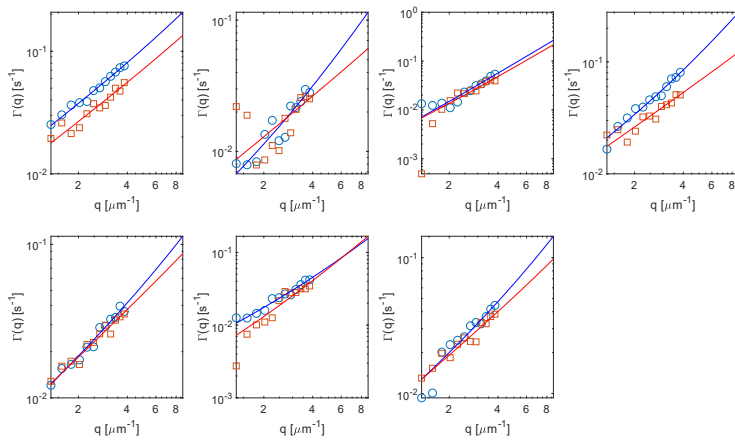
<i>Single-particle tracking values (<math>\mu\text{m s}^{-1}</math>)</i>			
Wildtype			<i>KhcRNAi</i>
Mitochondria	Rab7		Rab7
0.154	0.450	0.319	0.395
0.171	0.350	0.279	0.319
0.424	0.331	0.286	0.330
0.107	0.641	0.577	0.378
0.154	0.372	0.602	0.505
0.190	0.703	0.519	0.490
0.137	0.336	0.260	0.381
0.184	0.596	0.498	0.430
0.196	0.630	0.246	
0.446	0.375	0.312	
0.372	0.633	0.260	
0.159	0.523	0.230	
0.125	0.340	0.268	
0.190	0.349	0.233	
0.143	0.420	0.310	
0.263	0.353	0.340	
0.269	0.585	0.255	
0.257	0.285	0.677	
0.170	0.523	0.346	
	0.406	0.458	
	0.294	0.516	
	0.222	0.392	
	0.368	0.468	
	0.391	0.474	
	0.297	0.239	
	0.555	0.278	
	0.483	0.523	
	0.868	0.356	
	0.326	0.258	
	0.648	0.517	
	0.659	0.551	
	0.538		



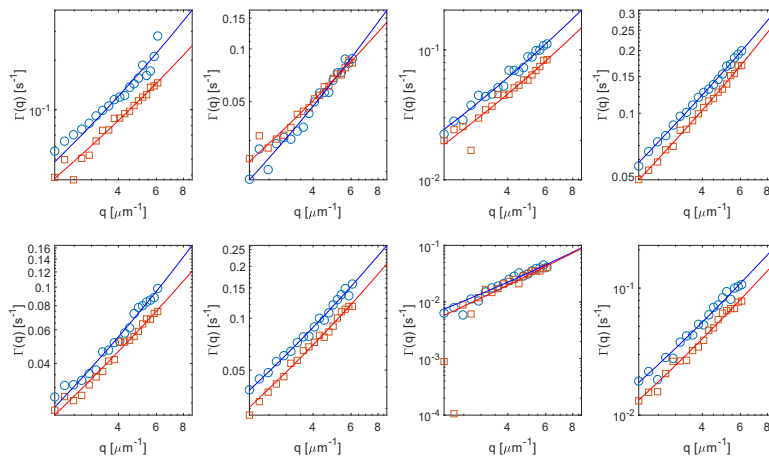
Section 5. Example DDM decorrelation rates  $\Gamma_1(q)$  and  $\Gamma_2(q)$  plotted against the wave vector  $q$  for YFP-tagged organelles and DIC vesicles for each experimental condition.

$\Gamma_1(q)$ , which accounts for the ballistic contribution to the motion of the vesicles (orange squares), exhibits a linear scaling  $\Gamma_1(q) = v_{ves}q$  while  $\Gamma_2(q)$  describes a diffusive-like relaxation process (blue squares) and is fitted to a quadratic law  $\Gamma_2(q) = D_{ves}q^2$ .

*spire.mito* (control)

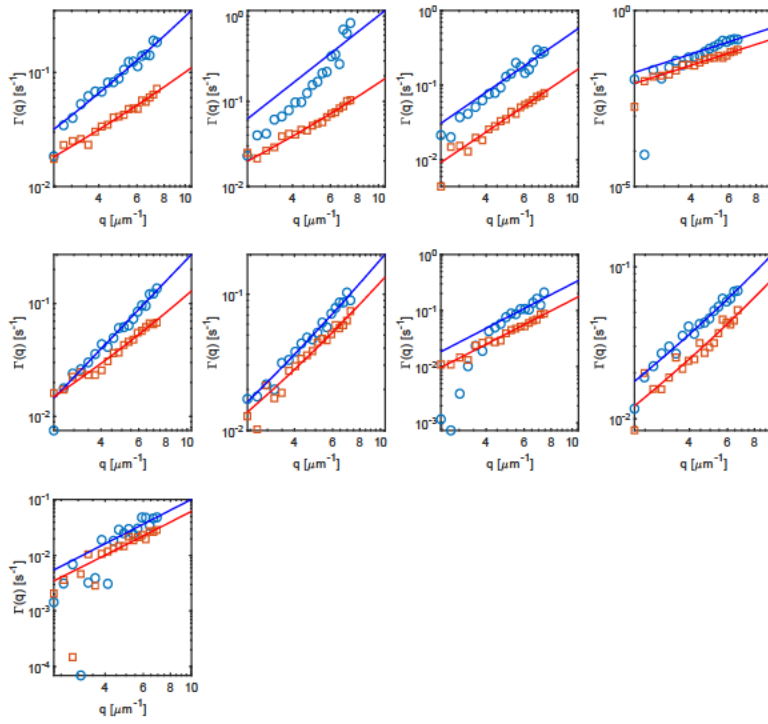


*nos.mito* (control)

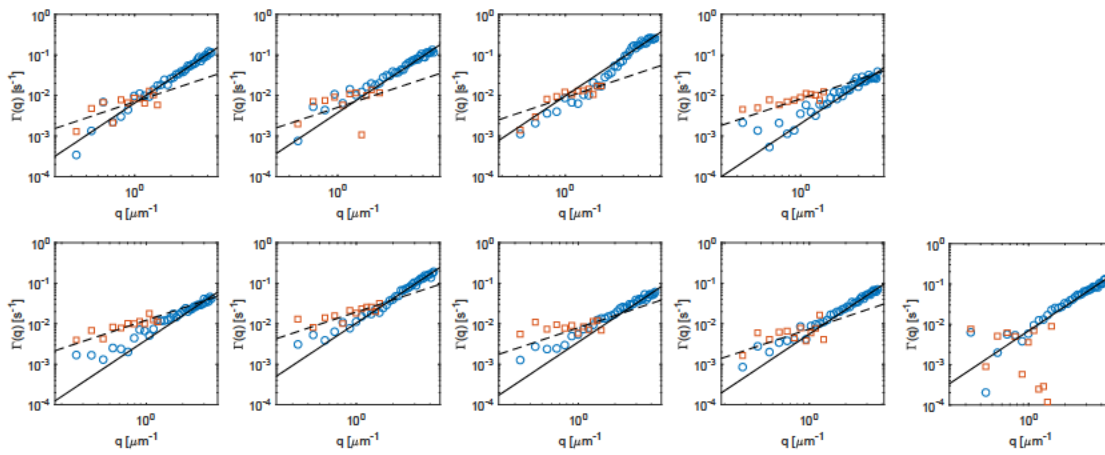




### Rab7 (control)



### Mitochondria (1-day)



Section 6. Attempt to enhance edges of mitochondria in mutant backgrounds using the Fiji (ImageJ) "Find Edges" function.

